

A Thesis Submitted for the Degree of PhD at the University of Warwick

Permanent WRAP URL:

<http://wrap.warwick.ac.uk/152661>

Copyright and reuse:

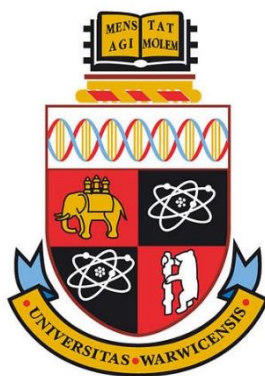
This thesis is made available online and is protected by original copyright.

Please scroll down to view the document itself.

Please refer to the repository record for this item for information to help you to cite it.

Our policy information is available from the repository home page.

For more information, please contact the WRAP Team at: wrap@warwick.ac.uk



Electrochemical and Scanning Probe Studies of Active Pharmaceutical Ingredient Release from Polymer-Coated Multiparticulate Oral Dosage Forms

Shrina Bhagat

*Thesis submitted to the University of Warwick
for the degree of Doctor of Philosophy*

Supervisor: Prof. Patrick R. Unwin

Molecular Analytical Science Centre for Doctoral Training

Department of Chemistry

December 2020



For my loving family

“Science and everyday life cannot and should not be separated”

– Dr. Rosalind Franklin

Acknowledgements

Firstly, I would like to sincerely thank my supervisor, Prof Patrick Unwin for giving me the opportunity to be part of the Warwick Electrochemistry and Interfaces Group, and for his invaluable support and encouragement throughout my PhD. I would also like to thank Prof Julie Macpherson for inspiring me to pursue a PhD in electrochemistry.

I would like to thank my industrial supervisors from Pfizer: Dr Fiona Harvey-Doyle and Dr Lourdes Contreras and AstraZeneca: Dr James Mann. I would also like to thank the members of staff from the MAS CDT: Naomi Grew, Dr Nikola Chmel, and Prof Steven Brown.

I would like to truly thank several postdocs: Dr Ian McPherson, Dr Alan Wemyss and Dr David Perry for their time, patience, incredible guidance, and expertise, as well as fellow PhD students turned doctors: Dr Faduma Maddar, Dr Bryn Jones, Dr James Teahan and Dr Lee Simcox for their advice, friendship, and support.

I would like to thank current and past members of the Warwick Electrochemistry and Interfaces Group and the MAS CDT, particularly, Enrico Daviddi, Dr Slava Shkirskiy, Dr Gabriel Meloni, Dr Haytham Hussein, Georgia Wood, Emily Braxton, Dr Ashley Page, and Dr Rob Johnson.

Finally, I would like to thank my family for their love and support, without whom I would not be where I am today. To my parents who instilled a passion for learning, I am truly grateful for all you have done for me. My sisters and my brother who have always encouraged me and kept my spirits up. Last but not least, my best friend for always making me laugh.

Declaration

This thesis is submitted to the University of Warwick in support of my application for the degree of Doctor of Philosophy. I confirm that this thesis has been composed by myself and has not been submitted in any previous application for any degree. The work presented (including data generated and data analysis) was carried out by the author except in the cases outlined below:

The Kollicoat[®] Smartseal 30 D polymer used throughout this this thesis was supplied by BASF, Ludwigshafen, Germany. The multiparticulate oral dosage form samples used throughout this thesis were made by Dr Lourdes Contreras (Pfizer) and myself at Pfizer, Sandwich, Kent UK.

Chapter 3: The SEM images in were taken by myself under the supervision of Haytham Hussein during my Masters research project and were submitted to the University of Warwick as part of my MSc degree. The optical images for the particle size distribution only were taken by Blane Keating.

Chapter 4: Preliminary data not shown in this thesis and partial results of the acetate and citrate buffer were collected by Jordan Curtis under my supervision. These were submitted as part of his MChem thesis at the University of Warwick.

Chapter 5: The polymer film coated glass slide samples for AFM analysis (partially for SICM analysis in Chapter 6) and the polymer suspension samples for DMA and NMR analysis were made by myself with the help of Dr Alan Wemyss. The NMR data were collected by Dr Ivan Prokes. The NMR spectra were analysed with the help of Alan Wemyss. GPC data was analysed with the help of Dr Alan Wemyss and James Town.

Chapter 6: The FEM modelling was undertaken by James Teahan. The model detailed was also used as part of his PhD thesis submission to the University of Warwick. The STEM images of the nanopipette were taken by Gabriel Meloni. The MATLAB[®] script used to analyse the SICM charge mapping data was written by David Perry.

The work presented in Chapters 3, 4 and 5 are being prepared for publication, of which I am the first author.

CONTENTS

Acknowledgements	i
Declaration	ii
Abbreviations	viii
Glossary of Symbols	xi
List of Figures	xiii
List of Tables	xxiii
Abstract	xxv
CHAPTER 1: Introduction	1
1.1. Oral Dosage Forms	2
1.1.1. Multiparticulate Formulations.....	3
1.1.2. Polymer-Coated Multiparticulates	4
1.2. Taste Masking	5
1.2.1. Taste Masking Techniques.....	5
1.2.2. Taste Masking Manufacturing Processes	6
1.3. Stimuli Responsive Polymers	9
1.3.1. pH Responsive Polymers	10
1.3.2. Kollicoat® Smartseal 30 D	12
1.3.3. Polymer Film Formation	14
1.3.4. Drug Release Mechanisms	15
1.4. Traditional Dissolution Testing	17
1.5. Electroanalytical Methods	19
1.5.1. Potentiometry	19
1.5.2. Dynamic Electrochemistry	21
1.5.3. Electrochemical Analysis of Pharmaceuticals	34
1.6. Scanning Probe Microscopy (SPM)	37

1.6.1. Atomic Force Microscopy (AFM)	37
1.6.2. Scanning Ion-Conductance Microscopy (SICM).....	40
1.7. Research Aims	45
1.8. References	47
CHAPTER 2: Experimental.....	58
2.1. Chemicals and Materials	59
2.2. Preparation of Multiparticulate Formulation Beads	62
2.3. Preparation of Isolated Polymer Films	64
2.4. Electrode and Nanopipette Fabrication	67
2.4.1. Ultramicroelectrode Fabrication	67
2.4.2. Microwire Electrode (MWE) Fabrication	68
2.4.3. Nanopipette Fabrication for SICM.....	69
2.5. Instrumentation, Analysis and Characterisation	70
2.5.1. Characterisation of Microelectrodes	70
2.5.2. Scanning Ion Conductance Microscopy Set up.....	71
2.5.3. Atomic Force Microscopy.....	71
2.5.4. Nuclear Magnetic Resonance (NMR)	72
2.5.5. Dynamic Mechanical Analysis (DMA).....	73
2.5.6. Field Emission - Scanning Electron Microscopy	75
2.6. References	76
CHAPTER 3: Multiparticulate Formulations: Single Bead Dissolution Analysis	78
3.1. Introduction	79
3.2. Experimental.....	81
3.2.1. Multiparticulate Formulation Samples.....	81
3.2.2. Sample Imaging using Optical and Scanning Electron Microscopy	82

3.2.3. Dissolution Media Solutions	83
3.2.4. Electrochemical Materials and Instrumentation.....	83
3.3. Results and Discussion	85
3.3.1. Size Distribution of Multiparticulate Beads.....	85
3.3.2. Cyclic Voltammetry on Total Dissolution of Acetaminophen only Single Multiparticulate Bead	95
3.3.3. Direct Acetaminophen Detection from a Single Polymer-Coated Multiparticulate Bead	99
3.4. Further work	108
3.5. Conclusions	109
3.6. References	110

CHAPTER 4: *In Situ* Rotating Disc Electrode Dissolution Measurement of Acetaminophen from Suspended Polymer-Coated Multiparticulates

4.1. Introduction	115
4.2. Experimental.....	117
4.2.1. Multiparticulate Formulation	117
4.2.2. Dissolution Solution Media.....	117
4.2.3. Electrochemical Materials and Rotating Disc Electrode Instrumentation ...	119
4.2.4. Rotating Disc Electrode Detection Method of Acetaminophen.....	120
4.3. Results and Discussion	121
4.3.1. Rotating Disc Electrode Calibration for HCl and Simulated Saliva Dissolution Media.....	121
4.3.2. Effect of pH and Temperature on Dissolution in HCl Media	124
4.3.3. Dissolution Rate in HCl and Simulated Saliva Media	130
4.3.4. Rotating Disc Electrode Calibration for Acetate and Citrate Buffer Dissolution Media.....	135
4.3.5. Effect of Acetate, Citrate and Simulated Saliva Buffered Media on Dissolution	136

4.3.6. Estimation of Timescale for the Protonation of the KCSS Polymer Surface	143
4.4. Conclusions	147
4.5. References	148

CHAPTER 5: Microstructural Characterisation of the Kollicoat® Smartseal 30D Polymer Film During Dissolution.....152

5.1. Introduction	153
5.2. Experimental.....	155
5.2.1. Solutions.....	155
5.2.2. Preparation of Polymer Film Glass Slides	155
5.2.3. AFM and Optical Microscopy.....	155
5.2.4. AFM Image Analysis using SPIP™.....	156
5.2.5. NMR Sample Preparation and Spectroscopy	157
5.2.6. Dynamic Mechanical Analysis (DMA).....	157
5.3. Results and Discussion	158
5.3.1. Dissolution of Isolated Films	158
5.3.2. Dissolution Comparison of Polymer Isolated Films to Polymer Coated Multiparticulates.....	171
5.3.3. ¹ H NMR of Acid Treated Kollicoat® Smartseal 30 D Emulsion	173
5.4. Conclusions	175
5.5. References	176

CHAPTER 6: Surface Charge Mapping of Polymer-Coated Multiparticulates: The Application of Scanning Ion Conductance Microscopy.....179

6.1. Introduction	180
6.1.1. Surface Charge and the Electric Double Layer	182
6.1.2. Ion Current Response	184
6.2. Experimental.....	187

6.2.1. Solutions.....	187
6.2.2. Substrate Preparation.....	187
6.2.3. Nanopipettes and Electrodes	188
6.2.4. Scanning Ion Conductance Microscopy Instrumentation	188
6.2.5. Scanning Ion Conductance Microscopy Maps.....	189
6.2.6. Atomic Force Microscopy.....	189
6.2.7. Finite Element Method Simulations.....	189
6.3. Results and Discussion	190
6.3.1. Topographical Mapping of Polymer Film on a Glass Slide.....	190
6.3.2. Simultaneous Topographical and Surface Charge Mapping of a Single Multiparticulate in various pHs.....	191
6.4. Conclusions	202
6.5. References	203
 CHAPTER 7: Conclusions	 206
 APPENDIX	 I

Abbreviations

AC	Alternating Current
AFM	Atomic Force Microscopy
APAP	Acetaminophen, Paracetamol
API	Active Pharmaceutical Ingredient
Ag/AgCl	Silver/Silver Chloride Reference Electrode
Au	Gold
BHT	Butylated Hydroxy Toluene
C–C	Carbon-Carbon
Conc.	Concentration
CV	Cyclic Voltammogram
DEAEMA	2-(Diethylamino)ethyl Methacrylate
DC	Direct Current
DDL	Diffuse Double Layer
DM	Dissolution media
DMA	Dynamic Mechanical Analysis/Analyser
EDL	Electric Double Layer
FcTMA⁺	(Ferrocenylmethyl)trimethylammonium
FEM	Finite Element Method
FeSSGF	Fed State Simulated Gastric Fluid
FeSSIF	Fed State Simulated Intestinal Fluid
GI	Gastrointestinal
HCl	Hydrochloric Acid
HPLC	High-performance liquid chromatography
ICR	Ion Current Rectification
ID	Inner Diameter
ISE	Ion Selective Electrode
<i>i-t</i>	Current-Time
IHP/OHP	Inner/Outer Helmholtz Plane
KCl	Potassium Chloride
KCSS	Kollicoat [®] Smartseal 30 D
mag	Magnification
MCC	Microcrystalline Cellulose
MFFT	Minimum Film Forming Temperature

min	Minute
MMA	Methyl Methacrylate
MP	Multiparticulate
MPF	Multiparticulate Formulation
MWE	Microwire Electrode
N	Number of samples taken
NAPQI	N-acetyl-p-benzoquinone imine
NMR	Nuclear Magnetic Resonance
OD	Outer Diameter
PDEAEMA	Poly (2-(Diethylamino)ethyl Methacrylate)
PLGA	Poly (Lactic-co-Glycolic Acid)
PMMA	Poly (Methyl Methacrylate)
Pt	Platinum
PTFE	Polytetrafluoroethylene
QRCE	Quasi Reference Counter Electrode
RDE	Rotating Disk Electrode
RE	Reference Electrode
SCE	Saturated Calomel Electrode
SD	Standard Deviation
SEM	Scanning Electron Microscopy
SICM	Scanning Ion Conductance Microscopy
SIF	Simulated Intestinal Fluid
SIR	Surface Induced Rectification
SPM	Scanning Probe Microscopy
STEM	Scanning Transmission Electron Microscopy
SS	Simulated Saliva
TBD	Tip to Bead Distance
TEC	Triethyl citrate
T_g	Glass Transition Temperature
UME	Ultramicroelectrode
USP	United States Pharmacopoeia
UV	Ultra-Violet

WE Working Electrode
WD Working Distance

Glossary of Symbols

Symbol	Meaning
a	Activity of Species
γ	Activity Coefficient
A	Ampere
A	Area of Electrode
a	Electrode Radius
atm	Atmospheric Pressure
\varnothing	Diameter
C / C^*	Concentration / Bulk Concentration
C_s	Concentration of Species
d	Distance
D	Diffusion Coefficient
D_{H^+}	Proton Diffusion Coefficient
D_{APAP}	APAP Diffusion Coefficient
δ	Diffusion Length
δ_H	Hydrodynamic Boundary Layer
η	Dynamic Viscosity
E	Potential or Electrode Potential
E^0	Standard Rate Constant
E_a	Activation Energy
F	Faradays Constant
i	Current
i_{lim}	Limiting / Steady State Current
i_p	Peak Current
J	Flux
k	Rate Constant
k_t	Mass Transport Coefficient
k_r	Electron Transfer Coefficient
n	Number of Electrons
R	Molar Gas Constant

Symbol	Meaning
s	Second
σ	Surface Charge Density
τ	Breakthrough Time
t	Time
T	Temperature
v	Velocity
ω	Angular Velocity
V	Volt

List of Figures

Chapter 1

Figure 1.1. Regions of the gastrointestinal tract.....	2
Figure 1.2. Schematic of matrix and reservoir coated multiparticulate formulation ..	4
Figure 1.3. Classification of patented taste masking coatings	5
Figure 1.4. Various types of fluid bed coaters	7
Figure 1.5. Wurster fluidised bed spray coating system	7
Figure 1.6. Common stimuli and responses of smart polymers	9
Figure 1.7. Schematic of a drug loaded particle in a polybasic polymer coating, shown in a neutral to basic pH environment and in an acidic environment.....	11
Figure 1.8. Methyl methacrylate and diethylaminoethyl methacrylate copolymer, Kollicoat [®] Smartseal 30 D polymer structure	12
Figure 1.9. Schematic of film formation mechanism from aqueous polymer dispersions.....	14
Figure 1.10. Schematic of USP Apparatus I and II.....	17
Figure 1.11. Schematic of standard three electrode electrolytic cell (not to scale)...	21
Figure 1.12. Schematic of electron transfer and mass transport pathway at the surface of an electrode. (Adapted from Bard and Faulkner, 2001). ⁸⁶	23
Figure 1.13. Illustration of diffusion layer at an electrode in 1D, where δ is the length of the diffusion layer. ⁸⁶	24
Figure 1.14. Diffusion field profiles for a) macroelectrode, b) microelectrode and c) hemispherical electrode.....	25
Figure 1.15. Schematic of electric double layer at the electrode-solution interface for a positively charged electrode.	28
Figure 1.16. Cyclic voltammogram for an oxidation process again	29
Figure 1.17. Cyclic voltammogram for an oxidation process at a disc UME.....	30

Figure 1.18. Schematic of rotating disc electrode for (a) solution flow towards electrode surface and (b) flow of solution near the electrode surface.....	32
Figure 1.19. Current-time transient after a step in potential	33
Figure 1.20. Electrochemically behaviour of APAP under acidic conditions	35
Figure 1.21. Illustration of key aspects of AFM set up and scanning modes	38
Figure 1.22. Schematic of force curve for cantilever deflection vs. piezo movement. Approach of cantilever tip to surface (blue line) and retraction (red line).....	39
Figure 1.23. Schematic of scanning ion conductance microscope (SICM) set up....	40
Figure 1.24. Schematic of different SICM feedback modes	41
Figure 1.25. Scanning modes of SICM.....	43
 Chapter 2	
Figure 2.1. Preparation of the KCSS coating suspension	63
Figure 2.2. Steps of the film formation process for an aqueous polymeric dispersion	65
Figure 2.3. K Control Coater.....	66
Figure 2.4. Pt \varnothing 25 μm ultramicroelectrode.	67
Figure 2.5. Au \varnothing 75 μm microwire electrode (MWE) used for directly single MP bead dissolution analysis	68
Figure 2.6. Fabrication of nanopipette a laser puller	69
Figure 2.7. CV of a) Pt UME and b) Au MWE to validate the two-electrode set up in 500 μM FcTMA ⁺ solution at scan rate 0.01 V/s	70
Figure 2.8. Formation of NMR signal.....	72
Figure 2.9. Operation of Dynamic Mechanical Analyser	74

Chapter 3

Figure 3.1. Schematic of MP KCSS polymer coated placebo bead in a tube filled with acidic dissolution media in preparation for SEM imaging.....	82
Figure 3.2. Representative optical image with area boundary used to calculate the diameter at different formulation stages of the multiparticulate spherical beads	85
Figure 3.3. Average particle size distribution of bead size at different stages of formulation for parameters, diameter, circumference, perimeter, and circularity	86
Figure 3.4. Boxplots for statistical analysis on bead size at different formulation stages for parameters of a) calculated circumference (orange), perimeter (green), and b) circularity (multi-coloured).....	88
Figure 3.5. A graphical analysis of the means of comparison Tukey test method of the four formulation stage for a) calculated circumference, b) perimeter and c) circularity parameters	90
Figure 3.6. SEM images of MCC core – Formulation Stage 1	92
Figure 3.7. SEM images of APAP coated MCC cores – Formulation Stage 2.....	92
Figure 3.8. SEM images of KCSS polymer coated MCC cores – Formulation Stage 2b.....	93
Figure 3.9. SEM images of KCSS polymer coated APAP layered MCC cores – Formulation Stage 3	93
Figure 3.10. Wurster process in a fluid bed coater on coating of MP formulation beads	94
Figure 3.11. Cyclic voltammogram of resultant bulk solution from an APAP coated bead after a 24-hour period of dissolution in 1 mL of 0.1 M HCl using a Pt 25 μm UME as the working electrode and a scan rate of 0.01 V/s	96
Figure 3.12. Cyclic voltammogram of resultant bulk solution from an APAP coated bead in 1 mL of 0.1 M HCl, with <i>ca.</i> 2 minutes agitation of solution at the start and end of 24-hour period of dissolution using a Pt 25 μm UME as the working electrode and a scan rate of 0.01 V/s	98

Figure 3.13. a) Schematic of the electrochemical set up for API detection from single MP bead dissolution (not to scale). b) Image showing the micropositioner for the working electrode inside the Faraday cage, along with the Au MWE and placement of the petri dish for the sample.	100
Figure 3.14. MP spherical bead glued onto the glass slide surface with the Au MWE positioned above the centre	101
Figure 3.15. Averaged amperometric release profiles (<i>i-t</i> curves) in real-time of APAP dissolutions from multiparticulates at a fixed potential based on the steady state current (0.8 V). This demonstrates the effect of the presences of the KCSS polymer coating in a 1 mL solution of pH 1.0 and 2.0 at concentrations 0.1 M and 0.01 M HCl, respectively. The shading represents the SD, where $N = 3$	102
Figure 3.16. SEM images of individual beads after 60 minutes in acidic media....	103
Figure 3.17. Averaged amperometric release profiles (<i>i-t</i> curves) in real-time of APAP dissolutions from multiparticulates at a fixed potential based on the steady state current (0.8 V). This demonstrates the effect of the variation of MP bead size at a constant distance (<i>ca.</i> 60 μm) from the MWE in a 1 mL solution of 0.1 M HCl.	105
Figure 3.18. Example of the KCSS polymer-coated MP spherical bead before and after 2 hours of APAP dissolution in 0.1 M HCl acidic media.....	106
Figure 3.19. Averaged amperometric release profiles (<i>i-t</i> curves) in real-time of APAP dissolutions from multiparticulates at a fixed potential based on the steady state current (0.8 V). This demonstrates the effect of the variation of the distance between the bead and the tip of the MWE in a 1 mL solution of 0.1 M HCl.....	106

Chapter 4

Figure 4.1. Schematic of the rotating disc electrode apparatus to study the varying conditions required to breakdown the Kollicoat® Smartseal 30D (KCSS) polymer of the multiparticulate (MP) formulation beads, resulting in the electro-actively traceable dissolution of APAP, zoomed in on the cross-section of a MP bead. (not to scale).

.....120

Figure 4.2. (a) Rotating disc cyclic voltammograms of 2.0 mM APAP dissolved in acidic media at temperatures between 20 – 40 °C. (b) Calibration curve using limiting current at 1.0 V as a function of APAP concentration between 20 – 40 °C. Scan rate: 0.1 V/s and solution: HCl pH 2.0 for both (a) and (b)

121

Figure 4.3. Rotating disc cyclic voltammograms of APAP dissolved in acidic DM at 30 °C, where APAP concentration in HCl DM solution was 2.0 mM and 0.2 mM for pH 2.0 – 3.0, and pH 3.5 and 4.0 respectively, where the latter has been scaled x10, to lie on the same scale for 2.0 mM APAP at. Scan rate of 0.1 V/s. Limiting current at 1.0 V

122

Figure 4.4. Averaged amperometric release profiles (*i-t* curves) of APAPs dissolution ($N=3$) from 100 mg of MP beads in real-time at a fixed potential based on the limiting current (1.0 V), measured by current density (mA/cm^2) shown in (a) HCl DM at temperatures 20 °C (solid line) and 40 °C (dotted line), (b) HCl DM at temperatures 25 °C (solid line), 30 °C (dotted line), and 35 °C (solid line of alternate shades)...

125

Figure 4.5. Averaged amperometric release profiles (*i-t* curves) of APAPs dissolution ($N=3$) from 100 mg of MP beads in real-time at a fixed potential based on the limiting current (1.0 V), shown by the calculated APAP concentration (mM) at HCl DM pH range 2.0 – 4.0. Inset: Zoom from time 0 – 200 s at 20 °C

126

Figure 4.6. Fouling effect of acidic dissolution media (pH 2.0 – 3.0) at temperature (20 – 40 °C) on the Pt RDE surface

126

Figure 4.7. Average APAP concentration values after the averaged dissolution release profile from the MP beads where $N=3$, calculated with error bars from the limiting current density (i_{lim}) of cyclic voltammogram (at 1.0 V) after cleaning of the Pt WE, for (a) APAP conc. vs. temperatures 20 °C – 40 °C at different pHs, and (b) APAP conc. vs. pH range 2.0 – 4.0 at different temperatures.....

128

Figure 4.8. Amperometric release profile (*i-t* curve) up to 300s in real-time of APAP release from 100 mg of MP beads in HCl dissolution media at pH 2.0, at a fixed potential based on the limiting current (1.0 V), shown in APAP concentration (mM) at increasing temperatures. Inset: Zoom from time 0 – 50 s.....**131**

Figure 4.9. Amperometric release profile (*i-t* curve) up to 300s in real-time of APAP release from 100 mg of MP beads in HCl dissolution media, at a fixed potential based on the limiting current (1.0 V) shown in APAP concentration (mM) at increasing temperatures at (a) pH 2.5, (b) pH 3.0, and (c) pH 3.5 and 4.0 at APAP concentration (μM). Inset for a) and b) indicates the zoom the breakthrough time, τ , with the grey dotted line.....**132**

Figure 4.10. (a) Arrhenius plots showing the rate of dissolution of APAP for pH 2.0 – 3.0 at 0.05 mM and pH 3.5 and 6.8 (SS) at 0.005 mM, where τ is 1/time (s) vs. temperature (*T*) in K. The slope is $-E_a/R$ from the Arrhenius equation. (b) Activation energies (E_a) in kJ/mol for calculated at 50 μM and 5 μM for pH 2.0 – 3.0 and pH 3.5 and 6.8 (SS) respectively.....**133**

Figure 4.11. Example calibration curve for APAP (powder) dissolved in dissolution media 100 mM acetate buffer, for pH range 3.6 – 5.0, at limiting current 1.0 V**135**

Figure 4.12. Averaged amperometric release profiles (*i-t* curve) across APAP dissolutions ($N=3$) from 100 mg of MP beads, at a fixed potential based on the limiting current (1.0 V), in (a) acetate buffer and (b) citrate buffer dissolution media at pH range 3.0 – 5.0 measured by current density (mA/cm^2) at buffer concentrations of 25 mM (dotted line) and 100 mM (solid line)**137**

Figure 4.13. Fouling effect of buffered dissolution media (acetate and citrate) at concentration levels 25 and 100 mM on the Pt RDE surface**139**

Figure 4.14. Averaged amperometric release profiles (*i-t* curve) across APAP dissolutions ($N=3$) from 100 mg of MP beads at a fixed potential based on the limiting current (1.0 V), measured by current density (mA/cm^2) and calculated APAP concentration values for SS DM at 6.8 at temperature 20 °C. Inset: zoom on first 2100 s of dissolution for temperatures 20 – 40 °C.....**140**

Figure 4.15. Rate plot of APAP dissolution at pH 3.6 – 5.0 and pH 3.0 – 5.0 for acetate and citrate buffers respectively at buffer concentrations of 25 and 100 mM. Calculated at an APAP concentration of 0.25 mM, τ is the log of the reciprocal of time, T (s) vs. pH.....**141**

Figure 4.16. log-log values of breakthrough time, τ as a function of pH for estimated and experimental values of τ**145**

Figure 4.17. Schematic overview of dissolution process of pH-dependent taste masking Kollicoat® Smartseal 30D (KCSS) polymer, releasing the API (APAP) into the 25 mL bulk at various pHs of buffered and unbuffered simulated acidic GI tract fluid**146**

Chapter 5

Figure 5.1. DMA thermogram of lyophilised KCSS polymer. The inflection point is defined as the midpoint**157**

Figure 5.2. Polymer film formation examined by AFM in air, under conditions of a) formed at 70 °C and b) formed at 90 °C, before acidic treatment with 0.01 M HCl**158**

Figure 5.3. Schematic of swelling activity of pH responsive polymers. A polybasic polymer shows a collapsed state in a high pH and a swelled state in a low pH**159**

Figure 5.4. 1D schematic of solvent diffusion and resultant polymer dissolution..**160**

Figure 5.5. Set 1 AFM topographical maps of the KCSS polymer film prepared at 70 °C after treatment with 0.01 M HCl, for times 2, 4, 8, 12, 16, and 18 minutes.....**161**

Figure 5.6. Set 2 AFM topographical maps of the KCSS polymer film prepared at 70 °C after treatment with 0.01 M HCl, for times 2, 4, 6, 10, 14, and 20 minutes. Outline of pore analysis is shown at 6 minutes as an example**162**

Figure 5.7. Set 3 AFM topographical maps of the KCSS polymer film prepared at 70 °C after treatment with 0.01 M HCl, for times 2, 4, 8, 10, 12, and 16 minutes. Outline of pore analysis is shown at 10 minutes as an example**162**

Figure 5.8. Schematic of ‘pore’ formation of the polymers surface from the expansion of polymer chains in response to an external acidic environment**163**

Figure 5.9. AFM cross-sectional line analysis of film prepared at 70 °C at 8 minutes, colour coded corresponding to graphical line profile distribution for a 10×10 μm area	163
Figure 5.10. Averaged graphical representation of the pore analysis (<i>N</i> = 26 samples) relative to the structural changes upon dissolution of the KCSS polymer made at 70 °C within a 10×10 μm area, where a) the number of pores, b) the mean area of pores and c) the mean depth of the pores. Spearman rank graphical correlations shown for the normalised three variables studied, d) area per pore vs the no. of pores, e) depth per pore vs no. of pores and f) depth per pore vs area per pore	165
Figure 5.11. AFM topographical maps of the KCSS polymer film prepared at 90 °C after treatment with 0.01 M HCl. At times 4, 12, 16, 20, 30, and 45 minutes, with the corresponding graphical representation of cross-sectional profiles across	168
Figure 5.12. Morphology of polymer films prepared at 90 °C using bright field transmitted light post contact with 0.01 M HCl. At times 2, 4, 8, 12, 16, 20, 30, and 45 minutes. Area of polymer chains opening highlighted at 20 minutes	169
Figure 5.13. AFM topographical maps of a KCSS polymer coating formed at 70 °C onto a MCC bead, using the Wurster process in fluidised bed coater, a) before addition of acid and b) after 20 minutes of contact with acid (0.01 M HCl)	171
Figure 5.14. Corresponding line profile for cross-sectional analysis of AFM topographical map of MP bead (Figure 5.13), before (blue) and after (red) 20 minutes of contact with 0.01 M HCl	172
Figure 5.15. KCSS polymer structure before and after treatment with 0.01 M HCl	173
Figure 5.16. NMR spectra of pure KCSS polymer (blue), and 0.01 M HCl acid treated polymer after 24 h (yellow) and after 28 days (red)	174

Chapter 6

- Figure 6.1.** Schematic of SICM set up with electrolyte solution filled in the nanopipettes and in the substrate contained bath. One QRCE is placed in the nanopipette, and the other in the bulk electrolyte solution181
- Figure 6.2.** Models of the electric double layer at a positively charged surface. a) The Helmholtz model, b) the Gouy-Chapman model, and c) the Stern model.....182
- Figure 6.3.** Schematic of current-voltage curve for the dependence of surface charge on a nanopipette in bulk solution184
- Figure 6.4.** AFM and SICM topographical image of KCSS polymer film cast onto a glass slide. a) 10×10 μm area of polymer imaged by in air, b) and c) 6×6 μm area mapped by SICM in 50 mM KCl at pH 7190
- Figure 6.5.** Schematic of SICM set up for analysis of a placebo KCSS MP bead in an electrolyte bath, with two QRCE – one placed inside the glass nanopipette and the other placed directly in the bulk (Not to scale)192
- Figure 6.6.** AFM image of a 10×10 μm area KCSS polymer coated of a MP placebo bead in air.....192
- Figure 6.7.** Topography and surface charge (as reflected in the normalised current measurement) of a 6×6 μm area of a placebo KCSS coated MP bead at pH 5. a) – d) indicates different scans of different placebo beads, topographical maps (left) and corresponding surface charge maps (right)194
- Figure 6.8.** Topography and surface charge (as reflected in the normalised current measurement) of a 6×6 μm area of a placebo KCSS coated MP bead at pH 7. a) and b) indicates different scans of different placebo beads, topographical maps (left) and corresponding surface charge maps (right)195
- Figure 6.9.** Topography and surface charge (as reflected in the normalised current measurement) of a 6×6 μm area of a placebo KCSS coated MP bead at pH 9. a) – c) indicates different scans of different placebo beads, topographical maps (left) and corresponding surface charge maps (right)196
- Figure 6.10.** STEM images of sister nanopipettes used in SICM mapping of KCSS polymer coated placebo beads197

Figure 6.11. Schematic of typical nanopipette geometry used in FEM simulation modelling of the boundary conditions, where no flux is applied to the nanopipette walls and bulk boundaries. Obtained and reproduced from COMSOL	198
Figure 6.12. Current-voltage graphs obtained from the electrolyte bulk. a) experimentally for pH 5 and b) FEM simulation in bulk for both pH 5 and 7	199
Figure 6.13. Simulated dependence of the normalised current on the surface charge density values in mC m^{-2} of the KCSS coated placebo MP bead, used to generate the quantified charge maps shown for pH 5 and 7 in Figure 6.8	200
Figure 6.14. FEM calculated surface charge for the KCSS polymer layer of a placebo MP bead at pH 5 and 7	201

List of Tables

Table 1.1. Regions of gastrointestinal tract and corresponding pH and transit times	3
Table 2.1. List of chemicals used in this thesis	59
Table 2.2. List of materials used in this thesis	60
Table 3.1. Stages and details for the formulation of MP beads	81
Table 3.2. Mean particle-size distribution of bead size at each formulation stage for parameters, diameter, circumference, perimeter, and circularity	86
Table 3.3. Tukey means of comparison test at the 95 % confidence level stating the significant difference between each of the 4 formulation stages for the parameters of circumference, perimeter, and circularity	89
Table 3.4. Steady state (limiting) current based on the corresponding CVs from dissolution of MP beads into a 1 mL solution of 0.1 M HCl and the calculated mass of APAP from each corresponding MP bead	96
Table 3.5. Particle size distribution and the dosage of APAP (μg) from the dissolution of single MP APAP coated bead with motion	98
Table 3.6. Bead size before and after single bead dissolution in 1 mL of 0.1 M HCl dissolution media calculated by measuring the diameter of the bead, and the calculated distance between the MWE tip and the centre of the bead	104
Table 3.7. Calculated values of the total concentration of APAP released from the <i>i-t</i> dissolution profiles for variables for the presence of polymer, bead size and tip to bead distance	108
Table 4.1. Calibration slopes for acidic (HCl, pH 2.0 – 4.0) and simulated saliva (pH 6.8) dissolution media	123
Table 4.2. Average current density and APAP concentration values at 1.0 V corresponding to i_{lim} for HCl DM for pH 2.0 – 4.0 and SS at pH 6.8 at temperatures 20 – 40 °C	129

Table 4.3. The corresponding linear slopes to the Arrhenius plots for HCl dissolution media at pH 2, 2.5, 3, 3.5 and 6.8. pH 2.0 – 2.5 calculated at concentrations 50 – 750 μM , pH 3 at 50 – 500 μM and pH 3.5 and pH 6.8 calculated at 5 μM	134
Table 4.4. Calibration slopes for dissolution media acetate and citrate buffers pH 3.6 – 5.0 and pH 3 – 5.0 respectively at concentrations 25 mM and 100 mM	136
Table 4.5. Average current density and APAP concentration values at 1.0 V corresponding to i_{lim} for acetate and citrate buffer DM for pH 3.6 – 5 and pH 3.0 – 5.0, respectively	138
Table 4.6. APAP dissolution rate of buffers vs. HCl DM.....	142
Table 4.7. Calculated variables for the protonation of the KCSS polymer surface	144
Table 4.8. Values for the calculation of time taken to protonate the polymer surface and the experimental breakthrough time, τ of APAP.....	145
Table 5.1. Spearman rank correlation values for pore variables in terms of number, area, and depth for p-value < 0.001	166

Abstract

This thesis explores the application of novel electrochemical and scanning probe techniques to study the dissolution of taste masking polymer, Kollicoat[®] Smartseal 30 D (KCSS, BASF) and how it controls the release of model active pharmaceutical ingredient (API) acetaminophen from a multiparticulate (MP) oral dosage form under the pH conditions of the GI tract. MP drug delivery systems consist of small API-containing particles, beads, often coated in a protective or taste masking polymer layer. These polymers are typically pH responsive, allowing release of the API only in specific pH conditions e.g., in the stomach.

Understanding such polymer dissolution is a crucial quality control procedure in pharmaceutical science, as that determines the rate at which an API is released from the formulation and, consequently, the rate at which it becomes available for absorption in the gastrointestinal (GI) tract. Traditional dissolution testing typically analyses the resultant dissolution media at specific time intervals, requiring the use of an *ex situ* analytical technique, such as HPLC. As a result, a continuous, *in situ*, dissolution profile is not obtained, and valuable information regarding the start of dissolution may be lost.

This thesis focuses on the implementation and development of electrochemical methods for dissolution testing on the micro- (single bead, ultramicroelectrode) and macro- (MP dose, rotating disc electrode) scale, to investigate the rate of API release from a taste masking polymer-coated MP, *in situ* under pH conditions of the GI tract in real time. Additionally, this thesis investigated the effectiveness of taste masking polymer under simulated oral conditions. A variable temperature study resulted in the kinetic analysis of the API dissolution. The effects of physiological buffers were also explored. These studies led to the further investigation of the microstructural and morphological changes occurring in the KCSS polymer film in an acidic environment using *ex situ* atomic force microscopy (AFM). This was complemented by scanning ion conductance microscopy (SICM) to investigate *in situ* the charge distribution of the polymer layer of MP beads under a range of pH conditions.

Overall, the development and application of electrochemical methods for real-time dissolution measurements are demonstrated and the mechanisms associated with dissolution under different pH conditions are discussed with reference to scanning probe microscopy data.

Chapter 1

Introduction

This thesis studies the dissolution of a polymer-coated taste masked multiparticulate formulation bead, prepared using acetaminophen as the active pharmaceutical ingredient and the Kollicoat® Smartseal 30 D as the taste masking polymer. In this introductory chapter a review is given on the various related topics covered in this study. The basic concepts of oral drug delivery are introduced, specifically multiparticulate formulations with a focus on taste masking properties. Multiparticulate oral dosage forms are explored, showing the importance of the formulation process and stimuli responsive polymers as a taste masker. In addition, this chapter highlights and discusses various dissolution techniques, with an emphasis on electrochemical methods on a micro- and macro- scale for dissolution. Lastly, an overview is given of scanning probe microscopy techniques for application in the study of a pH responsive taste masking polymer.

1.1. Oral Dosage Forms

A dosage form refers to the combination of the drug(s) or active pharmaceutical ingredient (API) and the inactive compound(s) referred to as excipient(s) to facilitate dosing, administration, and delivery of medication to the patient. Thus, the drug products are referred to as a drug delivery system.¹

There are many routes of administration of drugs into the body in various physical forms, such as solutions, creams, suppositories, powders, capsules, and compressed tablets to name a few. The most preferred route is the enteral or oral route as it offers high patient acceptability, compliance, and ease of administration.^{1,2} Here, the drug product is swallowed and dissolves in the gastrointestinal (GI) fluid, which is absorbed through the mucous membrane of the GI tract and into the blood stream for the general circulation within the body (Figure 1.1 and Table 1.1).^{1,2}

There is no ‘ideal’ drug delivery system, and the oral route is not without its drawbacks. The main challenges that this route of drug delivery face is primarily palatability and dysphagia (difficulty swallowing), both of which affect patient compliance.^{3,4} Dysphagia particularly affects paediatric and geriatric patients, but can affect people of any age.⁵

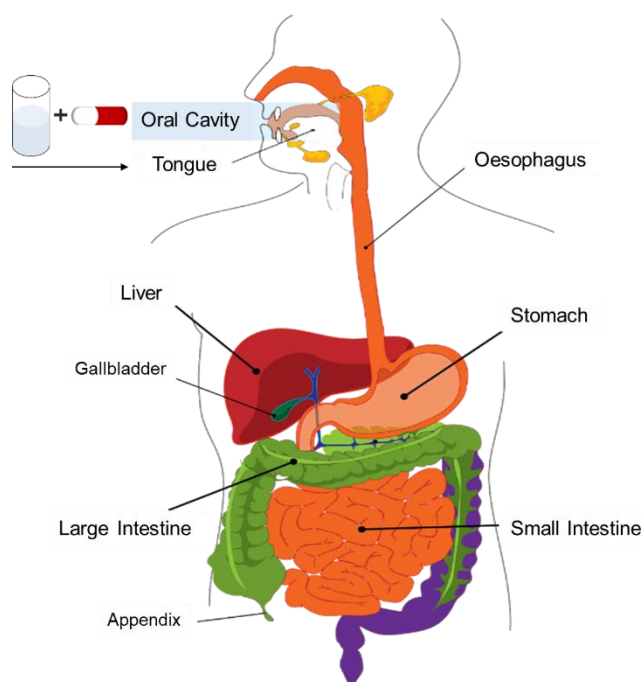


Figure 1.1. Regions of the gastrointestinal tract.

Table 1.1. Regions of gastrointestinal tract and corresponding pH and transit times.^{2,6-8}

Gastrointestinal Tract	pH	Transit times
Oral Cavity / Oesophagus	6.8 – 7.0	10 – 14 s, can take up to 1 min
Stomach	1.0 – 2.5 (up to 5 in fed state)	Half empty after <i>ca.</i> 80 min
Small intestine	6.0 – 7.5	3.2 ± 1.6 h
Colon (large intestine)	5.0 – 7.0	10 h to several days

Additionally, there are other drawbacks to solid dosage form administration including, i) bioavailability from drugs that have slow dissolution rates and/or have low permeability for sufficient absorption in the GI tract,⁹ ii) or those with high absorption in the GI tract, iii) hygroscopic drugs which are unsuitable for oral dosage forms,¹⁰ iv) gastric irritation which can harm the GI tract mucosa,¹¹ and v) encapsulation of tablets, coatings and complex processes of capsules can increase production costs.¹²

The advantages of solid dosage forms typically outweigh the shortcomings, however, the use of multiparticulate formulations addresses some of these concerns and therefore make it an increasingly popular choice for oral administration.

1.1.1. Multiparticulate Formulations

Oral multiparticulate(s) (MP) formulations/systems are multi-unit solid dosage forms that consist of many small discrete drug delivery units.¹³⁻¹⁵ The concept and technology of this type of drug delivery system was first introduced in the 1950s, but has gained increasing popularity over the last few decades.^{16,17} They are referred to under numerous terminologies, a non-exhaustive list includes, multiple units, pellets, beads, granules, and micro- and mini- tablets. They vary in size, with diameters as small as 150 μm for example as a taste-masked MP or as large as 2 – 3 mm.¹³ For the delivery of the total recommended dose, these MP units may be swallowed directly, filled into sachets or capsules, compressed into tablets or sprinkled over a meal.^{4,5,13,14,18} Other technologies include the utilisation of various dosing dispensers.¹⁸

The MP drug delivery system offers many biopharmaceutic advantages over traditional single unit (monolithic) dosage forms. As MP are small and occur as multiple units, they occupy a large surface area for drug release when they disperse along the GI tract. This maximises absorption, minimises side effects and thus reduces the risk of dose dumping (excessive, premature release of drug), whilst also avoiding the risk of local irritation of the GI tract. Furthermore, they have a shorter, more predictable transit time through the GI tract (gastric emptying), thus reducing the inter- and intra-patient variability.^{14,16,17} Moreover, MP offers other advantages such as ease of swallowing, flexibility in dose titration, demonstrated suitability for controlled drug release and taste masking. These abilities are particularly beneficial for paediatric, geriatric and patients that suffer from dysphagia.⁴

1.1.2. Polymer-Coated Multiparticulates

An inert core is defined as starting material that is used as a carrier for the layering of a drug. The substrate comprises of one or more ingredients, typically starch, sucrose or microcrystalline cellulose (MCC). This core can then be coated to achieve a controlled drug release MP formulation, either delayed-, sustained- or immediate release.¹⁶

The coating of the core occurs in two ways; either i) directly with a polymer-drug solution/dispersion (matrix coated) or ii) drug coated core using a layering/coating technique where the drug is layered first, followed by a coating of a polymeric solution/dispersion (reservoir coated), as shown in Figure 1.2.¹⁹⁻²¹

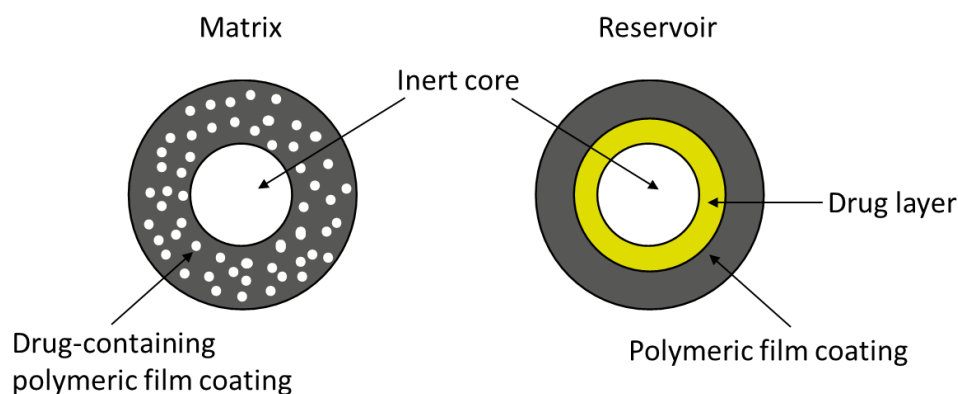


Figure 1.2. Schematic of matrix and reservoir coated multiparticulate formulation.

1.2. Taste Masking

As many drugs are bitter and unpleasant, taste masking techniques are employed to enhance palatability and therefore increase patient compliance.²² Three main approaches to achieve taste masking are:

- i. using peripheral interactions, where specific compounds are used to antagonise particular taste receptors;
- ii. utilising central cognitive interactions whereby a strong taste or aroma is used to reduce the perception of unpleasant drugs to the brain;
- iii. encapsulation, where the drug is physically prevented from interaction with the active sites by either modifying solubility or by using a physical barrier, *i.e.* coatings.^{22,23}

Various techniques in the approach to taste masking include the use of flavourings, sweeteners and amino acids, polymer coating of the drug, ion exchange resin for binding to acidic bitter compounds, inclusion complexes, and microencapsulation.^{23,24}

1.2.1. Taste Masking Techniques

Generally, taste masking using the addition of sweeteners, flavourings and amino acids are the simplest method, particularly for paediatric formulations, liquid formulations, and chewable tablets. However, for extremely bitter drugs, particularly those of a high dose and highly water-soluble drugs, it is far less effective.^{25,26} Therefore, the application of coatings is one of the more effective and widely used taste masking methods. The various types of taste masking coating systems are shown in Figure 1.3.^{24,26}

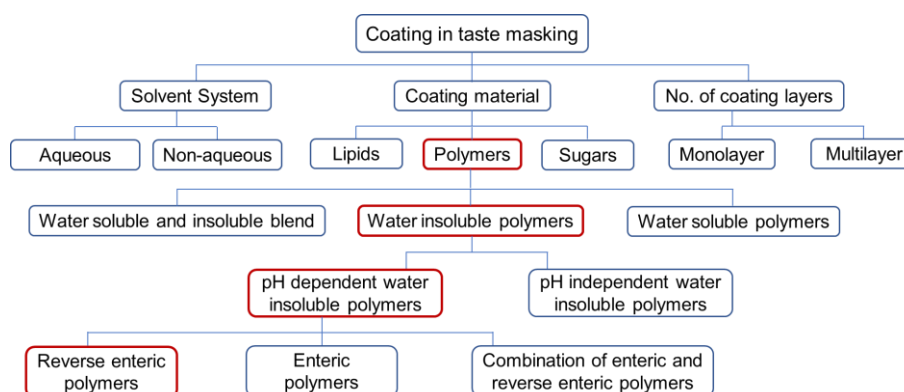


Figure 1.3. Classification of patented taste masking coatings, where the system used in this study is highlighted in red. (Adapted from Bansal *et al.*, 2009).²⁶

1.2.2. Taste Masking Manufacturing Processes

There are numerous manufacturing processes for the application of taste masking coatings, which include melt and liquid extrusion, spray and freeze-drying from aqueous dispersions, and coatings with lipids or waxes to name a few. Coating applications are the most effective for taste masking of tablets or mini tablets due to the application of a uniform physical barrier.¹⁶

Conventional methods for applying coatings include liquid melt or powder coatings with lipids, waxes, or polysaccharides. More modern methods use film coatings, widely used in taste masking multi-unit solid dosage forms, where coatings can be applied by continuous manufacturing process, usually spray coating (or drying) and hot melt extrusion,²⁷ or the process of microencapsulation.²²

1.2.2.1. Spray Coating by a Fluidised Bed Coater Technology

In addition to taste masking, coatings serve other purposes as well, such as protection against moisture and UV, control of bioavailability of drugs, and to improve cosmetic appearance.²⁸ Spray coating is a common method to apply polymer and/or drug solution or aqueous dispersion onto drug containing cores. Tablets and larger oral dosage forms are typically coated using a drum coater, whilst fluid bed coaters are used for particulates.^{28,29}

In a fluid bed coater, the particulates are placed into a processing chamber and maintained in the fluidised state controlled by a heated air current, which keeps the particulates in motion, whilst a liquid suspension (coating fluid) is uniformly sprayed on and quickly dried onto the particulates.³⁰⁻³² There are several techniques in which to spray the aqueous dispersion in a fluid bed coater, such as top spray, bottom spray, wurster (most common for small particulates), and rotator with side spray (Figure 1.4).^{32,33}

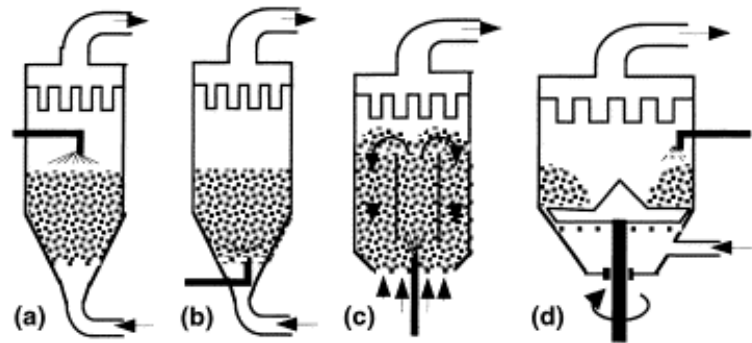


Figure 1.4. Various types of fluid bed coaters, (a) top spray, (b) bottom spray, (c) wurster, and (d) rotator with side spray. (Teunou and Poncelet, 2002).³³

The wurster process is a form of bottom spray coating (Figure 1.5), whereby the spray nozzle is built-in to the base, which results in the spray pattern occurring alongside the air flow feed.³¹ This fluid bed system is fitted with a wurster chamber (draft tube), which is a cylindrical column that separates the bed coater into different regions. Particles are drawn in and move upwards by the air flow current into the spray region of the wurster chamber and are wetted by the coating liquid. This coating of particles occurs concurrently as the atomising air is simultaneously injected with the coating liquid through the spray nozzle.^{31,33,34}

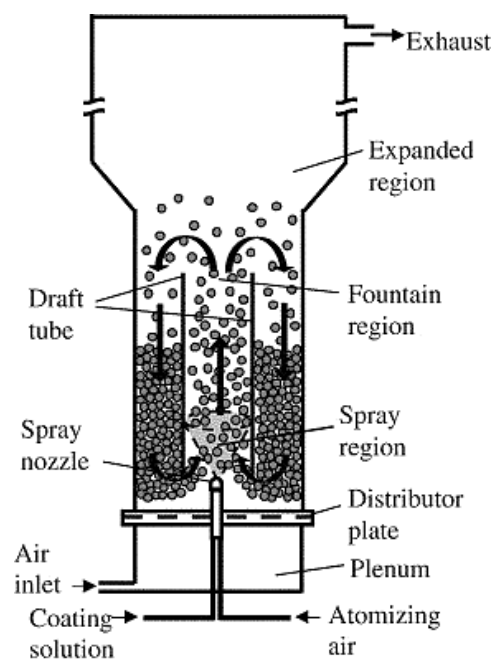


Figure 1.5. Wurster fluidised bed spray coating system. (KuShaari *et al.*, 2006).³⁴

Next, the drying process occurs in the expanded region, the upper part of the chamber, where the particles are suspended to prevent agglomeration. The coated particles then fall downwards through the fountain region and flow to the bottom, where they are drawn in again by the air flow current, resulting in a continuous coating process. The wurster chamber allows for increased acceleration and continuous recirculation of particles which increases collisions between droplets and particles in the spray region, thereby improving the coating efficiency and reducing the spray drying time compared to other fluid bed coaters.^{31,33,34}

1.3. Stimuli Responsive Polymers

Stimuli responsive or ‘smart’ polymers are polymers that are characterised by changes in their physicochemical properties in response to the changes in their surrounding environment from an external stimulus.^{35–37} These characteristic changes can be alterations in conformation and/or solubility, alterations of the hydrophobic/hydrophilic balance or the release of a bioactive (drug) molecule.³⁸

Their response is typically determined by the presence of functional groups on or within the polymer chain.^{35,36} The stimuli that trigger a response can be classified into three main groups: physical (e.g. temperature, electric field, light, ultrasound, mechanical stress), chemical (e.g. pH, ionic strength), and biological (e.g. enzymes, biomolecules), shown in Figure 1.6 along with typical responses.^{36–39}

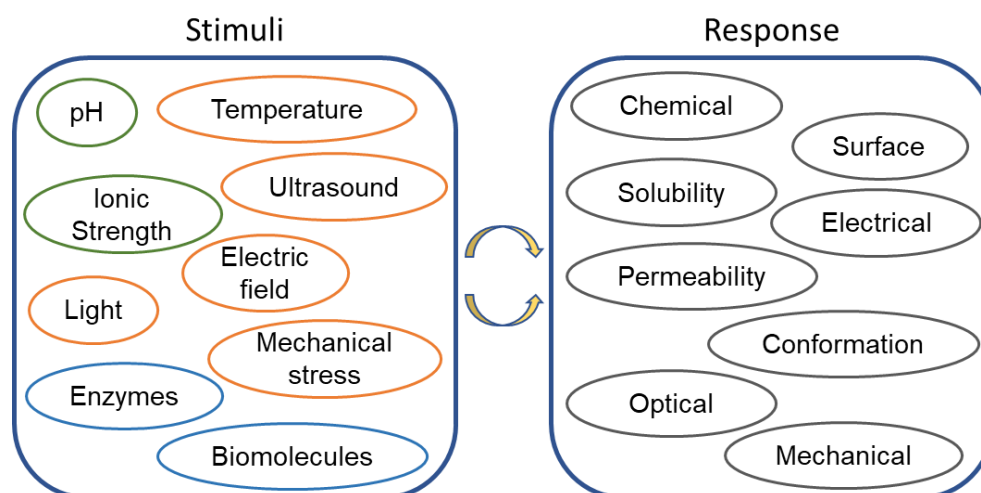


Figure 1.6. Common stimuli and responses of smart polymers. Stimuli highlighted according to physical (orange), chemical (green), and biological (blue) classification. (Adapted from Schmaljohann, 2006).³⁸

The most important stimuli systems, particularly in the biomedical field are those polymers sensitive to pH and temperature.⁴⁰

1.3.1. pH Responsive Polymers

pH responsive polymers are susceptible to numerous changes, such as conformation and structural changes, surface activity, solubility, chain configuration and many more in response to changes of the surrounding pH solution.³⁹ The range of pH along the GI tract varies greatly from the moment of consumption, from the neutral environment of the saliva in the oral cavity, to the acidic environment of the stomach to the basic environment of the intestines (Table 1.1).³⁸ For this reason, pH responsive polymers are highly suitable for targeted and controlled oral drug delivery.³⁹

pH responsive polymers have an ionisable group attached to a hydrophobic backbone.^{39,40} They are defined as polyelectrolytes due to the presence of weakly acidic or basic groups that can either donate or accept protons respectively, in response to the pH of their surrounding environment.^{37,39,41} Upon the ionisation of the pendant functional groups, the resultant protonation or deprotonation leads to changes in the net electrostatic charge of the polymer chain. In turn this alters the conformational structure and hydrodynamic volume,^{37,39,42} which can result in shrinkage, swelling or dissolution.^{39,41} The effects of protonation and deprotonation can result in an increase of electrostatic charge, causing electrostatic repulsion between polymer chains and consequently the opening or extension of polymer chains from a collapsed state. For a decrease in electrostatic charge the opposite effect would occur.^{35,39,43}

It should be noted that ionisation of polyelectrolytes is more complex than the monoacidic or monobasic counterparts, due to of electrostatic repulsion exerted by adjacent ionised groups. This therefore results in the differing dissociation constant (K_a).⁴⁰

1.3.1.1. Types of pH Responsive Polymers

pH responsive polymers can be classified into two groups, i) polymers with acidic functional groups (polyacids or polyanions) and ii) polymers with basic functional groups (polybases or polycations).^{39,42,44}

Polyacids generally have a carboxylic acid (-COOH) functional group. Common examples include poly acrylic acid (PAA) or poly methacrylic acid (PMA).^{39,41}

Polyacids at low pHs (pK_a dependent) are in a collapsed ‘unswollen’ state as the pendant acidic group will be in its protonated, unionised form.⁴¹ However, in basic pHs it donates protons and thus forms an anionic charged molecule, causing physical changes (swelling) of the polymer due to their electrostatic repulsion. Thus, for polybases the inverse is true.^{41,42}

Polybases typically have an ammonia ($-NH_2$) functional group, for example poly(*N,N*-dimethylaminoethyl methacrylate) (PDMAEMA) or, poly(*N,N*-diethylaminoethyl methacrylate) (PDEAEMA).^{41,44} The pendant functional group accepts protons at low pH values, forming a cationic polyelectrolyte and increasing the electrostatic charge between protonated neighbouring functional groups. This leads to expansion of polymer chains, an increase of the hydrodynamic diameter of the polymer, and induces swelling.^{35,41} In other words, polybasic pH responsive polymers swell at $pH < 7$ and thus can be utilised as a polymer coating to inhibit the release of drug in the oral cavity, as illustrated in Figure 1.7. Consequently, this makes an ideal polymer for taste masking.^{43,45}

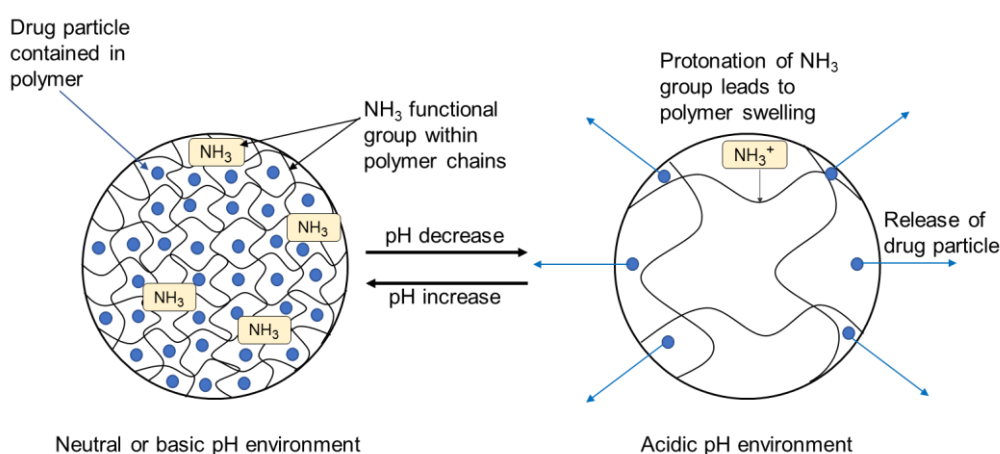


Figure 1.7. Schematic of a drug loaded particle in a polybasic polymer coating, shown in a neutral to basic pH environment and in an acidic environment. The former is the collapsed state where the tertiary amine group is in the unprotonated form and thus the drug remains encapsulated. The latter shows the amine groups to where they are protonated in the low pH environment, and swell in response, thus releasing the drug into the external environment. (Adapted from Grainger and El-Sayed, 2010).⁴²

1.3.2. Kollicoat® Smartseal 30 D

The Kollicoat® Smartseal 30 D (KCSS, Figure 1.8) is a synthetic, lipophilic, aqueous dispersion of a methyl methacrylate (MMA) and diethylaminoethyl methacrylate (DEAEMA) polybasic copolymer,⁴⁶ and as such, it contains a C–C backbone which classifies it as a linear non-biodegradable polymer.⁴⁷ KCSS is synthesised by free radical emulsion polymerisation.⁴⁶

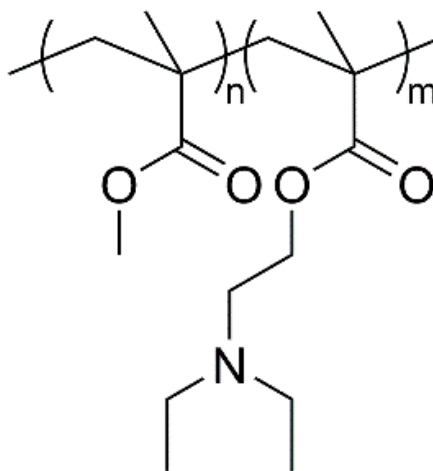


Figure 1.8. Methyl methacrylate and diethylaminoethyl methacrylate copolymer, Kollicoat® Smartseal 30 D polymer structure, where $n = 7$ and $m = 3$.⁴⁶

The copolymer dispersion has a solids content of 30 %, stabilised with approximately 0.6 % macrogol cetostearyl ether and 0.8 % sodium lauryl sulfate.^{22,46,48} It occurs as a milky white liquid, with a faint characteristic odour.^{22,46} Both MMA and DEAEMA are known to be hydrophobic.^{42,49,50} Therefore, KCSS is a brittle, lipophilic polymer and therefore requires a plasticiser to fully function as a film forming polymer, KCSS has a glass transition temperature (T_g) of *ca.* 63 °C and a minimum film forming temperature (MFFT) of 57 °C.^{46,51}

KCSS has a reported molar ratio of monomers MMA and DEAEMA in the copolymer is 7:3. It also has a reported molecular weight of *ca.* 200,000 g/mol determined by size exclusion chromatography (SEC) coupled with light scattering. Laser scattering determined that the average particle size of polymer droplets in the dispersion is *ca.* 150 nm.^{46,51} These properties of the KCSS polymer were examined by nuclear magnetic resonance (NMR) and gel permeation chromatography (GPC).

From NMR analysis, it was found that the calculated molar ratio differs from that of the reported value for MMA:DEAEMA at 10:4. The GPC data revealed a similar molecular weight, where KCSS has a number average molar mass, M_n and dispersity, D values of 270,00 g/mol and 8.39 respectively.

The pH responsiveness of the KCSS polymer is due to the tertiary functional amine groups of the DEAEMA polymer and thus its hydrophilicity is dependent upon the pH environment.⁵⁰ In acidic conditions (a pH lower than DEAEMAs pK_a of *ca.* 7.3) the tertiary amine groups are protonated and become more hydrophilic thus resulting in an increased solubility.^{50,52,53} KCSS is therefore insoluble at basic and neutral pH media and rapidly dissolves at $pH < 5.5$ due to the protonation of DEAEMAs tertiary amine.^{51,54} As a result, it can be referred to as a ‘reverse enteric coating polymer’.^{29,48} These changes in solubility in response to pH are important in enabling drug release in the GI tract. Also, it is used to mask the taste of drugs by providing a physical barrier against physiological pH of saliva (5.8 – 7.6),⁵⁵ as well as for moisture, which preserves the potency of the drug as well as masking any odour.⁴⁶

The pH responsiveness of this polymer coating is used to exploit the differences in pH of the GI tract for drug targeting and delivery. When a drug is orally administered, it experiences pH conditions ranging from *ca.* pH 7 to 1 as it travels through the GI tract.^{48,56} Therefore, the KCSS coating offers an effective barrier against dissolution in saliva.

1.3.3. Polymer Film Formation

Aqueous polymer dispersions have characteristically low viscosity and high solid contents, which leads to a rapid coating process. On the other hand, organic solutions present considerable disadvantages, for example residual solvents left in the film coating. Furthermore, aqueous polymeric dispersions offer safer and more environmentally friendly alternative to the use of solvents. Consequently, aqueous polymeric dispersions are favoured for pharmaceutical formulations.⁵⁷

The process of film formation for aqueous polymeric dispersions is complex, beginning with the atomisation of fine droplets from the dispersion onto the substrates surface, followed by water evaporation in the drying stages, where the polymer particles/spheres come into close contact with one another. Continued drying and further water evaporation allows the polymer particles to deform, coalesce and the polymer chains to fuse resulting in the formation of a continuous film.^{58,59} The process is outlined in the schematic shown in Figure 1.9.

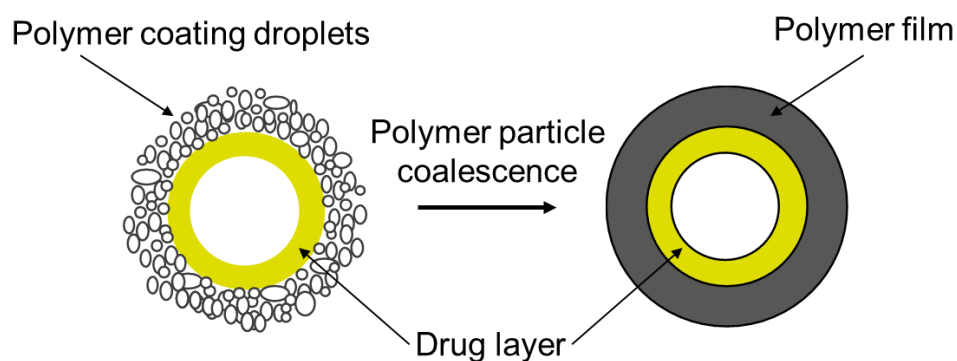


Figure 1.9. Schematic of film formation mechanism from aqueous polymer dispersions. (Adapted from Sonar and Rawat, 2015).⁶⁰

1.3.4. Drug Release Mechanisms

There are several biological and chemical mechanisms in which drugs can be released, including, but not limited to, dissolution, diffusion, osmosis, partitioning, creation of hydrostatic pressure, swelling, and erosion. Commonly, drug delivery involves one or more of these mechanisms of release.^{11,61,62} The transport of solutes from a non-degradable polymeric system is predominately considered as diffusion driven. Hence, these polymers are typically fabricated into ‘matrix’ or ‘reservoir’ systems, as shown previously in Figure 1.2.¹⁹ The mechanism in which drug release occurs from reservoir coated beads/pellets is a complex process depending on many variables such as the type and thickness of coating, the type of drug and inert core used.^{63–65}

1.3.4.1. Drug Release Mechanisms from Reservoir Polymer-Coated Multiparticulates

One such mechanism is diffusion of drug release through a continuous polymer film that surrounds a drug loaded inert core (reservoir system), which serves as a rate-controlling membrane.^{19,21,63} Drug release from a diffusion-controlled system typically occurs in a two-step process: i) the surrounding medium penetrates the release unit and dissolves the contained drug, which forms a concentration gradient of dissolved drug, and ii) the dissolving drug will diffuse through the pore of the release unit or the surrounding membrane and therefore be released.¹¹

An ideal drug release from a reservoir system via diffusion, based on Fick’s law (*vide infra*, Section 1.5.2.1.1) can be distinguished into two subclasses, either i) non-constant activity source (first order release), or ii) a constant activity source (zero order release). Where the former describes the situation at which the released drug molecules are not replaced, the drug concentration at the surface of the inner membrane continuously decreases with time. For the latter, drug released molecules are replaced by the (partial) dissolution of drug crystals or amorphous aggregates, resulting in a saturated solution at the inner membranes surface.⁶² If there is no swelling or dissolving of the polymer coating (rate controlling membrane) then the system is to be in perfect sink conditions. However, in practice these systems are far from perfect, with the norm more inclined to a ‘non-ideal’ system.

A non-ideal system can include crack formations within the film coating from the build-up of hydrostatic pressure due to swelling or (partial) dissolution. Therefore, mathematical calculations based on this theory of release kinetics is complex and insufficient.^{62,66,67} Furthermore, if a coating is heterogeneous and contains pores or cracks, these pores can fill with solution upon contact with the aqueous medium and thus facilitate diffusion.^{63,68}

Dissolution can be defined as the process where solute molecules (e.g. APIs) are dissolved in a solvent vehicle. This process, specifically for drug release, involves the transfer of drug molecules or ions from its solid phase into the external surrounding medium, typically water or tissue. It occurs as the drug molecules are solvated and thus separated from the solid. The solution becomes saturated when it reaches the limit of the solubility of the drug.^{11,61}

Osmosis can be defined as the movement of a solvent from a compartment with a low concentration of solute to a compartment with a high concentration. For multiparticulates, the drug solution can flow through the pores formed during the uptake of water. The mechanism of osmosis can occur when the aqueous media passes through the film coating, which results in the dissolution of the soluble components (the drug and excipients) from within the core, generating an osmotic pressure inside the coated MP, which influences the rate of drug release from these pores.^{11,63}

Furthermore, some coatings are fabricated with the intent to gradually erode with time, subsequently releasing the contained drug within the MP bead/pellet in a controlled approach. This therefore defines the drug release mechanism of erosion.¹¹ It should also be noted that the type of drug used contributes greatly to the drug release as it depends on the solubility of the drug into the aqueous medium. A high drug solubility results in a high concentration gradient and consequently a faster release of drug.^{55,63} The overall drug release and its corresponding rate from a coated MP bead is governed by one or more of the release mechanisms described above.

1.4. Traditional Dissolution Testing

In the pharmaceutical industry, *in vitro* dissolution testing is employed to validate initial testing of potential drug formulations and to identify crucial manufacturing variables.⁶⁹ It is vital process in the development and quality control of a solid dosage form. Dissolution testing is routinely used to determine the rate of release of a drug/API, as the intended drug would rapidly dissolve in the test medium.^{70,71}

The United States Pharmacopoeia (USP) guidelines of dissolution testing require the use of a cylindrical dissolution vessel with a hemispherical base filled with an aqueous solution, at a stable temperature of 37 °C and stirred at a constant rate.^{72,73} There are seven types of USP dissolution apparatuses outlined in the USP Chapter <711>.^{69,74} However, official methods and regulations primarily recommend the use of USP Apparatus I and II, particularly for solid oral dosage forms, and are shown in Figure 1.10.^{74,75} In USP Apparatus I, the dosage form is placed in a basket attached to the end of a rotating spindle, usually rotated at 100 rpm, which introduces agitation into the system.^{8,74} USP Apparatus II, on the other hand uses a paddle typically rotated between 50 – 75 rpm, and the oral dosage form is released directly into the vessel. Typically, both Apparatus I and II have a medium volume of 900 mL, though this can vary between 500 – 1000 mL.⁸

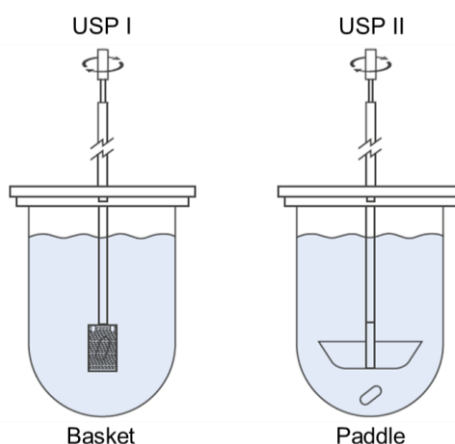


Figure 1.10. Schematic of USP Apparatus I and II. (Reproduced from Antech).⁷⁶

USP dissolution testing methods require a complimentary method of analysis. The resultant dissolution media is typically analysed through a series of sample aliquots taken at varying time intervals, which measure the concentration of drug release with time.^{8,72,77}

The most widely used analytical techniques are UV-visible spectrometry and high-performance liquid chromatography (HPLC).^{8,72,77} However, these traditional dissolution methods rely on the drug release into the bulk, increasing with time, measured at regular intervals. Therefore, this methodology lacks the ability to measure the solution concentration in real-time.

Whilst USP apparatuses have attempted to replicate the conditions of the GI tract and have been used routinely for many years, none of these methodologies have been able to accurately replicate *in vivo* conditions.⁷⁸ Although the USP Apparatus II has been a staple in industry dissolution testing for over 30 years, there remain several drawbacks associated with it. These limitations include poor reproducibility of results and high variability of results, and complex hydrodynamics dependent upon the positions of the oral dosage form, which can land at various locations within the vessel which can significantly alter the velocities and strain rate, thus introducing variability into the dissolution testing system.^{69,71} Furthermore, factors such as tablet size and shape can influence the movement of the tablet during dissolution testing.⁷⁹

There have been many studies that indicate that the hydrodynamics of USP Apparatus II plays a significant role in the lack of reproducible results, however this comes with no substantial resolve in the matter. The complex hydrodynamics can be attributed to the regions above and below the paddle impeller. Axial velocities are much smaller than the tangential velocities and therefore the recirculation in the USP Apparatus II is inadequate, resulting in a weak flow.⁸⁰ Furthermore, below the paddle a ‘coning’ effect can be observed where a tablet rapidly disintegrates during a dissolution test, resulting in aggregating particles forming a rotating cone under the paddle impeller.⁸

Ultimately, the hydrodynamics located near the bottom of the dissolution vessel where the tablet typically resides largely contributes to the high variability of results from dissolution testing.⁷¹ It should also be noted that the large volume of dissolution media required for USP Apparatus I and II are unphysiologically realistic.⁸¹ Therefore, a reproducible placement of the tablet within a smaller volume of dissolution media is highly desirable. Thus, this thesis endeavours to resolve and improve upon the hydrodynamic concerns using a rotating disc electrode approach as well as employing simultaneous real-time analysis of the dissolution process, building upon the existing

industrial dissolution testing methods and eliminating the need of a secondary method of analysis.

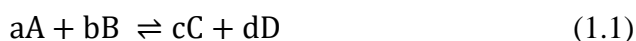
1.5. Electroanalytical Methods

The use of electrochemical methods in analytical chemistry can be utilised to study an analyte by measuring the current and/or potential difference detected by electrodes within an electrochemical cell containing electrolyte(s). The chemical phenomena involved in electrochemistry is associated with charge separation, where this often leads to charge transfer, which can occur homogeneously in solution, or heterogeneously on electrode surfaces.⁸² Electrochemical based applications are becoming increasingly employed to study *in vitro* electroactive compounds of pharmaceutical forms and physiological fluids.^{83,84}

1.5.1. Potentiometry

Potentiometry is a static interfacial electroanalytical method, whereby the concentration of an analyte is determined by the measurement of a potential difference (in volts) as a result of charge transfer between two interfaces, a reference electrode and indicator electrode.⁸⁵ As a static system, there is no net electrochemical reaction and therefore no flow of current, essentially in a state of equilibrium.^{86,87}

The following equation demonstrates an overall general electrochemical cell reaction:



where, a is the number of moles for its corresponding chemical species A and so on.

The electrode potential, E , is measured in relation to the redox reactions occurring at the two electrodes, demonstrated by the Nernst equation:^{85,86}

$$E = E^0 - \frac{RT}{nF} \ln \left(\frac{a(C)^c \cdot a(D)^d}{a(A)^a \cdot a(B)^b} \right) \quad (1.2)$$

where, E^0 is the standard rate constant, R is the molar gas constant in $\text{J K}^{-1} \text{mol}^{-1}$, T is the temperature in K , n is the number of electrons transferred, F is Faradays constant (96495 C mol^{-1}) and a is the activity of the species involved, defined by:

$$a = \gamma C \quad (1.3)$$

where, γ is the activity coefficient and C is the concentration.

The activity coefficient is a thermodynamic factor to validate for any nonconformities from an ideal behaviour in a chemical mixture, and typically has a value between 0 and 1. In low concentrations of solute the behaviour is close to ideal, and thus has an activity coefficient close to 1.^{85,88,89} Therefore, under these conditions the Nernst equation can be applied using concentration,

$$E = E^{0*} + \frac{2.303RT}{nF} \log \left(\frac{[A]^a \cdot [B]^b}{[C]^c \cdot [D]^d} \right) \quad (1.4)$$

where E^{0*} is stated as,

$$E^{0*} = E^0 + \frac{RT}{nF} \log \left(\frac{\gamma_A^a \cdot \gamma_B^b}{\gamma_C^c \cdot \gamma_D^d} \right) \quad (1.5)$$

Reference electrodes have a stable and well-known, reproducible electrode potential and operates to preserve a constant potential independent of the solution conditions. The internationally accepted reference electrode is the standard hydrogen electrode (SHE).^{85,86} Common reference electrodes include the silver/silver chloride (Ag/AgCl) and mercurous chloride (Hg/Hg₂Cl₂), referred to as the saturated calomel electrode (SCE).⁹⁰ Typically, the reference electrode is encased in glass tube, containing a saturated chloride solution (KCl) and a ceramic frit, depicted in Figure 1.11.

Potentiometry can also be applied to ion selective electrodes (ISEs), by which ion concentration can be determined via the ion transfer across a glass membrane. The difference in charge either side of this membrane results in a potential difference. The most common ISE is a pH electrode, made from a glass membrane that is highly sensitivity to H⁺ ions.⁸⁵ pH is defined by,

$$pH = -\log (a_{H^+}) \quad (1.6)$$

Therefore, the potential difference measured across the glass membrane can be correlated via a calibration curve to the concentration of H⁺ ions in solution, resulting in the measurement of pH.⁸⁵

1.5.2. Dynamic Electrochemistry

If we consider a one electron redox reaction of a species between its reduced form, R, and its oxidised form O,



where k_f is the forward rate constant and k_b is the backward rate constant. Where no external driving force is applied, the forward and backward reactions occur at the same rate ($k_f = k_b$) and thus the species are in equilibrium.⁸⁶

In dynamic electrochemistry, the application of an applied potential perturbs the typical equilibrium of a redox couple. This therefore drives the reaction in one direction resulting in a net electron transfer which is simultaneously measured as the faradaic current.^{85,86} Figure 1.11 shows a standard three electrode electrolytic cell typically employed in dynamic electrochemistry.

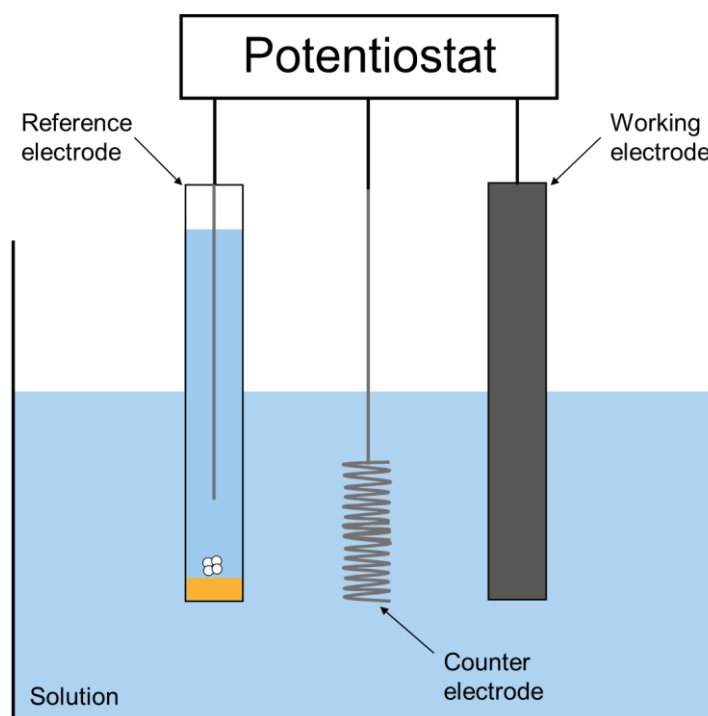


Figure 1.11. Schematic of standard three electrode electrolytic cell (not to scale).

A potential is applied via the potentiostat between the working and reference electrodes, which results in the transfer of electrons at the surface of the working electrode, producing a measurable current (i).

The potentiostat applies an equal opposing current ($-i$) to the counter electrode, allowing the current flow between the working and counter electrode.^{85,86}

The working electrode is commonly fabricated using a metal or carbon. Its surface is a crucial element within an electrochemical cell, as the electrode material, geometry, and topographical irregularities can impact the electrochemical response.⁹¹ Electrodes come in a variety of sizes (ranging from macro to nanoelectrodes) and geometries, such as inlaid-disc, hemispherical, band and ring to name a few.⁹²

Resistance, R , is a typical occurrence within electrochemical cells, arising due to current passing through electrodes, wiring, through solution and the electrode-solution interface. If the current generated is too large (in the μA range and above), then the presence of a counter electrode is necessary to prevent the passing of current between the working and reference electrode and to counteract the effect of ohmic drop (iR), which occurs when R from the passing current becomes too large. This would therefore result in a disproportion between potential applied and the potential experienced at the working electrode, and consequently reduce the current flow. A Pt wire with a large surface area is a commonly employed as a counter electrode. Additionally, the ohmic drop effect can be counteracted by the addition of high concentrations of inert salt (background electrolyte), to decrease the solution resistance.^{85,86}

1.5.2.1. Electrode Reaction Rates and Mass Transport

The electrode reaction pathway (current) can be complex and occurs in a sequence involving several steps (Figure 1.12). The rate of these reactions is thus determined by the slowest step of the sequence, the processes include: i) mass transport of electroactive species to the electrode surface, ii) electron transfer at the electrode surface, iii) chemical and/or surface processes, such as adsorption or desorption, that precede or succeed the electron transfer. The net rate of reaction, i.e. the measured faradaic current is ultimately limited by either the rate of mass transport, defined by the mass transport coefficient (k_t) or by the rate electron transfer, defined by the electron transfer coefficient (k_r).^{85,86,90}

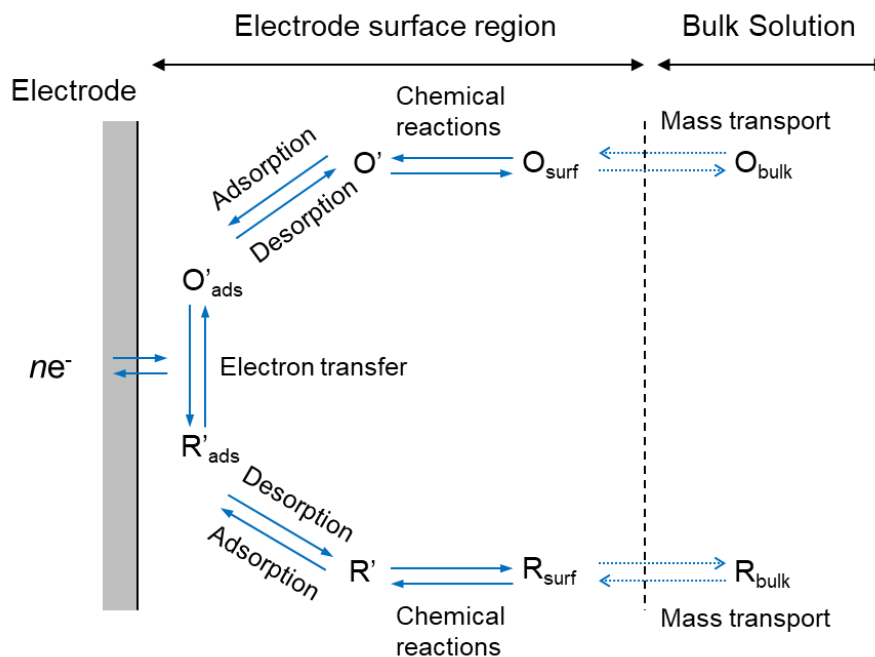


Figure 1.12. Schematic of electron transfer and mass transport pathway at the surface of an electrode. (Adapted from Bard and Faulkner, 2001).⁸⁶

The faradaic current that occurs from the electron transfer at the electrode-solution interface, and is proportional to the rate of reaction, can be expressed by Equation 1.8:^{85,86}

$$i = nAFJ \quad (1.8)$$

where n is the number of electrons transferred in the faradaic process, A is the electrode area (cm^2), and J is the flux ($\text{mol cm}^{-2} \text{s}^{-1}$).

Reactions controlled by mass transport to the surface of an electrode can occur by either one or a combination of three different modes: diffusion, convection, and migration.

1.5.2.1.1. Diffusion

Diffusion is defined as the net movement of chemical species down a concentration gradient, from regions of high concentration to regions of lower concentration. When a chemical species undergoes a redox reaction at the surface of a working electrodes, the surface concentration of the species, C_s , is lower than that of the bulk concentration, C^* .^{85,86}

Species consequently diffuse from the bulk to the surface, moving down the concentration gradient, generating a diffusion layer with time.^{85,86} This process is illustrated in Figure 1.13.

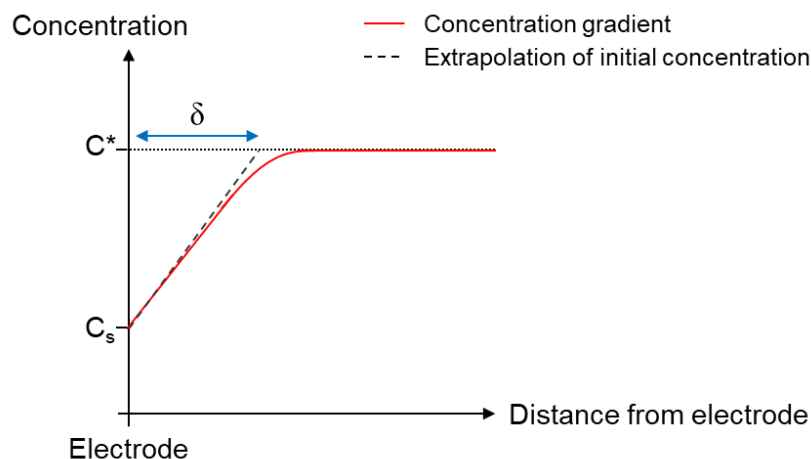


Figure 1.13. Illustration of diffusion layer at an electrode in 1D, where δ is the length of the diffusion layer.⁸⁶

a) *Fick's Laws of Diffusion*

Fick proposed two laws that govern diffusion in solution, as shown in Equations 1.9 – 1.13 below. They demonstrate the relationship between the flux of a substance and its concentration as a function of time and position.^{85–87}

Fick's first law states that the flux of a species, i.e. the rate of diffusion, is directly proportional to the concentration gradient,

$$J = -D \frac{\partial c^*}{\partial x} \quad (1.9)$$

For a one-dimensional system (x dimension), where D is the diffusion coefficient in $\text{cm}^2 \text{s}^{-1}$, and $\delta c^*/\delta x$ is the concentration gradient.

Under a mass transport-controlled process, governed by diffusion only, the following equation can be applied:

$$J = -k_t C^* \quad (1.10)$$

Where k_t is defined as:

$$k_t = \frac{D}{\delta} \quad (1.11)$$

where, δ is the diffusion length in cm.

Fick's second law is valid for planes parallel to one another and perpendicular to the diffusional direction, *i.e.* linear diffusion conditions. It associates the change in concentration with time, relative to the change in flux at point x .

$$\frac{\partial c}{\partial t} = D \frac{\partial^2 c}{\partial x^2} \quad (1.12)$$

For diffusion towards a spherical electrode, where the lines of flux are not parallel but rather perpendicular to the sphere, Fick's second law is expressed as:

$$\frac{\partial c}{\partial t} = D \frac{\partial^2 c}{\partial r^2} + \frac{2}{r} \frac{\partial c}{\partial r} \quad (1.13)$$

where r is the distance from the centre of the electrode.

b) *Geometry of Electrodes*

In the three dimensions, the geometry of the working electrode will contribute to the shape of the diffusion field that arises, as well as the timescale at which the experiment occurs. A macroelectrode typically has a radius on the millimetre or centimetre scale.⁹³ Linear (or planar) diffusion controls mass transport to the electrodes surface.⁹² When the radius of the electrode surface is reduced, the electrode can be defined as a microelectrode, with dimensions on the micrometre or sub-micrometre scale (but smaller than 50 μm).⁸⁷ Ultramicroelectrodes (UMEs) typically have a diameter range of 1 – 25 μm .⁹⁴ This ultimately increases the diffusional flux of species to the electrode surface. Therefore, microelectrodes have a non-planar or radial diffusion field.⁹³ The diffusion fields for different electrodes geometries are shown in Figure 1.14.

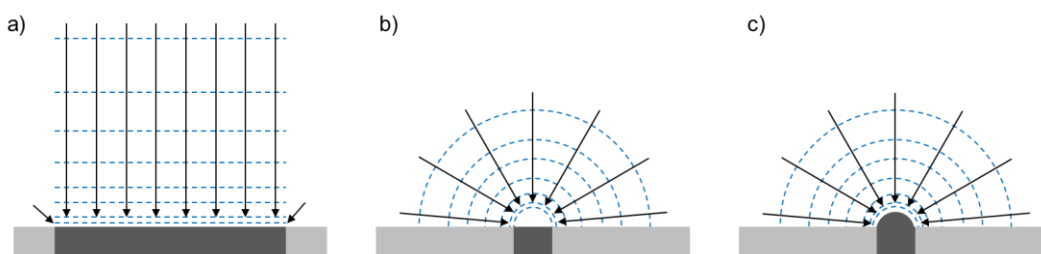


Figure 1.14. Diffusion field profiles for a) macroelectrode, b) microelectrode and c) hemispherical electrode.

1.5.2.1.2. Convection

Convection is the movement of species, either by force attributed to a temperature, pressure, or mechanical gradient, or by natural convection due to density gradients.^{85,86}

In one dimension it can be expressed as:

$$J_x = v_x C^* \quad (1.14)$$

where, J_x , and v_x is the flux and velocity in the x -direction, respectively.

In solution, convection is typically generated by heating, stirring (hydrodynamics), such as the use of the rotating disc electrode.^{85,86}

1.5.2.1.3. Migration

Migration is the movement of charged species along an electric field, down a potential gradient.^{85,86} Here, in a one-dimensional potential field, it can be expressed as:

$$J_x = -\frac{zF}{RT} DC^* \frac{\partial \phi}{\partial x} \quad (1.15)$$

where, z is the charge of the species, and $\delta\phi/\delta x$ is the potential gradient. The effects of migration are usually mitigated by addition of background electrolyte.

1.5.2.1.4. Nernst-Planck Equation

As previously described, the flux, J , measures the rate of mass transport to an electrode, and therefore Equations 1.9, 1.14 and 1.15 can be combined to describe the one-dimensional mass transport to an electrode, shown by the Nernst-Planck equation:

$$j_x = -D \frac{\partial c^*}{\partial x} - \frac{zF}{RT} DC^* \frac{\partial \phi}{\partial x} + v_x C^* \quad (1.16)$$

The three terms represent diffusion, which is described by Fick's first law, migration of species in a solution, and convection of the solution, respectively.

Mass transport can be simplified and easier to quantify by making one or more of the terms in the Nernst-Planck equation negligible by experimental design. The convection term can be made redundant by maintaining room temperature and atmospheric pressure (1 atm), whilst also avoiding the flow or stirring of solution for the duration of the experiment. As previously mentioned, the effects of migration can be mitigated by the addition of background electrolyte, typically the addition of an inert salt in excess (0.1 M KCl, KNO₃). The background electrolyte concentration is normally of 100-fold increase of the analyte (faradaic species) concentration. Its presence therefore increases conductivity of the solution and decreases the size of the diffusion layer at the electrode-solution interface.^{85–87} This reduces the change in potential to within electron tunnelling distance, which allows for diffusion-control to the electrode surface.⁸⁶

1.5.2.2. The Electrode-Solution Interface

The electrode/solution interface was originally established by Helmholtz, which was later modified by Gouy, Chapman and Stern.^{85–87,95,96} In 1853, Helmholtz identified that at an electrode/electrolyte interface, two layers of oppositely charged ions would form, separated by a distance, denoted H .^{96,97} The Helmholtz model was later modified by Gouy in 1910,⁹⁸ and Chapman in 1913.^{96,99} The Gouy-Chapman model took into consideration that ions are mobile in aqueous electrolyte, whereby the ions are not closely packed together near the electrode surface, but rather the ions of opposing charge to the electrode are distributed into a region of thickness, larger than H . This region can be identified as the diffuse double layer (DDL).^{85–87,95,96} In 1924, Stern¹⁰⁰ then incorporated both the Helmholtz model and the Gouy-Chapman model, which included both the compact layer consisting of solvated ions close to the electrode and the DDL.⁹⁶

Therefore, the electrode/solution interface can be described as an electrical double layer comprised of the electrical charge at the electrode surface and the charge of the ions within the solution located at a small distance from the surface of the electrode. When a surface is placed in an electrolyte solution, this electrical double layer forms owing to the assembly of counter ions at the electrode-solution interface to balance the charge. Hence, a positively charged electrode would attract a layer of negative ions and *vice versa*. The two parallel layers that form the double layer are referred to as the

Inner Helmholtz Plane (IHP) and the Outer Helmholtz Plane (OHP).⁸⁵⁻⁸⁷ A more general model for the electrical double layer is shown in Figure 1.15.

The IHP is the layer closest to the electrode, consisting of solvent molecules and surface-adsorbed (desolvated) ions, whilst the OHP consists of solvated ions at the closest approach to the surface. These solvated ions at the OHP are freer than those at the IHP and therefore can disperse into the three-dimensional region (the DDL) which extends into the bulk solution.⁸⁵⁻⁸⁷

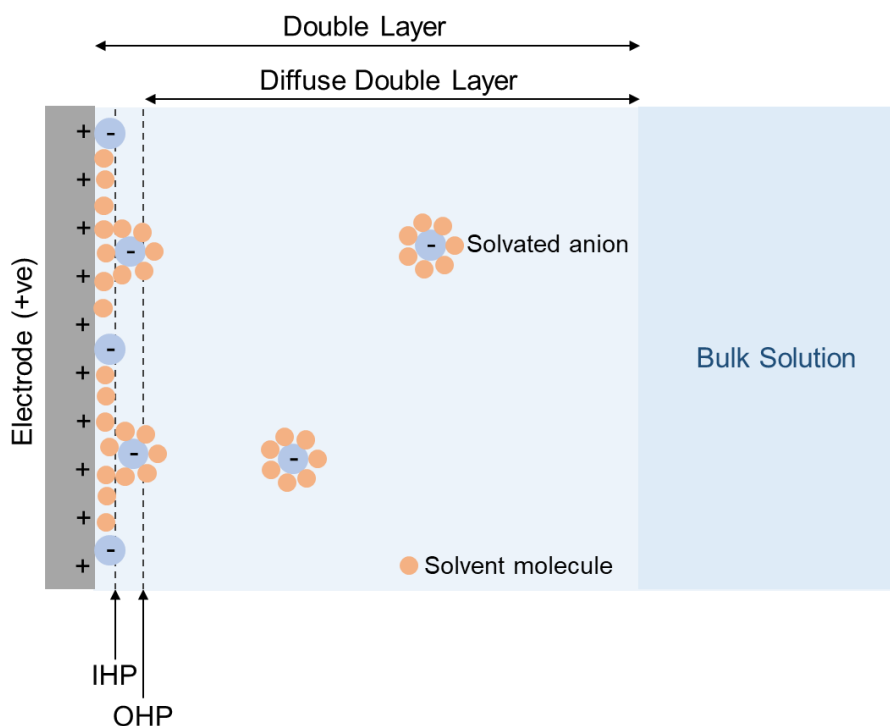


Figure 1.15. Schematic of electric double layer at the electrode-solution interface for a positively charged electrode.

The double layer structure acts as a capacitor enabling the storage of charge. Therefore, when a potential is applied to an electrode, the presence of the double layer results in a charging (non-faradaic) current to pass through the cell.⁸⁵⁻⁸⁷

1.5.2.3. Voltammetry

Voltammetry is one of the simplest and most common electrochemical techniques. Here, the current is measured as the potential applied at the working electrode is altered with time, which initiates a redox process. The potential is typically scanned linearly from a point where there is no electron transfer (ET) to a potential that is past E^{0*} , at a scan speed measured in Vs^{-1} . This difference between $E - E^{0*}$ is known as the overpotential, η . In linear sweep voltammetry (LSV), only the forward scan is carried out, whereas cyclic voltammetry (CV) scans in both the forward and reverse direction. The typical response for a one electron oxidation process, for the potential change with time and the current response as a function of applied potential is illustrated in Figure 1.16, at a macroelectrode disc.^{82,85–87,101}

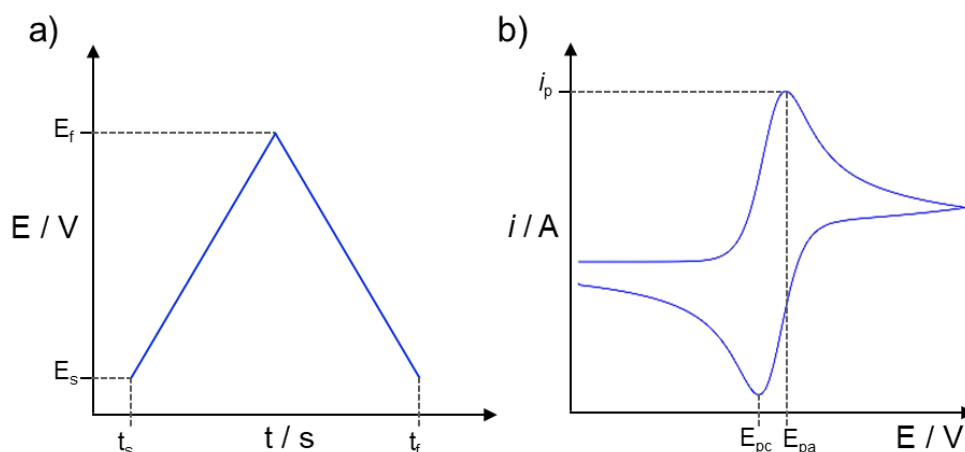


Figure 1.16. Cyclic voltammogram for an oxidation process, a) potential sweep – voltage with time, b) current response with time. Potential is swept from E_s to E_f to E_s again. The anodic and cathodic peak potentials are shown by E_{pa} and E_{pc} respectively, with i_p as the peak current for the forward scan.

The oxidation or reduction of an analyte at a potential is identified as a positive anodic peak or negative cathodic peak, respectively. The distinctive peaks in a cyclic voltammogram (CV) are formed from the formation of the diffusion layer close to the electrodes surface. As the potential at the working electrode increases in the forward scan, this causes the oxidation of the analyte, and thus the electrons are transferred to the electrode at an increasing rate, which results in the rise of the current.

The chemical species linearly diffuse down the concentration gradient to the electrodes surface (Figure 1.13), until the point at which diffusion is unable to sustain the rate of surface ET. Thus, the current reaches its peak (i_p) at E_{pa} and subsequently decays (Figure 1.16). For a reversible reaction (diffusion-controlled), in the backward direction, the potential sweep is reversed, therefore, species that were oxidised before are now reduced, producing the peak at E_{pc} .^{82,85–87,101}

1.5.2.3.1. Ultramicroelectrodes (UMEs)

For disc-shaped UMEs, the resulting cyclic voltammogram shape obtained differs from that of a macroelectrode. For a diffusion controlled reversible system, the current rises, reaches a steady state and subsequently retraces the curve for the reverse potential, as shown in Figure 1.17.^{82,85–87,101} This steady state response is due to the hemispherical diffusion, as the smaller electrode surface enhances the mass transport rate (Figure 1.14).

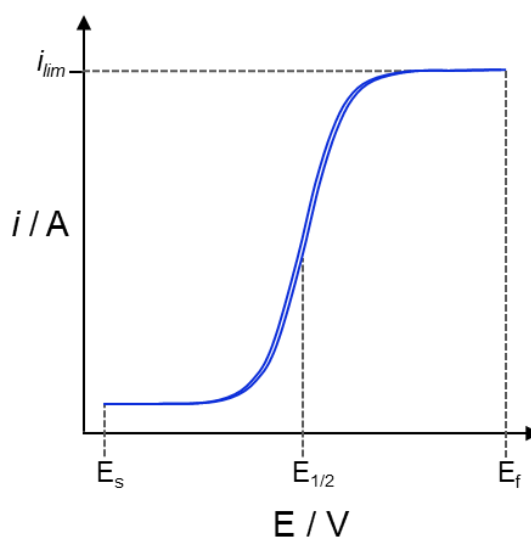


Figure 1.17. Cyclic voltammogram for an oxidation process at a disc UME, where i_{lim} is the steady state (limiting) current and $E_{1/2}$ is the half wave potential.

The steady state, or limiting current is related to the electrode radius and the concentration of species, which can be described by Equation 1.17,

$$i_{lim} = 4nFDaC^* \quad (1.17)$$

where, a is the radius of the (ultra) microelectrode (in cm).

1.5.2.3.2. *Hydrodynamic Voltammetry*

As discussed previously, convection (Equations 1.14 and 1.16) can be a contributing factor in mass transport, by increasing the flux towards the electrode surface and thus increasing the current (via rotation of the electrode or heating of solution or electrode). Therefore, hydrodynamic methods can benefit from this increased faradaic signal via convection.

a) Rotating Disc Electrode (RDE)

Since the establishment of the convective-diffusion equation for mass transport-controlled processes by Levich in 1942,¹⁰² the rotating disc electrode (RDE) has been an important tool to study electrode reaction mechanisms and their kinetics.¹⁰³ When an electrode is rotated, the mass transport is controlled by convective-diffusional mechanisms. This flow obeys the theory of hydrodynamics, hence the name hydrodynamic voltammetry.¹⁰⁴

The benefits of the RDE are, i) development of a diffusion layer where the thickness does not change with time, ii) an electric double-layer that has an insignificant effect on the measurement, and iii) defined theory and mathematical constructs to relate experimental parameters to the mass transport of the reactants to the electrodes surface almost completely due to convection.^{104,105}

When the working electrode is rotated about its vertical axis, the solution responds to this motion by the formation of a layer (referred to as the hydrodynamic boundary layer), which creates a centrifugal force where the electrolyte solution moves away from the centre of the electrode disk surface. Bulk solution moves upwards by laminar flow, perpendicular to the electrode to replace the boundary layer, as shown in the schematic in Figure 1.18. This rotational movement results in a well-defined solution flow pattern.^{85,86,92,105} The electroactive reactant is transported to the electrode surface via convective diffusion. Equation 1.18 evaluates the thickness of this hydrodynamic boundary layer (δ_H),^{86,92,104,106}

$$\delta_H = 3.6 (\nu/\omega)^{1/2} \quad (1.18)$$

where, ν is the kinematic viscosity of the solution in cm^2/s and mass transport is dependent on the angular velocity, ω ($\omega = 2\pi f/60$, where f is the rpm).^{85,86,104}

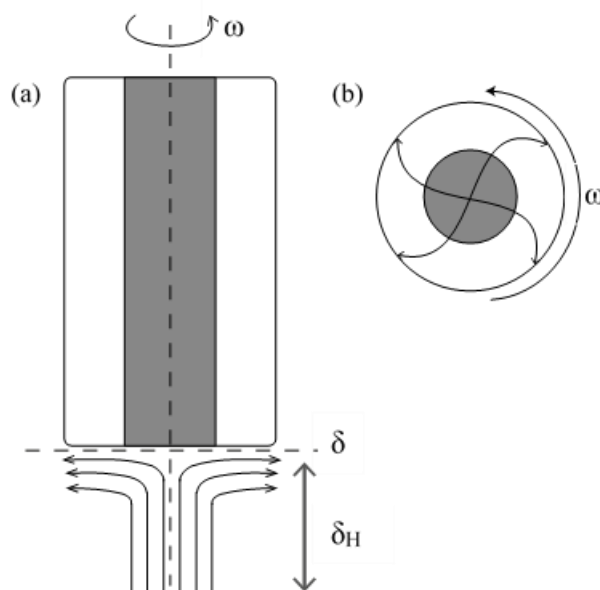


Figure 1.18. Schematic of rotating disc electrode for (a) solution flow towards electrode surface and (b) flow of solution near the electrode surface, where the vertical dotted line represents the diffusion layer, δ and δ_H is the hydrodynamic boundary layer. The grey area indicates the electrode surface and white area indicates the (PTFE) insulating material.^{86,107}

The thickness of the diffusion layer, δ , can be related to the diffusion coefficient, D , and the rotation speed of the electrode,^{85,92,105} given by,

$$\delta = 1.61 D^{1/3} \omega^{-1/2} \nu^{1/6} \quad (1.19)$$

Rotation speeds of 100 – 4000 rpm correspond to δ values in the range of 5 – 50 μm .^{85,105} The typical diffusion coefficient of species is approximately $10^{-5} \text{ cm}^2 \text{ s}^{-1}$.^{104,108}

Equation 1.19 indicates that the diffusion layer thickness is independent of the disk diameter, thus providing a uniform layer across the surface. The steady state (limiting) current in a reversible system is therefore proportional to the square root of the angular velocity, described by the Levich equation,^{85,86,92,108}

$$i_{lim} = 0.62nFAD^{2/3}\omega^{1/2}\nu^{-1/6}C^* \quad (1.20)$$

The hydrodynamics present in the GI tract are partly due to the contractions within the stomach and the small intestine, as well as the presence of liquids and solids.⁷⁸ The fluid in the gastric lumen is typically assumed to exhibit laminar flow.^{109,110}

Furthermore, mathematically modelling studies of the small intestine have also assumed laminar flow.¹¹¹ This therefore suggests that the RDE is an appropriate technique to use as an *in vitro* method for dissolution.

1.5.2.4. Amperometry

Amperometry or chronoamperometry is a technique where the oxidation or reduction of an electroactive species occurs upon the application of an appropriate applied potential at an electrode from a steady state anodic or cathodic current of the analyte. The working electrode potential is stepped and held at a constant value and the resulting current generated from the faradaic reaction is directly proportional to the concentration of the analyte, which is measured as a function of time. Therefore, when a potential step is applied, from one at which no reaction occurs, to a constant potential where ET transfer occurs at a diffusion-controlled rate, the process is controlled by mass transport with the development of a diffusion field previously shown in Figure 1.14. Illustrated in Figure 1.19 is the resulting current as a function of time.^{85,86,93,112}

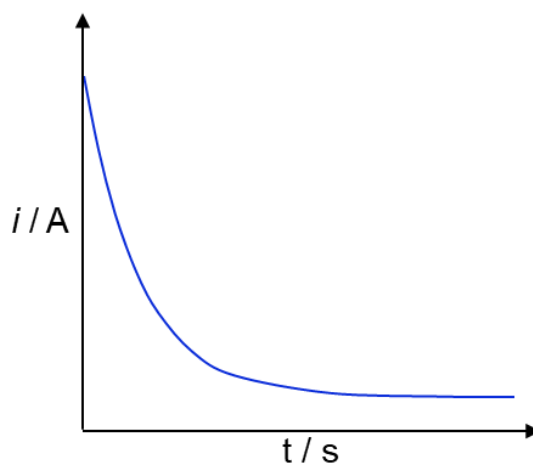


Figure 1.19. Current-time transient after a step in potential.

Amperometry can utilise the current measurement as a function of time to determine the behaviour of a drug dissolution rate over time. However, it is important to note that for extended periods of time, analytes can cause fouling of the electrodes surface and therefore this must be taken into experimental consideration. This is an issue that is explored in Chapter 4.

1.5.3. Electrochemical Analysis of Pharmaceuticals

Whilst electrochemistry is well-established in the analytical field, it is an emerging tool for use in analysis in the pharmaceutical industry. Many active pharmaceutical ingredients are electrochemically active compounds, and as such are suitable for analysis by electrochemical methods. Furthermore, electrochemical methods have several advantages including, rapid analysis times, simultaneous determination of several analytes, a wide range of temperatures, solvents, electrolytes and small sample volumes can be used.¹¹³

Electrochemical methods of detection are not without its limitations, however with the knowledge of these limitations, experiments can be crafted to overcome them. As mentioned previously, fouling of an electrodes surface is a primary concern in an electroanalytical measurement. Fouling can be mitigated by use of inert materials for the electrodes surface, application of synthetic membranes, or a short/pulsed electrochemical detection.¹¹⁴ Furthermore, for the detection of multiple analytes it is imperative to know the electrochemical potentials of the redox reactions of each analyte to determine which analyte is responsible for each signal.

1.5.3.1. Acetaminophen – An Electroactive Compound

Acetaminophen (APAP, also known as paracetamol; N-acetyl-p-aminophenol) is one of the most commonly prescribed and widely available over the counter non-steroidal anti-inflammatory drug, used as an antipyretic and painkiller.^{83,84,115} Not only is APAP economical and easy to manufacture, but it is also an electroactive substance, with a distinct electrochemical signature. It is therefore for these reasons that makes APAP an ideal substance to study as a model API in electrochemical based dissolution experiments, as carried out in this thesis. APAP has been extensively studied electrochemically under several different types of techniques and working electrodes, thus the overpotentials observed for the oxidation process vary in the literature depending on the experimental conditions, such as pH.^{83,84,115–122}

APAP undergoes electrochemical oxidation in solution to its oxidised state, N-acetyl-p-benzoquinone-imine (NAPQI), which is a quasi-reversible two-electron transfer (ET) process in the anodic region.^{83,84,121} This protonated form of NAPQI can convert to *p*-benzoquinone following a series of chemical reactions (Figure 1.20).^{83,118,123}

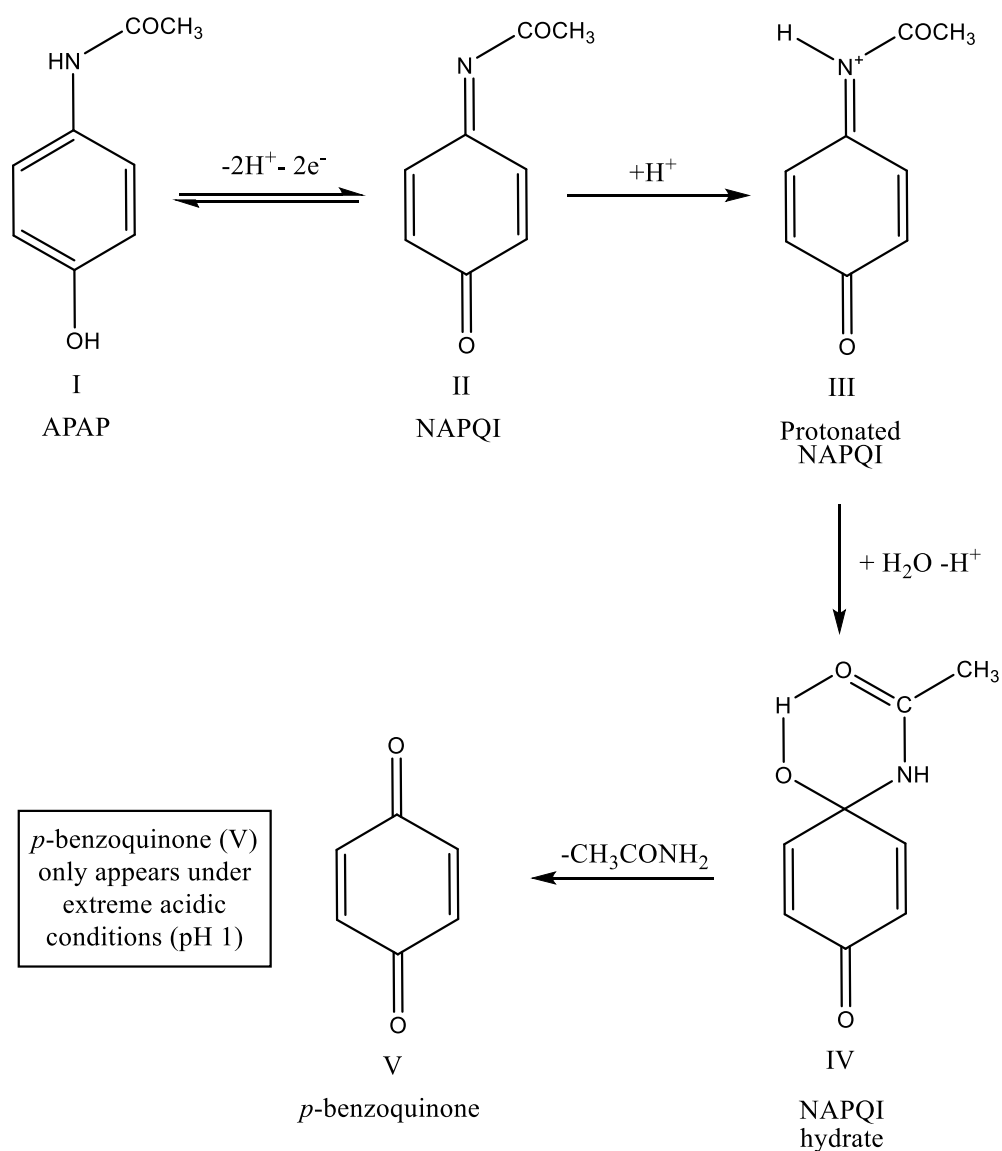


Figure 1.20. Electrochemically behaviour of APAP under acidic conditions. APAP undergoes an oxidation mechanism to form NAPQI (II) undergoes protonation reaction to form intermediate III, which is less stable but still electrochemically active, this intermediate rapidly yields a subsequent hydrate, intermediate IV, which is electrochemically inactive. Only under extreme acidic conditions is *p*-benzoquinone (V) formed, which is a slow transformation from (IV).^{83,118}

As the mechanism involves protons, the reversibility (peak to peak separation from E_{pa} to E_{pc}) is therefore pH dependent.⁸⁴ It should be noted that the occurrence of NAPQI is pH dependent. APAP is oxidised to NAPQI, by the loss of two electrons and two protons, and at pH values above 5 NAPQI is relatively stable in its unprotonated form.^{83,84,124}

Under acidic conditions NAPQI is protonated, to a less stable form, intermediate III, which is still however electrochemically active. This protonated form of NAPQI is then quickly transformed to a hydrate, intermediate IV, which is not electrochemically active. However, the transformation from intermediate IV to p-benzoquinone (V) is very slow and only occurs under extreme acidic conditions of *ca.* $\text{pH} \leq 1$.^{83,84,124}

Due to APAPs pH dependence, NAPQI and its subsequent reactions are not present in appreciable concentrations at the electrode surface during the cyclic sweep.⁸³ Thus, the cathodic (reduction) peak is unsuitable for quantitative analysis. However, the anodic (oxidative) peak can be used as the peak is proportional to the concentration of APAP.⁸³ It is for these reasons that the cyclic voltammograms studied in this thesis focuses solely on the anodic region.

The type of polymer and applicability of the taste masking approaches discussed previously varies depending on the drug used and the desired dosage form. Currently there is no universal inhibitor of drug bitterness that does not affect other taste modes, such as sweetness.²⁵ APAP is one such API suitable for coating by a water-insoluble polymer, such as the KCSS, as it possess a bitter taste, is characteristically slightly water soluble, and is suited as a dosage form as a multiparticulate.^{25,125,126} Therefore, along with these and the electrochemical properties described, APAP is highly suited as a model drug to test the KCSS polymers dissolution parameters.

1.6. Scanning Probe Microscopy (SPM)

Scanning probe microscopy (SPM) incorporates a series of techniques adept in measuring surface topography. SPM stems from the scanning tunneling microscope (STM), which was first established by Binnig and Rohrer in 1981.^{127,128} SPM techniques utilise a fine probe tip, often with piezoelectric actuators that can control movement with precision across a surface. This results in three-dimensional, high-resolution images which can reach nanometre to sub nanometre ranges dependent on the technique, the number of data points, and the size, quality, and sharpness of the probe. These SPM techniques are applied to study the polymer film surface as an isolated film and as a multiparticulate.

1.6.1. Atomic Force Microscopy (AFM)

One SPM technique is the atomic force microscopy (AFM), first introduced by Binnig and Rohrer in 1986.¹²⁷ AFM is a widely used technique to study biological cells, crystalline properties, characterisation of pharmaceutical drugs and polymer properties.^{66,127,129,130}

AFM maps the topography of a substrates' surface by using a sharp silicon or silicon nitride tip (< few tens of nm radius), attached to the end of a cantilever, which is generally 50 – 300 μm long, 20 – 60 μm wide and 0.2 – 1 μm thick. This tip (or probe) is moved in and out of contact with the sample surface in the z plane by the use of a piezo crystal but remains held in close proximity (100 \AA or less) to the surface of the sample of interest. Whilst the tip scans the surface in the xy plane, tracing and retracing the surface, the attractive or repulsive forces sensed by the tip results in the deflection to the cantilever, thus producing the topographical map of the surface. The cantilever deflections are detected by a laser beam which is reflected from the back side of the reflective cantilever and into a photodiode detector.¹²⁹ A schematic of the fundamental components of an AFM are shown in Figure 1.21.

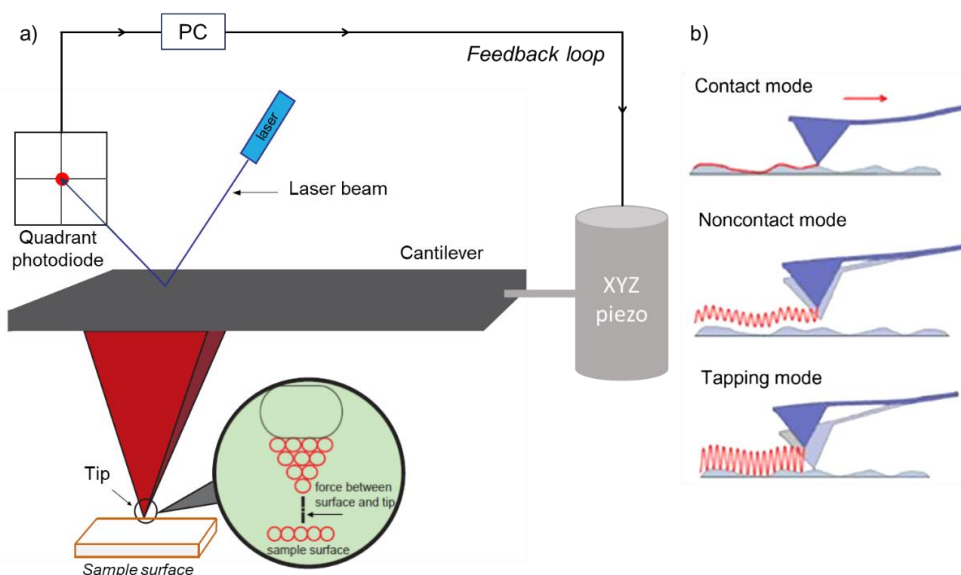


Figure 1.21. Illustration of key aspects of AFM set up and scanning modes. a) Schematic of AFM detection method, the laser beam is reflected from the back of the reflective cantilever and into the photodiode detector, which measures the cantilever deflection (not to scale) and b) illustration of the movement of the cantilever in each mode. (Part b reproduced from Asmatulu and Khan, 2019).¹³¹

1.6.1.1. Principle Modes of AFM Imaging

There are three common modes for AFM: i) contact mode, ii) non-contact mode and iii) tapping mode, shown in Figure 1.21b. In contact mode is where the tip is brought to the surface and remains in contact with the surface for the duration of the scan. The tip therefore experiences a small force (nN) due to the interaction of the atoms of the surface. A feedback loop is utilised to maintain the deflection cantilever constant. As the cantilever is deflected by the laser the z height is adjusted by the piezoelectric scanner to return to the original deflection point, or 'set point'. Contact mode uses constant force and height. Therefore, this mode is typically used for substrates that are hard and flat, where contact with the tip causes minimal damage to the surface.^{129,132}

For softer samples, tapping mode is usually preferred. Here the tip comes into to contact with the surface and then withdraws as it scans, thus minimising surface damage. The cantilever oscillates near the surface at its resonant vibrational frequency. As the cantilever oscillates the tip establishes intermittent tip-surface contact. The topography of the surface is mapped by a feedback mechanism in which the z -height of the cantilever is altered in order to maintain the oscillation amplitude.^{129,130,132,133}

Conversely, in non-contact mode, the tip does not make contact with the substrate surface. Similarly, to tapping mode the cantilever tip is oscillated in the air at its resonant frequency (at a smaller amplitude than in tapping mode).¹²⁹

During the AFM scan the cantilever deflection versus the movement of the piezo is measured (Figure 1.22), which can be converted into a force versus tip-sample separation measurement, by the calibration of the spring constant and the sensitivity of deflection, calculated by Hooke's law,¹²⁹

$$F = -kx \quad (1.21)$$

where, F = force (N), k = the cantilever spring (probe force) constant, (N/m) and x is the deflection distance (m).

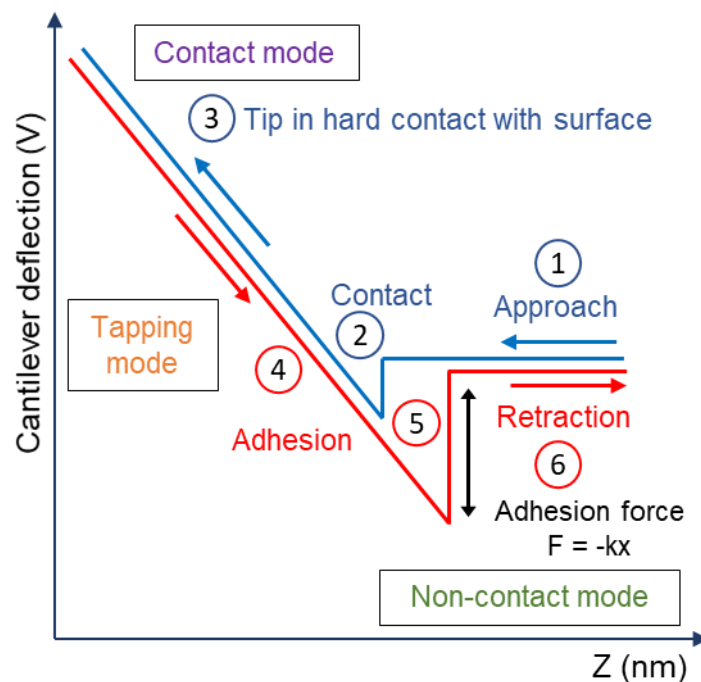


Figure 1.22. Schematic of force curve for cantilever deflection vs. piezo movement. Approach of cantilever tip to surface (blue line) and retraction (red line), where k is the cantilever spring constant and x is the deflection of the cantilever. Contact mode operates where the Coulomb force is highly repulsive. Non-contact mode operates far away from the surface and is sensitive to attractive van der Waals forces. Tapping mode oscillates in the region between contact mode and non-contact mode.

1.6.2. Scanning Ion-Conductance Microscopy (SICM)

Scanning electrochemical probe microscopy (SEPM) is a class of SPM techniques in which an electrochemical signal is used to detect and map the surface of a substrate. One such technique is scanning ion conductance microscopy (SICM), which was first introduced by Hansma *et al.* in 1989 to image nonconductive surfaces submerged in an electrolyte solution. As a non-contact and non-invasive method, SICM is suitable for imaging soft samples, such as biological cells.^{134–137}

SICM operates in a conducting electrolyte solution bath (typically of high ionic strength). It utilises a feedback mechanism of the current produced between two Ag/AgCl quasi-reference counter electrodes (QRCEs), in which one electrode is placed into a glass or quartz nanopipette and the other is used as a stand-alone electrode, positioned in the bulk electrolyte solution. A potential bias is applied between these two QRCEs in order to initiate and drive an ionic current through the end of the nanopipette, illustrated in Figure 1.23.^{135,136,138}

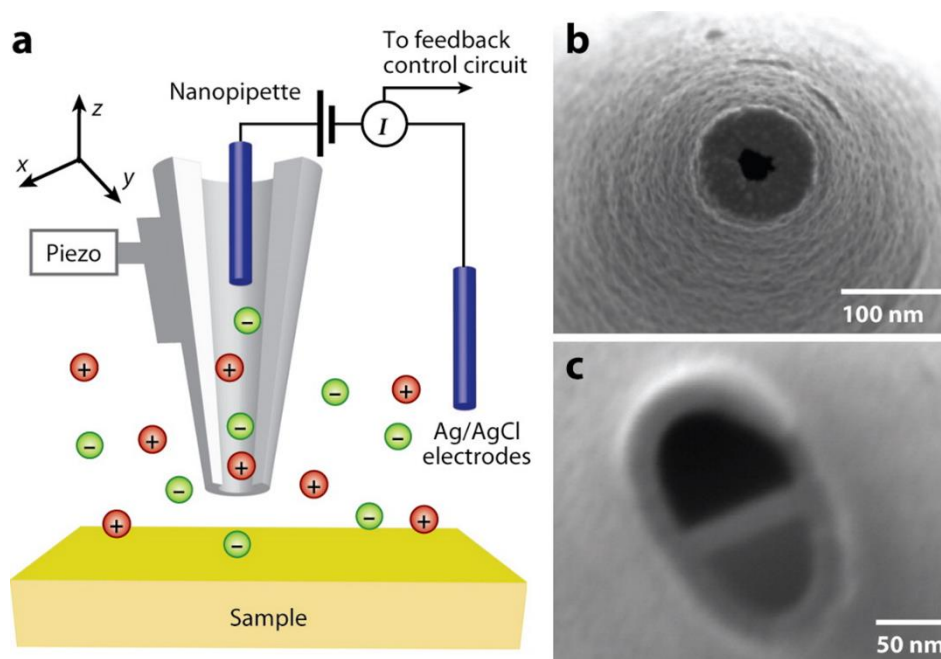


Figure 1.23. Schematic of scanning ion conductance microscope (SICM) set up. a) A nanopipette filled with electrolyte in close proximity to the sample surface. The applied bias between the electrode inside the nanopipette and the electrode in the bulk generates a n ion current, which is utilised in feedback control. The nanopipette is mounted on a piezoelectric positioner which controls the movement of the nanopipette in the x , y , and z directions. b) and c) show typical nanopipettes, where b) is a single and c) is dual barrel pipette, both of which operate as probes in SICM. (Reproduced from Chen, Zhou and Baker, 2012).¹³⁵

The magnitude of the generated ion current is characterised by the resistance between the probe and the electrolyte solution when the tip of the probe is positioned away from the substrate surface in the bulk. When the probe is positioned closer to the substrate surface the ionic current consequently decreases. This change in the ionic current response is used as the feedback signal, or a sensor to map the topography of the substrates surface as the tip moves in the x, y plane.^{135,136,139}

1.6.2.1. Feedback and Scanning Modes

1.6.2.1.1. Feedback Modes

SICM can operate using the two most common feedback modes, i) direct current mode (DC) (non-modulated), ii) distance modulated mode (DM). More recently, the bias modulation mode (BM) has been introduced.^{135,136,140} All three feedback modes and their corresponding approach curves are illustrated in Figure 1.24.

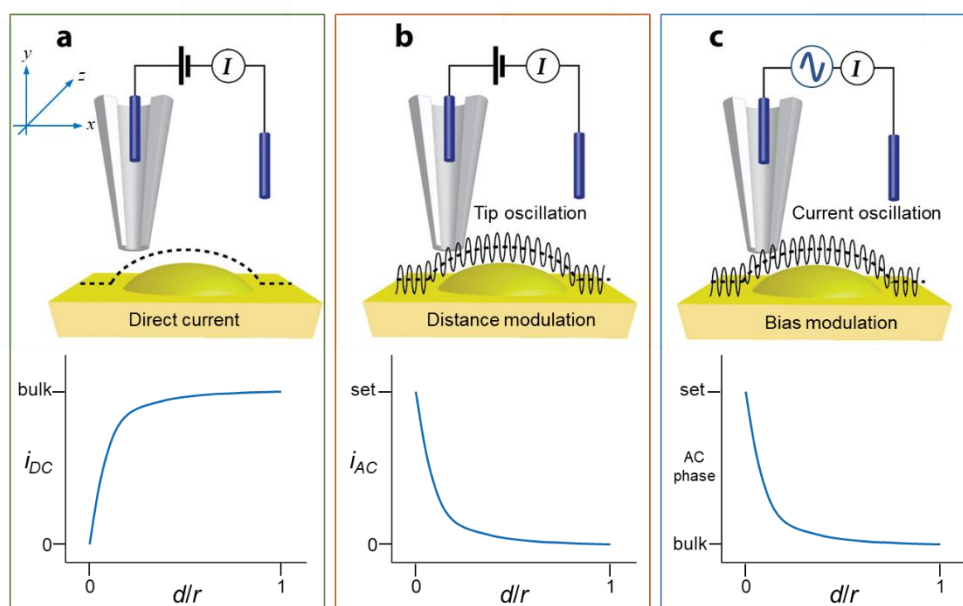


Figure 1.24. Schematic of different SICM feedback modes. a) Direct current mode, where the surface is detected by a decrease in the ionic current, b) distance modulation mode, where the probe is oscillated in the vertical direction, thereby producing an AC signal between the two QRCEs at the tip-substrate separation, and c) bias modulation mode, where harmonic oscillation is applied to the voltage between the two QRCEs and the surface is detected through a change in the AC phase. (Diagrams edited and reproduced from Chen, Zhou and Baker, 2012 and graphical schematic adapted from Kang *et al.*, 2016).^{135,136,140}

The approach curves illustrated along with their corresponding feedback modes in Figure 1.24 show the feedback response of the relative probe-to-substrate distance, d/r , where d is the physical probe-substrate separation and r is the opening radius of the probe. The set value for curves for Figure 1.24b and 1.24c relates to a set point at a value used to prevent the tip from moving closer to the surface, it can therefore be used for feedback during imaging.¹⁴⁰

The DC feedback mode is the most widely used (Figure 1.24a). Here the probe approaches the surface, and the ionic current is observed for a percentage decrease (typically 1 – 5 %) from the value at which the probe was in the bulk. This reduction in current is the result from the increase in resistance from the system, when the distance resistance between the probe and the substrates surface is similar to that of the probe opening.^{136,141} Therefore, the DC ion current is sensitive to the tip-surface distance and used to sense the substrates surface.^{135,136}

The second feedback mode is distance modulation (Figure 1.24b), which utilises an induced alternating current (AC) as a feedback signal. In this mode, an oscillation is applied to the tip via the z piezoelectric positioner. Upon approach to the surface an AC signal of the ionic current is induced, which can then be recovered at the same frequency as the physical oscillation by the use of a lock-in amplifier. The AC amplitude of the ionic current increases as the probe approaches the surface.^{135,136,140}

The third feedback mode (Figure 1.24c) is a more recent development in SICM imaging by Unwin *et al.*¹⁴² This approach utilises bias modulation to achieve a feedback mechanism. Harmonic oscillation of the potential bias is applied between the two QRCEs, generates an oscillating ion current, which allows for the extraction of the AC phase for feedback and is therefore used to detect the surface topography.^{136,140,142} As the AC phase is very sensitive to the probe-substrate separation, it can be used for precise positioning of the probe.¹⁴⁰

1.6.2.1.2. Scanning Modes

Once a suitable feedback mode has been selected for an SICM experiment, the scanning of the probe relative to the surface must be considered. This can be achieved by either i) a raster scan pattern, ii) constant-distance mode, or iii) ‘hopping’ or ‘standing approach’ mode. For the raster scan pattern (Figure 1.25a), the substrate is moved after a series of measurements in the x direction, followed by a translation in the y direction. In constant-distant mode (Figure 1.25b), the z -positioner is frequently adjusted for the duration of the scan, in order to maintain a constant separation between the probe and the surface. However, if there are distinct features with a significant difference in height present on the surface, this can potentially damage the tip of the probe. ‘Hopping’ or ‘standing approach’ mode (Figure 1.25c) can overcome this issue, by retracting the probe to a safe distance. After a translation in the x or y direction an approach to the surface is made following a raster pattern, in which a pixel by pixel image is produced.^{135,136}

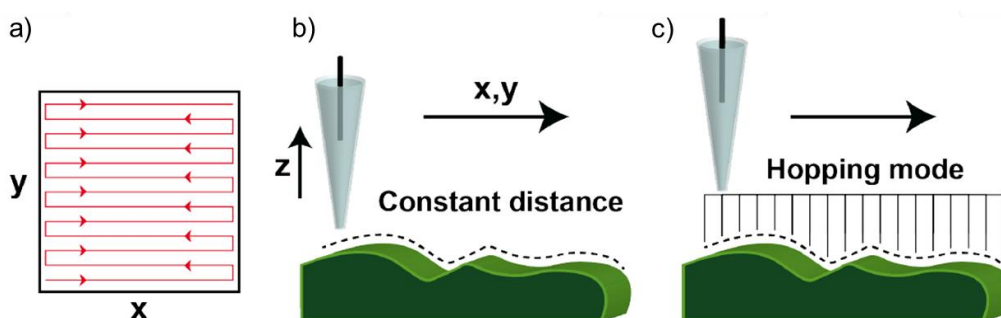


Figure 1.25. Scanning modes of SICM. a) Raster scan, showing a typical pathway of scanning by the probe relative to the substrates surface during an SICM experiment, b) constant distance scanning mode, where the probe-substrate separation is kept constant via the adjustment of the z positioner, thus maintaining the feedback threshold, and c) hopping mode, where the prob approaches the surface and withdraws before reaching the surface at each imaging point. (Reproduced from Page *et al.*,2017).¹³⁶

1.6.2.2. Surface Charge Mapping

Since its establishment in 1989, SICM has predominately been used in high resolution topographical imaging of soft samples, such as living cells.^{134,135,137} Over the years, the SICM technique has developed further than topographical mapping. Functional maps demonstrating interfacial properties such as charge separation within a sample can be mapped simultaneously, without probe-surface contact.^{138–140}

Surface charge occurs when a surface has either a net density of positively or negatively charged species, such as ions or electrons.¹⁴³ When a surface is placed into the SICM electrolyte bath, the surrounding electrolyte counteracts the charge discrepancy at the surface by the formation of a solvated layer of counter ions, *i.e.* the ions with the same charge as the surface are repelled. In other words, an electric double layer forms.

Surface charge is a central interfacial property which determines physical and chemical interactions at surfaces.^{139,144} Biological interfaces, catalysts, sensors and colloidal systems are known to have strong influences of surface charge.¹⁴⁴ Surface charge can also be present on surfaces such as glass or quartz.¹⁴⁵ Surfaces are usually characterised by both topographical features and heterogeneous charge distributions, therefore SICM presents itself as a suitable technique for probing the local surface charge simultaneously.¹³⁹ The presence of surface charge can occur through different characteristics, such as protonation or deprotonation of functional groups, adsorption of charge ions onto a surface. The magnitude of surface charge can be quantified to surface charge density, given by $C\ m^{-2}$.^{139,146} SICM and its ability to map the charge of a surface is utilised to study the charge distribution of the KCSS polymer in varying pH electrolyte solutions in Chapter 6.

1.7. Research Aims

The fundamental aims of this research are to understand the dissolution of an electrochemically active API from a pH responsive reverse enteric polymer coating in the form of a multiparticulate oral dosage form. Various electrochemical techniques are utilised to map the dissolution process in real time under *in vitro* conditions. Furthermore, imaging techniques are employed to fully comprehend the polymer coating as a single entity and what effect this may have on API release.

To begin with, Chapter 2 describes an overview of the materials, instrumentation and experimental techniques used throughout this thesis.

Chapter 3 focuses on the particle size distribution of the multiparticulate beads both quantitatively and qualitatively. This chapter also serves as a proof of concept that API dissolution from a single MP bead can be electrochemically detected, by both *ex situ* and *in situ* measurements, with and without the Kollicoat[®] Smartseal 30 D (KCSS) polymer coating. As a small-scale dissolution testing set up, it utilises microelectrodes to determine APAP release and concentration in a small volume of dissolution media.

Chapter 4 elaborates on the findings discovered in the previous chapter. Here, the electroanalytical techniques are applied in a bulk measurement of the multiparticulates. Here, the *in vitro* release of APAP from the KCSS polymer coating is from multiple units of MP beads in various dissolution media that mimic simplified simulated biological fluids at a temperature range of 20 – 40 °C. These include HCl as gastric fluid, acetate and citrate buffers, and simulated saliva.

Chapter 5 focuses on the polymer film as a single entity in the form of an isolated film cast on a glass slide. This study stresses the importance the effect of film formation can have on the API release. It takes a closer look at the physical and chemical mechanisms in which the polymer behaves under acidic media. The physical response of the polymer film is examined under the scanning probe techniques AFM, alongside NMR analysis of the chemical structure which demonstrates the chemical changes under acidic dissolution.

Chapter 6 utilises SPM techniques to further study the KCSS polymer film coating as part of the MP bead formulation. Using the non-invasive SICM technique, *in situ* topographical maps of the surface along with the corresponding charge distribution mapping of the surface were able to be determined in varying pHs.

Lastly, the final chapter summarises the findings of each chapter presented in this thesis.

1.8. References

1. Allen, L. V. & Zanoliniak, P. Pharmaceutical Dosage Forms. in *Ullmann's Encyclopedia of Industrial Chemistry* 1–45 (Wiley-VCH Verlag GmbH & Co. KGaA, 2014). doi:10.1002/14356007.a19_241.pub2
2. Marques, M. R. C., Loebenberg, R. & Almukainzi, M. Simulated biological fluids with possible application in dissolution testing. *Dissolution Technol.* **18**, 15–28 (2011).
3. Sastry, S. V., Nyshadham, J. R. & Fix, J. A. Recent technological advances in oral drug delivery – a review. *Pharm. Sci. Technol. Today* **3**, 138–145 (2000).
4. Lopez, F. L., Ernest, T. B., Orlu, M. & Tuleu, C. The effect of administration media on palatability and ease of swallowing of multiparticulate formulations. *Int. J. Pharm.* **551**, 67–75 (2018).
5. Lee, H. S. *et al.* Sprinkle formulations—A review of commercially available products. *Asian J. Pharm. Sci.* **15**, 292–310 (2019).
6. Abuhelwa, A. Y., Williams, D. B., Upton, R. N. & Foster, D. J. R. Food, gastrointestinal pH, and models of oral drug absorption. *Eur. J. Pharm. Biopharm.* **112**, 234–248 (2017).
7. Khutoryanskiy, V. V. Supramolecular materials: Longer and safer gastric residence. *Nat. Mater.* **14**, 963–964 (2015).
8. Long, M. & Chen, Y. Dissolution Testing of Solid Products. in *Developing Solid Oral Dosage Forms: Pharmaceutical Theory and Practice* 319–340 (Elsevier, 2009). doi:10.1016/B978-0-444-53242-8.00014-X
9. Gupta, S., Kesarla, R. & Omri, A. Formulation Strategies to Improve the Bioavailability of Poorly Absorbed Drugs with Special Emphasis on Self-Emulsifying Systems. *ISRN Pharm.* **2013**, 1–16 (2013).
10. *Pharmaceutical Dosage Forms: Tablets. Pharmaceutical Dosage Forms: Tablets* (CRC Press, 2008). doi:10.3109/9781420020281
11. Aulton, M. E. & Taylor, K. M. G. *Aulton's Pharmaceutics: The Design and Manufacture of Medicines.* (Elsevier Ltd., 2018).
12. Bodmeier, R. Tableting of coated pellets. *Eur. J. Pharm. Biopharm.* **43**, 1–8 (1997).
13. Rajabi-Siahboomi, A. R. Overview of Multiparticulate Systems for Oral Drug Delivery. in *Multiparticulate Drug Delivery Formulation, Processing and Manufacturing* (ed. Rajabi-Siahboomi, A. R.) 1–4 (Springer, New York, NY, 2017). doi:10.1007/978-1-4939-7012-4_1
14. Dey, N. S., Majumdar, S. & Rao, M. E. B. Multiparticulate Drug Delivery Systems for Controlled Release. *Trop. J. Pharm. Res.* **7**, 1067–1075 (2008).

15. Lopez, F. L. *et al.* Acceptability of placebo multiparticulate formulations in children and adults. *Sci. Rep.* **8**, 1–10 (2018).
16. Klein, S. Multiparticulate drug delivery: Formulation, Processing and Manufacturing. in *Multiparticulate drug delivery: Formulation, Processing and Manufacturing* (ed. Rajabi-Siahboomi, R. A.) 169–212 (2017).
17. Gandhi, B. & Baheti, J. Multiparticulates Drug Delivery Systems : A Review. *Int. J. Pharm. Chem. Sci.* **2**, 1620–1626 (2013).
18. Wening, K. & Breitzkreutz, J. Oral drug delivery in personalized medicine : Unmet needs and novel approaches. *Int. J. Pharm.* **404**, 1–9 (2011).
19. Fu, Y. & Kao, W. J. Drug release kinetics and transport mechanisms of non-degradable and degradable polymeric delivery systems. *Expert Opin. Drug Deliv.* **7**, 429–444 (2010).
20. Yang, W. & Pierstorff, E. Reservoir-Based Polymer Drug Delivery Systems. *J. Lab. Autom.* **17**, 50–58 (2012).
21. Uhrich, K. E., Cannizzaro, S. M., Langer, R. S. & Shakesheff, K. M. Polymeric Systems for Controlled Drug Release. *Chem. Rev.* **99**, 3181–3198 (1999).
22. Joshi, S. & Petereit, H. U. Film coatings for taste masking and moisture protection. *Int. J. Pharm.* **457**, 395–406 (2013).
23. Coupland, J. N. & Hayes, J. E. Physical approaches to masking bitter taste: Lessons from food and pharmaceuticals. *Pharm. Res.* **31**, 2921–2939 (2014).
24. Vummaneni, V. & Nagpal, D. Taste Masking Technologies : An Overview and Recent Updates. *Int. J. Res. Pharm. Biomed. Sci.* **3**, 510–524 (2012).
25. Sohi, H., Sultana, Y. & Khar, R. K. Taste masking technologies in oral pharmaceuticals: Recent developments and approaches. *Drug Dev. Ind. Pharm.* **30**, 429–448 (2004).
26. Ayenew, Z., Puri, V., Kumar, L. & Bansal, A. K. Trends in Pharmaceutical Taste Masking Technologies: A Patent Review. *Recent Pat. Drug Deliv. Formul.* **3**, 26–39 (2009).
27. Kelleher, J. F. *et al.* A comparative study between hot-melt extrusion and spray-drying for the manufacture of anti-hypertension compatible monolithic fixed-dose combination products. *Int. J. Pharm.* **545**, 183–196 (2018).
28. Sandadi, S., Pandey, P. & Turton, R. In situ, near real-time acquisition of particle motion in rotating pan coating equipment using imaging techniques. *Chem. Eng. Sci.* **59**, 5807–5817 (2004).
29. Silva, B. S. *et al.* Building Process Understanding of Fluid Bed Taste Mask Coating of Microspheres. *AAPS PharmSciTech* **20**, (2019).

30. Behzadi, S., Toegel, S. & Viernstein, H. Innovations in Coating Technology. *Recent Pat. Drug Deliv. Formul.* **2**, 209–230 (2008).
31. Jawahar, N. & Anilbhai, P. H. Multi Unit Particulates Systems (MUPS): A Novel Pellets for Oral Dosage Forms. *J. Pharm. Sci. Res.* **4**, 1915–1923 (2012).
32. Priese, F. & Wolf, B. Preparation of multi-particulate drug delivery systems by fluid bed pellet coating. *Sixth Jordan Int. Chem. Eng. Conf.* 1–7 (2012).
33. Teunou, E. & Poncelet, D. Batch and continuous fluid bed coating - Review and state of the art. *J. Food Eng.* **53**, 325–340 (2002).
34. KuShaari, K., Pandey, P., Song, Y. & Turton, R. Monte Carlo simulations to determine coating uniformity in a Wurster fluidized bed coating process. *Powder Technol.* **166**, 81–90 (2006).
35. Schattling, P., Jochum, F. D. & Theato, P. Multi-stimuli responsive polymers- the all-in-one talents. *Polym. Chem.* **5**, 25–36 (2014).
36. Karolewicz, B. A review of polymers as multifunctional excipients in drug dosage form technology. *Saudi Pharm. J.* **24**, 525–536 (2016).
37. Almeida, H., Amaral, M. H. & Lobão, P. Temperature and pH stimuli-responsive polymers and their applications in controlled and selfregulated drug delivery. *J. Appl. Pharm. Sci.* **2**, 01–10 (2012).
38. Schmaljohann, D. Thermo- and pH-responsive polymers in drug delivery. *Adv. Drug Deliv. Rev.* **58**, 1655–1670 (2006).
39. Mutalabisin, M. F., Chatterjee, B. & Jaffri, J. M. pH Responsive Polymers in Drug Delivery. *Res. J. Pharm. Technol.* **11**, 5115–5122 (2018).
40. Aguilar, M. R. & San Román, J. Smart Polymers and their Applications. *Smart Polym. their Appl.* **3**, 1–568 (2014).
41. Reyes-Ortega, F. *pH-responsive polymers: Properties, synthesis and applications. Smart Polymers and their Applications* (Woodhead Publishing Limited, 2014). doi:10.1533/9780857097026.1.45
42. Grainger, S. J. & El-Sayed, M. E. H. STIMULI-SENSITIVE PARTICLES FOR DRUG DELIVERY. in *Biologically-Responsive Hybrid Biomaterials* (eds. Jabbari, E. & Khademhosseini, A.) 171–190 (WORLD SCIENTIFIC, 2010). doi:10.1142/9789814295680_0008
43. Narang, A. S. & Boddu, S. H. *Excipient Applications in Formulation Design and Drug Delivery. Excipient Applications in Formulation Design and Drug Delivery* (Springer International Publishing, 2015). doi:10.1007/978-3-319-20206-8
44. Kocak, G., Tuncer, C. & Bütün, V. pH-Responsive polymers. *Polym. Chem.* **8**, 144–176 (2017).

-
45. Yoshida, T., Lai, T. C., Kwon, G. S. & Sako, K. pH- and ion-sensitive polymers for drug delivery. *Expert Opin. Drug Deliv.* **10**, 1497–1513 (2013).
 46. BASF. Kollicoat Smartseal 30 D Technical Information. *BASF* 1–13 (2019).
 47. Dinarvand, R., Dorkoosh, F., Hamidi, M. & Moghadam, S. H. Polymeric Delivery Systems for Biopharmaceuticals. *Biotechnol. Genet. Eng. Rev.* **21**, 147–182 (2004).
 48. Kolter, K., Guth, F. & Angel, M. Effective Taste-Masking Based on the New Coating Dispersion Kollicoat® Smartseal 30 D Effective Taste-Masking Based on the New Coating Dispersion Kollicoat® Smartseal 30 D. 1–2 (2010).
 49. Ko, J. *et al.* Hydrophilic surface modification of poly(methyl methacrylate)-based ocular prostheses using poly(ethylene glycol) grafting. *Colloids Surfaces B Biointerfaces* **158**, 287–294 (2017).
 50. Constantinou, A. P., Lan, T., Carroll, D. R. & Georgiou, T. K. Tricomponent thermoresponsive polymers based on an amine-containing monomer with tuneable hydrophobicity: Effect of composition. *Eur. Polym. J.* **130**, 1–11 (2020).
 51. BASF SE Care Chemicals Division Pharma Ingredients & Services. Kollicoat Smartseal 30 D Technical Information. *BASF Tech. Inf.* 1–12 (2011).
 52. Bütün, V., Billingham, N. C. & Armes, S. P. Synthesis and aqueous solution properties of novel hydrophilic–hydrophilic block copolymers based on tertiary amine methacrylates. *Chem. Commun.* 671–672 (1997). doi:10.1039/a700772h
 53. Darabi, A., Shirin-Abadi, A. R., Jessop, P. G. & Cunningham, M. F. Nitroxide-Mediated Polymerization of 2-(Diethylamino)ethyl Methacrylate (DEAEMA) in Water. *Macromolecules* **48**, 72–80 (2015).
 54. Chivate, A., Sargar, V., Nalawade, P. & Tawde, V. Formulation and development of oral dry suspension using taste masked Ornidazole particles prepared using Kollicoat® Smartseal 30 D. *Drug Dev. Ind. Pharm.* **39**, 1091–1097 (2013).
 55. Dashevskiy, A. *et al.* Micropellets coated with Kollicoat® Smartseal 30D for taste masking in liquid oral dosage forms. *Drug Dev. Ind. Pharm.* **43**, 1548–1556 (2017).
 56. Thorsten, C. Kollicoat® Smartseal 30 D. 1–39 (2010).
 57. Felton, Linda A., McGinity, J. W. *Aqueous Polymeric Coatings for Pharmaceutical Dosage Forms. Drugs and the Pharmaceutical Sciences* **176**, (CRC Press, 2016).
 58. Felton, L. A. Mechanisms of polymeric film formation. *Int. J. Pharm.* **457**, 423–427 (2013).
-

-
59. Ludwig, I., Schabel, W., Ferlin, P., Castaing, J.-C. & Kind, M. Drying, film formation and open time of aqueous polymer dispersions. *Eur. Phys. J. Spec. Top.* **166**, 39–43 (2009).
 60. Sonar, G. S. & Rawat, S. S. Wurster technology: Process variables involved and Scale up science. *Innov. Pharm. Pharm. Technol.* **1**, 100–109 (2015).
 61. L.Bruschi, M. Main mechanisms to control the drug release. in *Strategies to Modify the Drug Release from Pharmaceutical Systems* (ed. Bruschi, M. L.) 37–62 (Elsevier, 2015). doi:10.1016/B978-0-08-100092-2.00004-7
 62. Siepmann, J. & Siepmann, F. Mathematical modeling of drug delivery. *Int. J. Pharm.* **364**, 328–343 (2008).
 63. Ozturk, A. G., Ozturk, S. S., Palsson, B. O., Wheatley, T. A. & Dressman, J. B. Mechanism of release from pellets coated with an ethylcellulose-based film. *J. Control. Release* **14**, 203–213 (1990).
 64. Sadeghi, F., Ford, J. L. & Rajabi-Siahboomi, A. The influence of drug type on the release profiles from Surelease-coated pellets. *Int. J. Pharm.* **254**, 123–135 (2003).
 65. Lecomte, F., Siepmann, J., Walther, M., MacRae, R. J. & Bodmeier, R. pH-sensitive polymer blends used as coating materials to control drug release from spherical beads: Elucidation of the underlying mass transport mechanisms. *Pharm. Res.* **22**, 1129–1141 (2005).
 66. Borgquist, P., Zackrisson, G., Nilsson, B. & Axelsson, A. Simulation and parametric study of a film-coated controlled-release pharmaceutical. *J. Control. Release* **80**, 229–245 (2002).
 67. Marucci, M., Ragnarsson, G., Nyman, U. & Axelsson, A. Mechanistic model for drug release during the lag phase from pellets coated with a semi-permeable membrane. *J. Control. Release* **127**, 31–40 (2008).
 68. Borgquist, P., Nevsten, P., Nilsson, B., Wallenberg, L. R. & Axelsson, A. Simulation of the release from a multiparticulate system validated by single pellet and dose release experiments. *J. Control. Release* **97**, 453–465 (2004).
 69. Uddin, R., Saffoon, N. & Bishwajit, S. Dissolution and dissolution apparatus: a review. *Int. J. Curr. Biomed. Pharm. Res.* **1**, 201–207 (2011).
 70. Siewert, M. *et al.* FIP/AAPS guidelines to dissolution/in vitro release testing of novel/special dosage forms. *AAPS PharmSciTech* **4**, 43–52 (2003).
 71. Bai, G. *et al.* Hydrodynamic Investigation of USP Dissolution Test Apparatus II. *J. Pharm. Sci.* **96**, 2327–2349 (2007).
 72. Gray, V. *et al.* The Science of USP 1 and 2 Dissolution: Present Challenges and Future Relevance. *Pharm. Res.* **26**, 1289–1302 (2009).
-

-
73. FDA & CDER. *Dissolution Testing and Acceptance Criteria for Immediate-Release Solid Oral Dosage Form Drug Products Containing High Solubility Drug Substances Guidance for Industry*. (2018).
 74. United States Pharmacopeia. <711> DISSOLUTION. in *The United States Pharmacopeia & The National Formulary. The Official Compendia of Standards, USP 29-NF 24* **31(6)**, 1–8 (United States Pharmacopeial Convention, 2011).
 75. Klein, S. The Use of Biorelevant Dissolution Media to Forecast the In Vivo Performance of a Drug. *AAPS J.* **12**, 397–406 (2010).
 76. Antech. Introduction to Dissolution Testing. Available at: <https://antech.ie/introduction-to-dissolution-testing/>. (Accessed: 28th August 2020)
 77. Wang, Q. & Gray, V. Chapter 15 - HPLC in dissolution testing. in *Handbook of Pharmaceutical Analysis by HPLC* **6**, 379–400 (Elsevier Inc., 2005).
 78. Mudie, D. M., Amidon, G. L. & Amidon, G. E. Physiological Parameters for Oral Delivery and in Vitro Testing. *Mol. Pharm.* **7**, 1388–1405 (2010).
 79. Baxter, J. L., Kukura, J. & Muzzio, F. J. Hydrodynamics-induced variability in the USP apparatus II dissolution test. *Int. J. Pharm.* **292**, 17–28 (2005).
 80. Kaunisto, E., Nilsson, B. & Axelsson, A. Drug dissolution rate measurements evaluation of the rotating disc method. *Pharm. Dev. Technol.* **14**, 400–408 (2009).
 81. Culen, M., Rezacova, A., Jampilek, J. & Dohnal, J. Designing a Dynamic Dissolution Method: A Review of Instrumental Options and Corresponding Physiology of Stomach and Small Intestine. *J. Pharm. Sci.* **102**, 2995–3017 (2013).
 82. Brett, C. M. A., Maria, A. & Brett, O. *Electrochemistry Principle, Methods, and Applications*. (Oxford University Press, 1993).
 83. Nematollahi, D., Shayani-Jam, H., Alimoradi, M. & Niroomand, S. Electrochemical oxidation of acetaminophen in aqueous solutions: Kinetic evaluation of hydrolysis, hydroxylation and dimerization processes. *Electrochim. Acta* **54**, 7407–7415 (2009).
 84. Li, Y. & Chen, S. M. The electrochemical properties of acetaminophen on bare glassy carbon electrode. *Int. J. Electrochem. Sci.* **7**, 2175–2187 (2012).
 85. Joseph Wang. *Analytical Electrochemistry*. (Wiley-VCH, 2000).
 86. Bard, A. J. & Faulkner, L. R. *Electrochemical Methods: Fundamentals and Applications*. (2001).
 87. Zoski, C. G. *Handbook of Electrochemistry*. (Elsevier B.V., 2007).
-

-
88. Hemond, H. F. & Fechner, E. J. Basic Concepts. in *Chemical Fate and Transport in the Environment: Third Edition* 73 (Elsevier, 2014). doi:10.1016/C2011-0-09677-1
 89. Brückman, A. The activity coefficient at extremely low concentrations. *Thermochim. Acta* **245**, 231–233 (1994).
 90. Unwin, P. R. Introduction to Electroanalytical Techniques and Instrumentation. in *Encyclopedia of Electrochemistry* 3–23 (Wiley, 2003). doi:10.1002/9783527610426.bard030101
 91. García Azorero, M. D., Marcos, M. L. & González Velasco, J. Influence of changes in the total surface area and in the crystalline surface composition of Pt electrodes on their electrocatalytic properties with respect to the electro-oxidation of hydrazine. *Electrochim. Acta* **39**, 1909–1914 (1994).
 92. Bond, A. M. *et al.* *Electroanalytical Methods Guide to Experiments and Applications 2nd, revised and extended edition.* (Springer, 2009).
 93. Compton, R. G. & Banks, C. E. Voltammetry at Microelectrodes. *Underst. Voltammetry* 153–192 (2007). doi:10.1142/9789812779809_0005
 94. Unwin, P. R. & Bard, A. J. Scanning electrochemical microscopy. 14. Scanning electrochemical microscope induced desorption: a new technique for the measurement of adsorption/desorption kinetics and surface diffusion rates at the solid/liquid interface. *J. Phys. Chem.* **96**, 5035–5045 (1992).
 95. Oldham, K. B. A Gouy-Chapman-Stern model of the double layer at a (metal)/(ionic liquid) interface. *J. Electroanal. Chem.* **613**, 131–138 (2008).
 96. Burt, R., Birkett, G. & Zhao, X. S. A review of molecular modelling of electric double layer capacitors. *Phys. Chem. Chem. Phys.* **16**, 6519 (2014).
 97. Helmholtz, H. Ueber einige Gesetze der Vertheilung elektrischer Ströme in körperlichen Leitern mit Anwendung auf die thierisch-elektrischen Versuche. *Ann. der Phys. und Chemie* **165**, 211–233 (1853).
 98. Gouy, M. Sur la constitution de la charge électrique à la surface d'un électrolyte. *J. Phys. Théorique Appliquée* **9**, 457–468 (1910).
 99. Chapman, D. L. The London, Edinburgh, and Dublin Philosophical Magazine and Journal of Science Series 6 LI. A contribution to the theory of electrocapillarity. *London, Edinburgh, Dublin Philos. Mag. J. Sci.* **25**, 475–481 (1913).
 100. Stern, O. Zur Theorie der Elektrolytischen Doppelschicht. *Zeitschrift für Elektrochemie* **30**, 508–516 (1924).
 101. Elgrishi, N. *et al.* A Practical Beginner's Guide to Cyclic Voltammetry. *J. Chem. Educ.* **95**, 197–206 (2018).
-

-
102. Levich, V. G. & Landau, L. Dragging of a liquid by a moving plate. *Acta Physicochim. U.R.S.S.* **17**, 257 (1942).
 103. Levich, V. G. *Physicochemical hydrodynamics*. (Prentice Hall, Englewood Cliffs, NJ, 1962).
 104. Town, J. L., MacLaren, F. & Dewald, H. D. Rotating disk voltammetry experiment. *J. Chem. Educ.* **68**, 352 (1991).
 105. Nikolic, J., Expósito, E., Iniesta, J., González-García, J. & Montiel, V. Theoretical Concepts and Applications of a Rotating Disk Electrode. *J. Chem. Educ.* **77**, 1191 (2000).
 106. J. O'M. Bockris, B. E. C. *Modern Aspects of Electrochemistry No. 6*. (Springer US, 1971). doi:10.1007/978-1-4684-3000-4
 107. Xing, W., Yin, G. & Zhang, J. *Rotating Electrode Methods and Oxygen Reduction Electrocatalysts. Rotating Electrode Methods and Oxygen Reduction Electrocatalysts* (Elsevier B.V., 2014). doi:10.1016/C2012-0-06455-1
 108. Stevens, N. P. C. & Bond, A. M. The influence of migration on cyclic and rotating disk voltammograms. *J. Electroanal. Chem.* **538–539**, 25–33 (2002).
 109. Brandstaeter, S., Fuchs, S. L., Aydin, R. C. & Cyron, C. J. Mechanics of the stomach: A review of an emerging field of biomechanics. *GAMM-Mitteilungen* **42**, (2019).
 110. Ferrua, M. J. & Singh, R. P. Modeling the Fluid Dynamics in a Human Stomach to Gain Insight of Food Digestion. *J. Food Sci.* **75**, R151–R162 (2010).
 111. Karthikeyan, J. S. & Salvi, D. Modeling of fluid flow, carbohydrate digestion, and glucose absorption in human small intestine. *J. Food Eng.* 110339 (2020). doi:10.1016/j.jfoodeng.2020.110339
 112. Amine, A. & Mohammadi, H. Amperometry. *Encycl. Anal. Sci.* 85–98 (2019). doi:10.1016/B978-0-12-409547-2.14204-0
 113. Xu, Q. *et al.* Application of Electrochemical Methods for Pharmaceutical and Drug Analysis. *Curr. Pharm. Anal.* **5**, 144–155 (2009).
 114. Trouillon, R., Combs, Z., Patel, B. A. & O'Hare, D. Comparative study of the effect of various electrode membranes on biofouling and electrochemical measurements. *Electrochem. commun.* **11**, 1409–1413 (2009).
 115. Palakollu, V. N., Chiwunze, T. E., Liu, C. & Karpoormath, R. Electrochemical sensitive determination of acetaminophen in pharmaceutical formulations at iron oxide/graphene composite modified electrode. *Arab. J. Chem.* **13**, 4350–4357 (2020).

-
116. Alagarsamy, P. *et al.* Amperometric determination of acetaminophen (paracetamol) using graphene oxide modified glassy carbon electrode. *Int. J. Electrochem. Sci.* **13**, 7930–7938 (2018).
 117. López Zavala, M. Á., Vega, D. A., Álvarez Vega, J. M., Castillo Jerez, O. F. & Cantú Hernández, R. A. Electrochemical oxidation of acetaminophen and its transformation products in surface water: effect of pH and current density. *Heliyon* **6**, (2020).
 118. Miner, D. J., Rice, J. R., Riggin, R. M. & Kissinger, P. T. Voltammetry of Acetaminophen and Its Metabolites. *Anal. Chem.* **53**, 2258–2263 (1981).
 119. Kassa, A. & Amare, M. Electrochemical determination of paracetamol, rutin and sulfonamide in pharmaceutical formulations by using glassy carbon electrode – A Review. *Cogent Chem.* **5**, (2019).
 120. Chahiyani, H., Gharib, F. & Farajtabar, A. Thermodynamic studies on solubility and protonation constant of acetaminophen at different ionic strengths and various temperatures. *J. Mol. Liq.* **199**, 137–142 (2014).
 121. Mathivanan, J., Chang, Z., Galagedera, S. K. K. & Flechsig, G. Thermochemistry of Paracetamol - Studied at Directly Heated Micro-wire and Rotating Disk Electrodes. *Electroanalysis* **30**, 1479–1486 (2018).
 122. Filik, H., Çetintaş, G., Aslihan Avan, A., Koç, S. N. & Boz, I. Electrochemical sensing of acetaminophen on electrochemically reduced graphene oxide-nafion composite film modified electrode. *Int. J. Electrochem. Sci.* **8**, 5724–5737 (2013).
 123. Van Benschoten, J. J., Lewis, J. Y., Heineman, W. R., Roston, D. A. & Kissinger, P. T. Cyclic voltammetry experiment. *J. Chem. Educ.* **60**, 772–776 (1983).
 124. Chen, T. S. & Huang, K. L. Electrochemical detection and degradation of acetaminophen in aqueous solutions. *Int. J. Electrochem. Sci.* **7**, 6877–6892 (2012).
 125. Gupta, P., Tiwari, A. & Mishra, M. K. Taste masking of drugs: an extended approach. *Int. J. Curr. Adv. Res.* **6**, 2571–2578 (2017).
 126. Lachman, L., Lieberman, H. & Kanig, J. L. *The Theory and Practice of Industrial Pharmacy*. (Lea & Febiger, 1987).
 127. Parot, P. *et al.* Past, present and future of atomic force microscopy in life sciences and medicine. *J. Mol. Recognit.* **20**, 418–431 (2007).
 128. Binnig, G. & Rohrer, H. SCANNING TUNNELING MICROSCOPY. *Surf. Sci.* **126**, 236–244 (1983).
 129. Eaton, P. Atomic Force Microscopy Peter Eaton and Paul West. *MRS Bull.* **39**, 379–379 (2014).
-

-
130. Wang, D. & Russell, T. P. Advances in Atomic Force Microscopy for Probing Polymer Structure and Properties. *Macromolecules* **51**, 3–24 (2018).
 131. Asmatulu, R. & Khan, W. S. Characterization of electrospun nanofibers. in *Synthesis and Applications of Electrospun Nanofibers* 257–281 (Elsevier, 2019). doi:10.1016/B978-0-12-813914-1.00013-4
 132. Simpson, G. J., Sedin, D. L. & Rowlen, K. L. Surface Roughness by Contact versus Tapping Mode Atomic Force Microscopy. *Langmuir* **15**, 1429–1434 (1999).
 133. Magonov, S. N., Elings, V. & Whangbo, M. H. Phase imaging and stiffness in tapping-mode atomic force microscopy. *Surf. Sci.* **375**, L385–L391 (1997).
 134. Hansma, P., Drake, B., Marti, O., Gould, S. & Prater, C. The Scanning Ion-Conductance Microscope. *Science* (80-.). **243**, 641–643 (1989).
 135. Chen, C.-C., Zhou, Y. & Baker, L. A. Scanning Ion Conductance Microscopy. *Annu. Rev. Anal. Chem.* **5**, 207–228 (2012).
 136. Page, A., Perry, D. & Unwin, P. R. Multifunctional scanning ion conductance microscopy. *Proc. R. Soc. A Math. Phys. Eng. Sci.* **473**, (2017).
 137. Korchev, Y. E., Bashford, C. L., Milovanovic, M., Vodyanoy, I. & Lab, M. J. Scanning ion conductance microscopy of living cells. *Biophys. J.* **73**, 653–658 (1997).
 138. McKelvey, K., Kinnear, S. L., Perry, D., Momotenko, D. & Unwin, P. R. Surface Charge Mapping with a Nanopipette. *J. Am. Chem. Soc.* **136**, 13735–13744 (2014).
 139. Perry, D., Al Botros, R., Momotenko, D., Kinnear, S. L. & Unwin, P. R. Simultaneous Nanoscale Surface Charge and Topographical Mapping. *ACS Nano* **9**, 7266–7276 (2015).
 140. Kang, M., Momotenko, D., Page, A., Perry, D. & Unwin, P. R. Frontiers in Nanoscale Electrochemical Imaging: Faster, Multifunctional, and Ultrasensitive. *Langmuir* **32**, 7993–8008 (2016).
 141. Page, A. *et al.* Fast nanoscale surface charge mapping with pulsed-potential scanning ion conductance microscopy. *Anal. Chem.* **88**, 10854–10859 (2016).
 142. McKelvey, K., Perry, D., Byers, J. C., Colburn, A. W. & Unwin, P. R. Bias Modulated Scanning Ion Conductance Microscopy. *Anal. Chem.* **86**, 4636–4636 (2014).
 143. Verwey, E. J. W. Theory of the Stability of Lyophobic Colloids. *J. Phys. Colloid Chem.* **51**, 631–636 (1947).
-

144. Zhu, C., Zhou, L., Choi, M. & Baker, L. A. Mapping Surface Charge of Individual Microdomains with Scanning Ion Conductance Microscopy. *ChemElectroChem* **5**, 2986–2990 (2018).
145. Behrens, S. H. & Grier, D. G. The charge of glass and silica surfaces. *J. Chem. Phys.* **115**, 6716–6721 (2001).
146. Guo, W., Tian, Y. & Jiang, L. Asymmetric Ion Transport through Ion-Channel-Mimetic Solid-State Nanopores. *Acc. Chem. Res.* **46**, 2834–2846 (2013).

Chapter 2

Experimental

This chapter provides a brief overview of the chemicals and materials used, as well as sample preparation, instrumentation, and experimental set up. A more comprehensive description of the work undertaken is specifically detailed in each chapter.

2.1. Chemicals and Materials

All chemicals were used as received and all solutions were prepared with high purity water with a resistivity of 18.2 M Ω cm at 25 °C (Purite, Select HP or Direct-QUV3, Millipore). Chemicals were weighed using a four decimal place analytical balance (Sartorius, A2008) and pH measurements were performed using a Mettler Toledo InLab Expert Pro pH meter. The chemicals and materials used in this thesis are detailed in Tables 2.1 and 2.2. For simplicity, trademark symbols are not included in this chapter. It should be noted that the production of all samples used in this thesis was formulated by the author, with any assistance stated in the declaration.

Table 2.1. List of chemicals used in this thesis.

Chemical	Details	Supplier
Potassium Chloride	> 99.99 %	Sigma-Aldrich
Acetaminophen	99.99 % purity	Sigma-Aldrich
Hydrochloric Acid	37 %	Sigma-Aldrich
Acetic Acid	Glacial	Sigma-Aldrich
Sodium Acetate	Anhydrous, 99 %	Fisher Scientific
Citric Acid	99.5 %	Fisher Scientific
Sodium Citrate	Tribasic dihydrate	Sigma-Aldrich
Multiparticulate Formulation	Made at Pfizer	Pfizer
Kollicoat Smartseal 30 D	Aqueous dispersion	BASF
Triethyl Citrate	Plasticiser	Pfizer
Sodium Hydroxide	98 %	Sigma-Aldrich
Acetone	\geq 99 %	Sigma-Aldrich
Methanol-d ₄	\geq 99.8 atom % D	Sigma-Aldrich
Ferrocenylmethyltrimethylammonium (FcTMA ⁺) iodide	99 %	Strem Chemicals

Table 2.1. List of chemicals used in this thesis. (Continued)

Chemical	Details	Supplier
TRIS Buffer	99.9 %	Sigma-Aldrich
Sodium Chloride	> 99 %	Sigma-Aldrich
Sodium Bicarbonate	> 99.7 %	Sigma-Aldrich
Potassium Phosphate	Dibasic, 99+ %	Fisher
Magnesium Chloride Hexahydrate	99–102 %	Sigma-Aldrich
Calcium Chloride	> 96 %	Sigma-Aldrich
Sodium Sulfate	Anhydrous, \geq 99 %	Fisher
Sulfuric Acid	95-98 %	Sigma-Aldrich

Table 2.2. List of materials used in this thesis.

Material	Details	Supplier
Ag wire	99.99 % purity, 0.25 mm, and 0.125 mm diameter for bulk and nanopipette QRCE respectively	Goodfellow Cambridge Ltd
Au wire	75 μm Au diameter, purity 99.99 % PTFE insulation 12 μm thickness	Goodfellow Cambridge Ltd
Alumina Slurry	0.05 μm suspension	Buehler
Pt wire	Counter electrode	Goodfellow Cambridge Ltd
SCE reference electrode	Commercial standard	I J Cambria Scientific Ltd
Superglue		Loctite
Glass Capillaries	Borosilicate glass, 1.2 mm OD, 0.69 ID	Harvard Apparatus
Epoxy		Araldite
Luer lock syringe	1 mL	Medicina
Filter	0.2 μm	Sartorius Minisart
MicroFil	34 gauge	World Precision Instruments

2.2. Preparation of Multiparticulate Formulation Beads

The multiparticulate (MP) beads used in this thesis follows a reservoir coating system, as outlined in Chapter 1, Section 1.1.2. Briefly, the core of the formulation was made from microcrystalline cellulose (MCC) spheres (Cellets[®] 700, IPC GmbH, Germany) which have a typical diameter range of 700 – 1000 µm, were first coated by the API suspension, followed by the polymer suspension by a fluid bed coater (Glatt GmbH, Germany) using the bottom spray coating method (Wurster process) described in Chapter 1, Section 1.2.2.1.

The MCC cores were used as the starting material (Formulation Stage 1). The API used was 40 % w/w acetaminophen (APAP) with hydroxypropyl methylcellulose (HPMC) as a binder to form a liquid suspension, which then coated the MCC spheres in an 85 % w/w layer (Formulation Stage 2). A Kollicoat[®] Smartseal 30 D (KCSS) polymer suspension was prepared, comprised of 33.3% w/w methyl methacrylate and diethylaminoethyl methacrylate copolymer dispersion (BASF, Ludwigshafen, Germany), 1.5 % w/w of triethyl citrate (TEC) as plasticiser, 0.1 % w/w of butylated hydroxy toluene (BHT) as antioxidant, 8.4 % w/w of talc for anti-tacking, and 56.67 % w/w of purified water, resulting in a 20 % solid content spray suspension and 50 % polymer content in the dried film.

The coating suspension preparation process is illustrated in Figure 2.1. Briefly, BHT was dissolved in TEC and mixed for 5 min at 50 °C until a clear solution is obtained, before being allowed to cool to room temperature. Half of the required purified water was added to the copolymer dispersion whilst mixing. The BHT/TEC solution was slowly added to the KCSS solution over a period of 5 min. Any BHT/TEC remaining was washed with the remainder of purified water and then added to the KCSS solution. Talc was slowly combined into the KCSS solution over a 5 min period, and then mixed in a vortex for a minimum of 1 hour.

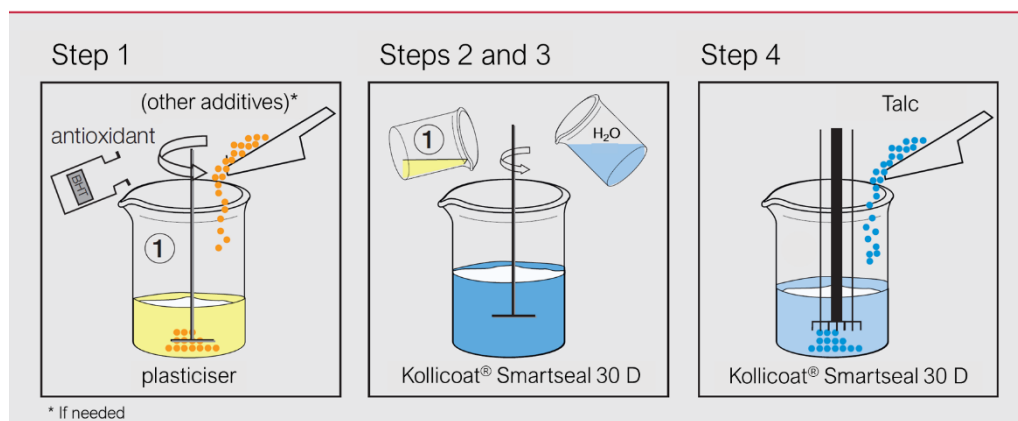


Figure 2.1. Preparation of the KCSS coating suspension. (Reproduced from BASF, 2019).¹

The API coated MCC spheres were then spray coated with 15 % (w/w) polymer layer (Formulation Stage 3). Each dispersion layer (APAP and KCSS polymer) was sprayed at atomised air pressure of 1.5 bar via the spray nozzle in the fluid bed coater. The process parameters for spray coating were adopted from the BASF guidelines.¹ Placebo beads were also made, where the MCC core was coated with the KCSS polymer only, with the absence of the API (Formulation Stage 2P). Placebo beads were produced without the API layer as some experiments (Chapter 6) required a sole focus on the polymer layer itself, thus making the presence of a middle layer redundant. The middle layer of the MP bead was not replaced with a non-active ingredient, as this may have unfavourably and inadvertently affected the experimental outcome. The final MP formulation beads were *ca.* 900 – 1000 μm in diameter. The size of which was determined by calibrated optical images of arrays of particles. The area of each individual bead was then calculated automatically and converted to a diameter assuming the beads were perfect spheres (detailed in Chapter 3, Section 3.3.1). All MP formulations produced, along with the corresponding materials were supplied by Pfizer, Sandwich, Kent, UK, except where stated.

2.3. Preparation of Isolated Polymer Films

An ideal polymer film exists when a continuous interpenetrated network of polymer chains is created, to produce a homogenous polymer film without defects.² Three key parameters for optimum film formation are the minimum film forming temperature (MFFT), the glass transition temperature (T_g) and the use of a plasticiser. For KCSS, the MFFT and T_g are approximately 57 °C and 63 °C respectively.³

The MFFT is the temperature required to form a continuous film under defined drying conditions. In the process of drying above this temperature, the particles become in direct contact with one another and form dense sphere packing, due to the evaporation and surface tension between the polymer and water. The process of film formation must occur at a temperature which exceeds the MFFT, to allow the polymer spheres to deform due to sufficient capillary force applied, coalesce and the polymer chains to fuse, resulting in the formation of a clear, continuous, homogenous film.⁴⁻⁷

The T_g is the temperature at which the mechanical behaviour of the polymer film begins to change. When the temperature increases above the T_g , it transforms the polymer from a hard, brittle 'glassy' state into a rubbery state. This change is due to the increased movement in the polymer chain and elasticity.^{4,6}

The KCSS polymer is comprised of methyl methacrylate (MMA) and diethylaminoethyl methacrylate (DEAEMA). Poly(MMA) homopolymer is a hard polymer, with a T_g of *ca.* 105 – 120 °C, and poly(DEAEMA) homopolymer is soft, with a T_g of *ca.* 20 °C.⁸ As the KCSS polymer has a single value for the T_g (63 °C),¹ it suggests that the two monomers are compatible within the copolymer, and a single phase is formed where the polymer chains amalgamate.⁹

Figure 2.2 outlines schematically the steps required for film formation from an aqueous polymer dispersion. Step 1 occurs as water evaporation takes place removing water at a constant rate, the temperature is increased above the MFFT and the polymer spheres being to deform (step 2). Coalescence occurs at step 3 at temperatures above the T_g forming a clear, continuous, homogenous film.⁴⁻⁷

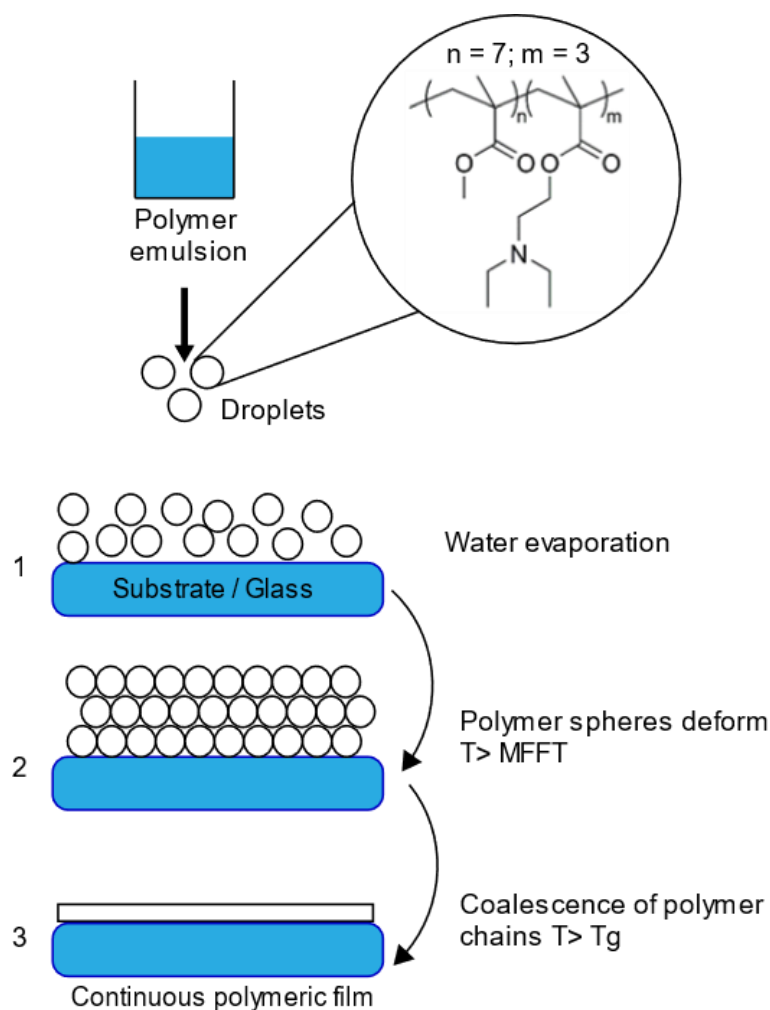
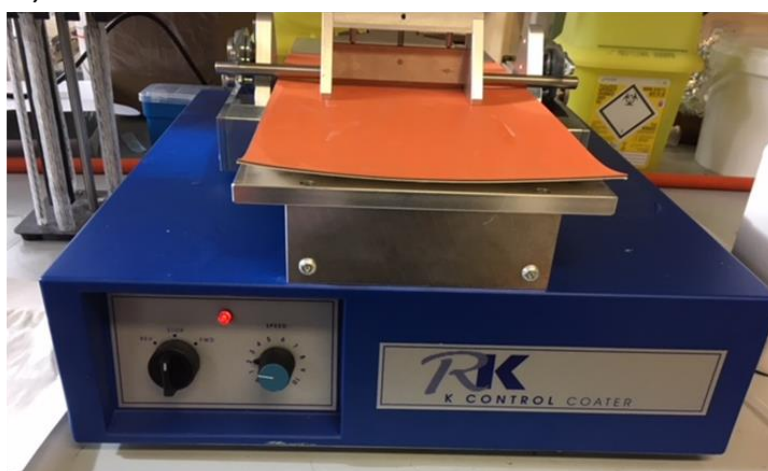


Figure 2.2. Steps of the film formation process for an aqueous polymeric dispersion.^{5,10}

Another important component in the film formation process is the use of a plasticiser, especially important for polymers brittle in nature, such as KCSS.³ Plasticisers not only reduce the intermolecular forces between the polymer chains and the internal stresses within the film, but they also allow for lowering of the T_g , thereby increasing the films flexibility of the polymer chain and decreasing the chances of cracking occurring. Furthermore, plasticisers can alter the mechanical properties of the film, as they soften the polymer spheres enabling coalescence with ease. For aqueous dispersions, the plasticiser must enter the polymer phase to be able to soften the polymer spheres.⁵

The polymer suspension for the film formation upon a glass slide was prepared using the KCSS aqueous dispersion (8.333 g, BASF), and 15 % w/w (0.375 g) of TEC as the plasticiser relative to the polymer. The resultant suspension was then pipetted on a precleaned (with acetone and allowed to dry) 15 mm × 15 mm × 0.55 mm glass slide (Agar Scientific), before being cast on using a K Control Coater (Model 101, RK PrintCoat Instruments Ltd.), fitted with a micrometre adjustable applicator at a constant speed of 2 m/min (Figure 2.3). After each film had been cast, the glass slide was annealed at either 70 °C or 90 °C for 18 hours. The resultant films were continuous, transparent, and free from visible defects.

a)



b)



Figure 2.3. K Control Coater. a) Model 101 and b) an example glass slide with the adjustable micrometer applicator.

2.4. Electrode and Nanopipette Fabrication

2.4.1. Ultramicroelectrode Fabrication

A 25 μm diameter Pt ultramicroelectrode (UME) disc was prepared by sealing Pt wire in a borosilicate glass capillary (with an inner diameter (ID) of 1.16 mm and outer diameter (OD) of 2 mm) (Figure 2.4). The UME fabrication procedure used here was originally developed by Wightman and Wipf in 1989.^{11,12}

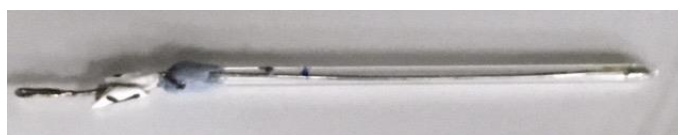


Figure 2.4. Pt \varnothing 25 μm ultramicroelectrode.

Firstly, the glass capillary was pulled into two separate halves using a heated coil micropipette puller (PB-7, Narishige Co. Ltd.). The end of the tip was heat sealed by rotating it in a Bunsen burner flame. A 0.5 cm length Pt wire was inserted into the glass capillary until it reached the sealed end. The glass was then melted around the metal wire by insertion into the heated coil of the micropipette whilst under vacuum via rubber tubing connected to the open end of the glass capillary.

A Cu wire (\varnothing 0.25 mm) was soldered to the Pt wire at the open end of the capillary, which was subsequently sealed using Araldite to ensure the connection did not break. The Pt wire at the opposite end of the glass capillary was revealed by coarse polishing using 600 grit polishing paper. Once the wire was revealed, the sides of the tip were polished into a conical shape to ensure the Pt wire was centrally located and to ensure a ratio of Pt wire to glass radius (*RG* value) of less than 10.

The tip surface was flattened and smoothed by bringing it into perpendicular contact with a 3 μm diamond lapping disc fixed onto a polishing wheel spinning at 200 rpm, followed by a 0.1 μm and finally 0.5 μm diamond lapping disc. The electrode was then polished by manually using an alumina polish suspension (0.05 μm MicroPolish™ slurry, Buehler) on a polishing pad (MicroCloth, Buehler). Followed by a further polish in water on a polishing pad. This manual polishing was carried out before and after every experiment.

2.4.2. Microwire Electrode (MWE) Fabrication

Similar to the UME fabrication, the borosilicate glass capillary was pulled in two using a heated coil micropipette puller (PB-7, Narishige Co. Ltd.). The sharp end of the tip was then cut off, exposing a small puncture at the tip. The Au 75 μm diameter wire was cut to a few mm long and the end of the wire was heated to produce small ball of gold, a long Cu wire (\varnothing 0.25 mm) was attached to the gold ball and affixed to the Au wire with silver conductive adhesive paint.

Once dry the Au/Cu wire was then pushed through the glass capillary so that the Au wire was exposed at the tip of the capillary. The remaining length of the Cu wire from the open end of the capillary was then wrapped around the top of the glass capillary. Both ends of the glass capillary are carefully sealed off with Araldite (Figure 2.5).



Figure 2.5. Au \varnothing 75 μm microwire electrode (MWE) used for directly single MP bead dissolution analysis.

A common cleaning method for such electrodes is cleaning by potential cycling, where the electrode is placed in a weak sulfuric acid solution and the electrode potential is cycled until a stable CV is attained.¹³ The MWE was cleaned by potential cycling in 0.5 M H_2SO_4 (Sigma-Aldrich) using an SCE reference electrode (IJ Cambria) and a potentiostat (CHI 730A, CHInstruments) at potentials -1 to 1.5 V for several cycles until a stable CV was achieved. However, a more effective cleaning method was to cut the exposed electrode surface. The electrode size was then re-characterised *vide infra* after any cutting of the MWE had occurred.

2.4.3. Nanopipette Fabrication for SICM

The nanopipettes used in the scanning ion conductance microscopy (SICM) experiments were fabricated from 150 nm borosilicate glass capillaries (o.d. 1.2 mm, i.d. 0.69 mm, Harvard Apparatus) that were pulled in two by a laser puller (P-2000, Sutter Instruments) using a custom-made two-line program. A schematic of the laser pulling procedure is shown in Figure 2.6.

The program parameters used are as follows:

Line 1: Heat 330, Fil 3, Vel 30, Del 220, Pul -;

Line 2: Heat 330, Fil 3, Vel 40, Del 180, Pul120.

The inner radius of the nanopipette probe was found to be 75 ± 8 nm, determined using a Zeiss Gemini 500 SEM operating in scanning transmission electron microscopy mode.

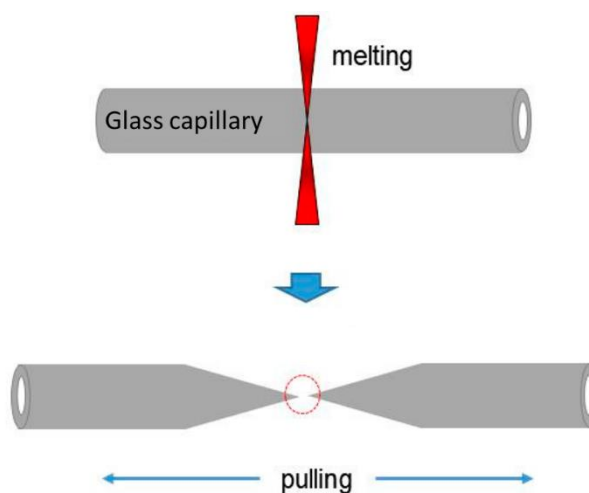


Figure 2.6. Fabrication of nanopipette a laser puller (P-2000, Sutter Instruments). (Reproduced from An and Jhe., 2019).¹⁴

2.4.3.1. Quasi-Reference Counter Electrode

The Ag/AgCl quasi-reference counter electrode (QRCE) were fabricated in house by electrolysis of a silver wire in saturated KCl solution. The working electrode that was placed into the nanopipette was made from 0.125 mm silver wire (99.99 % purity Goodfellow, Cambridge), and the bulk electrode was made from a 0.25 mm silver wire (99.99 % purity Goodfellow, Cambridge).

2.5. Instrumentation, Analysis and Characterisation

2.5.1. Characterisation of Microelectrodes

The Pt UME and Au MWE were characterised under the optical microscope and by the steady state current produced in 500 μM FcTMA⁺ to calculate the electrode surface, as described by Equation 1.17 (Chapter 1, Section 1.5.2.3.1) as is common practice in the literature.^{15,16} The resultant size of the electrodes were found to be 25 μm and 72.5 μm in diameter for Pt UME and Au MWE, respectively.

Furthermore, cyclic voltammograms were carried out in 500 μM FcTMA⁺ electrolyte with and without a Pt counter electrode to validate the use of a two-electrode set up in Chapter 3. The CVs shown in Figure 2.7, demonstrate the experimental set up with and without the use of a Pt counter electrode in 500 μM FcTMA⁺ electrolyte solution. This was carried out to confirm that the use of a counter electrode was not necessary.

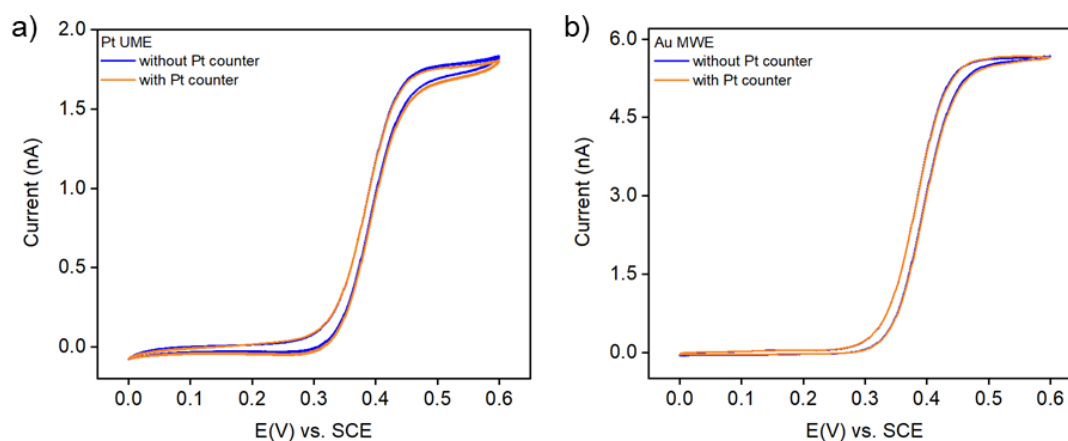


Figure 2.7. CV of a) Pt UME and b) Au MWE to validate the two-electrode set up in 500 μM FcTMA⁺ solution at scan rate 0.01 V/s.

As there is no substantial difference between the CVs with and without the Pt counter electrode for both the UME and MWE, the use of a two-electrode set up was therefore validated.

2.5.2. Scanning Ion Conductance Microscopy Set up

The fabricated nanopipettes were filled with electrolyte (50 mM KCl) using a 1 mL luer lock syringe (Medicina) passing through a 0.2 μm filter (Sartorius Minisart) and a MicroFil (World Precision Instruments, 34 gauge). Depending on the experiment the pH was adjusted using 0.1 M HCl and 0.1 M NaOH. The nanopipette electrolyte solution was filtered from the bulk solution. Two fabricated Ag/AgCl QRCE were used, with the smaller wire inserted into the nanopipette.

The nanopipette probe was mounted onto a micropositioner (Newport, M-461-XYZ-M) for rough positioning of the probe over the sample. A two-axis xy piezoelectric positioning system with a range of 300 μm (NanoBioS300, Mad City Laboratories, Inc.), while the vertical movement in the z direction to the substrate was controlled using a piezoelectric positioning stage of range 38 μm (P-753-3CD, Physik Intrumente). The piezoelectric positioners, along with the sample were mounted inside a thermal insulated faraday cage, assembled on an air pressurised optical table (Newport, RS 2000) to avoid mechanical vibrations.

The electrochemical measurements were collected by bespoke instrumentation built in-house. Control of probe position, voltage output, and data collection was *via* custom-made programs in LabVIEW (2017, National Instruments) through a field programmable graphics array (FPGA) card (7852R, National Instruments).

2.5.3. Atomic Force Microscopy

Atomic force microscopy (AFM) is a scanning probe technique used to map high resolution images on the nanoscale. AFM was used to image the polymer film cast onto a glass slide as well as the surface of MP beads. The morphology of these samples was extracted from AFM images produced using a Bruker Innova[®] AFM in tapping mode in air at room temperature. A silicon single cantilever probe (RFESP-75, Bruker) was used, with dimensions 225 μm length, 35 μm width and tip radius of 8 nm, resonance frequency of 75 kHz and spring constant of 3 N/m. The scan rate was 3 Hz with a resolution of 512 lines and 512 samples per line. All AFM images were processed using the Scanning Probe Image Processor program (SPIP 6.0.14, Image Metrology).

2.5.4. Nuclear Magnetic Resonance (NMR)

Nuclear magnetic resonance (NMR) spectroscopy has many advantages in pharmaceutical and polymer applications due to its ability to provide quantitative information on a molecular level. It is a powerful tool to determine a polymers structure and detect the presence of functional groups.¹⁷ The foundation of NMR is built upon the magnetic properties of atomic nuclei. A spectrum can be generated for a molecule that contains atoms whose nuclei have non-zero magnetic moments, such as ^1H , ^{13}C , ^{14}N , ^{15}N , and ^{19}F .¹⁸

A sample is placed inside a radio frequency (rf) coil in a magnetic field of known strength. Rf pulses are used to characterise the resonant frequency of atomic nuclei depending on its chemical or environmental surroundings. The interaction of the nuclear magnetic moment with the external magnetic field, B_0 , produces a nuclear energy level diagram.¹⁸ When the nucleus is perturbed from its original equilibrium state, the nucleus exhibits a characteristic decay signal back to the equilibrium. The signal produces a spectrum that can map the chemical structure of the molecule (Figure 2.8).¹⁹

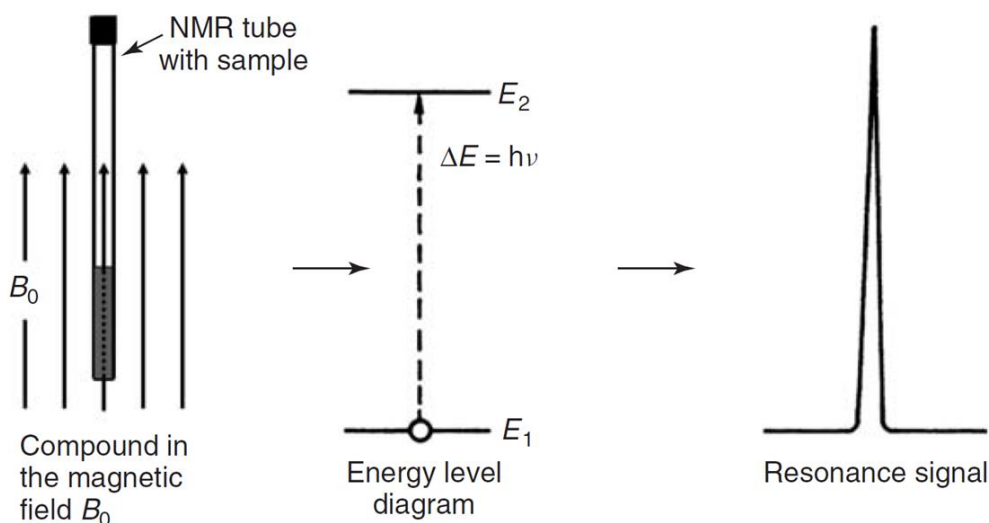


Figure 2.8. Formation of NMR signal

The atom's electrons are circulated along the direction of the applied magnetic field, causing a small opposing magnetic field at the nucleus. As the electron density around the nuclei varies depending on the nuclei and the molecule bonds, resulting in different opposing magnetic fields. This phenomenon is referred to as a chemical shift and this information is utilised in the characterisation of the molecular structure.^{18,19}

NMR spectroscopy was used to analyse the KCSS polymer emulsion and the acid treated KCSS emulsion, where 50 mL HCl (0.01 M) was added to the KCSS emulsion and under continuous stirring for 28 days. Aliquots of the acid treated KCSS were taken after 24 hours, 7, 14, 21 and 28 days. All emulsion samples were subsequently lyophilised (water removed and freeze dried under vacuum to produce a solid phase sample). Deuterated methanol was added to each lyophilised sample to give a concentration of 40 mg/mL before NMR spectroscopy was performed by ¹H NMR with the Bruker Avance III HD 500 MHz.

2.5.5. Dynamic Mechanical Analysis (DMA)

Dynamic mechanical analysis (DMA) refers to the application of an oscillating force to a sample and analysing the materials response to that force.²⁰ It is a technique commonly used to characterise a material's property as a function of temperature, time, frequency, stress, and atmosphere.²¹

One common use of DMA is the measurement of various temperature transitions of a polymer. DMA has a greater sensitivity to measure the T_g compared to that of differential scanning calorimeter (DSC) or the differential thermal analyser (DTA). DMA applies an oscillatory force at a set frequency to the samples and reports the changes in damping (energy dissipation in a material) and elasticity (ability to recover from deformation).²⁰

DMA works by supplying an oscillatory force, which applies a sinusoidal stress to the sample, this generates a sinusoidal strain. By the measurement of both the amplitude of the deformation at the peak of the sine wave and the lag between the stress and strain sine waves, quantities like the modulus, viscosity, and damping can be calculated (Figure 2.9). The applied force is referred to as stress, σ , and when a material is subjected to a stress the material is exhibit a deformation or strain, γ .²⁰

DMA measure the stiffness and damping which are reported as the storage modulus and $\tan\delta$, respectively. The modulus is dependent on the temperature and the applied stress, it indicates how the material will work in certain real world applications.^{20,21}

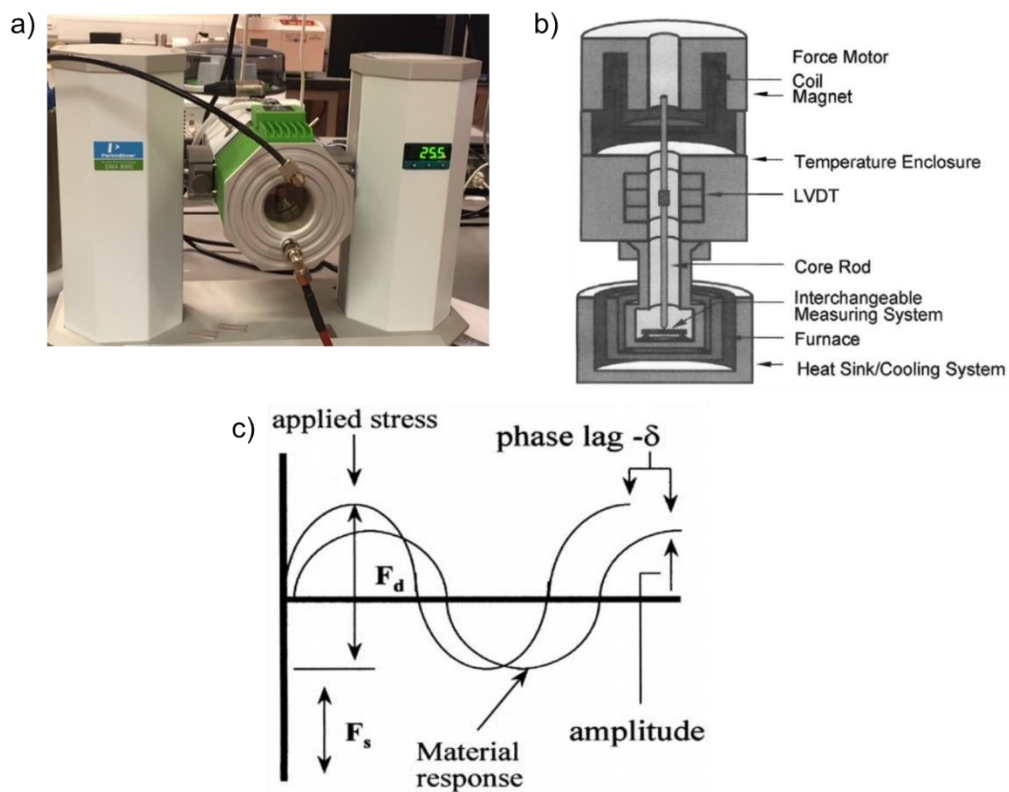


Figure 2.9. Operation of Dynamic Mechanical Analyser. a) Perkin Elmer DMA 8000, b) Analytic train, where the force motor is used to generate the sinusoidal wave, c) The relationship of the applied sinusoidal stress to strain, with the resultant phase lag and deformation, where F_d is the dynamic (or oscillatory) force and F_s is the static (or clamping) force. (a and b Reproduced from Menard, 1999).^{20,21}

DMA was performed using the Perkin Elmer DMA 8000 on a lyophilised KCSS powder heated from of $-30.00\text{ }^{\circ}\text{C}$ to $280.00\text{ }^{\circ}\text{C}$ at $2.00\text{ }^{\circ}\text{C}/\text{min}$.

2.5.6. Field Emission - Scanning Electron Microscopy

Field emission - scanning electron microscopy (FE-SEM) is used to image the topography of a surface with a resolution of 10 nm; advanced instruments can achieve *ca.* 2.5 nm resolution.²²

A high energy electron beam is generated under vacuum via an electron gun with an accelerating voltage (0.1 – 30 kV) towards the surface of the sample. The electron beam is focused onto the sample and scans the surface. As the electrons interact with the sample, emission of photons and electrons occur, such as secondary electrons, backscattered electrons. Secondary electrons reveal the surface structure and thereby provide topographical information.^{23,24}

For the SEM images of the MP beads, the beads were first sputter coated with gold in a *ca.* 80 nm thick layer (Emitech/Quorum sputter Quorum technologies), which provided a conductive layer to improve the quality of the images acquired. The MP bead samples were then recorded using the secondary electron detector on a Zeiss Supra 55-VP operating at 15 kV.

In scanning transmission electron microscopy (STEM) mode, the electron beam is focused to a fine spot, and raster scanned over the samples surface and signals are collected point by point to form an image.²⁵

The geometry of the nanopipettes were recorded by using the in-lens and STEM detector on the Zeiss Gemini 500 SEM (operating in scanning transmission electron microscopy mode at 21 kV).

2.6. References

1. BASF. Kollicoat Smartseal 30 D Technical Information. *BASF* 1–13 (2019).
2. Siepman, J. & Siepman, F. Stability of aqueous polymeric controlled release film coatings. *Int. J. Pharm.* **457**, 437–445 (2013).
3. BASF SE Care Chemicals Division Pharma Ingredients & Services. Kollicoat Smartseal 30 D Technical Information. *BASF Tech. Inf.* 1–12 (2011).
4. Nollenberger, K. & Albers, J. Poly(meth)acrylate-based coatings. *Int. J. Pharm.* **457**, 461–469 (2013).
5. Felton, L. A. Mechanisms of polymeric film formation. *Int. J. Pharm.* **457**, 423–427 (2013).
6. Felton, Linda A., O'Donnell, P., McGinity, J. W. Mechanical Properties of Polymeric Films Prepared from Aqueous Dispersions. in *Aqueous Polymeric Coatings for Pharmaceutical Dosage Forms* (ed. Felton, L. A.) 105–128 (2008).
7. Ludwig, I., Schabel, W., Ferlin, P., Castaing, J.-C. & Kind, M. Drying, film formation and open time of aqueous polymer dispersions. *Eur. Phys. J. Spec. Top.* **166**, 39–43 (2009).
8. Thermal Transitions of Homopolymers: Glass Transition & Melting Point. *Sigma Aldrich* Available at: <https://www.sigmaaldrich.com/technical-documents/articles/materials-science/polymer-science/thermal-transitions-of-homopolymers.html>.
9. Yang, C.-F., Wang, H.-C. & Su, C.-C. Enhancing the Compatibility of Poly (1,4-butylene adipate) and Phenoxy Resin in Blends. *Materials (Basel)*. **10**, 692 (2017).
10. Kucera, S. A., Felton, L. A. & McGinity, J. W. Physical aging in pharmaceutical polymers and the effect on solid oral dosage form stability. *Int. J. Pharm.* **457**, 428–436 (2013).
11. Wightman, M. R. & Wipf, D. O. Voltammetry at Ultramicroelectrodes. in *Electroanalytical Chemistry Volume 15* (ed. Bard, A. J.) 267–353 (Marcel Dekker, 1989).
12. Hermans, A. & Wightman, R. M. Conical tungsten tips as substrates for the preparation of ultramicroelectrodes. *Langmuir* **22**, 10348–10353 (2006).
13. Fischer, L. M. *et al.* Gold cleaning methods for electrochemical detection applications. *Microelectron. Eng.* **86**, 1282–1285 (2009).
14. An, S. & Jhe, W. Nanopipette/Nanorod-Combined Quartz Tuning Fork–Atomic Force Microscope. *Sensors* **19**, 1794 (2019).

15. Conyers, J. L. & White, H. S. Electrochemical characterization of electrodes with submicrometer dimensions. *Anal. Chem.* **72**, 4441–4446 (2000).
16. McKelvey, K. *et al.* Fabrication, characterization, and functionalization of dual carbon electrodes as probes for scanning electrochemical microscopy (SECM). *Anal. Chem.* **85**, 7519–7526 (2013).
17. Madhav, H., Singh, N. & Jaiswar, G. Thermoset, bioactive, metal–polymer composites for medical applications. in *Materials for Biomedical Engineering* 105–143 (Elsevier, 2019). doi:10.1016/B978-0-12-816874-5.00004-9
18. Gunther, H. *NMR Spectroscopy: Basic Principles, Concepts, and Applications in Chemistry*. (Wiley-VCH Verlag GmbH & Co. KGaA, 2013).
19. Stark, N. M., Yelle, D. J. & Agarwal, U. P. Techniques for Characterizing Lignin. in *Lignin in Polymer Composites* 49–66 (Elsevier, 2016). doi:10.1016/B978-0-323-35565-0.00004-7
20. Menard, K. P. *Dynamic Mechanical Analysis: A Practical Introduction*. (CRC Press, 1999).
21. PerkinElmer Inc. Dynamic Mechanical Analysis (DMA) - A Beginner's Guide. *Introd. to DMA* 1–23 (2008).
22. Raval, N. *et al.* Importance of Physicochemical Characterization of Nanoparticles in Pharmaceutical Product Development. in *Basic Fundamentals of Drug Delivery* 369–400 (Elsevier, 2019). doi:10.1016/B978-0-12-817909-3.00010-8
23. Goldstein, J. I. *et al.* *Scanning Electron Microscopy and X-ray Microanalysis*. *Scanning Electron Microscopy and X-ray Microanalysis* (Springer US, 2003). doi:10.1007/978-1-4615-0215-9
24. Watt, I. M. *The Principles and Practice of Electron Microscopy*. *The Principles and Practice of Electron Microscopy* (Cambridge University Press, 1997). doi:10.1017/cbo9781139170529
25. Nellist, P. D. Scanning Transmission Electron Microscopy. in *Springer Handbooks* 49–99 (Springer, 2019). doi:10.1007/978-3-030-00069-1_2

Chapter 3

Multiparticulate Formulations: Single Bead Dissolution Analysis

Multiparticulates are useful as oral drug delivery systems, particularly for paediatric and geriatric patients who suffer from difficulty swallowing. Therefore, it is common for multiparticulates to be coated in a taste masking polymer. It is known that heterogeneity exists in individual multiparticulate (MP) beads. However, current dissolution methods do not detect for these differences as testing is usually done on a large number of particles at once. In this study, microelectrodes of two different geometries are used to analyse the time evolution of the diffusion field of an active pharmaceutical ingredient (API) as it is released from individual MP beads. The differences are observed and discussed in terms of microscopic analysis of particle morphology. This analysis allowed for the factors affecting the formulation and uniformity of multiparticulates to be identified. A number of variables were investigated, including the presence of a pH responsive polymer coating, the MP bead size, pH, and the distance of the electrode from the MP bead. From this small scale study, it was shown that the agitation of the MP bead in the dissolution media resulted in a more uniform API release. Furthermore, mechanistic information was obtained with respect to the start of the dissolution process, whereby sequential spikes of API release were observed. This technique allows for the detection of individual MP bead behaviour in dissolution media, which can be utilised to better understand how MP beads behave collectively as a dose.

3.1. Introduction

Oral drug delivery is the most common and popular route for drug administration for several reasons, primarily patient compliance.^{1,2} Challenges remain regarding palatability and dysphagia (difficulty in swallowing) however, particularly among paediatric and geriatric patients.^{1,3} Altering oral drug medication palatability has generally been achieved through the sensory modification of taste via the addition of flavourings and sweeteners to the formulation, however, more effective methods involve a sugar or polymer coating.^{4,5} Multiparticulate (MP) formulations often provides a solution to both dysphagia and taste masking issues, whilst also incurring the benefits of improved stability, reduced bulkiness and weight, and more accurate dosing.⁶ MP formulations are predominately oral dosage forms that consist of multiple small discrete drug delivery units, often spherical particles 0.15 – 3.0 mm in diameter.⁶⁻⁸ MP formulations can be used to modify the release of the drug or to mask the taste by coating the spherical particles in a film protection layer.⁶⁻⁹

When an oral drug is ingested it experiences a range of different pHs on its journey from the oral cavity through the gastrointestinal (GI) tract,^{10,11} enabling release to be targeted via the use of a coating with a pH-dependent solubility.¹² One such coating is based on a methyl methacrylate (MMA), 2-(diethylamino)ethyl methacrylate copolymer (DEAEMA), (marketed as Kollicoat[®] Smartseal 30D, KCSS). It contains a tertiary amine functional group which is unprotonated at a neutral pH but becomes protonated in acidic media, resulting in swelling and dissolution of polymer and an immediate release of the drug.^{4,13-21}

MP formulations can be administered in a variety of ways, such as through compression into tablets, dosages contained in capsules, sachets, or in a dispenser which can be further administered by sprinkling it onto food.^{3,6,22-24} Furthermore, MP formulations facilitate dosage specificity due to the small drug containing particles, thus allowing flexibility for dose-weight proportionality, as well as modulation of drug release by the application of coatings resulting in distinct drug release profiles.⁶ Therefore, this highlights the importance of understanding the MP beads at a singular level.

Polymeric coatings in MP formulations can occur in either a matrix (monolithic) system or reservoir system. In matrix systems the drug is dispersed within a water-insoluble polymer matrix, whereas in a reservoir system the polymer film surrounds the drug.^{25,26} Both of these can be described as diffusion-controlled release systems.²⁵ In this study, a reservoir coated system is used, where a microcrystalline cellulose (MCC) core is coated with a layer of an active pharmaceutical ingredient (API), which is then encapsulated with a layer of KCSS polymer.

In vitro dissolution testing in industry is required for oral dosage forms, particularly in the early stages of development. However, much of the dissolution testing occurs in bulk and over a long time periods, with analysis taken at intervals.²⁷ This method can miss out on the dissolution behaviour at earlier times. Acetaminophen (APAP, also known as paracetamol or N-acetyl-p-aminophenol) was selected as the API in the MP formulation as a model case. APAP is an electroactive substance, and is also one of the most commonly prescribed and widely available over the counter non-steroidal anti-inflammatory drugs, used as an antipyretic and painkiller.²⁸⁻³⁰ Its redox activity arises from the quasi-reversible two-electron oxidation to from N-acetyl-p-benzoquinone-imine (NAPQI).²⁹⁻³¹ Using an API with redox activity, enables the use of electrochemical detection methods. Therefore, individual MP formulation beads can be analysed *in situ* to understand the variation in dissolution amongst individual beads and thus better understand dosage levels required.

Herein, the particle size distribution of the MP beads at each stage of the coating/layering stages during the formulation process were investigated. The resultant variations observed were then studied to determine whether they had any effect on the amount of API released. This was achieved by the employment of microscale electrochemical techniques to detect API dissolution *in situ*, enabling the release rate to be quantified and comparisons made based on the presence of the KCSS polymer. Dissolution measurements were carried out under various experimental conditions and parameters, testing release of APAP as a consequence of the polymers response to pH media that mimics gastric fluid (HCl).

3.2. Experimental

3.2.1. Multiparticulate Formulation Samples

The multiparticulate bead samples were prepared according to Chapter 2, Section 2.2 and detailed in Table 3.1, by spray coating method using a fluid bed coater via the wurster process. The microcrystalline cellulose (MCC) cores (Cellets[®] 700, IPC GmbH, Germany) were the starting material for the MP beads and thus Stage 1 of the formulation process. A layer of APAP coats the MCC cores producing the MCC+APAP beads at Stage 2. Upon the APAP layer, the polymer KCSS encapsulates the bead, forming a three-layer MP bead, MCC+APAP+KCSS at Stage 3. Placebo beads (MCC+KCSS) were also used in this study, where the MCC core was coated with the KCSS polymer directly, in a two-layer MP bead absent of the ‘middle’ API layer, Stage 2P.

Table 3.1. Stages and details for the formulation of MP beads.

Formulation Stage (FS)	Materials	Details
1	MCC core	Starting material/ inert core
2	MCC core + APAP layer	API layer only
2P	MCC core + KCSS layer	Placebo beads
3	MCC core + APAP + KCSS layers	Final formulation polymer coating encapsulating the API layer

3.2.2. Sample Imaging using Optical and Scanning Electron Microscopy

The size distribution of the MP beads was characterised using optical microscopy. Image analysis was performed using ImageJ. Calibrated optical images of arrays of particles were automatically segmented using the threshold and watershed algorithms. The area of each individual bead was then calculated automatically and converted to a diameter assuming the beads were perfect spheres. Furthermore, the MP beads sizes were examined before and after dissolution. The MP beads at different stages of formulation were adhered to a scanning electron microscope (SEM) stub using carbon tape and a thin layer of super glue, the MP beads were then sputtered with gold before being examined under the Field Emission SEM at an accelerating voltage of 15.00 kV, unless stated otherwise. For examination of topographical effects under varying pH media, individual placebo KCSS coated MP beads were adhered to SEM stubs, placed in 25 mL of either 0.1 M or 0.01 M HCl solution with a magnetic stirrer at a rotation speed of 700 rpm and left for an hour at room temperature, as shown in Figure 3.1. These MP beads were then subsequently sputtered with gold and examined under the SEM, as described in Chapter 2, Section 2.5.6.

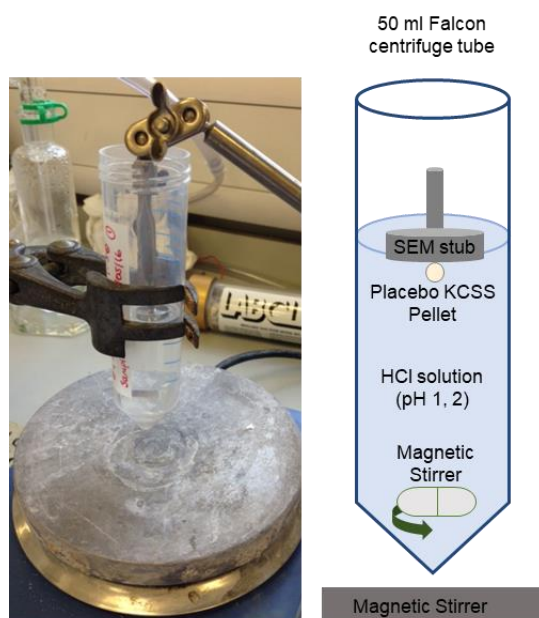


Figure 3.1. Schematic of MP KCSS polymer coated placebo bead in a tube filled with acidic dissolution media in preparation for SEM imaging. MP placebo bead adhered to SEM stub and placed downwards into the acidic solution of HCl (0.1 or 0.01 M), with a magnetic stirrer placed at the bottom of the tube, where the apparatus is held over a magnetic stirrer. (not to scale).

3.2.3. Dissolution Media Solutions

The HCl solutions were made by diluting HCl (37 %, Sigma-Aldrich, UK) to make 0.1 M and 0.01 M HCl, corresponding to pH of 1.0 and 2.0, respectively. All solutions were prepared in deionised water (18.2 M Ω cm at 25 °C, Direct-QUV3, Millipore). The pH of solutions was measured using pH probe (Mettler Toledo, InLab[®] Expert Pro) connected to pH meter (Mettler Toledo, SevenEasy[™]). Due to the concentration of HCl used and the small scale set up, the addition of supporting electrolyte was not required.

3.2.4. Electrochemical Materials and Instrumentation

Electrochemical measurements were performed using a two electrode set up mounted inside a Faraday cage (to reduce electrical noise) on top of an optical table (Newport, RS 2000), connected to potentiostat (CHI 730A, CHInstruments), with a saturated calomel electrode (SCE, IJ Cambria) as the reference electrode and either a \varnothing 25 μ m Pt ultra-microelectrode (UME) or a \varnothing 72.5 μ m Au microwire electrode (MWE) in diameter as the working electrode depending on the type of experiment. To confirm that a two-electrode set up was suitable *i-v* (current-voltage) curves with and without a (Pt) counter electrode were measured and found to be the same.

To measure the total amount of APAP in each MP bead, individual MP beads at Stage 2 of the formulation process (no KCSS polymer coating) were placed in separate vials containing 1 mL of 0.1 M HCl dissolution media and left for a 24-hour period. In this way dissolution occurred in a stagnant solution; thus, motion was introduced to the same parameters to determine the effect this had on the release of APAP. Vials were agitated for *ca.* 2 minutes using a vortex mixer (Classic Vortex mixer, Fisher Scientific) at 200 rpm as soon as the DM was added and just before the electrochemical measurements were taken, at the start and end of the 24-hour period.

Cyclic voltammograms (CVs) were then measured on the resultant solution using a Pt UME. Before a CV measurement, the Pt UME, was gently polished to a mirror finish with an aqueous alumina slurry (0.05 μm , MicroPolish™, Buehler) against a soft microfiber polishing pad (MicroCloth, Buehler), which was then subsequently polished on a clean wetted microfiber polishing pad, to produce clean reproducible electrode surfaces.

For direct API detection from a single bead, an Au MWE was used as the working electrode. The MWE surface protrudes out of the tapered glass capillary, and thus allows for a more hemispherical diffusion and a shorter distance from the tip of the electrodes to the beads surface, compared to that of an inlaid disc UME, a crucial configuration given the curvature of the beads surface. Furthermore, the larger size of the MWE compared to that of the UME increases the sensitivity to small concentrations.

The MP bead was adhered onto a square-shaped scored glass slide using a thin layer of superglue (Loctite®) and then analysed under the optical microscope before and after dissolution. The glass slide holding the bead was then adhered to the base of a 10 mL glass petri dish using adhesive double-sided tape. These experiments were performed within a Faraday cage, where the Au MWE was positioned above the MP bead using a z -axis micropositioner (Physik Instrumente) for precise movement and translation of the MWE in the vertical direction under control. This was executed under the observation through a 3-megapixel digital camera (PixeLink PL-B776U) with a 4X magnification lens, as shown in Figure 3.13. The distance of MP bead and the MWE tip was captured to calculate the distance between the two. Once the electrode was positioned, the desired potential (0.8 V) was applied. The dissolution media (DM) was added last due to ensure the initial response was recorded.

3.3. Results and Discussion

3.3.1. Size Distribution of Multiparticulate Beads

This study focuses on the API dissolution analysis from a polymer coated single MP bead. To determine the variation of the MP bead size, microscopic analysis was performed on beads at the different stages of formulation. Here, the layering stage of the formulation process that contributed to the most variation was established.

The diameter, circumference (circum.), perimeter, and circularity were calculated using ImageJ analysis from the area outlined of each individual bead at each stage of formulation. Representative images used in the analysis are shown in Figure 3.2, starting with the microcrystalline cellulose (MCC) cores (a), then the addition of the APAP layer (b), a placebo MP bead with layer of the KCSS polymer only coating the MCC core (c) and the final formulation comprising of all three layers (d).

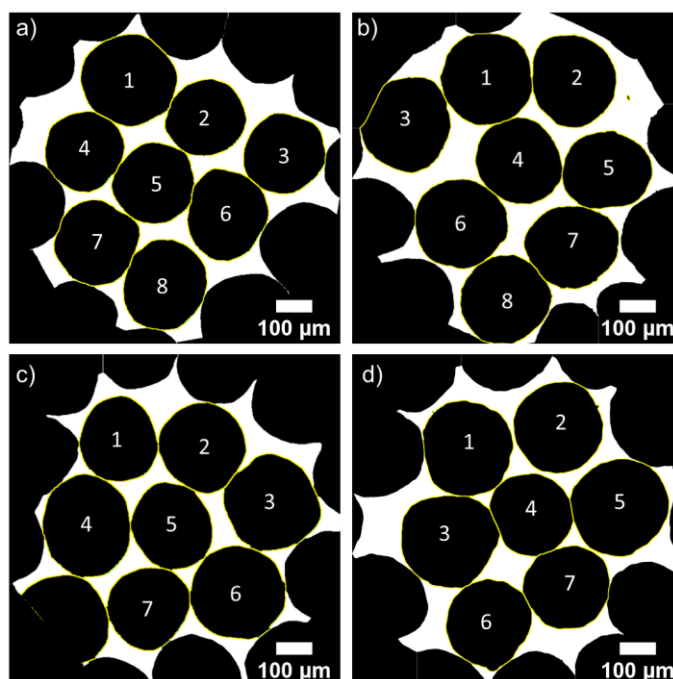


Figure 3.2. Representative optical image with area boundary used to calculate the diameter at different formulation stages of the multiparticulate spherical beads, a) MCC core (Cellets® 700), b) MCC core with the APAP layer, c) Placebo bead - MCC core with KCSS layer, and d) MCC core, with APAP layer and KCSS outer layer.

The average bead size values for the particle size distribution for the different formulation stages (FS) are shown in Table 3.2 and Figure 3.3. From this data, the calculated thickness of the APAP layer and the KCSS polymer layer are approximately 32.5 μm and 12.5 μm , respectively.

Table 3.2. Mean particle-size distribution of bead size at each formulation stage for parameters, diameter, circumference, perimeter, and circularity.

Bead Type (Formulation Stage)	Mean Diameter (μm)	Mean Circum.* (μm)	Mean Perimeter** (μm)	Mean Circularity [†]	N
MCC Core (FS 1)	876 \pm 50	2751 \pm 156	2966 \pm 188	0.87 \pm 0.03	34
MCC+APAP (FS 2)	941 \pm 36	2955 \pm 113	3206 \pm 125	0.86 \pm 0.01	30
MCC+KCSS (FS 2P)	884 \pm 61	2776 \pm 191	3014 \pm 204	0.87 \pm 0.01	29
MCC+APAP +KCSS (FS 3)	966 \pm 47	3035 \pm 149	3277 \pm 160	0.87 \pm 0.01	28

* Circum. is the calculated circumference from the diameter

** Perimeter is the outline of the bead

[†] Circularity is defined by $4\pi(\text{area}/\text{perimeter}^2)$

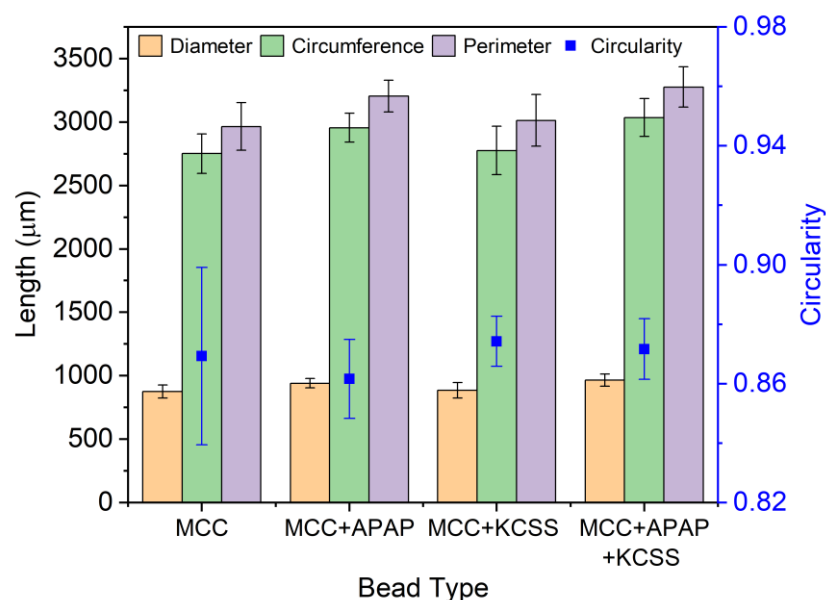


Figure 3.3. Average particle size distribution of bead size at different stages of formulation for parameters, diameter, circumference, perimeter, and circularity. The left axis shows diameter, circumference and perimeter are shown graphically as bar charts with their corresponding error bars. Circularity is given by the right axis with the average shown along with its corresponding error bars.

From Table 3.2 and Figure 3.3 the difference between the circumference and perimeter values shows a difference between the roundness of the bead size. The perimeter values and its corresponding standard deviation are larger than the calculated circumference values (from the diameter), suggesting that the calculated circumference has undergone a smoothing process based on a perfect circular shape. Furthermore, the circularity has been calculated where a value of 1.0 indicates a perfect circle, and a value closer to 0.0 represents an increasing elongated shape.

As the circumference has been calculated from the diameter, it assumes a perfect circle, and therefore can be considered as a smoothing process. However, the perimeter data is given by the outline of the bead itself. Therefore, the comparison between the circumference and perimeter can be compared, suggesting a deviation from a perfect sphere. A box plot for the calculated circumference, perimeter, and circularity for the bead sizes at the different formulation stages is shown in Figure 3.4.

From Figure 3.4a, both the circumference and perimeter follow the same trend in bead size and therefore both can be used to determine the difference in size between the different stages of formulation. Furthermore, for both perimeter and circumference, the MCC+KCSS (FS 2P) is shown to have the largest interquartile range (IQR), whilst MCC+APAP (FS 2) has the smallest. However, for both these parameters the mean of FS 2P is similar of the MCC starting material itself. This suggests that the KCSS polymer may require the APAP layer to evenly coat the multiparticulate. The calculated circumference has outliers whilst the perimeter parameter does not. Given that the circumference was calculated through the diameter and therefore assumes a perfect circle this was not unanticipated. From the circularity data shown in Figure 3.4b, the demonstrates similar trends in mean, median and IQR across all formulation stages. However, the MCC core showed the most outliers, and this therefore highlights the importance of the sieving stage before starting the formulation process. Additionally, the MCC+ APAP (FS 2) data shows a larger deviation in the MP circular shape at this stage. This correlates to the roughness observed in the corresponding SEM images *vide infra*.

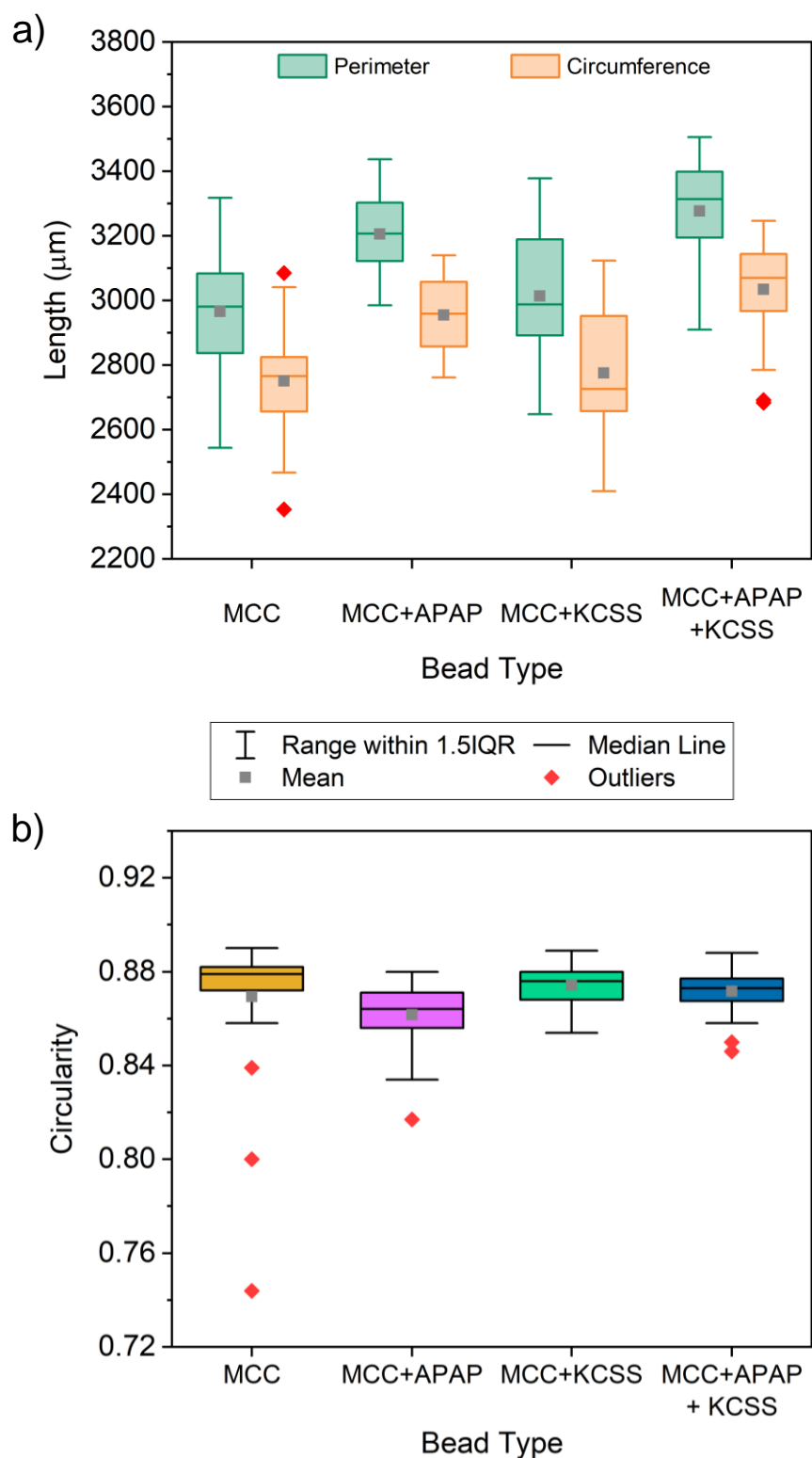


Figure 3.4. Boxplots for statistical analysis on bead size at different formulation stages for parameters of a) calculated circumference (orange), perimeter (green), and b) circularity (multi-coloured) with corresponding mean (grey square), median (central line), the IQR is shown where the whiskers extend to 1.5x of the IQR and the outliers (red diamond) are values that lie outside this range.

A one-way analysis of variance (ANOVA) test was used to determine whether the different bead sizes at each formulation stage had any statistically significant differences. A significant difference in bead size was observed at the different stages of the formulations for the three parameters circumference, perimeter, and circularity ($p < 0.05$).

The differences between the four formulation stages were established by the Tukey post-hoc test shown in Table 3.3 and Figure 3.5. The parameters for both circumference and perimeter show the same trend in significant difference for all factors. However, as seen previously the circularity parameter appears to have a smaller deviation in bead size across the different formulation stages, suggesting that the addition of each layer does not significantly change the circular shape. The Tukey test supports this data in all cases, except for factor MCC+KCSS compared with MCC+APAP where a difference in circularity has been deemed to be significant.

Table 3.3. Tukey means of comparison test at the 95 % confidence level stating the significant difference between each of the 4 formulation stages for the parameters of circumference, perimeter, and circularity. A difference where $p < 0.05$ is considered to be significant.

Formulation Stages	Significant Difference		
	Circum.	Perimeter	Circularity
MCC+APAP / MCC	$p < 0.05$	$p < 0.05$	$p = 0.3$
MCC+KCSS / MCC	$p = 0.9$	$p = 0.7$	$p = 0.7$
MCC+KCSS / MCC+APAP	$p < 0.05$	$p < 0.05$	$p < 0.05$
MCC+APAP+KCSS / MCC	$p < 0.05$	$p < 0.05$	$p = 1.0$
MCC+APAP+KCSS / MCC+APAP	$p = 0.2$	$p = 0.4$	$p = 0.1$
MCC+APAP+KCSS / MCC+KCSS	$p < 0.05$	$p < 0.05$	$p = 0.9$

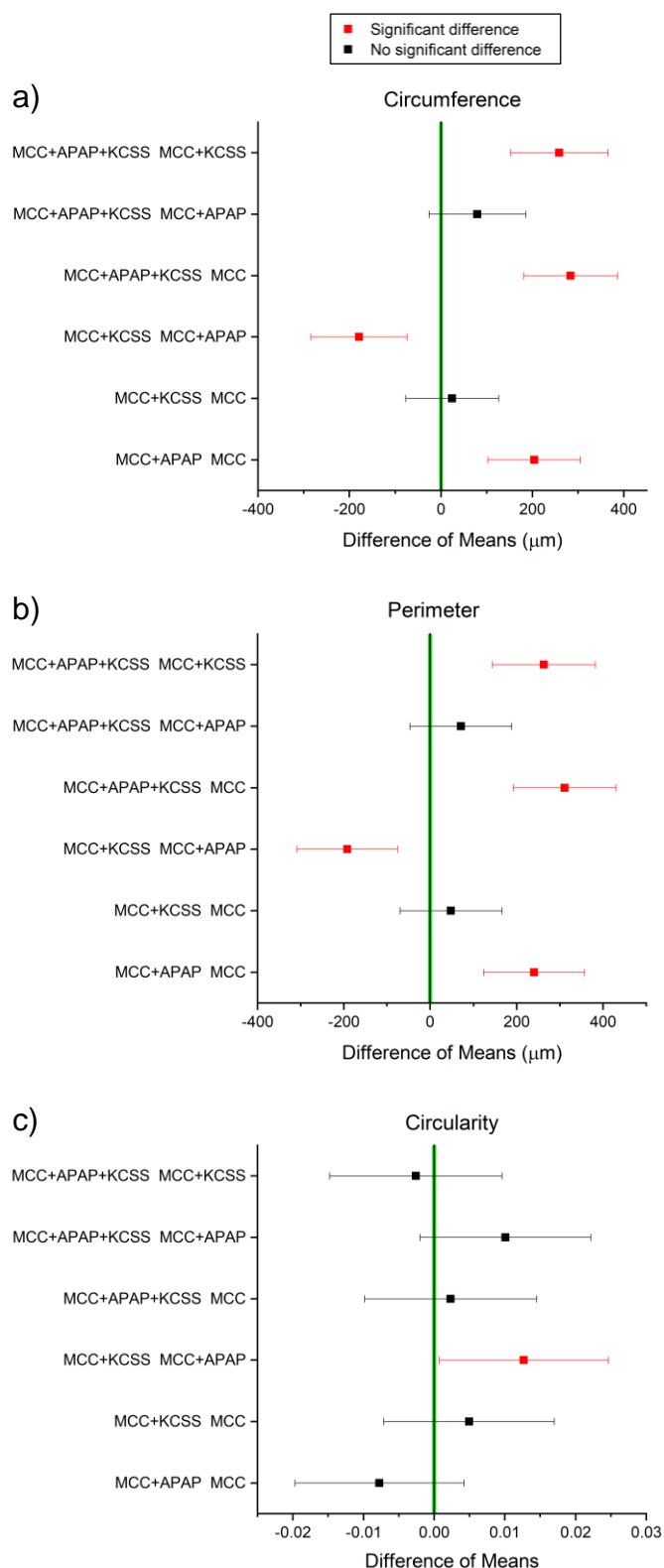


Figure 3.5. A graphical analysis of the means of comparison Tukey test method of the four formulation stage for a) calculated circumference, b) perimeter and c) circularity parameters. Red line indicates a significant difference and black lines indicates no significant difference. If the data range line does not contain zero (does not cross the vertical interval line at 0) the corresponding means are significantly different).

Table 3.3 and Figure 3.5 show that there is no significant difference between MCC+KCSS (FS 2P) and MCC (FS 1) or between MCC+APAP+KCSS (FS 3) and MCC+APAP (FS 2) for all parameters. This therefore suggests that the KCSS layer has no significant effect on the bead size in terms of the calculated circumference, perimeter, and circularity. However, a significant difference is observed between MCC+KCSS (FS 2P) and MCC+APAP (FS 2), this suggests that the majority of the bead size contribution can be attributed to the APAP layer. This is also observed in Figure 3.4. Overall, circularity is largely similar across the formulation stages and the statistical analysis shows that KCSS polymer layer generally has the least impact on the bead size.

Further to the statistical analysis conducted, SEM images were taken to visually investigate the structural changes that each coating layer made, Figures 3.6 – 3.9. The MCC (Figure 3.6) is relatively smooth, with minimal contoured topography. With the addition of the APAP layer (Figure 3.7), the MP bead surface becomes rougher with a flaky appearance and drug particles can be observed. The addition of the KCSS polymer layer (Figure 3.9), the surface of the final MP bead becomes smoother again. The placebo bead (Figure 3.8) however, appears smoother than that of the MCC core, with cracks similar to FS 3 observed. This suggests that the ‘cracking’ is due to the polymer layer itself, rather than the substrate underneath.

When combined with the statistical analysis, this could suggest that the KCSS layer fills any gaps within the topography of the APAP layer, and therefore has minimal contribution to the overall bead size. The results obtained here for the final stage of the formulation is comparable to that of the literature for the spray coating Wurster process.³²

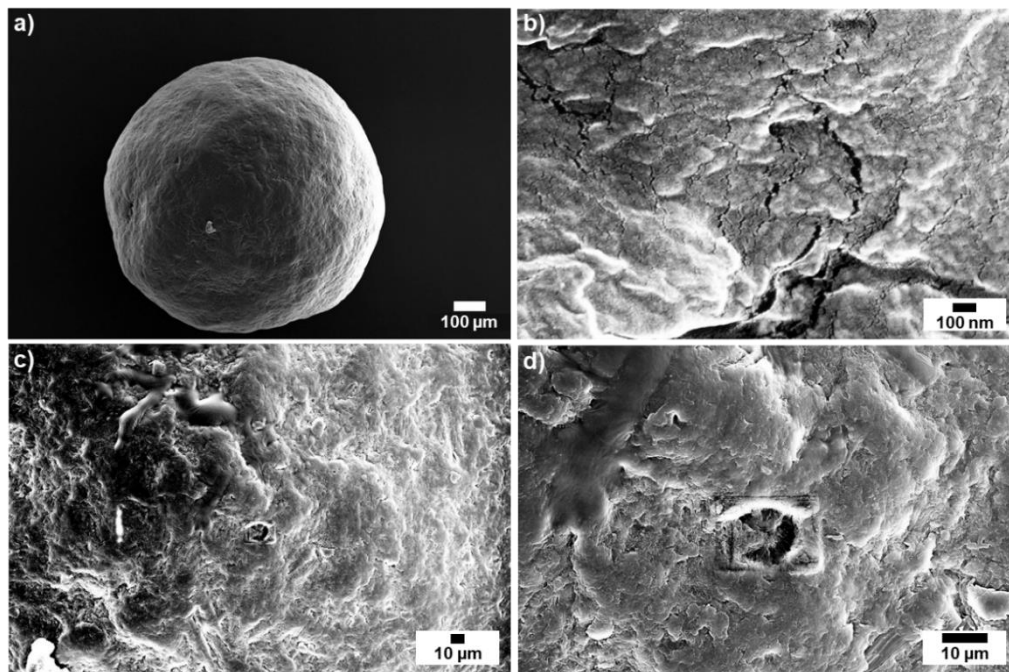


Figure 3.6. SEM images of MCC core – Formulation Stage 1. a) mag = 70 X, WD = 8 mm, b) mag = 50 K X, WD 4 mm, c) mag = 1 K X, WD 4 mm, d) mag = 300 X, WD 4 mm.

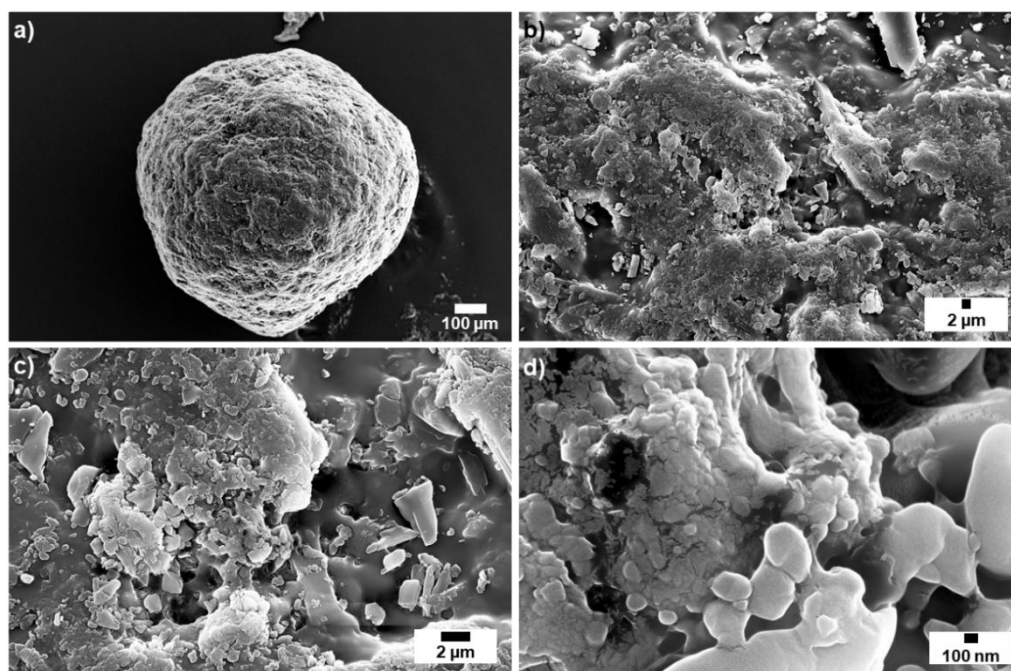


Figure 3.7. SEM images of APAP coated MCC cores – Formulation Stage 2. a) mag = 70 X, WD = 7 mm, b), mag = 1 K X, WD = 4 mm, c) mag = 3 K X, WD 4 mm d) mag = 30 K X, WD = 4 mm.

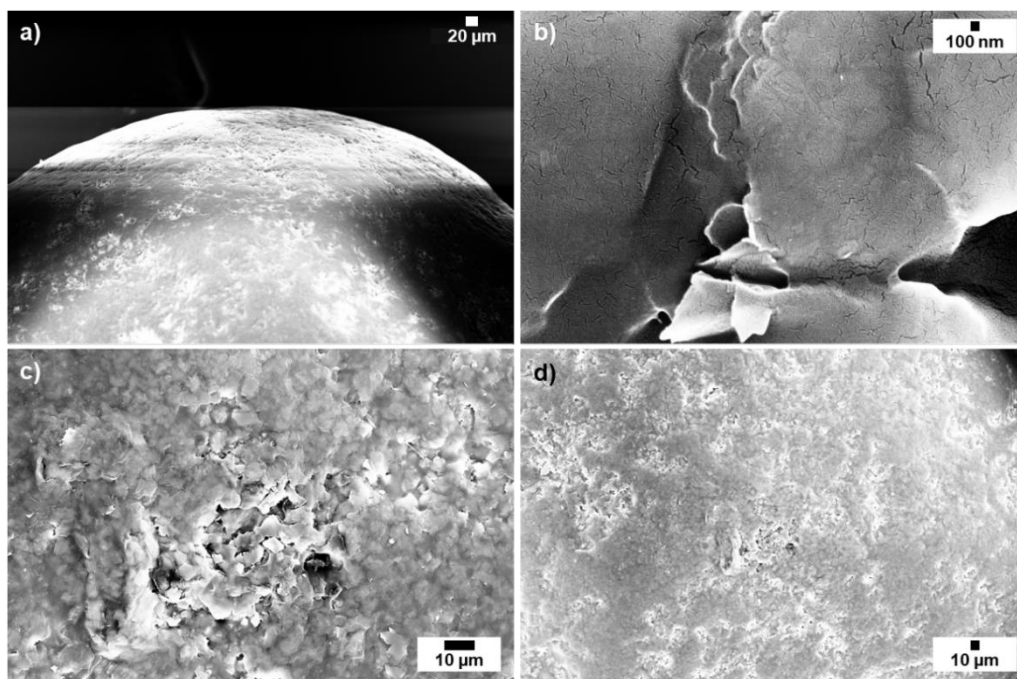


Figure 3.8. SEM images of KCSS polymer coated MCC cores – Formulation Stage 2b. a) mag = 200 X , WD = 4 mm, b) mag = 30 K X, WD = 4 mm, c) 1 K X, WD = 4 mm, d) mag = 300 X, WD = 4 mm.

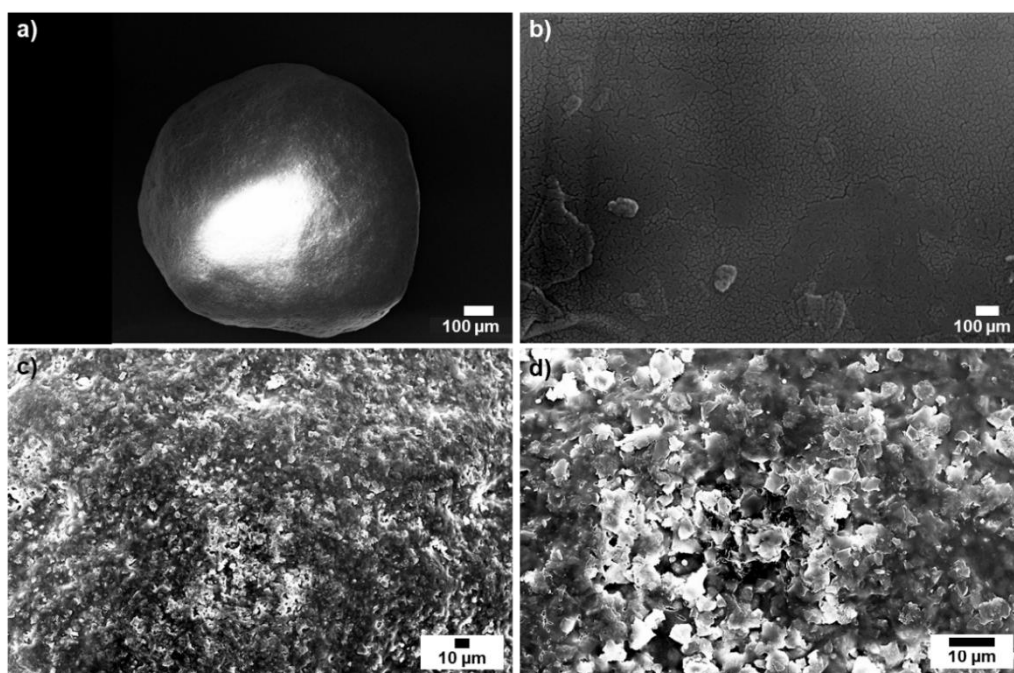


Figure 3.9. SEM images of KCSS polymer coated APAP layered MCC cores – Formulation Stage 3. a) mag = 65 X, WD = 7mm, b) mag = 50 K X, WD = 4 mm, c) mag = 1 K X, WD = 4 mm, d) mag = 300 X, WD = 4mm.

The data and statistical analysis shown in Tables 3.2 and 3.3, along with Figures 3.3 – 3.5, demonstrate that there are several variations in particle size observed between the different stages of formulation. The origin of similar variations when using a conventional bottom spray Wurster process (Figure 3.10) have been investigated in previous studies. Firstly by Sudsakorn and Turton in 2000,³³ and then by Luštrik *et al.* in 2012.³⁴ Both these studies have used single layer coatings, in contrast to the two layer coatings used here.

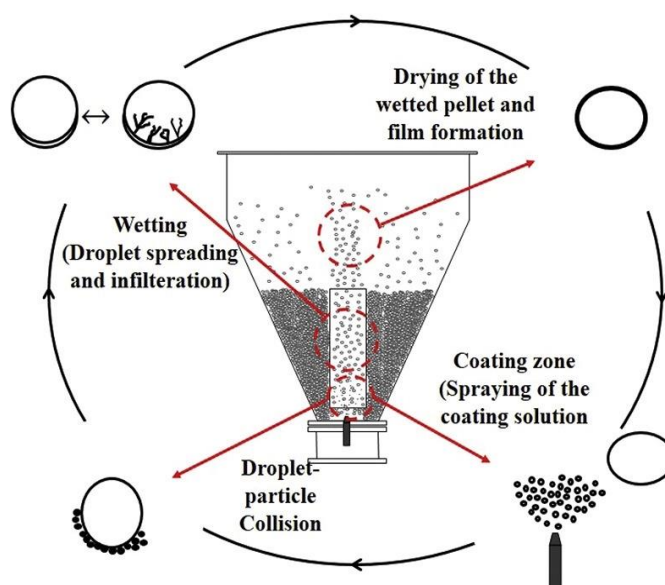


Figure 3.10. Wurster process in a fluid bed coater on coating of MP formulation beads. (Reproduced from Foroughi-Dahr *et al.*, 2019).³⁵

Sudsakorn and Turton suggested that this variation is due to the mass of coating deposited on the bead sizes of different diameters. Here, larger particles accelerate in the vertical direction slower than smaller particles, which allowed the larger ones to move closer to the centre of the tube and consequently closer to the spray area. As the smaller particles have a more prominent vertical acceleration this causes them to move closer to the wall of the chamber and therefore further away from the spray zone. As a result, smaller particles are shielded from the coating dispersion droplets by the larger particles. It is also suggested that the mass coating per particles is not necessarily proportional to the surface area of the particle, but there is a strong correlation between the average mass of coating gained by a given particles and the diameter of the particle.³³

Luštrik *et al.*, suggested that the variation was due to the uniformity of the coating thickness, where the largest beads gained more of the coating dispersion compared to that of the smaller beads. This attributed to the possibility that larger particles entered the chamber spray zone more often as smaller particles and had a greater acceleration and consequently higher velocities compared to their larger counterparts. This meant that smaller particles had longer trajectories and therefore longer circulation times causing in a decrease in turns through the spray zone, resulting in a reduced layer of coating.³⁴

3.3.2. Cyclic Voltammetry on Total Dissolution of Acetaminophen only Single Multiparticulate Bead

3.3.2.1. Dissolution without Agitative Motion

To determine whether APAP could be detected from a single MP bead, individual beads without the complex nature of the KCSS polymer coating (Stage 2 of the formulation) were left for an extended period of time to allow complete APAP release into solution which could then be analysed electrochemically. This experiment further lends itself to the detection of the variation in APAP dosage per MP bead, as suggested by the variation in the sizes of the beads themselves. Individual MP beads were placed in 1 mL of 0.1 M HCl dissolution media and left for a 24-hour period. Cyclic voltammograms were then measured on the resultant solution using a Pt 25 μm UME.

The CVs of the resultant solution from the single bead dissolutions are shown in Figure 3.11, where the differences in the dosage of APAP in individual beads are demonstrated. Here, it can be confirmed that small amounts of APAP from a single MP bead can be detected electrochemically. From this, the concentration of APAP was calculated from the CVs using Equation 3.1 for diffusion to a disc-shaped UME for the steady-state current at 0.9 V,³⁶⁻³⁸

$$C^* = \frac{i_{lim}}{4nFDa} \quad (3.1)$$

where, i_{lim} is the current at steady state in Amperes, C^* is the concentration in mol cm^{-3} , n is the number of electrons involved in the reaction, where APAP has a reversible two-electron oxidation, F is Faraday's constant, 96485 C mol^{-1} , D is the

diffusion coefficient of APAP at $4.12 \times 10^{-6} \text{ cm}^2/\text{s}$ (for a 1 mM APAP solution using a $\varnothing 25 \text{ }\mu\text{m}$ Pt UME),³⁹ and a is the Pt electrode radius in cm. From this, the calculated concentration of APAP was converted into mass (dosage) of APAP contained in a single MP bead, with a mass range of 82 – 155 μg , with an average of $115 \pm 33 \text{ }\mu\text{g}$, as detailed in Table 3.4.

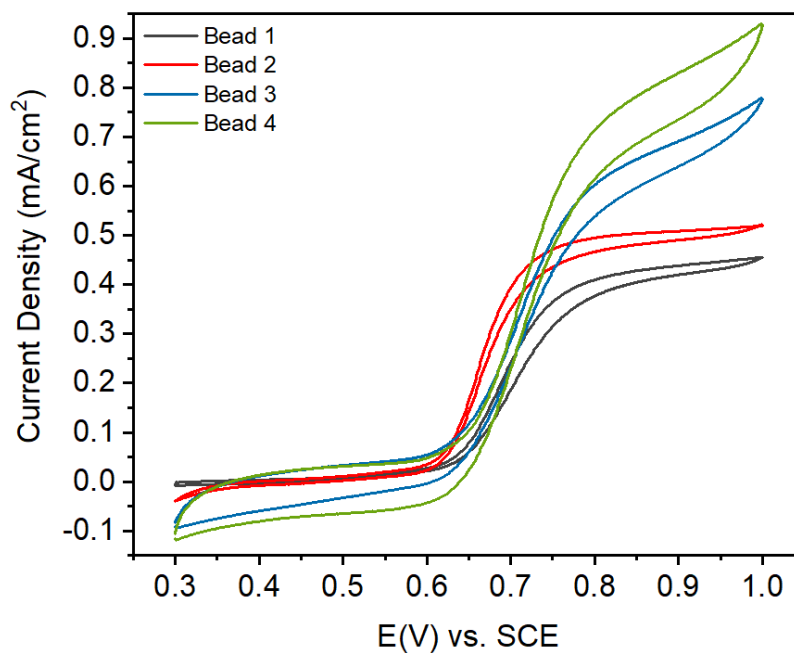


Figure 3.11. Cyclic voltammogram of resultant bulk solution from an APAP coated bead after a 24-hour period of dissolution in 1 mL of 0.1 M HCl using a Pt 25 μm UME as the working electrode and a scan rate of 0.01 V/s.

Table 3.4. Steady state (limiting) current based on the corresponding CVs from dissolution of MP beads into a 1 mL solution of 0.1 M HCl and the calculated mass of APAP from each corresponding MP bead.

Bead	i_{lim} (10^{-9} A)	APAP mass (μg)
1	2.15	82
2	2.50	95
3	3.39	129
4	4.07	155
Average	3.03	115 ± 33

The current density observed in Figure 3.11 suggests a significant variation in APAP concentration. This current density variation supports the particle size distribution of the MP beads observed in Section 3.3.1.

3.3.2.2. Dissolution with Agitative Motion

As the dissolution occurred under stagnant conditions the local concentration detected may not represent the average bulk concentration. Therefore, the experiment was repeated (with an APAP coated bead in the absence of the KCSS polymer) with the addition of solution agitation to establish if this provided a more uniform release of APAP. As the acidic DM was added to the single bead, motion was applied for *ca.* 2 minutes at the start and end of the 24-hour dissolution period, where the ‘start’ of dissolution occurred immediately after the MP APAP coated bead had been placed in the solution and the ‘end’ just before the electrochemical measurement commenced. Additionally, analysis of the MP bead size under the optical microscope before and after the dissolution process were taken.

Agitation of the dissolution media led to higher current densities, as well as a more consistent CV profile as shown in Figure 3.12, thus indicating the significance of motion for the completion of the dissolution. As the size of each MP bead was analysed before and after dissolution, Table 3.5 can quantitatively support the particle size distribution observed in Section 3.3.1, where the APAP concentration and thus its consequent dosage was also calculated using Equation 3.1.

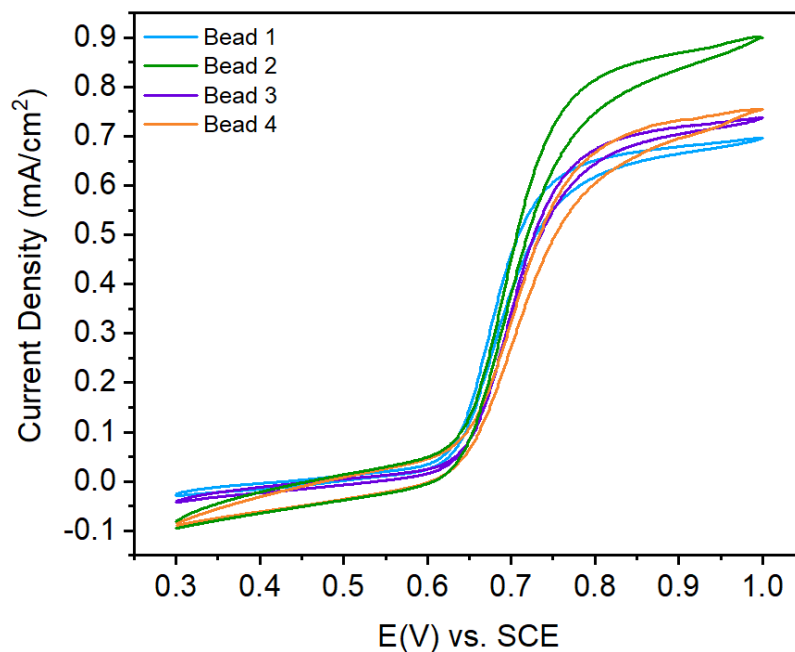


Figure 3.12. Cyclic voltammogram of resultant bulk solution from an APAP only coated bead in 1 mL of 0.1 M HCl, with *ca.* 2 minutes agitation of solution at the start and end of 24-hour period of dissolution using a Pt 25 μm UME as the working electrode and a scan rate of 0.01 V/s.

Table 3.5. Particle size distribution and the dosage of APAP (μg) from the dissolution of single MP APAP only coated bead with motion.

Bead	APAP Mass (μg)	Bead Size		Percentage Difference (%)
		Before (μm)	After (μm)	
1	127	1076	1030	4.3
2	162	950	920	3.2
3	134	920	895	2.7
4	137	975	930	4.6
Average	139.8 \pm 15.4	980 \pm 68	944 \pm 59	3.7 \pm 0.9

Here, the largest bead size (represented by its diameter) did not necessarily equate the largest mass of APAP. Furthermore, the bead with the highest dosage of APAP did not have the largest decrease in size. Additionally, the size of the MP bead is unable to be attributed to a specific stage in the formulation, as the size of a particular MCC core before coating it with the API layer is unknown.

It is possible, however, to indicate from this that the thickness of the coating of the API layer is on average 3.7 ± 0.9 % of the total diameter. However, these observations must be mitigated due to the small sample size analysed.

3.3.3. Direct Acetaminophen Detection from a Single Polymer-Coated Multiparticulate Bead

The detection of APAP from dissolution into the bulk DM with agitation showed an average concentration of 139.8 ± 15.4 $\mu\text{g}/\text{cm}^3$ as demonstrated in Section 3.3.2.2. Direct detection of the dissolution of APAP from a MP bead with and without the polymer coating into the acidic DM of varying pH can be investigated in real time to determine the effect of APAP dissolution rate the KCSS polymer coating has, given by the measured *i-t* profile.

For direct analysis of a single bead, time dependant APAP release was detected in situ, in real time. Given the curvature of the MP bead sample, a MWE was used instead of an in-laid disc UME as the protrusion of the tapered electrode surface in the MWE allowed for a shorter distance between the bead and the electrode tip (which proved to be of great importance, *vide infra*), whilst allowing a more hemispherical diffusion to the electrode tip.

A single APAP containing KCSS polymer coated MP bead was adhered onto a glass slide which was itself adhered to a small glass petri dish. Optical images were taken of the adhered bead to the glass slide before and after dissolution of a two-hour period. The Au MWE was lowered towards the centre of the bead. Preliminary testing of the MP bead coated with the KCSS polymer demonstrated that a measuring potential of 0.8 V ensured the current was mass transport limited for pH 1.0 – 2.0. Once the potential was applied the dissolution media was then added. The schematic shown in Figure 3.13 demonstrates the experimental set up. Using a camera, the distance between the bead and MWE tip was captured. The tip to bead distance (TBD) was estimated by calibrating the distance to the size of the bead from optical microscopy using ImageJ, and then the distance observed between the top of the bead and the tip of the MWE was calculated relative to the bead size, as shown in Figure 3.14.

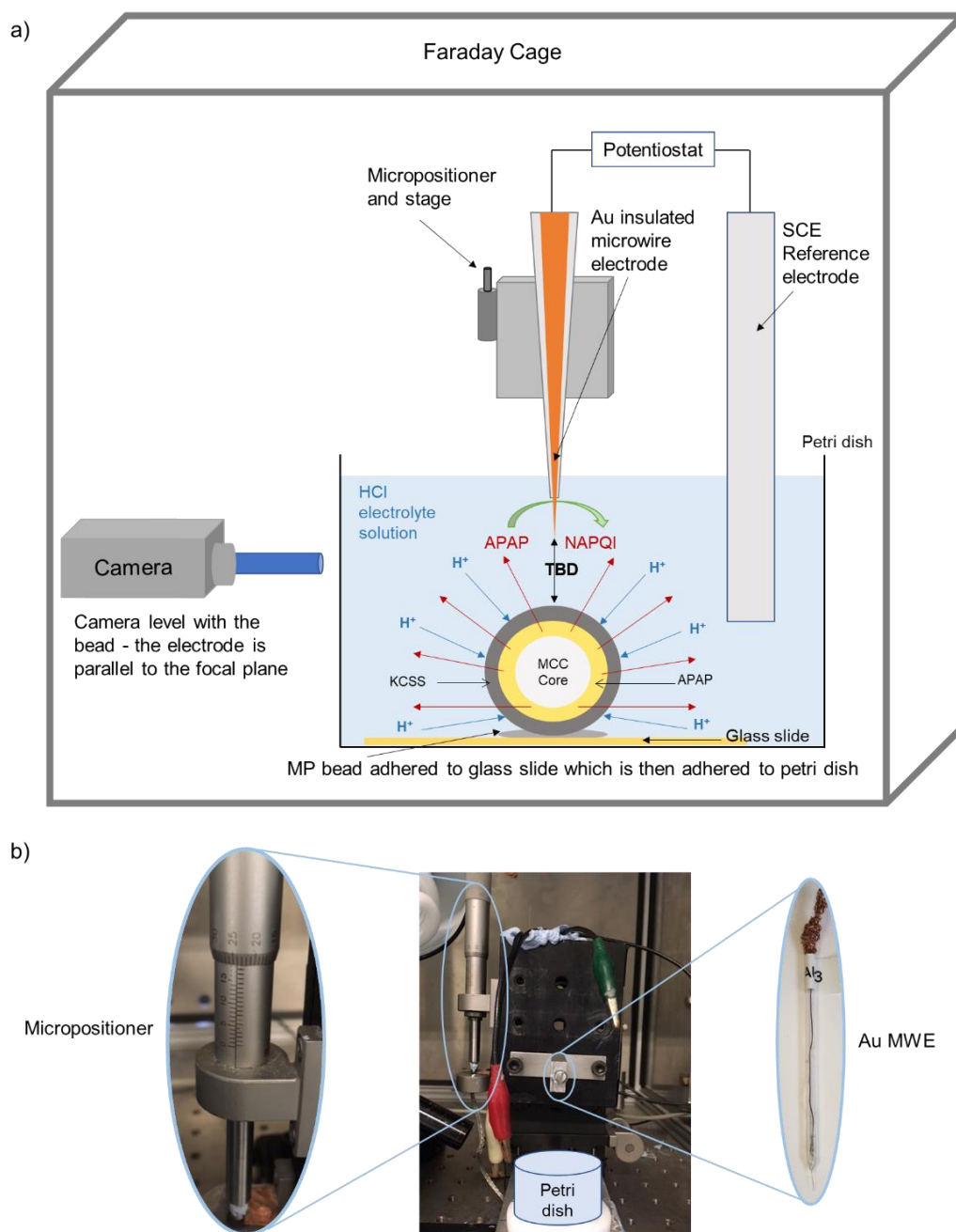


Figure 3.13. a) Schematic of the electrochemical set up for API detection from single MP bead dissolution. MP bead adhered to glass slide attached to the bottom of the petri dish and the camera positioned on the same plane as the MP bead. The Au MWE positioned centrally over the bead using the micropositioner, with the SCE reference electrode in the bulk. (not to scale). b) Image showing the micropositioner for the working electrode inside the Faraday cage, along with the Au MWE and placement of the petri dish for the sample.

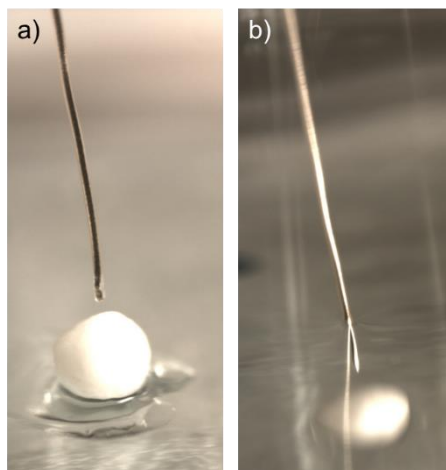


Figure 3.14. MP spherical bead glued onto the glass slide surface with the Au MWE positioned above the centre, demonstrating the set up before (a) and after (b) the addition of solution.

3.3.3.1. Factors Affecting Single Bead Dissolution Detection

From the size distribution discussed above in Section 3.3.1, visual differences were observed in the layering of the formulation process resulting in bead size variation. Further to this, dissolution of APAP only MP bead demonstrated discrepancies in the APAP concentration per bead. Thus, this was used as a basis to investigate the effect that KCSS polymer coated APAP MP bead size had upon the dissolution profile.

3.3.3.1.1. Effect of polymer coating and pH on release of APAP

Here, the release of APAP from a FS 2 MP (APAP only MP bead) was compared to that of FS 3 MP where the KCSS polymer coating is present, in DM ranging from 0.01 M to 0.1 M HCl. An average of three repeats for each *i-t* curve with the standard deviation (SD) is shown in Figure 3.15. For the APAP only MP bead an almost instant spike results in the detection of APAP defined by the increase in current density that occurs at *ca.* 6 s. This, therefore, demonstrates that APAP is highly soluble under these conditions, as there is not the physical barrier of a polymer film. The rate of drug permeation through a (polymer) film coating is dependent on the solubility of the drug in the dissolution media, therefore high solubility results in a high concentration gradient, and thus a faster release of drug.¹³ From the literature, the dissolution of APAP, is not known to be pH dependant between pH 1 and 7.⁴⁰ Thus, the difference with pH (Figure 3.15) is likely due to the presence of the KCSS polymer.

Faster protonation of the tertiary amine groups on the polymer at lower pHs, increases the polymer's solubility, which ultimately releases more of the drug. A low average lag time is observed for *ca.* 80 s before a significant increase in current density for the KCSS coated beads in 0.1 M HCl DM. However, a slower, less distinct lag time for 0.01 M HCl is observed. This therefore supports the notion that for this system drug release occurs faster at lower pHs.

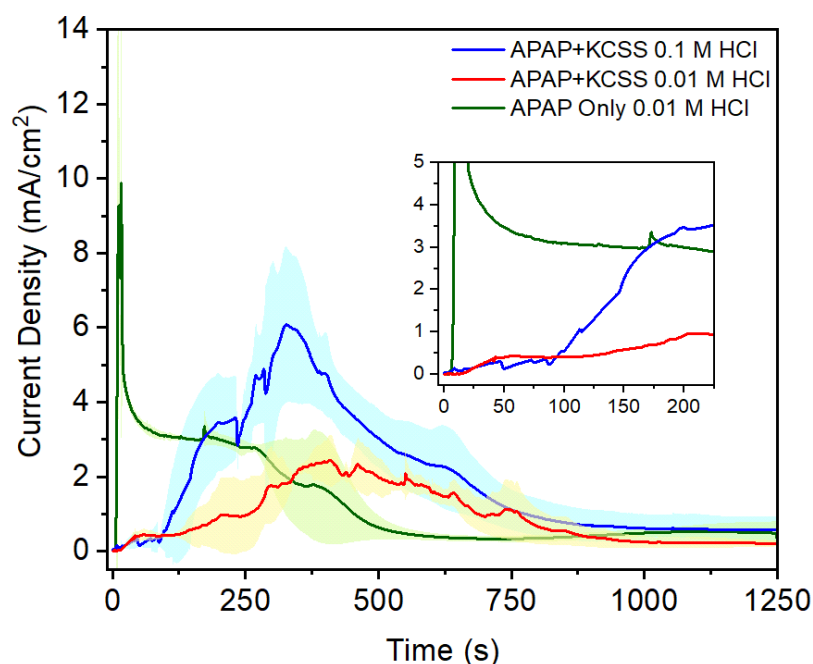


Figure 3.15. Averaged amperometric release profiles (*i-t* curves) in real-time of APAP dissolutions from multiparticulates at a fixed potential based on the steady state current (0.8 V). This demonstrates the effect of the presences of the KCSS polymer coating in a 1 mL solution of pH 1.0 and 2.0 at concentrations 0.1 M and 0.01 M HCl, respectively. The shading represents the SD, where $N = 3$.

It should be considered that part of this lag time is due to the dissolved APAP reaching the electrode. As a general rule, the timescale for diffusion based on a random walk can be given by,^{37,41}

$$t = \frac{d^2}{D} \quad (3.2)$$

where, d is the distance in cm based on an average TBD of 66 μm , with the value of the diffusion coefficient, D as $4.12 \times 10^{-6} \text{ cm}^2/\text{s}$. Thus, the time taken for the diffusion APAP to reach the electrode is calculated at 5.3 s.

The SEM images in Figure 3.16 show the topographical changes of the KCSS polymer coated placebo beads after 60 minutes of dissolution in 0.1 M HCl and 0.01 M HCl (*ca.* pH 1 and pH 2) respectively. At 0.1 M there are more changes to the surface, showing an increased surface roughness compared to that at 0.01 M HCl. Both, however, demonstrates topographical changes after compared to before dissolution (Figure 3.8). These topographical changes relate to the dissolution profiles shown at the corresponding pHs.

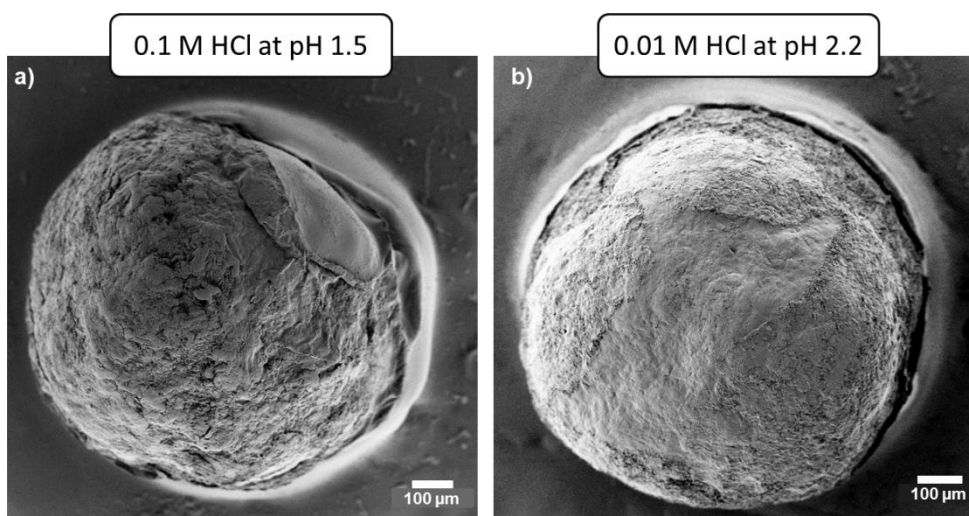


Figure 3.16. SEM images of individual beads after 60 minutes in acidic media: a) 0.1 M HCl, EHT = 3 kV, mag = 65 X, WD = 5 mm. b) 0.01 M HCl, EHT = 2 kV, mag = 70 X, WD = 7 mm.

3.3.3.1.2. *Effect of Bead Size and Tip-Bead Distance*

There are experimental aspects to consider that may affect the outcome of the dissolution profile. As previously discussed, the difference in the MP bead size contributed variation in the dosage of APAP, therefore the bead size was investigated by direct detection from a single bead. Furthermore, the placement of the MWE may present an importance in the resulting dissolution profile, thus the distance between the tip of the MWE was another factor that was investigated.

Table 3.6 shows the results and the corresponding parameters from the beads investigated. After dissolution, the bead size is expected to decrease as APAP has been confirmed to dissolve into the DM. Furthermore, the SEM images shown in Figure 3.16 show signs of erosion of the polymer layer which indicates that the polymer layer has been reduced, this is notion is explored further in Chapter 5.

Table 3.6. Bead size before and after single bead dissolution in 1 mL of 0.1 M HCl dissolution media calculated by measuring the diameter of the bead, and the calculated distance between the MWE tip and the centre of the bead.

Bead	Diameter		Difference		Tip-bead Distance (μm)
	Before (μm)	After (μm)	(μm)	(%)	
1	1025	970	55	5.37	120
2	1020	910	110	10.78	20
3	1033	1010	23	2.23	63
4	990	955	35	3.54	61
5	1160	1030	130	11.21	66
Average	1046 \pm 66	975 \pm 47	71 \pm 47	6.6 \pm 4.1	66 \pm 36

From the size distribution discussed above in Section 3.3.1, there are visual differences observed in the layering of the formulation process. This was used as a basis to investigate the effect that KCSS polymer coated APAP MP bead size had upon the dissolution profile. Three sizes (990 – 1160 μm) were investigated as shown in Figure 3.17. In order for the bead size to be analysed, the resulting dissolution profiles were compared to those with consistent tip-bead distance at *ca.* 60 μm . Here, largest bead produces highest peak current density which correlates to the release of APAP and its subsequent conversion to its oxidised state.

The dissolution profile and data found in Figure 3.17 and Table 3.6 respectively, indicates that the bead size is not necessarily indicative of the APAP dosage per bead, which corresponds to the data detailed and discussed in Section 3.3.2. However, an interesting trend in lag time is demonstrated by the increasing size of the bead shown in the inset of Figure 3.17, where the lag time for initial spike increases at *ca.* 88 s, 99 s and 145 s corresponding to bead sizes 990 μm , 1033 μm and 1160 μm respectively. This could be due to a larger surface area for protonation of the tertiary amine groups to occur, thus increasing the time take for APAPs response.

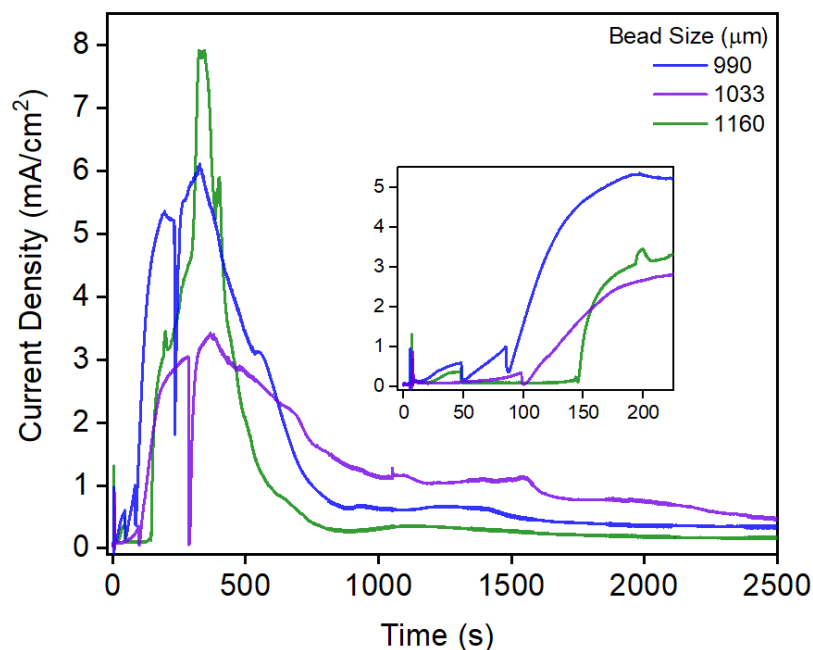


Figure 3.17. Averaged amperometric release profiles ($i-t$ curves) in real-time of APAP dissolutions from multiparticulates at a fixed potential based on the steady state current (0.8 V). This demonstrates the effect of the variation of MP bead size at a constant distance (*ca.* 60 μm) from the MWE in a 1 mL solution of 0.1 M HCl.

Sequential spikes of similar trend are observed for the three varying bead sizes. This could suggest sudden dissolution events occurring through larger expansions of the polymer chains within the coating. This demonstrates the value of mechanistic information from single dose measurement in which may be lost in dissolution testing of bulk/whole dosage. These spikes in the data, therefore, suggest that the dissolution profile is not homogeneous.

Further to this, Figure 3.18 shows the visual changes observed before and after dissolution as detailed in Table 3.6. From the loss of APAP from the bead and into the bulk, the bead size as expected decreases in size after dissolution and appear to have a smoother edge. It is likely that the majority of the size reduction size is due to the release of APAP from the encapsulated coating into the bulk DM. Moreover, as previously discussed, the SEM data *vide supra* suggests the dissolution of the polymer layer which would also contribute to the decrease in MP bead size.

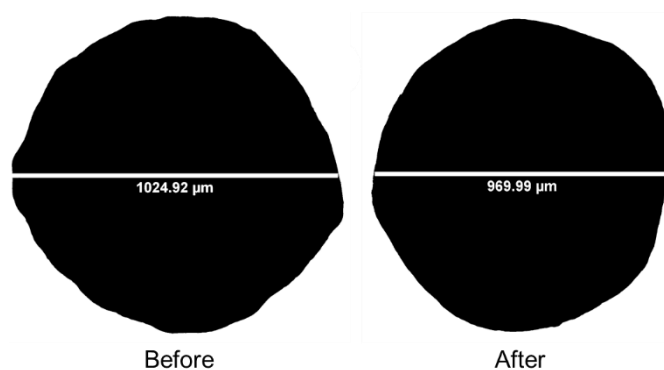


Figure 3.18. Example of the KCSS polymer-coated MP spherical bead before and after 2 hours of APAP dissolution in 0.1 M HCl acidic media.

The distance between the MWE tip and the centre of the MP bead were investigated at *ca.* 20, 60, 120 μm , which is shown in Figure 3.19. Here the dissolution profiles differ more significantly in relation to the distance from the MWE compared to the variation observed for the bead sizes. A TBD of 20 and 63 μm yield a similar lag time of *ca.* 120 and 100 s respectively, at 120 μm a longer lag time of *ca.* 190 s is observed in the inset.

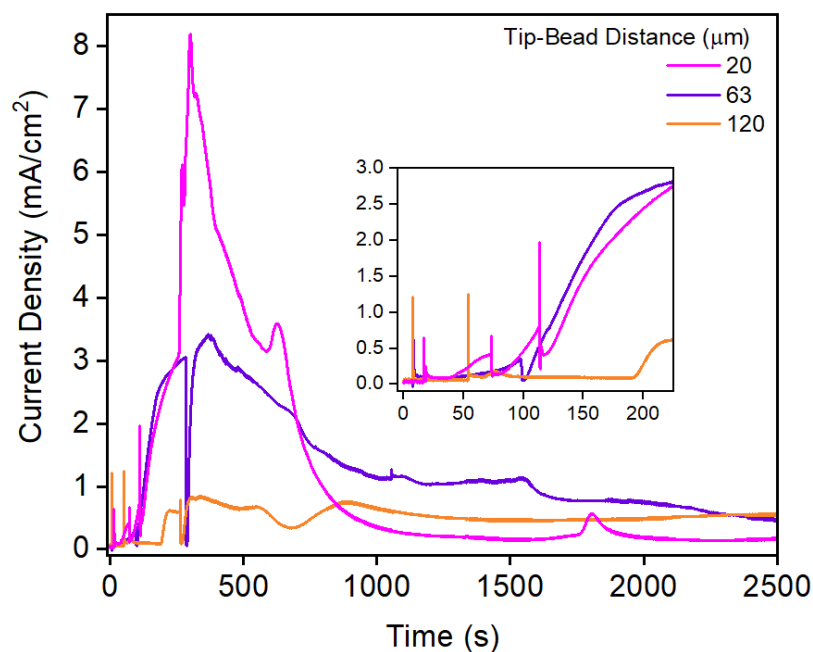


Figure 3.19. Averaged amperometric release profiles (*i-t* curves) in real-time of APAP dissolutions from multiparticulates at a fixed potential based on the steady state current (0.8 V). This demonstrates the effect of the variation of the distance between the bead and the tip of the MWE in a 1 mL solution of 0.1 M HCl.

In addition to this, the dissolution profiles peak at lower current densities the further away from the MWE tip. This data therefore demonstrates that the smaller separation distance means that the diffusion front reaches the electrode sooner and is more concentrated. As this diffusion field spreads out it becomes more dilute and thus the current density is lower when the electrode is at a further distance. This methodological approach offers an insightful way to investigate diffusion fields, however this method needs further development to achieve more consistent control of the distance separation between the electrode tip and the surface of the bead.

This study investigates the profile as APAP is released from the MP bead and then detected by the electrode. Therefore, the local concentration detected for a single bead may be higher. The findings shown in this study is comparative to a study led by Borgquist *et al.*, 2004,⁴² which demonstrated that single multiparticulates showed a wide range of drug release profiles, where size was the biggest contributor to variations in the dissolution profile. Furthermore, these variations significantly decreased when the number of MP beads is increased.⁴² Multiparticulates are usually taken in a dosage form rather than a single unit, therefore depending on the dosage required the variation effects can be minimised.

3.3.3.1.3. Comparison of Acetaminophens Total Concentration Detected

Integration of the area under each curve in Figures 3.15, 3.17, and 3.19, yields the total concentration of APAP detected for the variables; presence of polymer, bead size and tip to bead distance (Table 3.7).

When considering the presence of polymer (Figure 3.15), under pH 1 (0.1 M HCl) conditions approximately two times the concentration of APAP is released compared to that of pH 2 (0.01 M HCl). In contrast at pH 2, in the absence of the KCSS polymer, there is only a 33 % increase in APAPs total concentration. The bead size variable (Figure 3.17) seems to have less of an impact on the total concentration of APAP released, with the smallest bead size contributing to the largest amount of APAP released. For the tip to bead distance (Figure 3.19), there was minimal difference between a distance of 20 and 63 μm , but the total concentration released substantially reduced at a distance of 120 μm .

Table 3.7. Calculated values of the total concentration of APAP released from the *i-t* dissolution profiles for variables for the presence of polymer, bead size and tip to bead distance.

Variable	Conditions	APAP Conc. (μM)
Presence of polymer	APAP + KCSS, pH 1	1.29
	APAP + KCSS, pH 2	0.63
	APAP only, pH 2	0.84
Bead Size (polymer present, pH 1)	990 μm	1.82
	1033 μm	1.73
	1160 μm	1.18
Tip to Bead Distance (polymer present, pH 1)	20 μm	1.54
	63 μm	1.73
	120 μm	0.68

The calculated total concentrations of APAP release observe the same trend for their corresponding release profiles discussed previously. Furthermore, it is important to note that beyond reaching the peak of the dissolution profiles, the current density is continually decreasing due to fouling of the electrode surface, thus the total APAP concentration detected does not necessarily equate to the total concentration released. Also, given the small sample size it is ambitious to establish a solid pattern, however, this data gives a promising indication on the trends of API release for these different variables.

3.4. Further work

Current density demonstrates the rate of APAPs release, which is in theory proportional to the polymers dissolution, however as the pH of the surface is unknown and the rate of dissolution is proportional to pH surface, which is not well defined, the single bead dissolution analysis can only provide a basis for further work. Therefore, in the following chapter a rotating disc electrode (RDE) was used to control mass transport and other conditions and thus the rates can be calculated.

The results obtained in this study prove to be promising, however improved control over mass transport and smaller, more consistent electrode-bead separation are required. Scanning electrochemical microscopy (SECM) or scanning ion conductance microscopy (SICM) are both methods of precisely positioning electrodes near the bead which may offer such improvements. Furthermore, there is also the potential to laterally scan the electrode during dissolution to spatially map the dissolution profile and this is explored later (Chapter 6).

3.5. Conclusions

This study has demonstrated an experimental setup to detect APAP release during dissolution of single MP beads. The variability in the dissolution of each bead depended on the exact formulation, as well as its size. The role of agitation in ensuring total dissolution (as seen by much more consistent final APAP concentrations after 24 hours dissolution) was demonstrated. The fine control over the electrode positioning revealed the sensitivity of this technique to electrode positioning and highlighted the importance of this parameter for future studies. This demonstrated the benefit of using electrochemical detection in dissolution testing as not only can the dissolution-time profile be traced, but using a single bead utilises the electrochemical sensitivity of the system.

As a method development study, the aims set out have been achieved. The API release from individual beads has been successfully measured and it has been demonstrated how the polymer coating impacts dissolution rates. However, it has also been shown that the results are sensitive to agitation and electrode position, which adds uncertainty to the extrapolation of these individual results to a multiparticulate dose as a whole. Therefore, to evaluate the behaviour of potential ‘whole’ doses, a rotating disc electrode (RDE) approach will be introduced in the following chapter.

3.6. References

1. Sastry, S. V., Nyshadham, J. R. & Fix, J. A. Recent technological advances in oral drug delivery – a review. *Pharm. Sci. Technol. Today* **3**, 138–145 (2000).
2. Abuhelwa, A. Y., Williams, D. B., Upton, R. N. & Foster, D. J. R. Food, gastrointestinal pH, and models of oral drug absorption. *Eur. J. Pharm. Biopharm.* **112**, 234–248 (2017).
3. Lopez, F. L., Ernest, T. B., Orlu, M. & Tuleu, C. The effect of administration media on palatability and ease of swallowing of multiparticulate formulations. *Int. J. Pharm.* **551**, 67–75 (2018).
4. Felton, L. A. Use of polymers for taste-masking pediatric drug products. *Drug Dev. Ind. Pharm.* **44**, 1049–1055 (2018).
5. Gittings, S., Turnbull, N., Roberts, C. J. & Gershkovich, P. Dissolution methodology for taste masked oral dosage forms. *J. Control. Release* **173**, 32–42 (2014).
6. Rajabi-Siahboomi, A. R. Overview of Multiparticulate Systems for Oral Drug Delivery. in *Multiparticulate Drug Delivery Formulation, Processing and Manufacturing* (ed. Rajabi-Siahboomi, A. R.) 1–4 (Springer, New York, NY, 2017). doi:10.1007/978-1-4939-7012-4_1
7. Gandhi, B. & Baheti, J. Multiparticulates Drug Delivery Systems : A Review. *Int. J. Pharm. Chem. Sci.* **2**, 1620–1626 (2013).
8. Martinez Teran, M. E., Hoang Thi, T. H. & Flament, M. P. Multi-Particulate Dosage Forms for Pediatric Use. *Pediatr. Ther.* **07**, 1–6 (2017).
9. Lopez, F. L. *et al.* Acceptability of placebo multiparticulate formulations in children and adults. *Sci. Rep.* **8**, 1–10 (2018).
10. Mudie, D. M., Amidon, G. L. & Amidon, G. E. Physiological Parameters for Oral Delivery and in Vitro Testing. *Mol. Pharm.* **7**, 1388–1405 (2010).
11. Koziolk, M. *et al.* Investigation of pH and Temperature Profiles in the GI Tract of Fasted Human Subjects Using the Intellicap® System. *J. Pharm. Sci.* **104**, 2855–2863 (2015).
12. Drašković, M., Medarević, D., Aleksić, I. & Parojčić, J. In vitro and in vivo investigation of taste-masking effectiveness of Eudragit E PO as drug particle coating agent in orally disintegrating tablets. *Drug Dev. Ind. Pharm.* **43**, 723–731 (2017).
13. Dashevskiy, A. *et al.* Micropellets coated with Kollicoat® Smartseal 30D for taste masking in liquid oral dosage forms. *Drug Dev. Ind. Pharm.* **43**, 1548–1556 (2017).

14. BASF SE Care Chemicals Division Pharma Ingredients & Services. Kollicoat Smartseal 30 D Technical Information. *BASF Tech. Inf.* 1–12 (2011).
15. Hans, R., Thomas, S., Garla, B., Dagli, R. J. & Hans, M. K. Effect of Various Sugary Beverages on Salivary pH, Flow Rate, and Oral Clearance Rate amongst Adults. *Scientifica (Cairo)*. **2016**, 1–6 (2016).
16. Gittings, S., Turnbull, N., Henry, B., Roberts, C. J. & Gershkovich, P. Characterisation of human saliva as a platform for oral dissolution medium development. *Eur. J. Pharm. Biopharm.* **91**, 16–24 (2015).
17. Chivate, A., Sargar, V., Nalawade, P. & Tawde, V. Formulation and development of oral dry suspension using taste masked Ornidazole particles prepared using Kollicoat® Smartseal 30 D. *Drug Dev. Ind. Pharm.* **39**, 1091–1097 (2013).
18. Silva, B. S. *et al.* Building Process Understanding of Fluid Bed Taste Mask Coating of Microspheres. *AAPS PharmSciTech* **20**, (2019).
19. William R. Pfister and Tapash K. Ghosh. Intraoral Delivery Systems: An Overview, Current Status, and Future Trends. in *Drug Delivery to the Oral Cavity* (eds. Ghosh, T. K. & Pfister, W. R.) 1–40 (CRC Press, 2005).
20. Guth, F. & Kolter, K. Taste Masking with Kollicoat ® Smartseal 30 D – Dissolution Studies in Biorelevant Media. 2500 (2012).
21. Mutalabisin, M. F., Chatterjee, B. & Jaffri, J. M. pH Responsive Polymers in Drug Delivery. *Res. J. Pharm. Technol.* **11**, 5115–5122 (2018).
22. Dey, N. S., Majumdar, S. & Rao, M. E. B. Multiparticulate Drug Delivery Systems for Controlled Release. *Trop. J. Pharm. Res.* **7**, 1067–1075 (2008).
23. Lee, H. S. *et al.* Sprinkle formulations—A review of commercially available products. *Asian J. Pharm. Sci.* **15**, 292–310 (2019).
24. Wening, K. & Breitzkreutz, J. Oral drug delivery in personalized medicine : Unmet needs and novel approaches. *Int. J. Pharm.* **404**, 1–9 (2011).
25. Aulton, M. E. & Taylor, K. M. G. *Aulton's Pharmaceutics: The Design and Manufacture of Medicines*. (Elsevier Ltd., 2018).
26. Narang, A. S. & Boddu, S. H. *Excipient Applications in Formulation Design and Drug Delivery*. *Excipient Applications in Formulation Design and Drug Delivery* (Springer International Publishing, 2015). doi:10.1007/978-3-319-20206-8
27. Bai, G. *et al.* Hydrodynamic Investigation of USP Dissolution Test Apparatus II. *J. Pharm. Sci.* **96**, 2327–2349 (2007).

28. Palakollu, V. N., Chiwunze, T. E., Liu, C. & Karpoormath, R. Electrochemical sensitive determination of acetaminophen in pharmaceutical formulations at iron oxide/graphene composite modified electrode. *Arab. J. Chem.* **13**, 4350–4357 (2020).
29. Nematollahi, D., Shayani-Jam, H., Alimoradi, M. & Niroomand, S. Electrochemical oxidation of acetaminophen in aqueous solutions: Kinetic evaluation of hydrolysis, hydroxylation and dimerization processes. *Electrochim. Acta* **54**, 7407–7415 (2009).
30. Li, Y. & Chen, S. M. The electrochemical properties of acetaminophen on bare glassy carbon electrode. *Int. J. Electrochem. Sci.* **7**, 2175–2187 (2012).
31. Mathivanan, J., Chang, Z., Galagedera, S. K. K. & Flechsig, G. Thermochemistry of Paracetamol - Studied at Directly Heated Micro-wire and Rotating Disk Electrodes. *Electroanalysis* **30**, 1479–1486 (2018).
32. Felton, Linda A., McGinity, J. W. *Aqueous Polymeric Coatings for Pharmaceutical Dosage Forms. Drugs and the Pharmaceutical Sciences* **176**, (CRC Press, 2016).
33. Sudsakorn, K. & Turton, R. Nonuniformity of particle coating on a size distribution of particles in a fluidized bed coater. *Powder Technol.* **110**, 37–43 (2000).
34. Luštrik, M., Dreu, R., Šibanc, R. & Srčič, S. Comparative study of the uniformity of coating thickness of pellets coated with a conventional Wurster chamber and a swirl generator-equipped Wurster chamber. *Pharm. Dev. Technol.* **17**, 268–276 (2012).
35. Foroughi-Dahr, M., Sotudeh-Gharebagh, R. & Mostoufi, N. Effect of operation conditions on coating of pharmaceutical pellets with a film of HPMC/PEG in a Wurster coater. *Powder Technol.* **354**, 804–814 (2019).
36. Forster, R. J. Microelectrodes: new dimensions in electrochemistry. *Chem. Soc. Rev.* **23**, 289 (1994).
37. Bard, A. J. & Faulkner, L. R. *Electrochemical Methods: Fundamentals and Applications*. (2001).
38. Danis, L., Polcari, D., Kwan, A., Gateman, S. M. & Mauzeroll, J. Fabrication of Carbon, Gold, Platinum, Silver, and Mercury Ultramicroelectrodes with Controlled Geometry. *Anal. Chem.* **87**, 2565–2569 (2015).
39. Channon, R. B., Newland, J. C., Bristow, A. W. T., Ray, A. D. & Macpherson, J. V. Selective Detection of Hydrazine in the Presence of Excess Electrochemically Active Pharmaceutical Ingredients Using Boron Doped Diamond Metal Nanoparticle Functionalised Electrodes. *Electroanalysis* **25**, 2613–2619 (2013).

40. Shaw, L. R., Irwin, W. J., Grattan, T. J. & Conway, B. R. The effect of selected water-soluble excipients on the dissolution of paracetamol and ibuprofen. *Drug Dev. Ind. Pharm.* **31**, 515–525 (2005).
41. Codling, E. A., Plank, M. J. & Benhamou, S. Random walk models in biology. *J. R. Soc. Interface* **5**, 813–834 (2008).
42. Borgquist, P., Nevsten, P., Nilsson, B., Wallenberg, L. R. & Axelsson, A. Simulation of the release from a multiparticulate system validated by single pellet and dose release experiments. *J. Control. Release* **97**, 453–465 (2004).

Chapter 4

In Situ Rotating Disc Electrode Dissolution Measurement of Acetaminophen from Suspended Polymer-Coated Multiparticulates

Herein, the use of the rotating disc electrode (RDE) technique for in situ measurement of dissolution kinetics of polymer-coated (multiparticulate) MP formulations is demonstrated. A KCSS polymer-coated redox active acetaminophen core is used to study the effects of pH on dissolution in buffered and unbuffered media. Whilst in unbuffered media dissolution does not occur above pH 3.0, in the presence of buffers dissolution proceeds up to pH 5.0. This highlights the significant effect that buffer equilibria have on the process of dissolution. In general, the technique developed in this chapter improves the time resolution available for dissolution measurements by working in situ. It is applicable to the study of release of any electroactive species of interest, with the ability to identify key phases within the dissolution process.

4.1. Introduction

In vitro dissolution measurements are designed to quantify the amount of drug released into solution over time under well-defined conditions. U.S. Pharmacopeia (USP) Dissolution Apparatus II is the pharmaceutical industry standard when it comes to the measurement of dissolution rates of solid dosage forms. A solid is introduced into the dissolution media and stirred at a rate of 50 – 100 rpm, with sample aliquots extracted from the resultant solution at specified time points and analysed by UV spectrophotometry or high performance liquid chromatography (HPLC) techniques.^{1,2}

Such *ex situ* approaches have limited time resolution, however, which can be problematic when the measurement of fast dissolution kinetics is required, such as with instant release formulations. As a result *in situ* techniques involving the electrochemical detection of analytes are increasingly being employed in *in vitro* studies involving electroactive compounds of pharmaceutical forms and physiological fluids, as well as to obtain thermodynamic and kinetic data.^{3–5} Furthermore, these methods provide a continuous measurement without requiring titration or interval sampling.^{6,7}

Multiparticulates (MP) are versatile in their ability to be administered, for example they can be sprinkled on to food such as yoghurts, apple sauce or consumed in a liquid carrier.⁸ Therefore, a selection of unbuffered and buffered pHs along with a wide range of temperatures were selected for this study. Physiological fluid secreted by the stomach is primarily hydrochloric acid and is found to have a pH of *ca.* 1.0 – 2.0 ($[H^+] = 0.01 - 0.1$ M) in the fasted state and can range from pH 3 – 7 ($[H^+] = 1 - 10^{-4}$ mM) in the fed state.^{9–11} Temperatures of intake of food and fluids have been known to affect gastric function within the range of *ca.* 21 – 44 °C,¹² furthermore intra-oral conditions are known to experience a wide array of temperatures (*ca.* 5.6 – 58.5 °C) across a 24-hour period dependent on a variety of factors, not limited to the intake of food and fluids, with the most common temperature of 35 – 36 °C.^{13–15} Furthermore, food or drink carriers with a particularly low or high temperature or pH may alter the effectiveness of the polymers taste masking property.

This chapter builds upon the foundation of data seen in Chapter 3, here a dosage of MP beads is studied in a continually stirred environment rather than a single bead in a stagnant environment, with the notion of mimicking and enhancing the experimental parameters presented by USP Dissolution Apparatus II. One major issue with this USP apparatus is the complexity of the complex hydrodynamics involved depending upon the position of the drug particle in question.^{1,16}

The use of the rotating disc electrode (RDE) rectifies the experimental factors faced in the previous chapter, such as electrode position. Furthermore, the RDE method is a hydrodynamic steady-state technique in which the working electrode itself is in motion, allowing for the control of mass transport.^{17,18} The spinning motion causes solution at the electrode surface to be constantly removed in a direction parallel to the electrode surface due to the centrifugal force. The solution is then replaced by bulk solution moving perpendicular up to the surface. Existing pharmaceutical RDE methods use powders or pressed tablets confined to the centre of the electrode.^{6,19} The well-defined hydrodynamics at the surface of the RDE ensures dissolved compound is rapidly transported from the dissolving surface to the electroactive surface, allowing the current to provide near-instant feedback on the dissolution process. Despite the advantages, the RDE has yet to be extended to the analysis of modern oral dosage forms, where multiple active pharmaceutical ingredient (API) containing particles are fully suspended in the dissolution media of interest and instantaneously analysed.

Herein, the RDE method is demonstrated as a means of quantifying the dissolution kinetics of acetaminophen (APAP) polymer-coated MP formulations, which are fully suspended in the dissolution medium. Measurements were designed to mimic *in vivo* conditions as far as possible and follow the USP Apparatus II approach in terms of stirring and the use of multiple API particles. Variations in the dissolution rates as a function of pH, temperature, and the presence of pH buffers were examined.

4.2. Experimental

4.2.1. Multiparticulate Formulation

The multiparticulate bead samples were prepared according to Chapter 2, Section 2.2. Briefly, the core of the formulation was made from microcrystalline cellulose (MCC) spheres (Cellets[®] 700, IPC GmbH, Germany), which were coated by the API suspension, followed by the KCSS polymer suspension by a fluid bed coater (Glatt GmbH, Germany) using the bottom spray coating method (Wurster process).^{20,21} The API liquid suspension was made from APAP at 40 % w/w with hydroxypropyl methylcellulose (HPMC) as a binder, which coated the MCC spheres in an 85 % w/w layer. A suspension was made using the MMA-DEAEMA copolymer dispersion (Kollicoat[®] Smartseal 30 D, BASF, Ludwigshafen, Germany), resulting in a 20 % solid content in the spray suspension and 50 % polymer content in the dried film. The API coated MCC spheres was then spray coated with 15 % w/w polymer layer. Each dispersion layer (APAP and KCSS polymer) was sprayed at atomised air pressure of 1.5 bar via spray nozzle in the fluid bed coater. The resulting MP formulation bead size of the was on average *ca.* $966 \pm 47 \mu\text{m}$, characterised by the optical microscope in Chapter 3, Section 3.3.1. All MP formulations were produced at Pfizer, Sandwich, UK.

4.2.2. Dissolution Solution Media

Unbuffered HCl and buffered simulated saliva (SS) was used to simulate the dissolution response towards digestion in the stomach and within the oral cavity at a common temperature range for both physiological regions and to account for administrative temperatures, thus a temperature range of 20 – 40 °C was used.

Acetate and citrate buffers are commonly used to simulated biological fluids, in particular Simulated Intestinal Fluids (SIF).^{22–24} Acetate buffer solutions up to pH 5.0 were therefore used to represent the ‘middle’ fed state simulated gastric fluid (FeSSGF) and simulated intestinal fluid, specifically the duodenal fluid in the fed state (FeSSIF). For comparison, citrate buffer up to pH 5.0 was also used to represent FeSSIF.^{9,25–29} Furthermore, citric acid is commonly found in foodstuffs and known to cause acidity in the oral cavity.³⁰

The HCl solutions were made by diluting 1.0 M and 0.1 M stock of HCl (37 %, Sigma-Aldrich, UK) to the correct pH within the range 2.0 – 4.0 for a 25 mL solution. Acetate buffer stock (100 mM) was made from glacial acetic acid (Fisher scientific, UK) and sodium acetate anhydrous (Fisher scientific, UK) which was then diluted to a 25 mL solution corresponding to the pH range 3.6 – 5.0. A citrate buffer stock (100 mM) was made from citric acid (Fischer Scientific, UK) and sodium citrate (Sigma-Aldrich, UK), which was then diluted to a 25 mL solution corresponding to the pH range 3.0-5.0. The composition of simulated saliva (SS) used can be found in the study by Sun *et al.*, 2014.³¹ All dissolution media were ‘blanks’ as they were prepared without the addition of enzymes, surfactants or bile salts.

Each of the dissolution media had 0.1 M KCl (Sigma-Aldrich, UK) incorporated to them as supporting electrolyte to maintain a steady ionic environment for dissolution. All solutions were prepared in deionised water (18.2 M Ω cm at 25 °C, Integra HP, Purite, U.K.). The pH of all solutions was measured using pH probe (Mettler Toledo, InLab[®] Expert Pro) connected to pH meter (ultrabasic, Denver Instrument), directly before the first and after the last electrochemical measurement. The pH probe was calibrated using standard buffer solutions of pH 2, 4, 7 and 10 (Traceable to NIST, Fisher scientific, UK).

4.2.3. Electrochemical Materials and Rotating Disc Electrode Instrumentation

Traditional dissolution testing methods (USP apparatus) generally use a rotation rate of up to 150 rpm,³² however for this particular system it was imperative that the beads be suspended in solution, the lowest possible rotation rate to achieve this was 2000 rpm, given the weight of the MP beads which was necessary to suspend the MP into the bulk solution – i.e. to evenly disperse the solids through the dissolution media, as the GI tract is not a static system.³³ This resulted in a trade-off for accuracy of the hydrodynamic rates of dissolution against the level of fouling. RDE measurements were performed on a RDE710 rotating system (Gamry Instruments) at a constant rotation speed of 2000 rpm, connected to potentiostat (CHI 1105A, CHInstruments).

Electrochemical measurements were performed in a 3-neck 50 mL round-bottom flask to ensure a consistent flow of MP in suspension a system controlled by convective diffusion, using a standard three-electrode configuration, Pt counter electrode and a saturated calomel electrode (SCE) as the reference. Before each dissolution and cyclic voltammetry (CV) measurement, the Pt RDE working electrode (5 mm diameter), was polished to a mirror finish with an aqueous alumina slurry (0.05 μm , MicroPolish™, Buehler) against a soft microfiber polishing pad (MicroCloth, Buehler), which was then subsequently on a clean wetted microfiber polishing pad, to produce clean reproducible electrode surfaces. All experimental measurements took place in a temperature-controlled environment. Those measurements for 25 ± 1 °C and above were controlled by placing the round bottom flask in a water bath (Tempette® TE-8A, Techne) with temperature monitored by a glass thermometer.

4.2.4. Rotating Disc Electrode Detection Method of Acetaminophen

To demonstrate the use of the RDE in the analysis of fast dissolution kinetics, the release of APAP from a MP formulation was first measured in HCl solutions between pH 2.0 – 4.0, at temperatures between 20 – 40 °C. The particles studied consisted of a microcrystalline cellulose core coated in APAP and then encapsulated in KCSS with an average thickness of and 32.5 μm and 12.5 μm , respectively. In a typical experiment 100 mg of MP bead particles were loaded into a three-neck round bottom flask along with a Pt RDE, a Pt counter electrode, and an SCE reference electrode (Figure 4.1). Pt was chosen as the RDE material as it showed the least fouling at higher APAP concentrations in preliminary tests (as compared to Au and glassy carbon). Once the RDE was rotating and the desired potential applied, the dissolution media (DM) was added to start the dissolution.

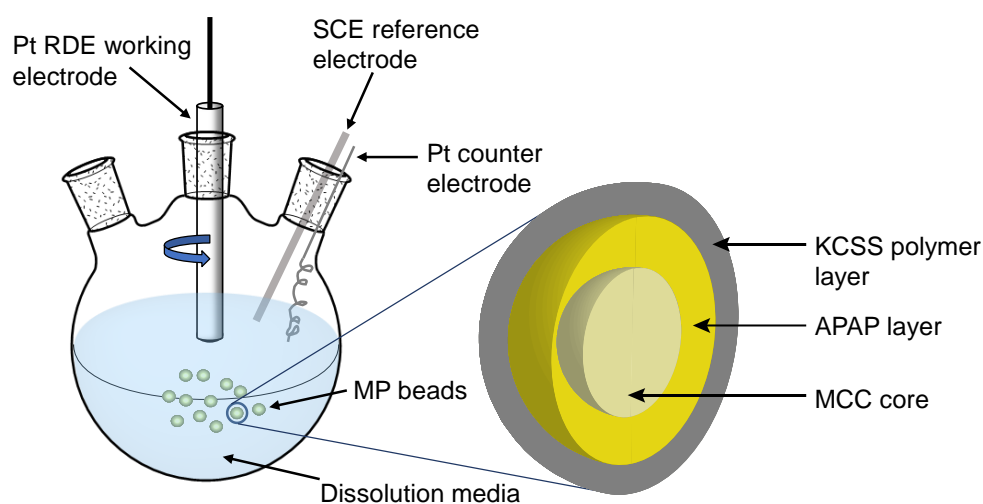


Figure 4.1. Schematic of the rotating disc electrode apparatus to study the varying conditions required to breakdown the Kollicoat[®] Smartseal 30D (KCSS) polymer of the multiparticulate (MP) formulation beads, resulting in the electro-actively traceable dissolution of APAP, zoomed in on the cross-section of a MP bead. (not to scale).

4.3. Results and Discussion

4.3.1. Rotating Disc Electrode Calibration for HCl and Simulated Saliva Dissolution Media

The RDE was held at 1.0 V versus SCE for all experiments, a potential at which APAP oxidation current is mass transport limited at all temperatures and pH values studied (Figure 4.2a). Since current density increases as a function of temperature the steady state (limiting) current density (i_{lim}) was calibrated to the APAP concentration at each experimental condition via a series of calibration measurements in APAP solutions of known concentration (Figure 4.2b and Table 4.1).

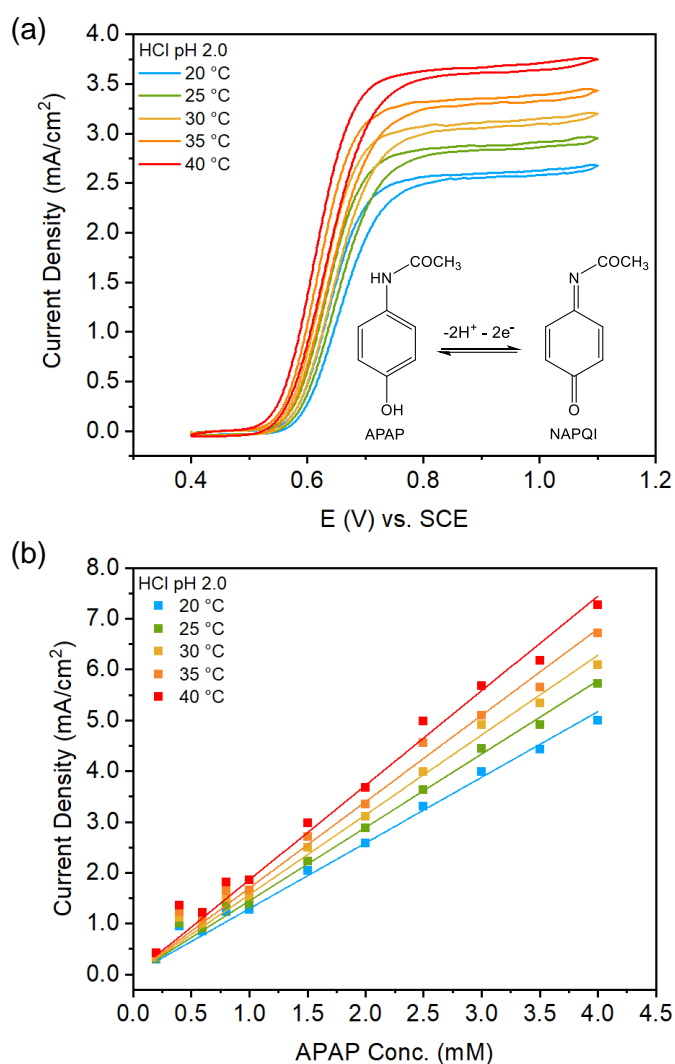


Figure 4.2. (a) Rotating disc cyclic voltammograms of 2.0 mM APAP dissolved in acidic media at temperatures between 20 – 40 °C. (b) Calibration curve using limiting current at 1.0 V as a function of APAP concentration between 20 – 40 °C. Scan rate: 0.1 V/s and solution: HCl pH 2.0 for both (a) and (b).

The calibrations show APAP powder dissolved in the corresponding bulk dissolution media at varying pHs and temperatures, with a response relative to concentration and the calibration found to be linear. Thus, the mass-transport-limited current from the oxidation of APAP can be used to determine APAPs concentration.

Typically, CVs for APAP in (buffered) solutions have shown small electrochemical shifts to the negative potentials with increasing pH, indicating proton involvement in the oxidation of APAP.^{4,5,34} However, these experiments occur within the steady state and all at a relatively low pH, therefore altering the pH within this acidic range at a fixed temperature (30 °C) shows minimal shifts in peak potential. This is observed in Figure 4.3, where similar CV responses are observed for different pHs. It should be noted that pHs above 3.5 had a different calibration range, focusing on the lower concentrations and therefore the calibration current density values for APAP concentration 0.2 mM were taken and scaled 10x for comparison to pH 2.0 – 3.0 at APAP concentration 2.0 mM, this is reflected in Figure 4.3, where pH 3.5 and 4.0 have a less pronounced sigmoidal shape due to the lower concentration of APAP used. Furthermore, the current density range for pH 2.0 – 4.0 is 3.1 – 3.5 mA/cm² at i_{lim} , showing a difference of 0.4 mA/cm² overall between the pH range.

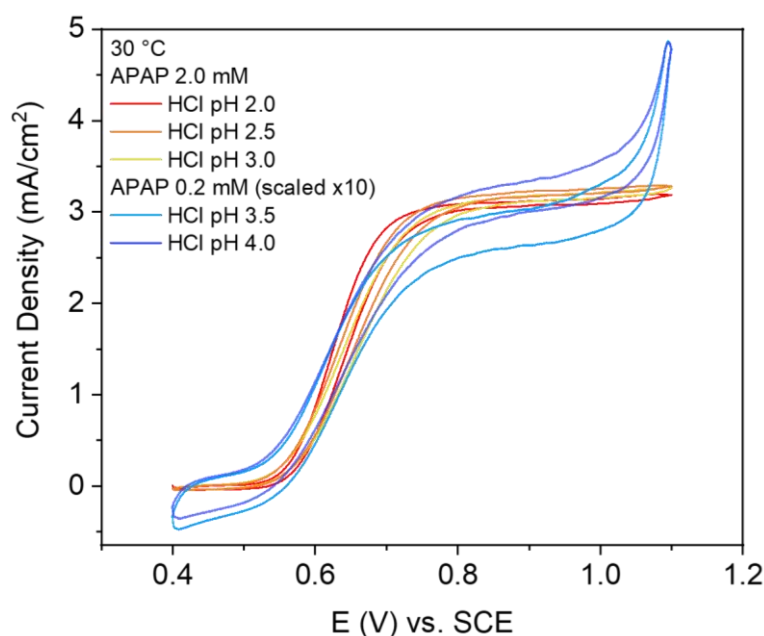


Figure 4.3. Rotating disc cyclic voltammograms of APAP dissolved in acidic DM at 30 °C, where APAP concentration in HCl DM solution was 2.0 mM and 0.2 mM for pH 2.0 – 3.0, and pH 3.5 and 4.0 respectively, where the latter has been scaled x10, to lie on the same scale for 2.0 mM APAP at. Scan rate of 0.1 V/s. Limiting current at 1.0 V.

These calibration curves show the effect of dissolved APAP powder in each DM, the peak steady state i_{lim} for pH 3.5 and 4, suggests a holding potential of slightly less than 1.0 V, *ca.* 0.95 V should be used. However, to ensure correct peak potentials were chosen for all pHs and temperatures based on real samples, extensive preliminary testing was carried out using the MP beads under the DM conditions that were used in the final experiments to test the limiting currents between 0.9 and 1.0 V. This ultimately showed that the i_{lim} of 1.0 V was the most appropriate potential across these pHs.

Table 4.1. Calibration slopes for acidic (HCl, pH 2.0 – 4.0) and simulated saliva (pH 6.8) dissolution media.

pH	Temp. (°C)	Slope	R ²	pH	Temp. (°C)	Slope	R ²
2.0	20	1.293	0.997	3.5	20	1.694	0.989
	25	1.446	0.998		25	1.839	0.989
	30	1.571	0.997		30	2.021	0.991
	35	1.700	0.996		35	2.163	0.992
	40	1.861	0.996		40	2.355	0.993
2.5	20	1.294	0.997	4.0	20	1.530	0.983
	25	1.438	0.997		25	1.669	0.986
	30	1.585	0.997		30	1.807	0.986
	35	1.728	0.997		35	1.967	0.987
	40	1.894	0.997		40	2.131	0.989
3.0	20	1.268	0.999	6.8	20	1.875	0.984
	25	1.399	0.999		25	2.082	0.975
	30	1.538	0.999		30	2.308	0.972
	35	1.673	0.999		35	2.524	0.970
	40	1.821	0.998		40	2.750	0.982

4.3.2. Effect of pH and Temperature on Dissolution in HCl Media

A similar amperometric response was observed during dissolution at all pH values up to and including pH 3.0 (Figure 4.4, showing average of 3 repeats). An initial spike at time, $t = 0$ s is observed, corresponding to the addition of the DM and the start of the dissolution measurement, followed by a rapid decay to a short-lived steady state with a pH-dependent lifetime, before then rising exponentially to a peak (i_p) and then decaying.

The rise in current corresponds to an increased rate of APAP oxidation at the electrode, as protonation of the tertiary amine group of the encapsulating KCSS polymer causes rapid dissolution and release of APAP (the mechanism of this occurrence is discussed in Chapter 5).^{4,19,35–38} The subsequent fall in current is attributed to fouling of the electrode via adsorption of APAP oxidation products.³⁹ This was confirmed by removing the RDE, polishing it to expose fresh electrode surface and replacing it in the solution. Subsequent cyclic voltammetry revealed limiting currents in excess of the original peak current (denoted by the 'x' end point in Figure 4.5), confirming the current decrease was not due to a decrease in APAP concentration. From the similar currents measured by post-dissolution cyclic voltammetry following experiments at pH values up to and including pH 3.0, at temperatures between 20 °C and 40 °C, it can be determined that complete APAP dissolution occurred in each case. The extent of fouling increased considerably from pH 2.0 to pH 3.0, but only slightly with increasing temperature (Figure 4.6).

At pH 3.5 and above there is a dramatic difference in the current response, with an order of magnitude lower current density, and no discernible peak or decay in current on the timescale of the measurement (Figure 4.5). Cyclic voltammetry after removing and polishing the electrode reveal some dissolution had occurred past the peak as shown by the difference of peak height, i_p (colour coded triangle) and the 'end point' from i_{lim} of the CV (shown on the $i-t$ curve as a colour coded 'x') for pHs 2.0 – 3.0. With increasing pH, the difference between the peak height and end point becomes greater, consistent with increasing fouling effect with increasing pH as shown in Figure 4.6.

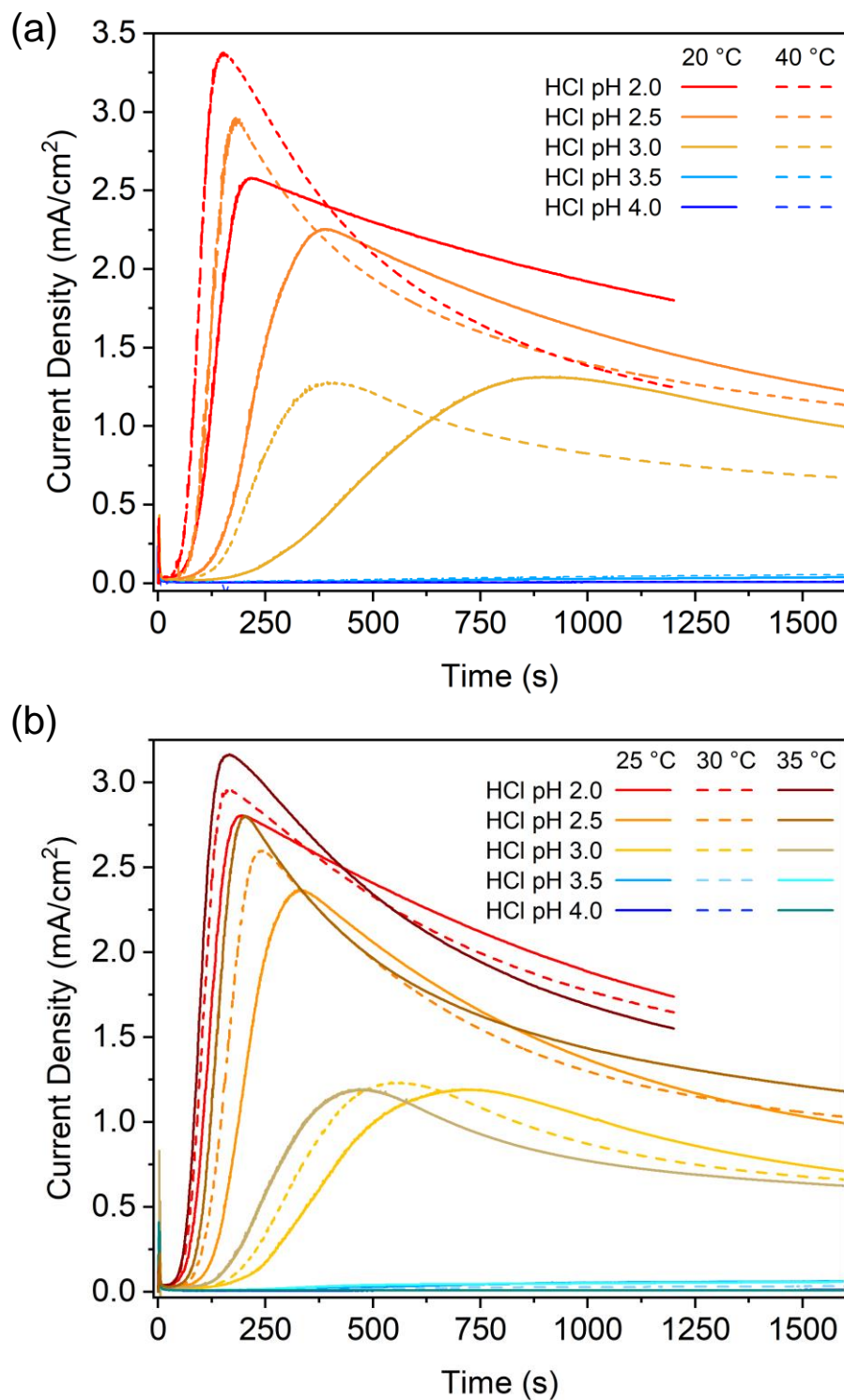


Figure 4.4. Averaged amperometric release profiles (*i-t* curves) of APAPs dissolution ($N=3$) from 100 mg of MP beads in real-time at a fixed potential based on the limiting current (1.0 V), measured by current density (mA/cm²) shown in (a) HCl DM at temperatures 20 °C (solid line) and 40 °C (dotted line), (b) HCl DM at temperatures 25 °C (solid line), 30 °C (dotted line), and 35 °C (solid line of alternate shades).

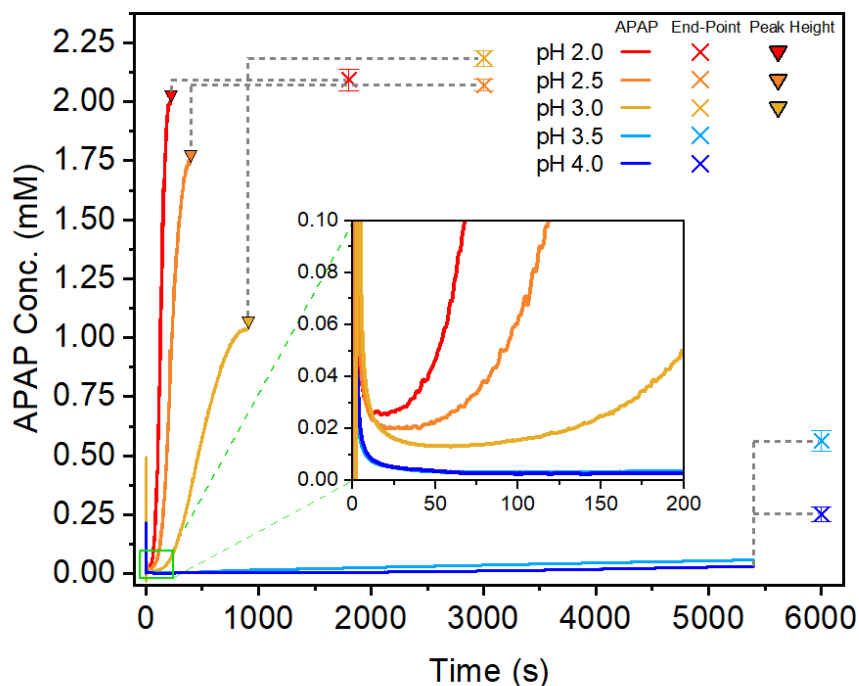


Figure 4.5. Averaged amperometric release profiles (i - t curves) of APAPs dissolution ($N=3$) from 100 mg of MP beads in real-time at a fixed potential based on the limiting current (1.0 V), shown by the calculated APAP concentration (mM) at HCl DM pH range 2.0 – 4.0. Inset: Zoom from time 0 – 200 s at 20 °C.

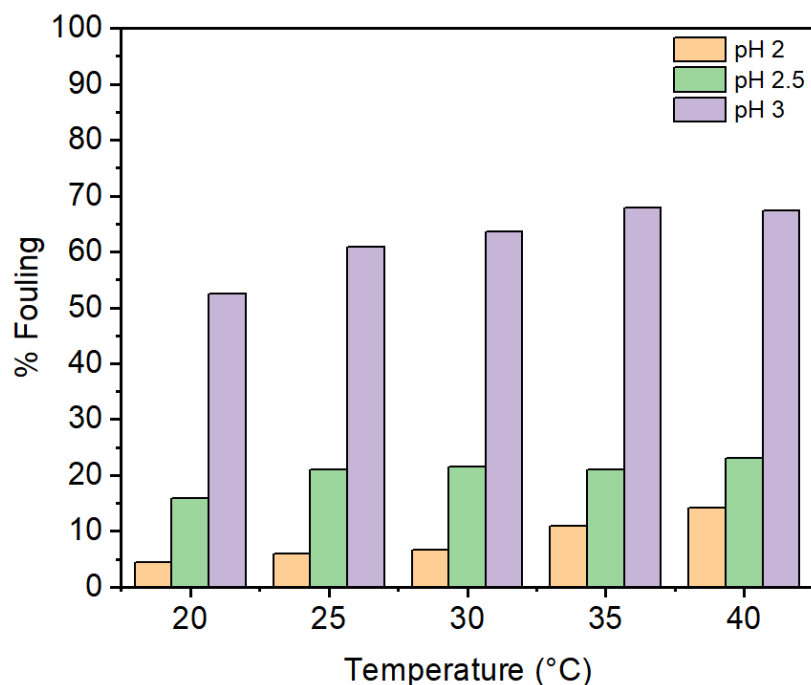


Figure 4.6. Fouling effect of acidic dissolution media (pH 2.0 – 3.0) at temperature (20 – 40 °C) on the Pt RDE surface, comparing the percentage change from the current density (mA/cm^2) at the peak height of the i - t curve and the limiting current density of the CV in the bulk solution post cleaning of Pt electrode surface. The % fouling is shown as $100 \times (i_{\text{lim}} - i_p)/i_{\text{lim}}$.

Following preliminary measurements (*i-t* curves) the dissolution experiments reported were stopped a minimum of *ca.* 10 minutes after the current peak. Taste masking guidelines suggest that less than 10 % dissolution should occur in 5 minutes in a neutral medium. Taste masking is achieved when the release of the API is minimal (and below the bitterness threshold of the oral cavity).⁴⁰

The final current densities, measured after polishing the electrode and therefore free of fouling effects, can be converted into APAP concentrations using the calibration curves introduced above (Figure 4.2b and Table 4.1) to illustrate the pH and temperature dependence of the dissolution (Figure 4.7), the current density values calculated from i_{lim} and the corresponding APAP concentration values are shown in Table 4.2. On the timescale of the final measurement, dissolution at $pH \leq 3.0$ is rapid but decreases significantly with increasing pH.

A two-way analysis of variance (ANOVA) statistical test was conducted to examine the effects of pH and temperature on the average APAP concentration post dissolution. There was a statistically significant interaction between the effects of pH and temperature on the average concentration of APAP, [$F(16, 50) = 2.57, p = 0.006$].

A Tukey post-hoc means of comparison analysis test was conducted. Between pH 2.0 and 2.5 for all temperatures there was no significant difference. Additionally, elevated temperatures of 35 and 40 °C showed no significant difference between pHs 2.0, 2.5 and 3.0. Normality checks and Levene's test were carried out and the assumptions were met. These pH and temperatures with no significant differences have been denoted in Figure 4.7 with a red line, and those with significant differences are not labelled. A significant difference was observed for all other pHs at all other temperatures ($p < 0.05$).

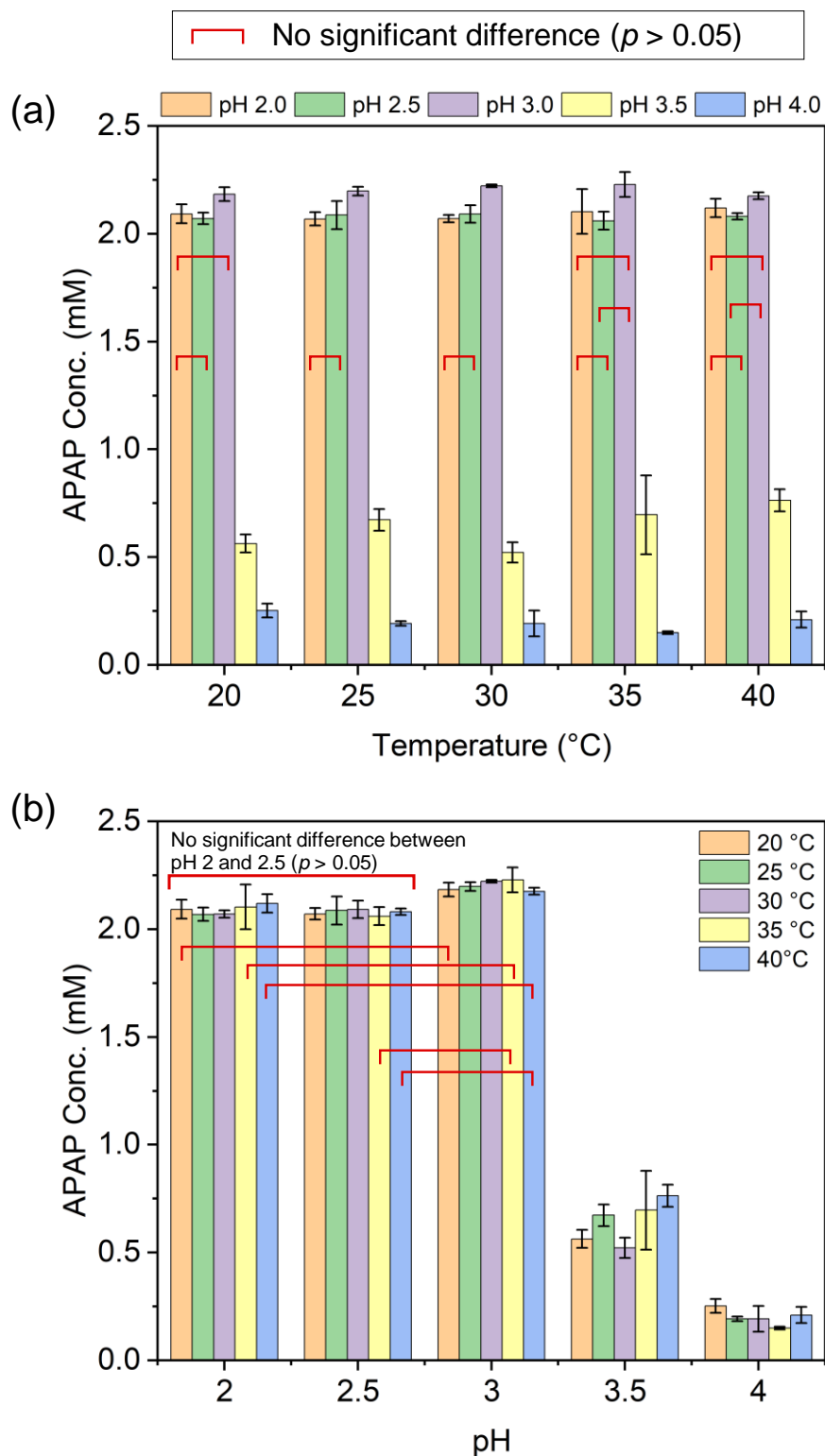


Figure 4.7. Average APAP concentration values after the averaged dissolution release profile from the MP beads where $N=3$, calculated with error bars from the limiting current density (i_{lim}) of cyclic voltammogram (at 1.0 V) after cleaning of the Pt WE, for (a) APAP conc. vs. temperatures 20 °C – 40 °C at different pHs, and (b) APAP conc. vs. pH range 2.0 – 4.0 at different temperatures. Those with no significant difference for a significance level of $\alpha = 0.05$ between given pHs and temperatures have been labelled with a red line.

Table 4.2. Average current density and APAP concentration values at 1.0 V corresponding to i_{lim} for HCl DM for pH 2.0 – 4.0 and SS at pH 6.8 at temperatures 20 – 40 °C.

pH	Temp. (°C)	Current Density (mA/cm ²)	Current Density (SD) (mA/cm ²)	APAP Conc. (mM)	APAP Conc. (SD) (mM)
2.0	20	2.7	0.1	2.1	0.04
	25	3.0	0.04	2.1	0.03
	30	3.3	0.03	2.1	0.02
	35	3.6	0.2	2.1	0.1
	40	3.9	0.1	2.1	0.04
2.5	20	2.7	0.03	2.1	0.03
	25	3.0	0.1	2.1	0.1
	30	3.3	0.1	2.1	0.04
	35	3.6	0.1	2.1	0.04
	40	3.9	0.03	2.1	0.02
3.0	20	2.8	0.04	2.2	0.03
	25	3.1	0.03	2.2	0.02
	30	3.5	0.01	2.2	0.01
	35	3.8	0.1	2.2	0.1
	40	4.0	0.03	2.2	0.02
3.5	20	1.0	0.1	0.6	0.04
	25	1.2	0.1	0.7	0.1
	30	1.1	0.1	0.5	0.1
	35	1.6	0.4	0.7	0.2
	40	1.8	0.1	0.8	0.1
4.0	20	0.4	0.1	0.3	0.03
	25	0.3	0.02	0.2	0.01
	30	0.3	0.1	0.2	0.1
	35	0.3	0.01	0.2	0.01
	40	0.4	0.1	0.2	0.04
6.8	20	0.7	0.1	0.4	0.03
	25	0.7	0.5	0.3	0.3
	30	0.9	0.2	0.4	0.1
	35	0.7	0.03	0.3	0.01
	40	0.5	0.03	0.2	0.01

4.3.3. Dissolution Rate in HCl and Simulated Saliva Media

More insight can be gained by taking advantage of the high time resolution intrinsic to the electrochemical methodology, and examining the current during the initial dissolution period, which conventional dissolution measurements would fail to capture. In this region minimal release has occurred so fouling is absent, and the current can accurately report on the solution concentration.

Here a breakthrough time, τ , is defined by the time taken for the measured APAP concentration to reach 50 μM (for pH 2.0 – 3.0) or 5 μM of APAP (for pH \geq 3.5 where polymer dissolution is much slower). These values were chosen to be a minimum level above the background that could be detected, and are small values compared to the concentration that could be attained if the full amount of APAP available were released. This shows in detail the pH dependence of the dissolution rate, which decreases significantly with increasing pH and becomes negligible by pH 3.5. This trend corresponds to the slower dissolution of the polymer, as demonstrated previously by drug release of similar pH-dependent polymers.⁴¹ This contrasts with the reported solubility below pH 5.5 as the obtained data shows that the polymer is not sufficiently soluble for API release to occur in simulated gastric fluid above pH 4.0.^{42,43} To gain further insight into the dissolution kinetics, the temperature dependence of the dissolution rate was measured. The transients at higher temperature show a similar shape to that observed at lower temperature but with a faster rise in current density (and APAP concentration) and a faster subsequent decay due to fouling (Figures 4.8 and 4.9). The breakthrough rate (τ^{-1}) was analysed using the Arrhenius equation,^{17,19,44}

$$\ln \frac{1}{\tau} = \ln A - \left(\frac{E_a}{RT} \right) \quad (4.1)$$

where A is the pre-exponential factor, E_a is the activation energy, R is the gas constant equal to 8.314 J/(mol K) and T is the temperature in kelvin (Figure 4.10a).

Note that due to the wide variation in dissolution rate, breakthrough times at pH 3.5 and in pH 6.8 for HCl and SS (*vide infra*), respectively, were calculated based on reaching an APAP concentration an order of magnitude lower (5 μM threshold) than that of the more acidic pHs (50 μM threshold). The derived activation energies are strongly pH dependent, increasing from 7 kJ/mol at pH 2.0 to 22 kJ/mol at pH 3.5

(Figure 4.10b, Table 4.3), consistent with the decrease in rate of APAP release as pH increases. The relatively low values of E_a for dissolution between pH 2.0 – 3.0 are indicative of solution diffusion control,¹⁹ while the larger values of E_a at higher pH values indicate that a different process begins to control the dissolution rate, such as the swelling and subsequent dissolution of the polymer coating. The gradual increase in E_a with pH suggests two (or more) processes contribute to the rate-determining step, and their relative importance shifts with pH. This is consistent with the literature where protonation of tertiary amine groups leads to swelling of the polymer, resulting in the expansion of the polymeric chains due to electrostatic repulsion and release of APAP into the dissolution medium (the mechanism of this process is discussed in further detail in Chapter 5).^{45–47}

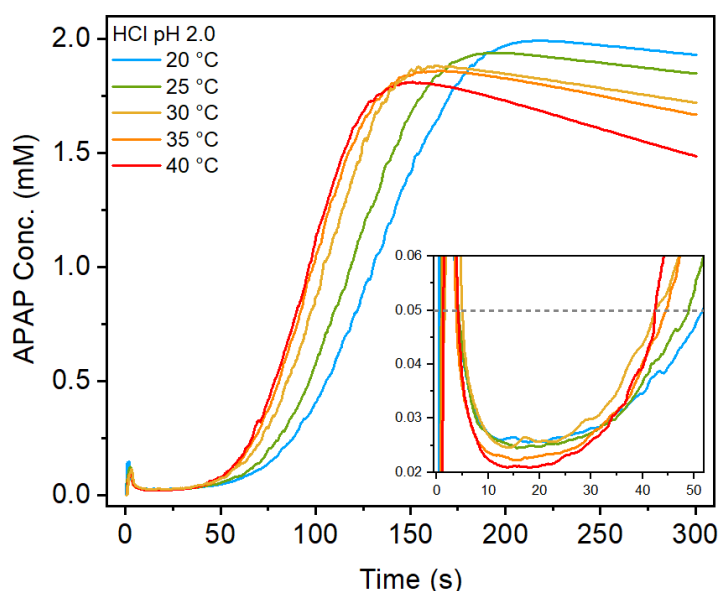


Figure 4.8. Amperometric release profile ($i-t$ curve) up to 300s in real-time of APAP release from 100 mg of MP beads in HCl dissolution media at pH 2.0, at a fixed potential based on the limiting current (1.0 V), shown in APAP concentration (mM) at increasing temperatures. Inset: Zoom from time 0 – 50 s, where the grey dotted line denotes the breakthrough time, τ . Note the apparent decrease in concentration at later times is due to a decrease in current due to fouling and does not represent a decrease in APAP concentration.

It should be noted that there is an offset in the APAP concentration relative to the pH shown in Figures 4.8 and 4.9. This is attributed to the varying rate of fouling of the electrode *vide supra* (Figure 4.6) and is not indicative of a decrease in concentration. The concentration level in the resultant bulk solution is confirmed by the subsequent CV with a polished electrode upon completion of the $i-t$ curve (Figure 4.7).

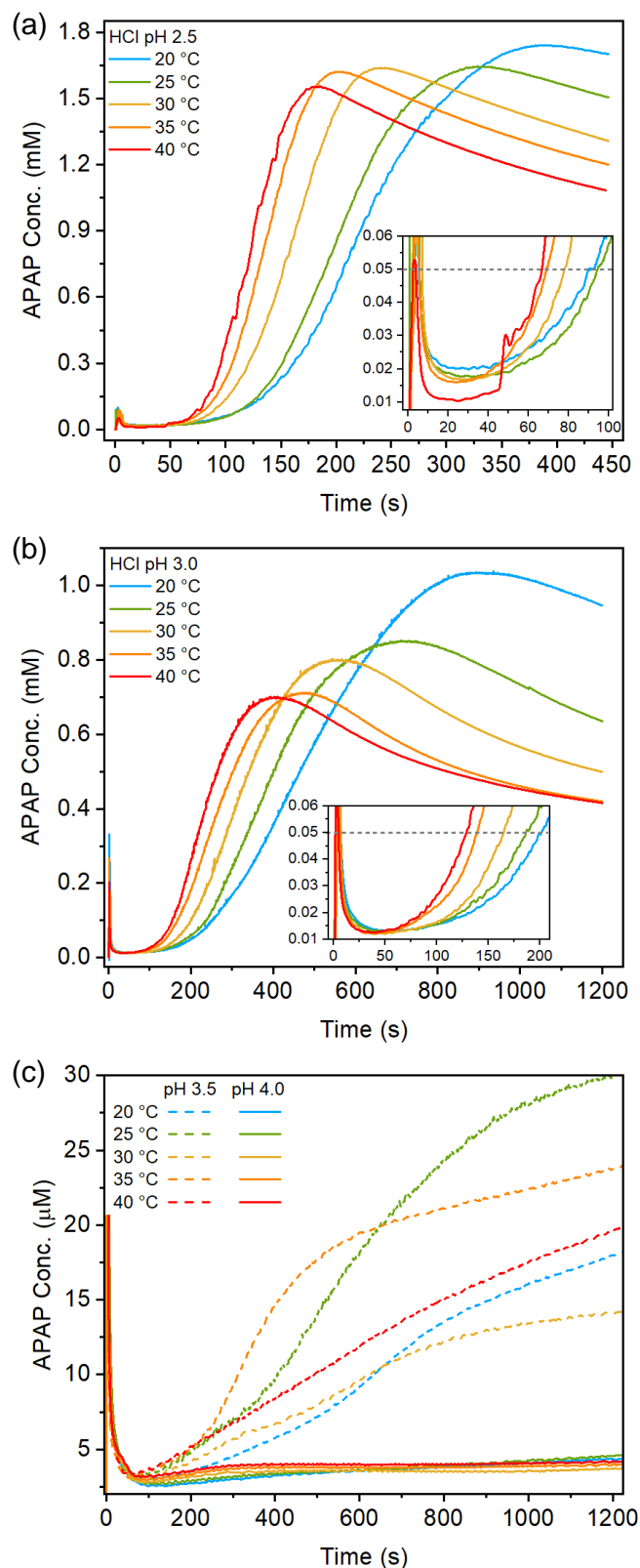


Figure 4.9. Amperometric release profile (i - t curve) up to 300s in real-time of APAP release from 100 mg of MP beads in HCl dissolution media, at a fixed potential based on the limiting current (1.0 V) shown in APAP concentration (mM) at increasing temperatures at (a) pH 2.5, (b) pH 3.0, and (c) pH 3.5 and 4.0 at APAP concentration (μ M). Inset for a) and b) indicates the zoom the breakthrough time, τ , with the grey dotted line.

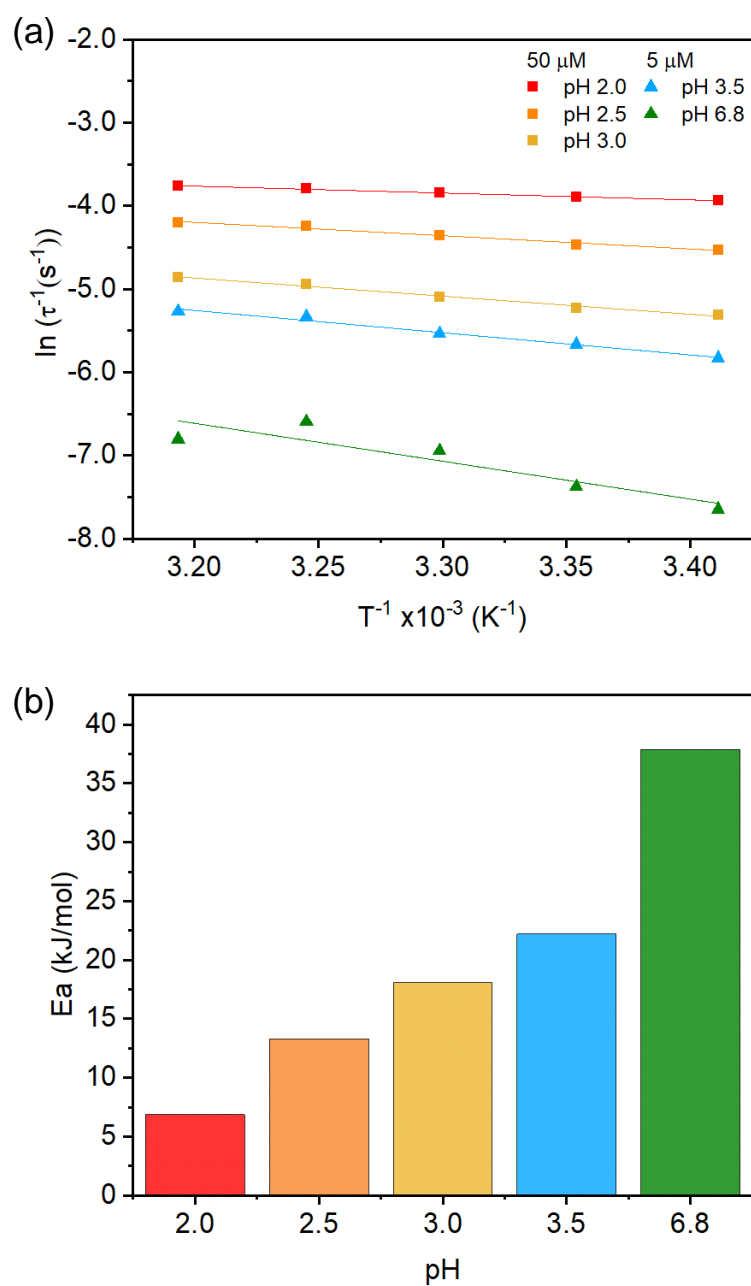


Figure 4.10. (a) Arrhenius plots showing the rate of dissolution of APAP for pH 2.0 – 3.0 at 0.05 mM and pH 3.5 and 6.8 (SS) at 0.005 mM, where τ is 1/time (s) vs. temperature (T) in K. The slope is $-E_a/R$ from the Arrhenius equation. (b) Activation energies (E_a) in kJ/mol for calculated at 50 μM and 5 μM for pH 2.0 – 3.0 and pH 3.5 and 6.8 (SS) respectively.

Table 4.3. The corresponding linear slopes to the Arrhenius plots for HCl dissolution media at pH 2, 2.5, 3, 3.5 and 6.8. pH 2.0 – 2.5 calculated at concentrations 50 – 750 μM , pH 3 at 50 – 500 μM and pH 3.5 and pH 6.8 calculated at 5 μM . The slope (m) is $-E_a/R$ from the Arrhenius equation.

pH	APAP Conc. (μM)	Slope	R ²	E _a (kJ/mol)
2	50	-826.56 \pm 41.24	0.993	6.9
	75	-1124.10 \pm 128.96	0.962	9.4
	100	-1173.39 \pm 71.45	0.989	9.8
	150	-1273.81 \pm 159.55	0.955	10.6
	200	-1228.67 \pm 138.78	0.963	10.2
	250	-1434.70 \pm 92.86	0.988	11.9
	500	-1495.97 \pm 90.39	0.989	12.4
	750	-1305.61 \pm 113.46	0.978	10.9
2.5	50	-1598.57 \pm 140.84	0.977	13.3
	75	-2018.52 \pm 234.86	0.961	16.8
	100	-2149.99 \pm 342.84	0.929	17.9
	150	-2369.40 \pm 273.65	0.962	19.7
	200	-2406.83 \pm 261.41	0.966	20.0
	250	-2461.94 \pm 207.69	0.979	20.5
	500	-2636.45 \pm 101.08	0.996	21.9
	750	-2666.66 \pm 201.94	0.983	22.2
3	50	-2174.69 \pm 153.26	0.985	18.1
	75	-2379.29 \pm 222.09	0.975	19.8
	100	-2433.05 \pm 235.15	0.973	20.2
	150	-2461.78 \pm 152.48	0.989	20.5
	200	-2601.69 \pm 92.60	0.996	21.6
	250	-2690.50 \pm 80.49	0.997	22.4
	500	-2569.60 \pm 53.18	0.999	21.4
3.5	5	-2672.25 \pm 183.56	0.986	22.2
6.8	5	-4555.25 \pm 1175.11	0.834	37.9

The RDE method has been used to confirm the pH-dependent solubility of KCSS in HCl solutions. The fast time resolution enables facile measurement of the dissolution kinetics at elevated temperature, and subsequent extraction of the apparent activation energy. This also suggests that temperature in particular of the food or liquid carrier may have an effect on the polymer taste masking ability, as there is the possibility that there is some degree of protonation of the tertiary amine group of the KCSS polymer, then some of the API may have been released and can be detected in the carrier itself. Interestingly the APAP release rate is shown to drop significantly above pH 3.0, with a concomitant increase in activation energy, in contrast to the reported solubility up to pH 5.5.^{42,43} Given the significance of this pH range *in vivo*, where solutions are naturally buffered, the origin of the pH-dependence was explored further in pH-buffered dissolution media.

4.3.4. Rotating Disc Electrode Calibration for Acetate and Citrate Buffer Dissolution Media

To investigate the effect of buffers on dissolution, the limiting current density was also calibrated to APAP concentration (Section 4.3.1) under the relevant buffer conditions. Typical calibration plots are shown in Figure 4.11 and calibration data are in Table 4.4.

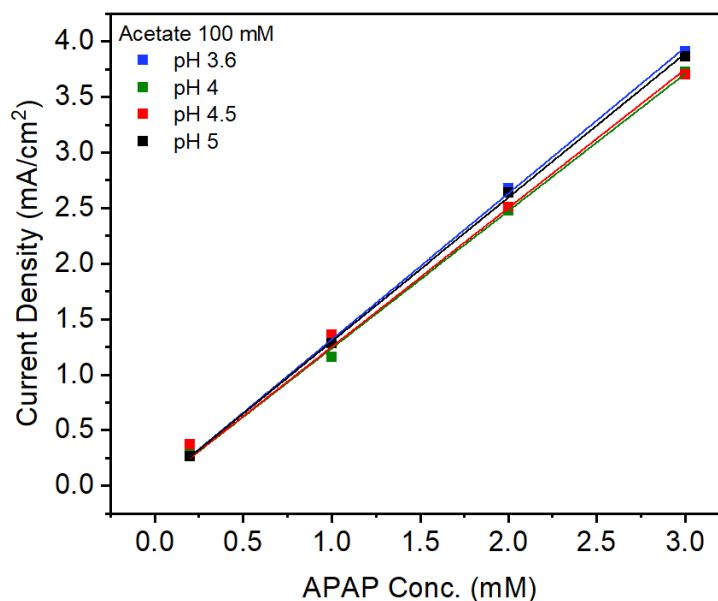


Figure 4.11. Example calibration curve for APAP (powder) dissolved in dissolution media 100 mM acetate buffer, for pH range 3.6 – 5.0, at limiting current 1.0 V.

Table 4.4. Calibration slopes for dissolution media acetate and citrate buffers pH 3.6 – 5.0 and pH 3 – 5.0 respectively at concentrations 25 mM and 100 mM.

Buffer	pH	Slope	R ²	Buffer	pH	Slope	R ²
Acetate 25 mM				Citrate 25 mM	3.0	1.248	0.995
	3.6	1.235	1.000		3.6	1.273	0.998
	4.0	1.234	0.994		4.0	1.310	0.999
	4.5	1.283	0.999		4.5	1.381	0.994
	5.0	1.284	0.998		5.0	1.258	0.999
Acetate 100 mM				Citrate 100 mM	3.0	1.249	0.999
	3.6	1.315	1.000		3.6	1.227	1.000
	4.0	1.236	1.000		4.0	1.225	0.997
	4.5	1.250	0.999		4.5	1.238	0.998
	5.0	1.297	1.000		5.0	1.185	1.000

4.3.5. Effect of Acetate, Citrate and Simulated Saliva Buffered Media on Dissolution

Many physiological fluids in the gastrointestinal tract are buffered, thus it is important to also study MP formulation dissolution in model buffered systems. Both acetate and citrate buffers are commonly used to simulated biological fluids with pH values of ≤ 5.0 , such as the fed state of intestinal fluids.^{22–24} Acetic acid has a pK_a of 4.76 at 25 °C (and 37 °C), and citric acid (a triprotic acid) has a similar pK_{a2} of 4.76 at 25 °C (4.75 at 37 °C).²²

RDE dissolution experiments were carried out over the useful pH range of each buffer, at both 25 mM and 100 mM buffer concentrations (Figure 4.12). Similar features to that seen from dissolution in HCl at pH ≤ 3.0 were observed at all pH values studied, with a pH-dependent steady state region, followed by a rapid rise in current and then a decay. Subsequent CV measurement of the APAP concentration with a polished electrode revealed that all cases showed *ca.* 2 mM APAP concentration values post dissolution (Table 4.5). A similar response is also observed for the HCl dissolution media.

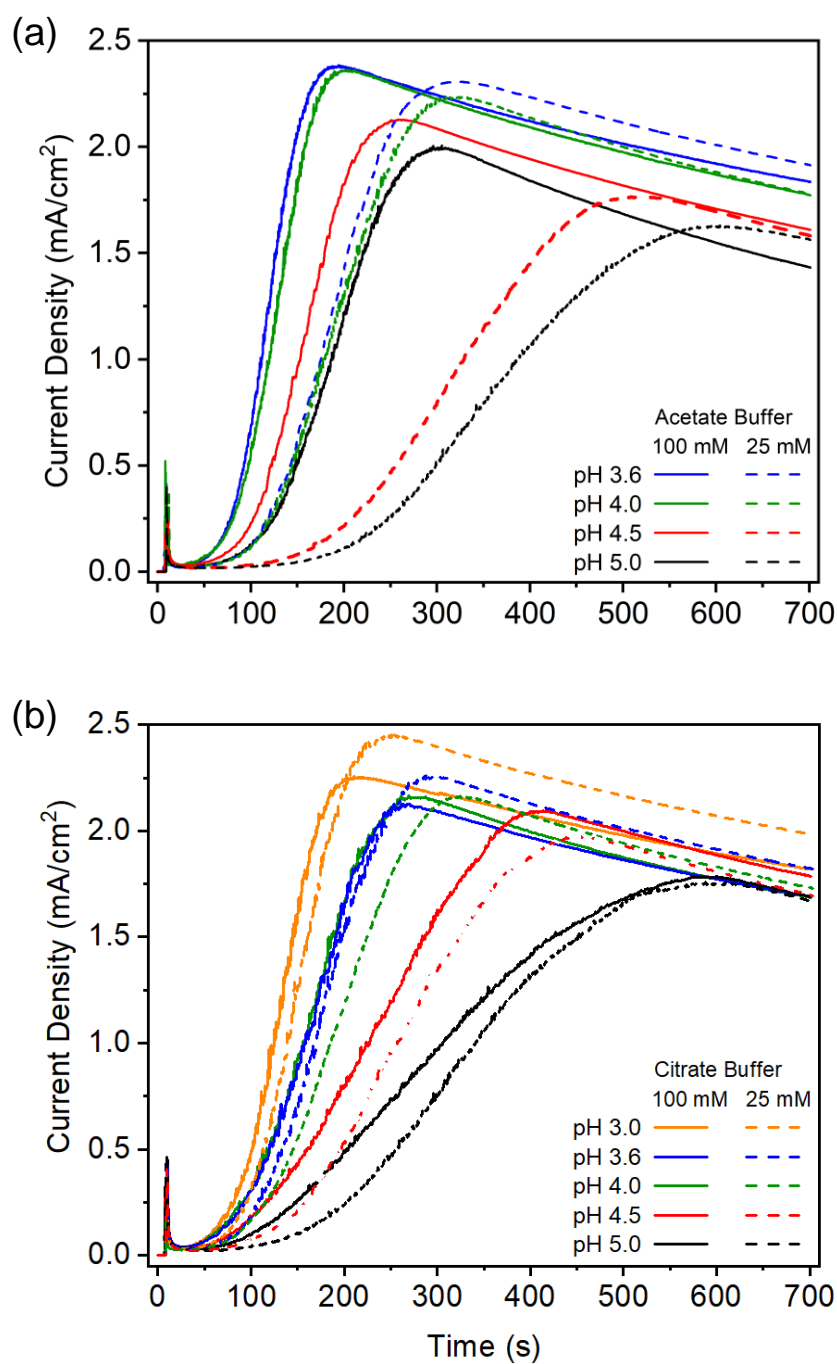


Figure 4.12. Averaged amperometric release profiles ($i-t$ curve) across APAP dissolutions ($N=3$) from 100 mg of MP beads, at a fixed potential based on the limiting current (1.0 V), in (a) acetate buffer and (b) citrate buffer dissolution media at pH range 3.0 – 5.0 measured by current density (mA/cm^2) at buffer concentrations of 25 mM (dotted line) and 100 mM (solid line).

Table 4.5. Average current density and APAP concentration values at 1.0 V corresponding to i_{lim} for acetate and citrate buffer DM for pH 3.6 – 5 and pH 3.0 – 5.0, respectively.

Buffer	pH	Current Density (mA/cm ²)	Current Density (SD) (mA/cm ²)	APAP Conc. (mM)	APAP Conc. (SD) (mM)
Acetate 25 mM	3.6	3.1	0.2	2.5	0.1
	4.0	2.9	0.1	2.3	0.04
	4.5	2.9	0.04	2.2	0.03
	5.0	3.1	0.1	2.4	0.1
Acetate 100 mM	3.6	2.9	0.1	2.2	0.04
	4.0	2.8	0.1	2.2	0.1
	4.5	2.8	0.2	2.2	0.2
	5.0	2.9	0.00	2.3	0.00
Citrate 25 mM	3.0	3.0	0.03	2.4	0.03
	3.6	3.0	0.2	2.4	0.1
	4.0	2.9	0.1	2.2	0.1
	4.5	2.9	0.01	2.1	0.01
	5.0	2.8	0.1	2.3	0.1
Citrate 100 mM	3.0	2.7	0.04	2.2	0.03
	3.6	2.8	0.1	2.3	0.1
	4.0	2.8	0.1	2.3	0.1
	4.5	2.9	0.1	2.3	0.04
	5.0	2.8	0.1	2.4	0.1

From Figure 4.13, the fouling percentage for buffered DM has a general increase as the pH increases, following the trend observed for the HCl DM (Figure 4.6). The levels of fouling for all buffered media are less than the fouling levels observed for HCl pH 3.0. This suggests that the overall fouling levels for buffered media are less than those for unbuffered, however, there is a caveat as the buffered pHs had shorter dissolution times. In which case, HCl DM at pH 2.0, has a similar dissolution timescale to the buffered media, which shows that during a short period of time buffers can cause a higher level of fouling compared to unbuffered media at pH 2.0. There also does not seem to be any particular pattern between the concentration of the buffers and the percentage of fouling.

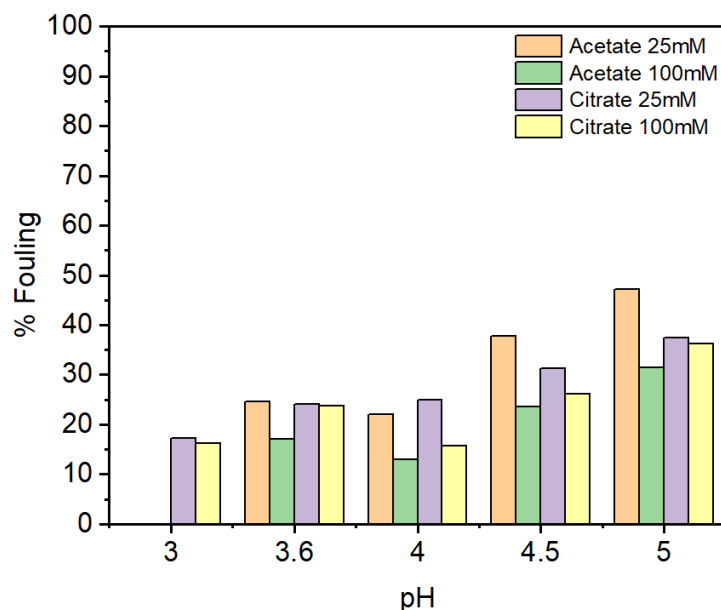


Figure 4.13. Fouling effect of buffered dissolution media (acetate and citrate) at concentration levels 25 and 100 mM on the Pt RDE surface, comparing the percentage change from the current density (mA/cm^2) at the peak height of the i - t curve and the limiting current density of the CV in the bulk solution post cleaning of Pt electrode surface. The % fouling is shown as $100 \times (i_{\text{lim}} - i_p)/i_{\text{lim}}$.

Measurements were also carried out in SS (pH 6.8), which showed a much longer steady state period and a much slower increase in current which did not reach a peak on the timescale of the measurement (Figure 4.14). This is consistent with the large activation energy measured for dissolution in SS, *vide supra* (Section 4.3.3). Significantly, the measurements reveal that dissolution occurs at pH values up to 5.0 in the presence of buffers, but does not occur at pH values above 3.5 for HCl DM.

The dissolution of APAP in the SS DM at pH 6.8, is seemingly negligible with the release of APAP equating to a concentration range of *ca.* 0.2 – 0.4 mM with an average of 0.31 ± 0.08 mM for temperatures 20 – 40 °C after a period of 90 minutes. Furthermore, the breakthrough rate, τ^{-1} , in buffered pH 5.0 solution is comparable to the fastest times in HCl at pH 2.0.

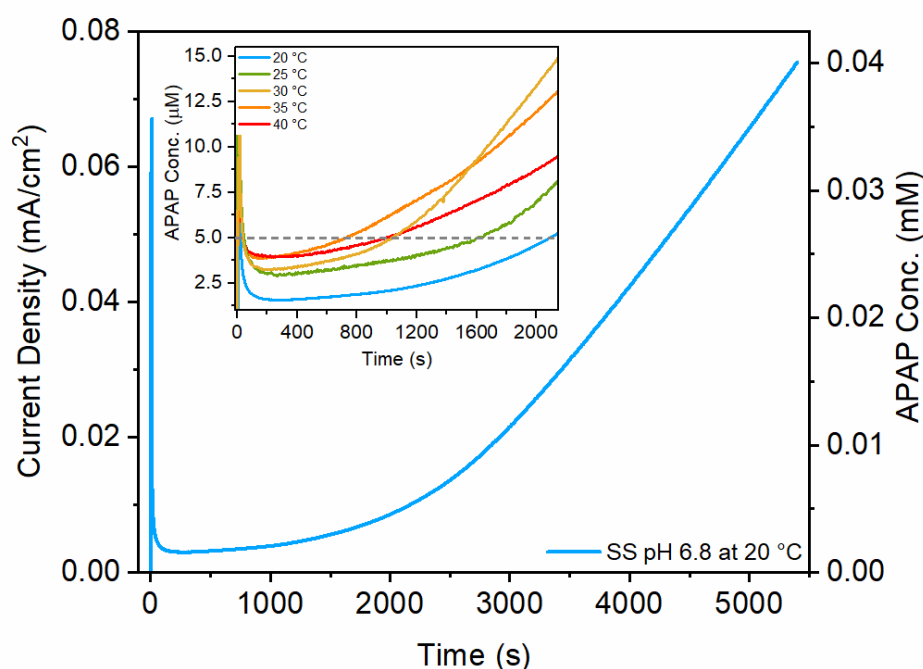


Figure 4.14. Averaged amperometric release profiles (i - t curve) across APAP dissolutions ($N=3$) from 100 mg of MP beads at a fixed potential based on the limiting current (1.0 V), measured by current density (mA/cm^2) and calculated APAP concentration values for SS DM at 6.8 at temperature 20 °C. Inset: zoom on first 2100 s of dissolution for temperatures 20 – 40 °C.

These results can be understood with reference to the mechanism of APAP release, which involves the polymer consuming free H^+ as the tertiary amine group becomes protonated. The electrostatic repulsion between the like-charged polymer chains causes swelling which subsequently facilitates the dissolution of the polymer coating, exposing the APAP layer to the dissolution media.^{45–47} The consumption of H^+ raises the local pH and leads to dissolution being limited by the rate of diffusion of H^+ to the polymer surface.

These buffer effects correlate to a similar trend in the literature for various KCSS polymer coated caffeine tablets, pellets and crystals under standard USP dissolution testing methods via HPLC analysis in biorelevant media FeSSIF at pH 5.8,⁴⁸ thus corroborating the trends elucidated are due to the protonation interaction of the KCSS polymer from the surrounding buffer media. This therefore confirms that KCSS can be protonated at pH 5.5 and below depending on the media being in the buffered state.

4.3.5.1. Experimental Buffering Effects on Dissolution Rates

In contrast to unbuffered solutions, buffer solutions of the equivalent pH have a high concentration of undissociated buffer at the surface which provides a reserve of H^+ via dissociation (Equation 4.2).³⁸



Thus, while the proton concentration at moderate pH can be substantially perturbed in unbuffered media, limiting the rate of dissolution, the concentration is maintained in the presence of buffers enabling continuing protonation, and therefore dissolution, of the polymer, and rapid exposure of the underlying APAP. The dissolution rate and its order with respect to H^+ concentration was analysed using log-log plots (Figure 4.15 and Table 4.6.)

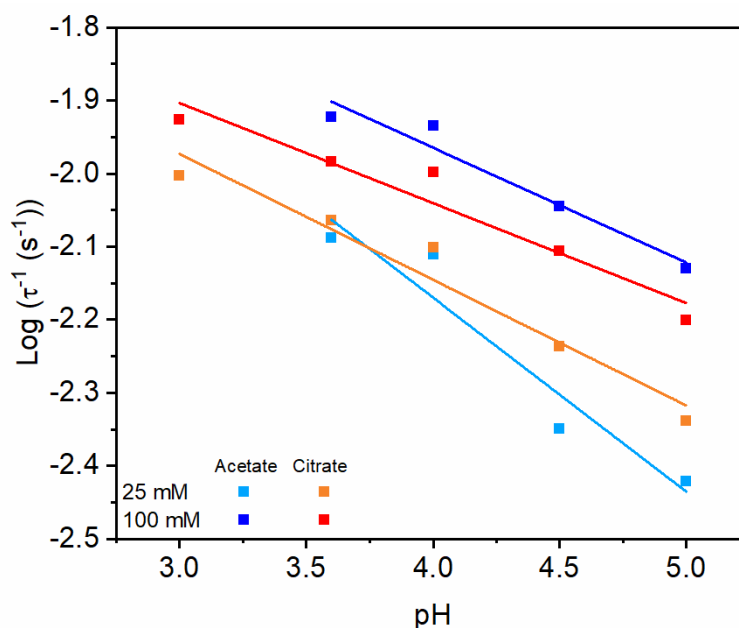


Figure 4.15. Rate plot of APAP dissolution at pH 3.6 – 5.0 and pH 3.0 – 5.0 for acetate and citrate buffers respectively at buffer concentrations of 25 and 100 mM. Calculated at an APAP concentration of 0.25 mM, τ is the log of the reciprocal of time, T (s) vs. pH. Lines show best fit from least squares regression.

Table 4.6. APAP dissolution rate of buffers vs. HCl DM

Dissolution Media	Temp. (°C) / Conc. (mM)	Gradient
HCl	20 °C	0.602
Acetate Buffer	25 mM	0.266
	100 mM	0.157
Citrate Buffer	25 mM	0.172
	100 mM	0.137

The dissolution rate is shown to increase with buffer concentration and have an order of much less than one with respect to the H^+ concentration, which therefore supports the idea that dissolution rate is limited by the supply of H^+ in unbuffered media.

In order to illustrate this analysis, the rate can be given by,

$$rate = k[H^+]^n \quad (4.3)$$

$$\log(rate) = \log k + n \log[H^+] \quad (4.4)$$

$$\log(rate) = \log k - n pH \quad (4.5)$$

Thus, the slope of the plot of $\log(rate)$ versus pH should be equivalent to the reaction order, which is shown in Figure 4.15.

4.3.6. Estimation of Timescale for the Protonation of the KCSS Polymer Surface

To rationalise why the buffers had such a dramatic effect, a simple model was formulated to estimate the timescale for complete protonation, using a series of experimental assumptions under unbuffered conditions. McNamara and Amidon,⁷ determined the effect of the buffer concentration by the calculation of pH at the surface of the drug versus pH in the bulk. Therefore, by applying this principle, the number of tertiary amine groups on the KCSS polymer surface can be calculated to determine the rate of protonation at a given pH.

In the case of HCl DM, the time required for the acid to protonate all the amine groups was calculated under the following assumptions, i) all tertiary amine groups are on the surface and ii) all tertiary amine groups are exposed to the solution and only release APAP after the polymer film has fully dissolved. For protonation to occur, the H⁺ must first diffuse to the polymer surface. Here, Fick's first law of diffusion is applied as shown in Equation 4.6,

$$J_{H^+} = -D_{H^+} \left(\frac{dc_{H^+}}{dx} \right) \quad (4.6)$$

where J is the diffusion flux in mol cm⁻² s⁻¹, D_{H^+} is the diffusion coefficient of H⁺ as seen in the literature⁴⁹ at 7.9×10⁻⁵ cm² s⁻¹ (accounting for the presence of electrolyte), dc_{H^+}/dx is the concentration gradient, given by the difference in concentration from the bulk to the surface (x -coordinate) in mol/cm³ (assuming zero concentration at the surface), with a the boundary layer thickness estimated at 100 μm,⁵⁰ which, as a system dependent value was therefore adjusted for the parameters for this system based on similar boundary conditions.⁵¹

The effective surface concentration of tertiary amine groups (under assumption i) was determined from the volume of the polymer layer on an average sized MP bead, the mass of the layer and the formula weight of the polymer and equated to 2.89 mol cm⁻² of amine groups on the surface. The number of amines on the surface was then divided by the calculated flux, J , to obtain the time in seconds it would take for sufficient H⁺ to reach the polymer's surface and to protonate all the available tertiary amines. The variables calculated are shown in Table 4.7, with the corresponding values at each pH of the HCl DM is observed in Table 4.8.

Table 4.7. Calculated variables for the protonation of the KCSS polymer surface.

Variable	Value	Units	Details
Radius Average bead size of MCC+APAP+KCSS	0.966	mm	
Volume of sphere	0.472	mm ³	
Average bead size of MCC+APAP only radius	0.941	mm	
Average bead size of MCC+APAP only volume	0.436	mm ³	
Resultant polymer volume	0.036	mm ³	
Calculated MW of KCSS polymer	1256.62	g/mol	Repeating units MMA = 7 and DEAEMA = 3
Resultant MW of total amine groups	418.87	g/mol	
KCSS polymer coating level	15	% w/w	
Average mass per bead	0.662	mg	Total mass
15 % of bead mass [†]	0.0863	mg	From 1 bead
50 % of KCSS polymer [‡]	0.0432	mg	
Polymer mass gain per bead [†]	8.64×10^{-5}	g	
Polymer mass in dried film [‡]	4.319×10^{-5}	g	
Polymer density	12097.63	g/m ³	Calc. from vol
Amine molar volume	2887.87	mol/m ³	Calc. from total amine groups
Amine density	2.89	M	
Polymer film thickness	12.5	μm	
Amines on polymer surface	3.61	mol/cm ²	Assumes flat surface
Boundary layer thickness	100	μm	Concentration boundary layer thickness
D _{H+} in electrolyte solution	7.9×10^{-5}	cm ² s ⁻¹	

[†] based on KCSS polymer coating level of 15 % w/w

[‡] based on 50 % polymer content in dried film

Table 4.8. Values for the calculation of time taken to protonate the polymer surface and the experimental breakthrough time, τ of APAP.

pH of HCl DM	ΔC (10^{-6} mol cm^{-3})	Flux, J (10^{-9} $\text{mol cm}^{-2} \text{s}^{-1}$)	Calculated time for H^+ to reach amine (s)	Exp. time to reach APAP threshold (s)	APAP threshold (μM)
2.0	10.00	79.00	46	51	
2.5	3.16	25.00	144	92	5
3.0	1.00	7.90	457	202	
3.5	0.316	2.50	1445	339	50
4.0	0.10	0.79	4569	-	-

The comparison of the theoretical and experimental breakthrough time, τ of APAP is shown in Figure 4.16, as well as numerically in Table 4.8. From this data, it is observed that the calculated time taken for the polymer to be protonated and consequently release APAP is longer overall than the experimental values observed. Given the R^2 of 0.995 for the experimental data it has a strong indication of a positive linear association between the pH and τ . It therefore suggests that the polymer protonation or breakdown is not directly proportional to the release of the API.

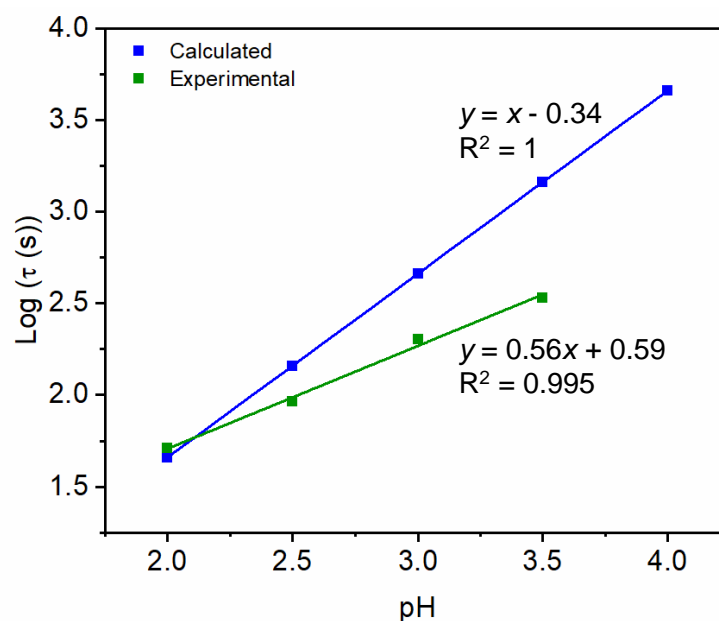


Figure 4.16. log-log values of breakthrough time, τ as a function of pH for estimated and experimental values of τ .

Whilst a simple model, it indicates that the calculated time to protonate all the available tertiary amines is longer than is experimentally observed for all except pH 2.0, suggesting: i) that as the polymer is protonated faster at lower pHs, and the solubility of APAP is independent of pH up to 7.0 approximately,^{52,53} APAP is released faster into the medium at lower pHs due to the faster protonation of the KCSS polymer under these acidic conditions; and ii) that the release of some APAP can occur before all the amine groups are fully protonated, as some groups may be protonated before others. The experimental times are much shorter than the calculated times, despite the calculation likely underestimating the time taken, as it excludes the time taken for diffusion of H^+ into the polymer coating (as not all the tertiary amine groups are on the surface as assumed) and the diffusion of APAP out of the polymer. However, the linear trend observed for both calculated and experimental values provide a valuable insight of the relationship between pH and the API breakthrough time.

A schematic overview of the proposed polymer protonation leading to the release of the API is shown in Figure 4.17.

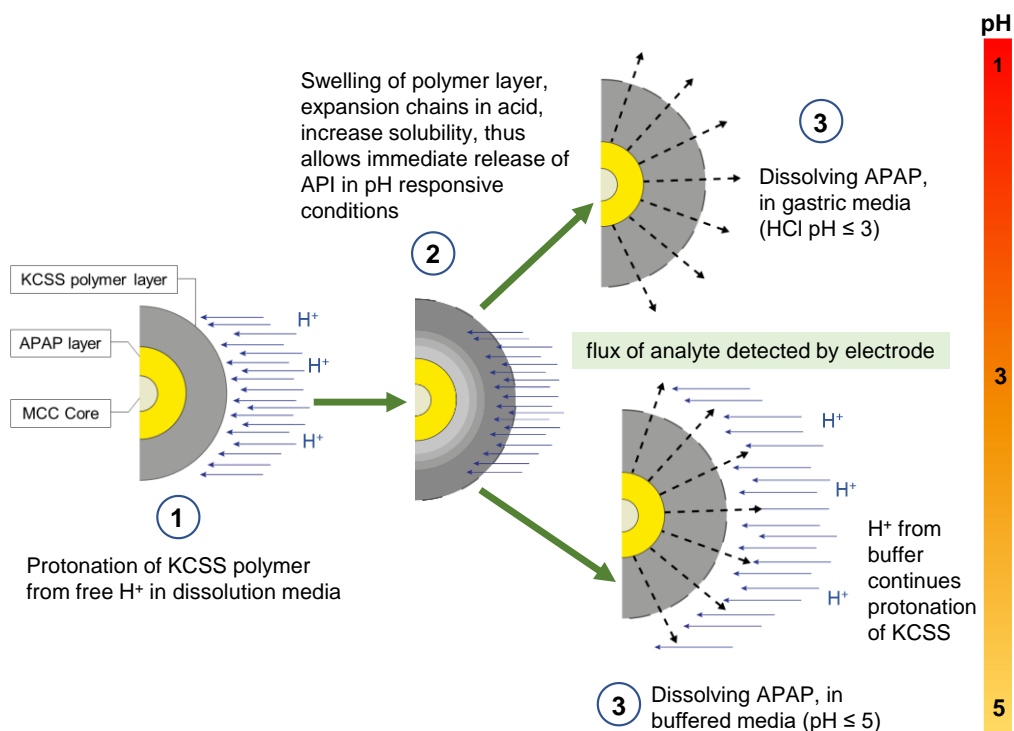


Figure 4.17. Schematic overview of dissolution process of pH-dependent taste masking Kollicoat® Smartseal 30D (KCSS) polymer, releasing the API (APAP) into the 25 mL bulk at various pHs of buffered and unbuffered simulated acidic GI tract fluid.

4.4. Conclusions

The use of the rotating disc electrode to measure the dissolution behaviour of multiparticulate solid dosage forms freely suspended in solution has been demonstrated. The high time resolution available enabled the kinetic parameters of an instant-release, reverse-enteric polymer-coated formulation to be measured. Furthermore, any electrode fouling effects were mitigated by comparing and analysing rates at early times. Not only was the strong pH-dependence of the polymer dissolution confirmed, whereby the majority dissolution occurred within less than 15 minutes in HCl media up to pH 3.0, but also a significant buffer effect was observed, consistent with a H⁺-diffusion limited dissolution mechanism in unbuffered media. Measurement of the apparent activation energies for dissolution in HCl were also consistent with a diffusion limited process. The observed buffer effect resulted in the complete dissolution of APAP at pHs above 3.0 in buffered media in contrast to that of HCl media at pH 3.5 and above, where dissolution was largely insignificant across an extended period of time. Simulated saliva, although a buffered media showed negligible amounts of APAP released over a 90 minute period. This confirms that KCSS is protonated to the extent where API release occurs below pH 5.5. Thus, demonstrating its effectiveness as a taste masking polymer. Furthermore, from the theoretical estimation of the breakthrough time, it suggests that APAP does not require the complete dissolution of the polymer in order to be released. The mechanism of release is investigated further using topographical mapping techniques in the following chapters. This RDE approach should prove useful for studies involving electroactive APIs where rapid release is anticipated.

4.5. References

1. Bai, G. *et al.* Hydrodynamic Investigation of USP Dissolution Test Apparatus II. *J. Pharm. Sci.* **96**, 2327–2349 (2007).
2. Wang, Q. & Gray, V. Chapter 15 - HPLC in dissolution testing. in *Handbook of Pharmaceutical Analysis by HPLC* **6**, 379–400 (Elsevier Inc., 2005).
3. Stevens, N. P. C. & Bond, A. M. The influence of migration on cyclic and rotating disk voltammograms. *J. Electroanal. Chem.* **538–539**, 25–33 (2002).
4. Nematollahi, D., Shayani-Jam, H., Alimoradi, M. & Niroomand, S. Electrochemical oxidation of acetaminophen in aqueous solutions: Kinetic evaluation of hydrolysis, hydroxylation and dimerization processes. *Electrochim. Acta* **54**, 7407–7415 (2009).
5. Li, Y. & Chen, S. M. The electrochemical properties of acetaminophen on bare glassy carbon electrode. *Int. J. Electrochem. Sci.* **7**, 2175–2187 (2012).
6. Kaunisto, E., Nilsson, B. & Axelsson, A. Drug dissolution rate measurements evaluation of the rotating disc method. *Pharm. Dev. Technol.* **14**, 400–408 (2009).
7. McNamara, D. P. & Amidon, G. L. Reaction plane approach for estimating the effects of buffers on the dissolution rate of acidic drugs. *J. Pharm. Sci.* **77**, 511–517 (1988).
8. Lee, H. S. *et al.* Sprinkle formulations—A review of commercially available products. *Asian J. Pharm. Sci.* **15**, 292–310 (2019).
9. Mudie, D. M., Amidon, G. L. & Amidon, G. E. Physiological Parameters for Oral Delivery and in Vitro Testing. *Mol. Pharm.* **7**, 1388–1405 (2010).
10. Abuhelwa, A. Y., Williams, D. B., Upton, R. N. & Foster, D. J. R. Food, gastrointestinal pH, and models of oral drug absorption. *Eur. J. Pharm. Biopharm.* **112**, 234–248 (2017).
11. Bai, J. P. F., Burckart, G. J. & Mulberg, A. E. Literature Review of Gastrointestinal Physiology in the Elderly, in Pediatric Patients, and in Patients with Gastrointestinal Diseases. *J. Pharm. Sci.* **105**, 476–483 (2016).
12. McArthur, K. E. & Feldman, M. Gastric acid secretion, gastrin release, and gastric emptying in humans as affected by liquid meal temperature. *Am. J. Clin. Nutr.* **49**, 51–54 (1989).
13. Michalesco, P. M., Marciano, J., Grieve, A. R. & Abadie, M. J. M. An in vivo recording of variations in oral temperature during meals: A pilot study. *J. Prosthet. Dent.* **73**, 214–218 (1995).
14. Moore, R. J., Watts, J. T. F., Hood, J. A. A. & Burritt, D. J. Intra-oral temperature variation over 24 hours. *Eur. J. Orthod.* **21**, 249–261 (1999).

15. Barclay, C. W., Spence, D. & Laird, W. R. E. Intra-oral temperatures during function. *J. Oral Rehabil.* **32**, 886–894 (2005).
16. Uddin, R., Saffoon, N. & Bishwajit, S. Dissolution and dissolution apparatus: a review. *Int. J. Curr. Biomed. Pharm. Res.* **1**, 201–207 (2011).
17. Bard, A. J. & Faulkner, L. R. *Electrochemical Methods: Fundamentals and Applications*. (2001).
18. Martin, R. D., Beeston, M. A., Unwin, P. R. & Laing, M. E. Rotating-disc electrode voltammetry as a probe of adsorption rates on solid particles in liquids. Application to ZnII adsorption at the hydroxyapatite/aqueous interface. *J. Chem. Soc. Faraday Trans.* **90**, 3109 (1994).
19. Mathivanan, J., Chang, Z., Galagedera, S. K. K. & Flechsig, G. Thermoelectrochemistry of Paracetamol - Studied at Directly Heated Micro-wire and Rotating Disk Electrodes. *Electroanalysis* **30**, 1479–1486 (2018).
20. Jawahar, N. & Anilbhai, P. H. Multi Unit Particulates Systems (MUPS): A Novel Pellets for Oral Dosage Forms. *J. Pharm. Sci. Res.* **4**, 1915–1923 (2012).
21. Glatt GmbH. *Fluid bed systems GPCG PRO/PLUS WST/G PRO/PLUS*. (2016).
22. Mauger, J. W. Physicochemical Properties of Buffers Used in Simulated Biological Fluids with Potential Application for In Vitro Dissolution Testing: A Mini-review. *Dissolution Technol.* **24**, 38–51 (2017).
23. Bannigan, P., Durack, E., Madden, C., Lusi, M. & Hudson, S. P. Role of Biorelevant Dissolution Media in the Selection of Optimal Salt Forms of Oral Drugs: Maximizing the Gastrointestinal Solubility and in Vitro Activity of the Antimicrobial Molecule, Clofazimine. *ACS Omega* **2**, 8969–8981 (2017).
24. Mudie, D. M., Samiei, N., Marshall, D. J., Amidon, G. E. & Bergström, C. A. S. Selection of In Vivo Predictive Dissolution Media Using Drug Substance and Physiological Properties. *AAPS J.* **22**, 1–13 (2020).
25. Klein, S. The Use of Biorelevant Dissolution Media to Forecast the In Vivo Performance of a Drug. *AAPS J.* **12**, 397–406 (2010).
26. Marques, M. R. C., Loebenberg, R. & Almukainzi, M. Simulated biological fluids with possible application in dissolution testing. *Dissolution Technol.* **18**, 15–28 (2011).
27. Fotaki, N. & Vertzoni, M. Biorelevant dissolution methods and their applications in in vitro in vivo correlations for oral formulations. *Open Drug Deliv. J.* **4**, 2–13 (2010).
28. Klein, S. *et al.* Improving glyburide solubility and dissolution by complexation with hydroxybutenyl- β -cyclodextrin. *J. Pharm. Pharmacol.* **61**, 23–30 (2009).

29. Hamed, R. *et al.* pH-Dependent Solubility and Dissolution Behavior of Carvedilol—Case Example of a Weakly Basic BCS Class II Drug. *AAPS PharmSciTech* **17**, 418–426 (2016).
30. Fuller, J. L. & Johnson, W. W. Citric acid consumption and the human dentition. *J. Am. Dent. Assoc.* **95**, 80–84 (1977).
31. Sun, Y. *et al.* Mode of action studies on the formation of enamel minerals from a novel toothpaste containing calcium silicate and sodium phosphate salts. *J. Dent.* **42**, S30–S38 (2014).
32. Kostewicz, E. S. *et al.* In vitro models for the prediction of in vivo performance of oral dosage forms. *Eur. J. Pharm. Sci.* **57**, 342–366 (2014).
33. Jennifer B. Dressman, Gordon L. Amidon, C. R. & V. P. S. Dissolution Testing as a Prognostic Tool for Oral Drug Absorption: Immediate Release Dosage Forms. *Pharm. Res.* **15**, 11–22 (1998).
34. Chen, T. S. & Huang, K. L. Electrochemical detection and degradation of acetaminophen in aqueous solutions. *Int. J. Electrochem. Sci.* **7**, 6877–6892 (2012).
35. Dashevskiy, A. *et al.* Micropellets coated with Kollicoat® Smartseal 30D for taste masking in liquid oral dosage forms. *Drug Dev. Ind. Pharm.* **43**, 1548–1556 (2017).
36. Miner, D. J., Rice, J. R., Riggin, R. M. & Kissinger, P. T. Voltammetry of Acetaminophen and Its Metabolites. *Anal. Chem.* **53**, 2258–2263 (1981).
37. Van Benschoten, J. J., Lewis, J. Y., Heineman, W. R., Roston, D. A. & Kissinger, P. T. Cyclic voltammetry experiment. *J. Chem. Educ.* **60**, 772–776 (1983).
38. Menjoge, A. R. & Kulkarni, M. G. Blends of reverse enteric polymer with enteric and pH-independent polymers: Mechanistic investigations for tailoring drug release. *Biomacromolecules* **8**, 240–251 (2007).
39. García Azorero, M. D., Marcos, M. L. & González Velasco, J. Influence of changes in the total surface area and in the crystalline surface composition of Pt electrodes on their electrocatalytic properties with respect to the electro-oxidation of hydrazine. *Electrochim. Acta* **39**, 1909–1914 (1994).
40. Gittings, S., Turnbull, N., Roberts, C. J. & Gershkovich, P. Dissolution methodology for taste masked oral dosage forms. *J. Control. Release* **173**, 32–42 (2014).
41. Yoshida, T., Lai, T. C., Kwon, G. S. & Sako, K. pH- and ion-sensitive polymers for drug delivery. *Expert Opin. Drug Deliv.* **10**, 1497–1513 (2013).

-
42. Chivate, A., Sargar, V., Nalawade, P. & Tawde, V. Formulation and development of oral dry suspension using taste masked Ornidazole particles prepared using Kollicoat® Smartseal 30 D. *Drug Dev. Ind. Pharm.* **39**, 1091–1097 (2013).
 43. BASF. Kollicoat Smartseal 30 D Technical Information. *BASF* 1–13 (2019).
 44. Mochizuki, K. & Takayama, K. Prediction of color changes in acetaminophen solution using the time–temperature superposition principle. *Drug Dev. Ind. Pharm.* **42**, 1050–1057 (2016).
 45. Schmaljohann, D. Thermo- and pH-responsive polymers in drug delivery. *Adv. Drug Deliv. Rev.* **58**, 1655–1670 (2006).
 46. Schattling, P., Jochum, F. D. & Theato, P. Multi-stimuli responsive polymers—the all-in-one talents. *Polym. Chem.* **5**, 25–36 (2014).
 47. Mutalabisin, M. F., Chatterjee, B. & Jaffri, J. M. pH Responsive Polymers in Drug Delivery. *Res. J. Pharm. Technol.* **11**, 5115–5122 (2018).
 48. Guth, F. & Kolter, K. Taste Masking with Kollicoat ® Smartseal 30 D – Dissolution Studies in Biorelevant Media. 2500 (2012).
 49. Macpherson, J. V. & Unwin, P. R. Determination of the Diffusion Coefficient of Hydrogen in Aqueous Solution Using Single and Double Potential Step Chronoamperometry at a Disk Ultramicroelectrode. *Anal. Chem.* **69**, 2063–2069 (1997).
 50. Slevin, C. J. & Unwin, P. R. Microelectrochemical Measurements at Expanding Droplets (MEMED): Mass-Transport Characterization and Assessment of Amperometric and Potentiometric Electrodes as Concentration Boundary Layer Probes of Liquid/Liquid Interfaces. *Langmuir* **15**, 7361–7371 (1999).
 51. Rudd, N. C. *et al.* Fluorescence confocal laser scanning microscopy as a probe of pH gradients in electrode reactions and surface activity. *Anal. Chem.* **77**, 6205–6217 (2005).
 52. Shaw, L. R., Irwin, W. J., Grattan, T. J. & Conway, B. R. The effect of selected water-soluble excipients on the dissolution of paracetamol and ibuprofen. *Drug Dev. Ind. Pharm.* **31**, 515–525 (2005).
 53. Sorasuchart, W., Wardrop, J., Ayres, J. W., Sorasuchart, W. & Wardrop, J. Drug Release from Spray Layered and Coated Drug-Containing Beads: Effects of pH and Comparison of Different Dissolution Methods. *Drug Dev. Ind. Pharm.* **25**, 1093–1098 (1999).

Chapter 5

Microstructural Characterisation of the Kollicoat[®] Smartseal 30 D Polymer Film During Dissolution

The use of a polymer coating is an effective way to taste mask active pharmaceutical ingredients (API). This study focuses on the physical and chemical response mechanism of a poly (methyl methacrylate) (PMMA) and poly (2-(diethylamino)ethyl methacrylate) copolymer (PDEAEMA), the Kollicoat Smartseal[®] 30 D (KCSS) to external acidic conditions. Dissolution of this polymer is pH responsive due to the tertiary amino groups in its structure, which undergo protonation in acidic media. Herein, the KCSS polymer has been studied as a continuous isolated film, as a basis for use as a multiparticulate formulation. A novel approach has been designed that combines scanning probe microscopy in the form of atomic force microscopy (AFM) and solution nuclear magnetic resonance (NMR) spectroscopy to analyse, monitor and quantify the physical and chemical dissolution of the KCSS polymer as an isolated film, thus advancing our knowledge of its effectiveness as a pH responsive taste masking polymer.

5.1. Introduction

Polymers with a pH dependent solubility are versatile in taste masking applications, as they can be spray dried onto the API, creating a physical barrier. Furthermore, they do not have significant issues with film thickness.^{1,2} The Kollicoat[®] Smartseal 30 D (KCSS), a methacrylic polymer, is chemically based on a C–C backbone and therefore is non-biodegradable.³ As such these polymers cannot be degraded (*in-vivo*) by hydrolysis and/or enzymes,^{4,5} and therefore, do not undergo degradation (defined by cleavage of polymer chains) or erosion (specifically defined as surface or bulk erosion) in the same way that as degradable polymers, such as PLGA (poly(lactic-co-glycolic acid)). However, it should be noted that all polymers degrade.^{6,7} Polymers that take longer to degrade than the duration of their application be defined as non-degradable polymers.⁷ For example, MMA hydrolysis half-life is *ca.* 3.9 years at pH 7 and 14.4 days at pH 9.⁸

Stimuli responsive polymers, such as the KCSS, are susceptible to change in their physical properties, such as solubility and surface activity, in response to the stimulus, which in this case is the change in the pH of the solution. Consequently, shrinkage, and swelling can occur when in contact with a stimulating pH.⁹ Therefore, visualisation of the mechanism of response of a polymer coating and consequently how drugs are released from solid dosage forms is an area of high interest.

To further comprehend the KCSS polymer as a coating for oral dosage forms, the polymer was studied as an isolated film. This however, has its own challenges in formulation where, an ideal polymer film exists when a continuous interpenetrated network of polymer chains is created, to produce a homogenous polymer film without defects.¹⁰ Furthermore, there are three key parameters for optimum film formation which the minimum film forming temperature (MFFT), the glass transition temperature (T_g) and the use of a plasticiser. The MFFT and T_g for KCSS are approximately 57 °C and 63 °C respectively.^{11,12}

Poly(methyl methacrylate) (PMMA) homopolymer is a hard polymer, with a T_g of *ca.* 105 – 120 °C, whilst poly(2-(diethylamino)ethyl methacrylate) (PDEAEMA) homopolymer is a soft polymer with a T_g of *ca.* 20 °C.¹³ As the KCSS polymer has a single value for the T_g , it suggests that the two monomers are compatible within the resultant copolymer, and a single phase is formed where the polymer chains amalgamate at the coalescence stage of film formation.¹⁴ The chains in the polymer emulsion are in an entangled state, and in the process of annealing these chains become fluid and move, however, once the film is cooled to room temperature and thus ‘fully’ formed, the chains solidify in the glassy state where the chains become ‘fixed’.¹⁵

Atomic force microscopy (AFM) is a useful tool to analyse polymeric films due to its capability for displaying surface structures with enhanced spatial resolution.¹⁶ Together with optical microscopy and nuclear magnetic resonance spectroscopy (NMR), which are two of the most common ways to study polymer dissolution,¹⁷ AFM was employed in this study. Herein, the effect an acidic environment had on a KCSS isolated film was qualitatively examined, to gain further insight to the morphological changes from the polymer’s response to external pH stimuli using AFM and optical microscopy. Also, the structural difference of the isolated film was compared to that of the polymer coating of the multiparticulate (MP) oral dosage form. Furthermore, to observe any changes to the chemical structure of the polymer in the form of an emulsion using NMR. As the study of polymers is complex, particularly copolymers coupled in a complex sample, the more understanding there is regarding the individual components, the better the evaluation is on the ingestion process.

This chapter investigates the importance on the effect that film formation has on drug release, built upon the dissolution profiles observed in Chapters 3 and 4. It is worth noting that this study predominately focuses on the polymer film as a single entity, with an emphasis on the polymer’s dissolution on a glass substrate, rather than as a multiparticulate.

5.2. Experimental

5.2.1. Solutions

The acidic solution for the physical dissolution of polymer films were prepared using HCl (37 %, Sigma-Aldrich, UK) at a concentration of 0.01 M. The pH was measured (at pH 2.3) using a pH meter (SevenEasy, Mettler Toledo). The polymer solutions for the film formation were prepared using Kollicoat[®] Smartseal 30 D aqueous dispersion (8.333 g, BASF), and 15 % (w/w) of triethyl citrate (TEC) as the plasticiser relative to the polymer (0.375 g), was added to aid film formation. The resultant solution was then applied to several glass slides. All solutions were prepared using high purity water (Purite, Select HP) with a resistivity of 18.2 M Ω cm at 25 °C.

5.2.2. Preparation of Polymer Film Glass Slides

The KCSS polymer suspension mixed with TEC was cast onto a pre-cleaned 15 mm \times 15 mm \times 0.55 mm glass slide (Agar Scientific) using a K Control Coater (Model 101, RK PrintCoat Instruments Ltd.) fitted with a micrometre adjustable applicator. Once coated, the polymer-coated glass slide was annealed (oven dried) at 70 °C and 90 °C for 18 hours, in accordance with the literature.¹⁸⁻²¹ The resultant films were clear and transparent, approximately 50 – 60 μ m thick once dry.

5.2.3. AFM and Optical Microscopy

An area on the underside of the slide was marked and was imaged before and after the addition of the prepared 0.01 M HCl (~ pH 2) acidic solution which were left in contact with the sample for 0 – 20 minutes, with 2-minute intervals, excess liquid was removed, and the sample was subsequently air dried ready for AFM analysis. Additional time intervals were acquired for films made at 90 °C. Time intervals were defined based on preliminary tests as well as the resultant data observed for the dissolution of MP beads in Chapters 3 and 4. It should be noted that the isolated film samples were not suited for in-situ AFM analysis, due to the swelling which results in the film becoming gel like (or ‘tacky’).

AFM analysis of the KCSS polymer coated glass slides were recorded in air, using an Innova[®] AFM in tapping mode, using a silicon single cantilever probe with resonance frequency 75 kHz and spring constant 3 N/m (RFESP-75, Bruker) at room temperature. The scan rate was kept at 3 Hz with a resolution of 512 lines and 512 samples per line. The images acquired were analysed using Scanning Probe Image Processor program (SPIP[™] 6.0.14, Image Metrology). Samples produced at 90 °C were also studied under bright field transmitted light using the optical microscope (Leica, DM4000M), to aid the investigation of the polymer's morphology. The storage and analysis of samples were carried out under room temperature and controlled humidity.

5.2.4. AFM Image Analysis using SPIP[™]

Multiple AFM images were taken; thus, the quantifiable data were averaged from three different scan areas (images) of one sample calculated for a 10×10 μm area. Firstly, a linewise 2nd order plane correction was applied to each image, followed by a zero offset method plane correction, where the bearing height is set to zero background. The bearing height is defined as the most dominant height, which is based on a histogram of height distribution, levelling the image so that it is set to zero. The value of the dominant height is identical to the highest frequency value in the height distribution histogram. This *z* offset method is independently applied after the 2nd order plane correction and does not distort the image. It is important to apply this when undergoing quantitative measurement utilising the particle and pore feature analysis of the software. The presence of 'pores' indicate the polymers physical breakdown and were defined at a threshold height below 0 nm, so that each image may be cross examined equally. Using this threshold, the particle and pore feature analysis was used to quantify the features of the polymer breakdown. For the image analysis of the isolated film samples made at 90 °C and for the KCSS coated placebo beads, a linewise cross-sectional profile was used with an average of 41 lines.

5.2.5. NMR Sample Preparation and Spectroscopy

For NMR analysis, 10 mL of KCSS emulsion was lyophilised to produce a white solid powder. The acid treated KCSS polymer sample had additional preparation steps, where the polymer emulsion was treated with 50 mL HCl (0.01 M, pH 2), left for continuous stirring 28 days. Aliquot samples were taken after 24 hours, 7, 14, 21 and 28 days. The subsequent solution was then lyophilised to produce ‘acid treated’ KCSS, forming a white crystalline solid. Thereafter, deuterated methanol was added to both the pure and acid treated KCSS at a concentration of 40 mg/mL. All (^1H) NMR measurements were performed with Bruker Avance III HD 500 MHz.

5.2.6. Dynamic Mechanical Analysis (DMA)

For investigation of the polymers glass transition temperature, *ca.* 20 mg of the lyophilised solid KCSS powder was packed into the metal sleeve sample holder and placed into the dynamic mechanical analyser (DMA 8000, PerkinElmer). Heating parameters was from $-30.00\text{ }^\circ\text{C}$ to $280.00\text{ }^\circ\text{C}$ at $2.00\text{ }^\circ\text{C}/\text{min}$. The resultant curve shown in Figure 5.1 is an average ($N = 2$), where the T_g is shown to be $71.50\text{ }^\circ\text{C}$. This is similar to the literature values, where Amit *et al.*, obtained a T_g value of $69.7\text{ }^\circ\text{C}$, using the differential scanning calorimetry (DSC) method.²² The mean T_g value obtained in this study and from the literature, are higher than manufacturers reported T_g value of $63\text{ }^\circ\text{C}$, which also used the DSC method.¹²

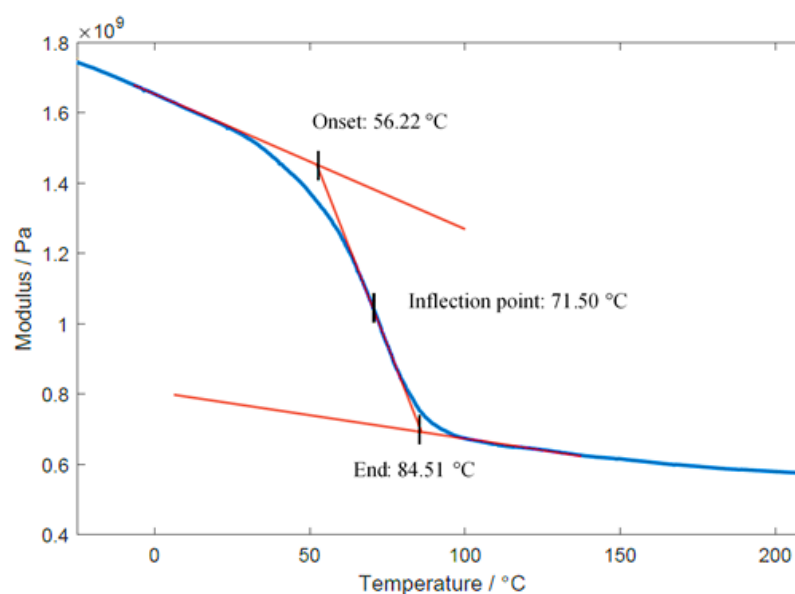


Figure 5.1. DMA thermogram of lyophilised KCSS polymer. The inflection point is defined as the midpoint.

5.3. Results and Discussion

5.3.1. Dissolution of Isolated Films

Firstly, the morphological changes of KCSS polymer films under acidic conditions at 0.01 M HCl (pH 2) were studied by optical microscopy and AFM imaging. Polymer films were made by annealing at two different temperatures (70 °C and 90 °C) to investigate the effect of environmental temperature on the quality of film formation.

AFM maps of the polymer films made at 70 °C and 90 °C prior acidic treatment is shown in Figure 5.2. Films formed at 70 °C, show the presence of many small spheres of which are similar in size (on average *ca.* 160-170 nm in diameter) on the surface (Figure 5.2a). However, those films formed at 90 °C formed a continuous film with no spherical particles observed (Figure 5.2b). The 70 °C and 90 °C samples both have differences in topographical height across the sample area illustrated by the darker contrasts of the image. The difference in the polymer spheres present at 70 °C and the continuous layer formed at 90 °C could suggest that during film formation, the polymer spheres did not fully deform and coalesce to form a continuous layer, however given the DMA shown in Figure 5.1 along with the literature suggests that 70 °C should be able to form continuous films.¹² However, the DMA data shown in Figure 5.1, could suggest that that 70 °C is not high enough as both the midpoint and the endpoint is above this temperature. The difference also demonstrates the sensitivity of the process and the importance of temperature control during film formation.

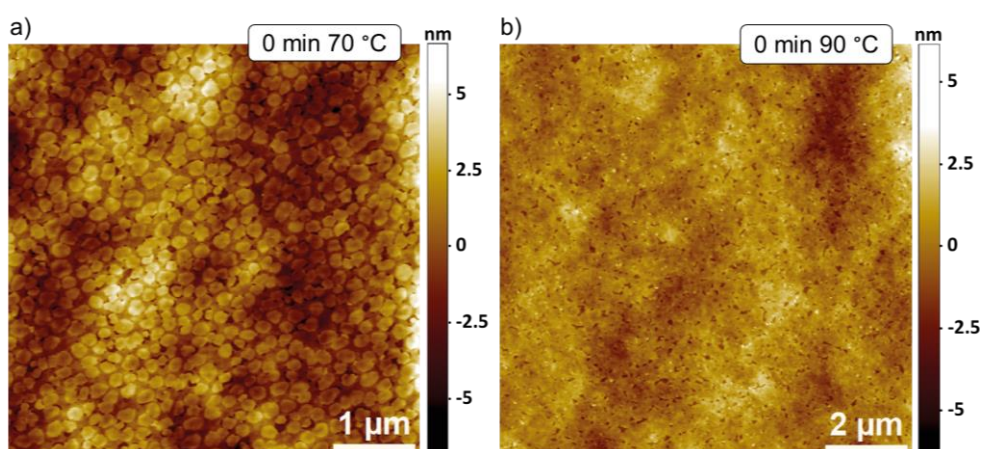


Figure 5.2. Polymer film formation examined by AFM in air, under conditions of a) formed at 70 °C and b) formed at 90 °C, before acidic treatment with 0.01 M HCl.

5.3.1.1. Dissolution of Polymer Films Prepared at 70 °C

It should be noted that *in-situ* AFM analysis was not possible due to the soft, gel-like nature of the polymer in contact with an acidic aqueous medium. Therefore, the structural changes for the polymer films were observed at timed intervals where the acid was removed after contact and subsequently air dried before AFM analysis. Time intervals were based on the imaging of preliminary test samples and the dissolution data observed in Chapters 3 and 4.

The structural observations are consistent with the literature where the polymer begins to swell in response to the acidic medium and thus the expansion (opening) of the polymer chains occurs, along with increased hydrophilicity thus increasing the polymer solubility, as shown in Figure 5.3.^{9,23,24}

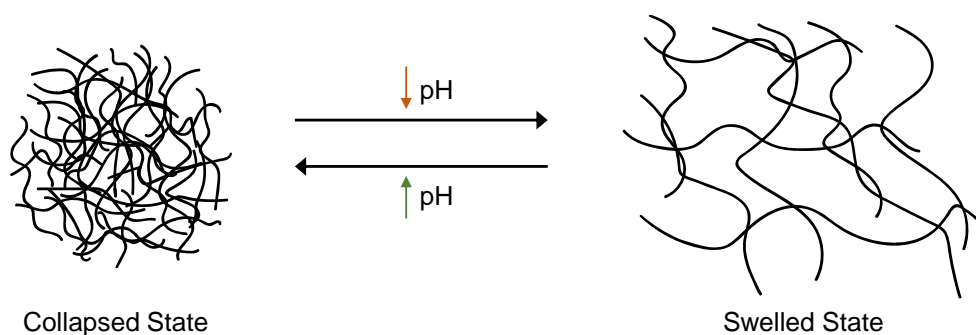


Figure 5.3. Schematic of swelling activity of pH responsive polymers. A polybasic polymer shows a collapsed state in a high pH and a swelled state in a low pH. (Adapted from Mutalabisin *et al.*, 2018).⁹

Furthermore, this demonstrates the dissolution process observed by the AFM images (Figures 5.5 – 5.7), in accordance with the literature. The polymer initially is in the ‘glassy state’ and upon penetration of the solvent the polymer makes the surface transition to the ‘rubbery state’, at concentrations above a critical level chain disentanglement occurs and true dissolution initiates, as shown in Figure 5.4. This layer appears ‘gel’ like.²⁵

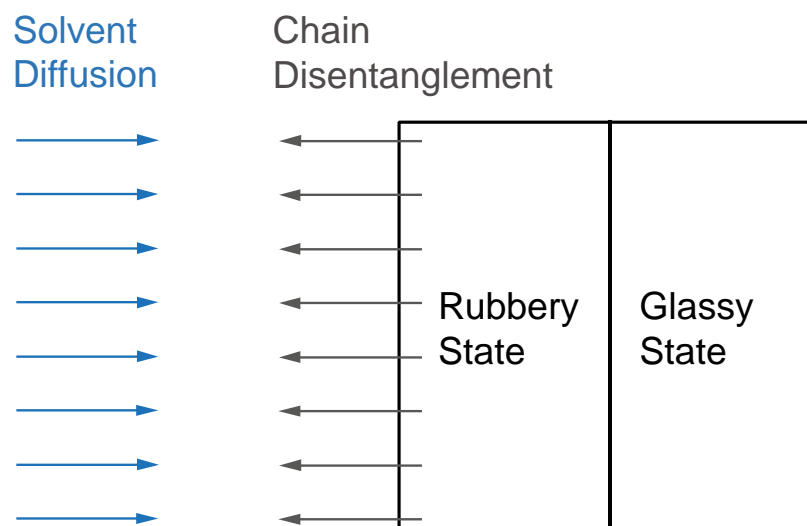


Figure 5.4. 1D schematic of solvent diffusion and resultant polymer dissolution. A glassy polymer swells due to the penetration of the solvent and transitions from the glassy state into the rubbery state, where at a high concentration chain disentanglement occurs. (Adapted from Narasimhan and Peppas, 1997).²⁵

Upon the acidic treatment of the polymer film formed at 70 °C topographical changes to the films structure are observed, as shown in Figures 5.5 – 5.7. Formation of ‘pores’ begin to occur within the film within 2 minutes of acid treatment and continue to grow. These pores are depicted as the darker shades corresponding to the z scale bar showing the depth of the pores in nm.

By 4 minutes, clear distinct pores are visible, they continue to grow in numbers and the surface becomes rougher and pores begin to merge creating larger clusters which can be observed at 8 min. The size of pores then gradually decreases around 14 minutes up until 20 minutes where the polymer has completely dissolved, leaving the glass slide underneath exposed. The topographical images provide qualitative visualisation of the changes within the polymers structure as an isolated film.

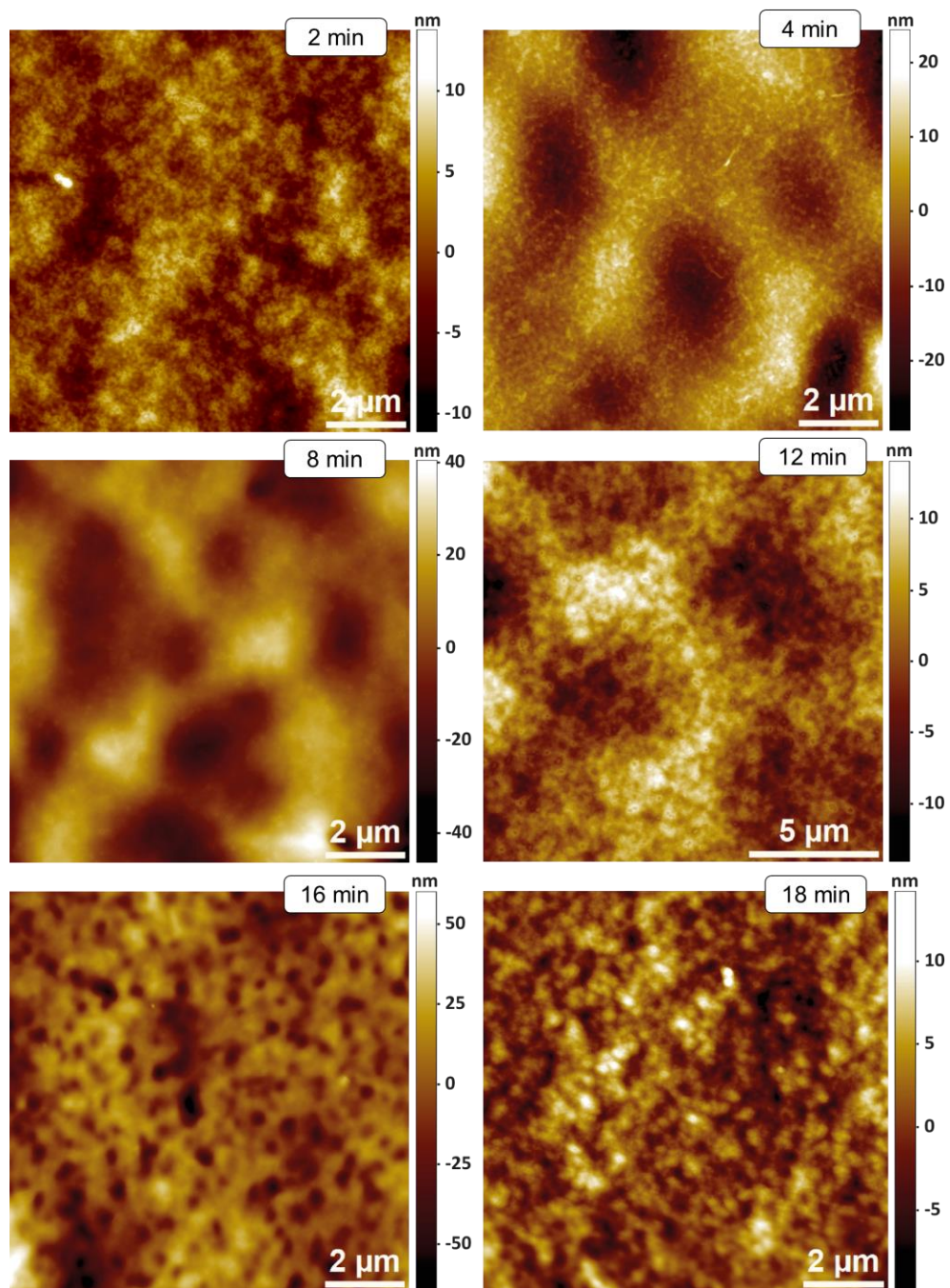


Figure 5.5. Set 1 AFM topographical maps of the KCSS polymer film prepared at 70 °C after treatment with 0.01 M HCl, for times 2, 4, 8, 12, 16, and 18 minutes.

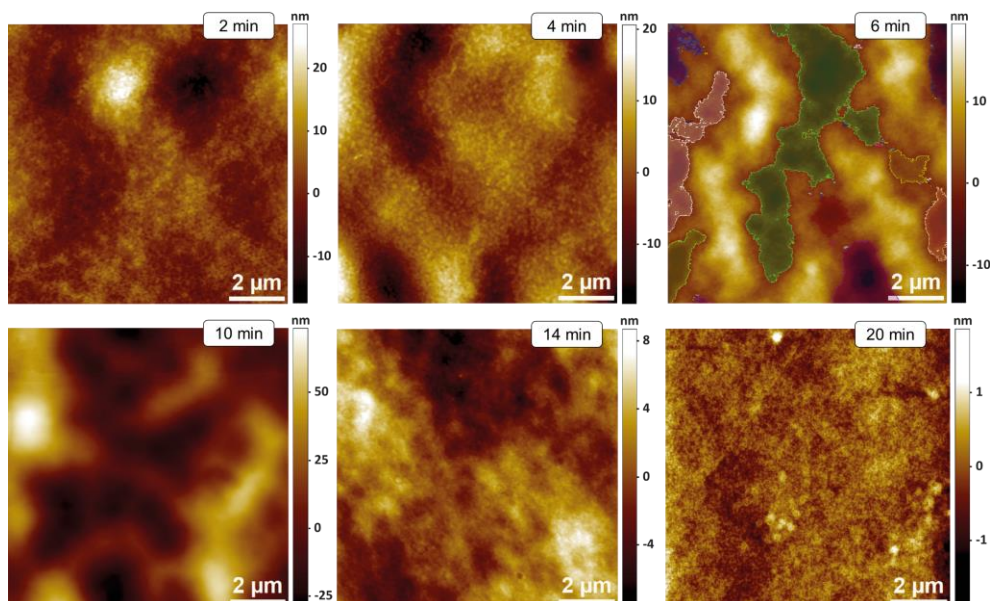


Figure 5.6. Set 2 AFM topographical maps of the KCSS polymer film prepared at 70 °C after treatment with 0.01 M HCl, for times 2, 4, 6, 10, 14, and 20 minutes. Outline of pore analysis is shown at 6 minutes as an example.

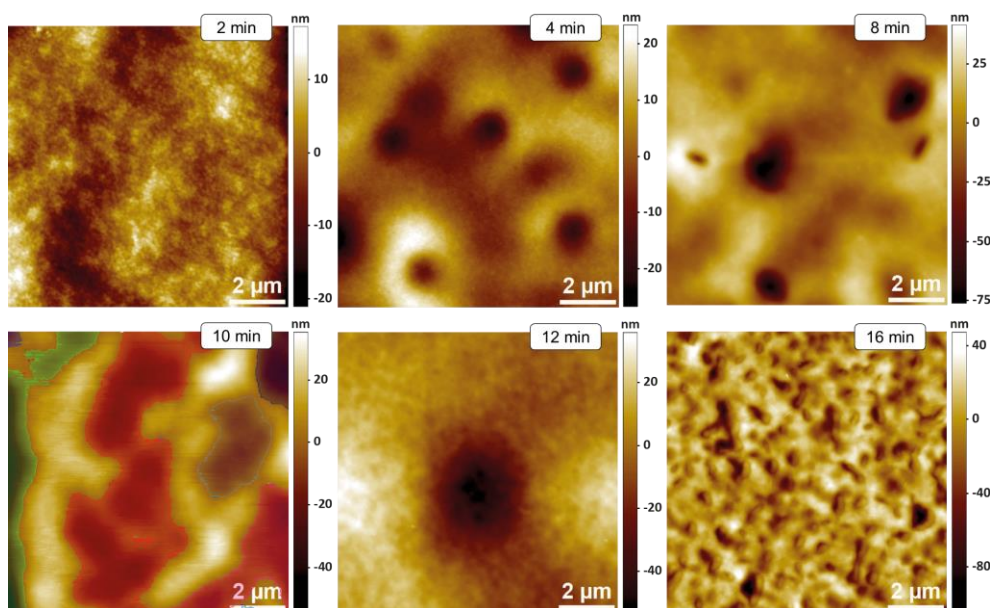


Figure 5.7. Set 3 AFM topographical maps of the KCSS polymer film prepared at 70 °C after treatment with 0.01 M HCl, for times 2, 4, 8, 10, 12, and 16 minutes. Outline of pore analysis is shown at 10 minutes as an example.

Figure 5.8 is a depiction of the physical changes to the polymer structure. As shown the polymer starts to physically erode, thus creating ‘pore-’ or ‘pit-’ like forms of erosion. Here, the mechanisms that can take place during polymer dissolution are illustrated. Figure 5.8 (a) appears to be the most common the starting point (emerging at 2 min), whereby the pore gradually increases in diameter and depth until reaching the layer of the glass slide (is appears as uniform dissolution).

Illustrated by Figure 5.8 (b) and (c) are where the pores can either grow wider or deeper. ‘Merging’ of these pores illustrated by Figure 5.8 (d) is shown to occur, specifically in a proximity to those that have already started the pore forming process. However, it also appears that the pore formation can occur at different rates, resulting in larger or deeper pits in comparison to those surrounding it at a given time, as illustrated in Figure 5.9.

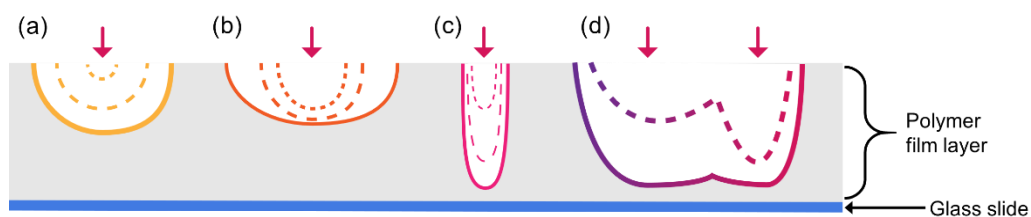


Figure 5.8. Schematic of ‘pore’ formation of the polymers surface from the expansion of polymer chains in response to an external acidic environment.

To confirm the hypothesised stages of dissolution, cross-sectional profiles across the area of pores were analysed as shown in Figure 5.9. An example AFM image with the Particle-Pore Feature Analysis colour coded extracted from Figure 5.5 (Set 1) at 8 min and the corresponding cross-sectional lines, along with a graphical representation of Particle-Pore profile is shown.

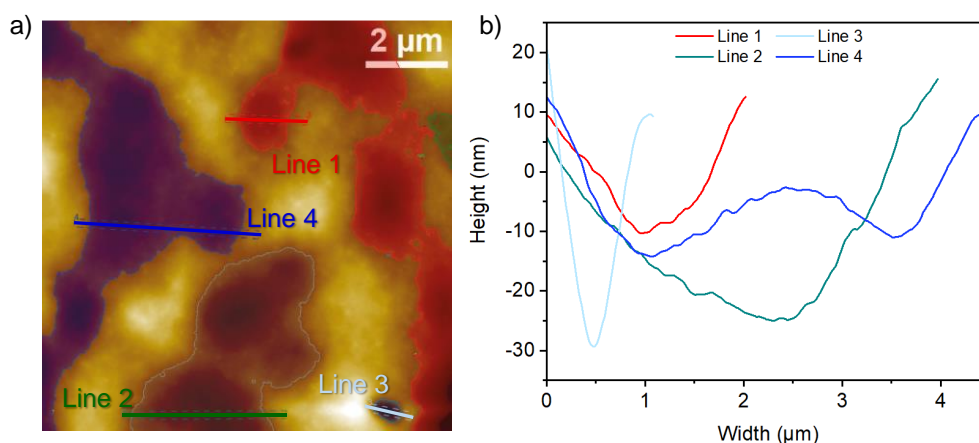


Figure 5.9. AFM cross-sectional line analysis of film prepared at 70 °C at 8 minutes, colour coded corresponding to graphical line profile distribution for a 10×10 μm area.

Here, the stages of dissolution are illustrated where pores are observed to be individual, merging and of varying widths and depths. The lines 1, 2, 3, and 4 correspond to the schematic demonstrating the types of pore formation of a, b, c, and d respectively as shown in Figure 5.8. This, therefore, elucidates and thus confirms the types of pore formation that occurs.

Using the Pore and Particle Feature Analysis Image Tool in the SPIP™ software, the analysis of these ‘pores’ and other structural changes were able to be quantified. Each image was analysed using a 10×10 μm of the sample’s areas. The surface coverage details the percentage of pores covering the surface, which ranges from 38 % to 55 % between 2 and 18 minutes of acid treatment. The number and area of the pores were also calculated along with the depth of each pore given by the *z* range from the threshold, which can be observed in Figure 5.10.

The area and depth of the pores follow a general increase with time until ‘halfway’ through the dissolution process (8 – 10 min), followed by a subsequent decrease in trend until completely dissolved. From the structural changes seen in these Figures 5.5 – 5.7, the pores appear to expand in size and depth and then shrink, seemingly dissolving until the film is no longer present. This is represented in Figure 5.10, where the number of pores and the area of pore are seen to have a contrast in trend. Upon 2 minutes of contact, the ‘starting’ point of analysis is where there is a considerably high number of pores as the polymers tertiary amine group becomes protonated and therefore becomes more soluble. The number of pores begin to decline at time 8 minutes as larger pores begin to form due to ‘merging’ this is shown by the increasing trend in the pore area. The peak of the pore area occurs at 10 minutes, which consequently has the smallest number of pores. As the time of contact with acid increases past 10 minutes there is a decline in area size of pores (and a subsequent increase in the number) due to most of the polymer ‘shrinking’ and dissolving, those larger ‘pores’ would have now dissolved leaving only a small remainder of the polymer behind. The depth of the pores follows a similar trend to the area, suggesting that as the pores become wider, they also become deeper. At 8 and 10 minutes the pores are the deepest as well as the widest, the deepest pores are observed at 16 minutes, where the area of the pores are now substantially smaller.

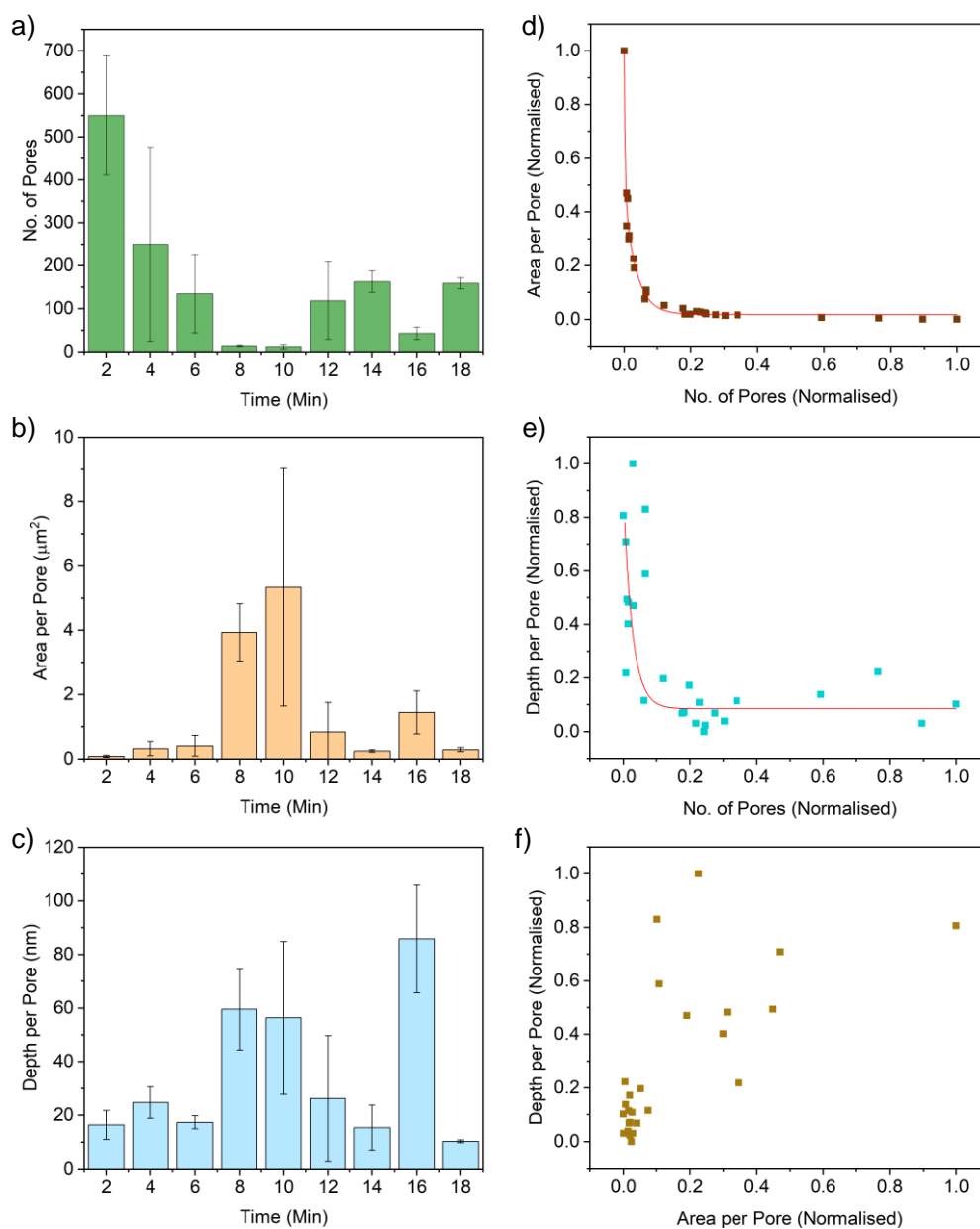


Figure 5.10. Averaged graphical representation of the pore analysis ($N = 26$ samples) relative to the structural changes upon dissolution of the KCSS polymer made at 70°C within a $10 \times 10 \mu\text{m}$ area, where a) the number of pores, b) the mean area of pores and c) the mean depth of the pores. Spearman rank graphical correlations shown for the normalised three variables studied, d) area per pore vs the no. of pores, e) depth per pore vs no. of pores and f) depth per pore vs area per pore.

To confirm whether the observed trends were valid, statistical analysis in the form of a spearman rank correlation was conducted. The correlation observed for each of the three variables are presented in its normalised state shown in Figure 5.10 (d) – (f) and Table 5.1. There is a very strong, negative correlation for area per pore vs the number of pores [$R_s(24) = -0.979$, $p < 0.001$] and a strong negative correlation for the depth per pore vs the number of pores [$R_s(24) = -0.694$, $p < 0.001$], which are both statistically significant. Conversely, there is a strong, positive correlation for the depth per pore vs the area per pore [$R_s(24) = 0.683$, $p < 0.001$], which is also statistically significant. This statistical significance confirms the trends observed where, as the number of pores declines the depth and area per pore increases and vice versa, as well as the general trend that the area and depth per pore follow a similar pattern in growth and decline.

Table 5.1. Spearman rank correlation values for pore variables in terms of number, area, and depth for p-value < 0.001 .

Variable 1	Variable 2	Spearman Rank Correlation Coefficient (R_s)*
Area per Pore	No. of Pores	-0.979
Depth per Pore	No. of Pores	-0.694
Depth per Pore	Area per Pore	0.683

*p-value < 0.001 , and N = 26 for all variables

The AFM image and analysis demonstrated that the dissolution of the polymer film is heterogeneous. This is also evident given the large variation in the standard deviation across each region of the topographical map (*vide supra*).

5.3.1.2. *Dissolution of Polymer Films Prepared at 90 °C*

The dry isolated film at 90 °C differed from those made at 70 °C, where spherical particles were still visible. Therefore, these films produced at 90 °C were analysed to not only to investigate the structural response to dissolution but also if the dissolution response differed from those made at 70 °C.

At 90 °C no ‘particles’ were visible (*vide supra*, Section 5.3.1), which suggested that for films prepared at 90°C the dissolution process may take longer. Analysis of the AFM images for films prepared at 90 °C, showed similar and dissimilar attributes to those prepared at 70 °C, as shown by the AFM images in Figure 5.11. Comparable to 70 °C films, swelling occurs as expected and pore formation is observed predominately from 12 minutes. Furthermore, these pores at 16 minutes are particularly distinguishable as well defined and spherical in shape. Dissimilarly, the pores took longer to appear and are much wider in size. This could have occurred as at 90 °C a more homogeneous film appeared to have formed, thus resulted in a reduced surface area in contact with the acidic solution. Whilst the swelling of the polymer was visible by the expansion of chains ‘pores’ were formed, but also larger structural differences that are better suited to be identified as ‘ridges’ shown in Figure 5.12.

Thus, the Pore and Particle Feature Analysis Image Tool in the SPIP™ software was not used to analyse the images for the films prepared at 90 °C, as it was unable to correctly identify between the ‘pore’ and the ‘ridges’ in the topographical features observed. To remedy this, horizontal cross-sectional profiles of the imaged area were used to determine the size and depth of both the ridges and pores. Furthermore, under acid treatment, these films produced large structures with a considerable topographical height difference in the imaged area and as a result were more challenging to image using AFM. Therefore, optical microscopy was used in conjunction, given the complexity in AFM imaging. The samples were therefore examined under the optical microscope for further investigation of morphology and to gain a clearer perspective on the polymer film dissolution. The corresponding cross-sectional analysis is observed under each AFM image shown in Figure 5.11.

These cross-sectional profiles for the films prepared at 90 °C, are also seen to correspond to the pore formation mechanisms observed for those films prepared at 70 °C (*vide supra*). At 16 min, there is a clear demonstration of phase (c) from Figure 5.8 occurring. However, at 90 °C the majority of the pore formation correlates to phase (d).

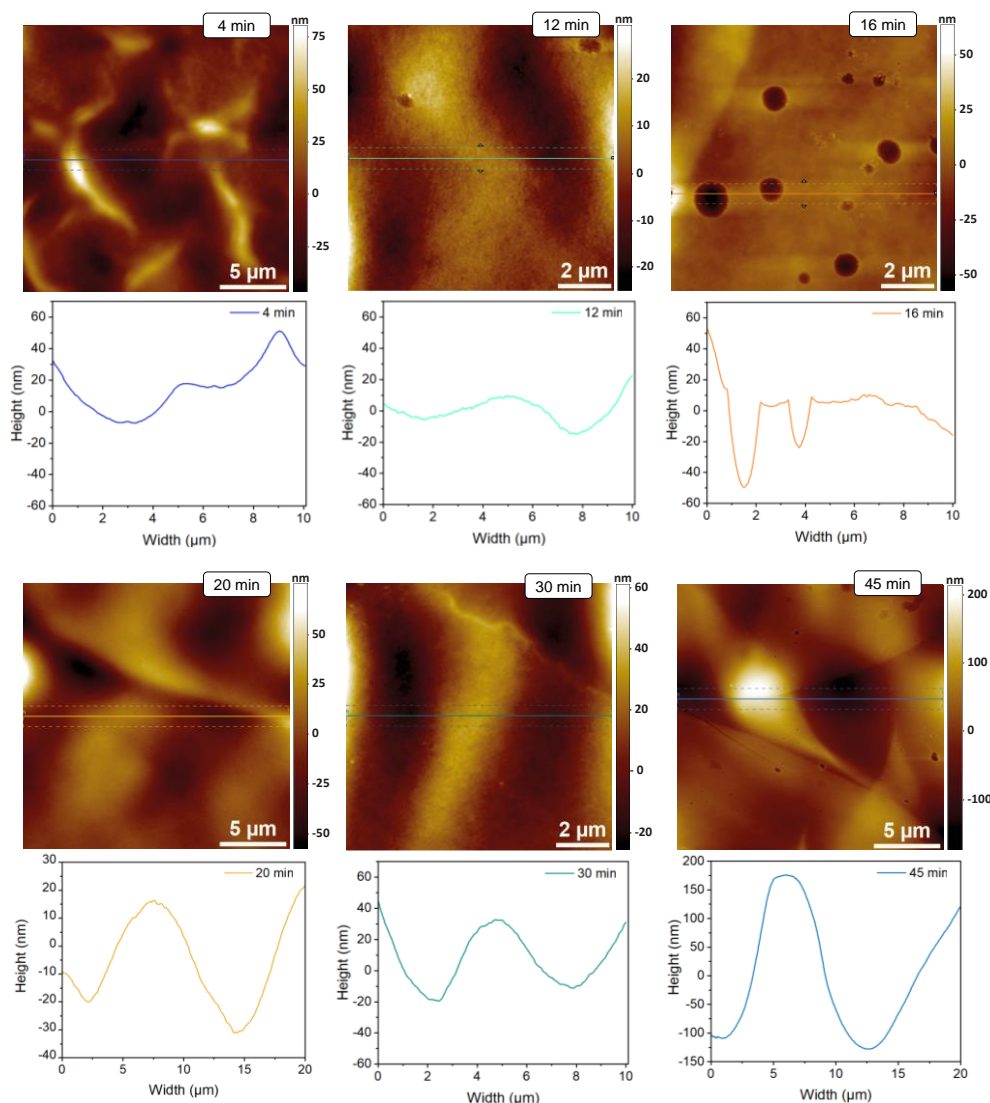


Figure 5.11. AFM topographical maps of the KCSS polymer film prepared at 90 °C after treatment with 0.01 M HCl. At times 4, 12, 16, 20, 30, and 45 minutes, with the corresponding graphical representation of cross-sectional profiles across.

Optical imaging allows for a non-contact visual observation of the polymer film in its current state as well as utilising the higher magnification levels, confirms the presence of the structures within the polymer film (Figure 5.12) observed by the images produced by AFM (Figure 5.11).

Figure 5.12 shows ‘cracking’ within the polymer structure at 2- and 4-minutes. By 8 minutes swelling is observed which continues until 30 minutes, along with overlapping of ridges. Opening of polymer chains is visible and within these pores the AFM images were taken (due to the flatter surface). At 45 min the morphology appears to suggest that the overlapping ridges of swelling have not reached dissolution leaving wide pores. This correlates to the observations detected with AFM at the same time. It took approximately 60 minutes to reach complete dissolution of the polymer film, almost triple the time it took for films prepared at 70 °C.

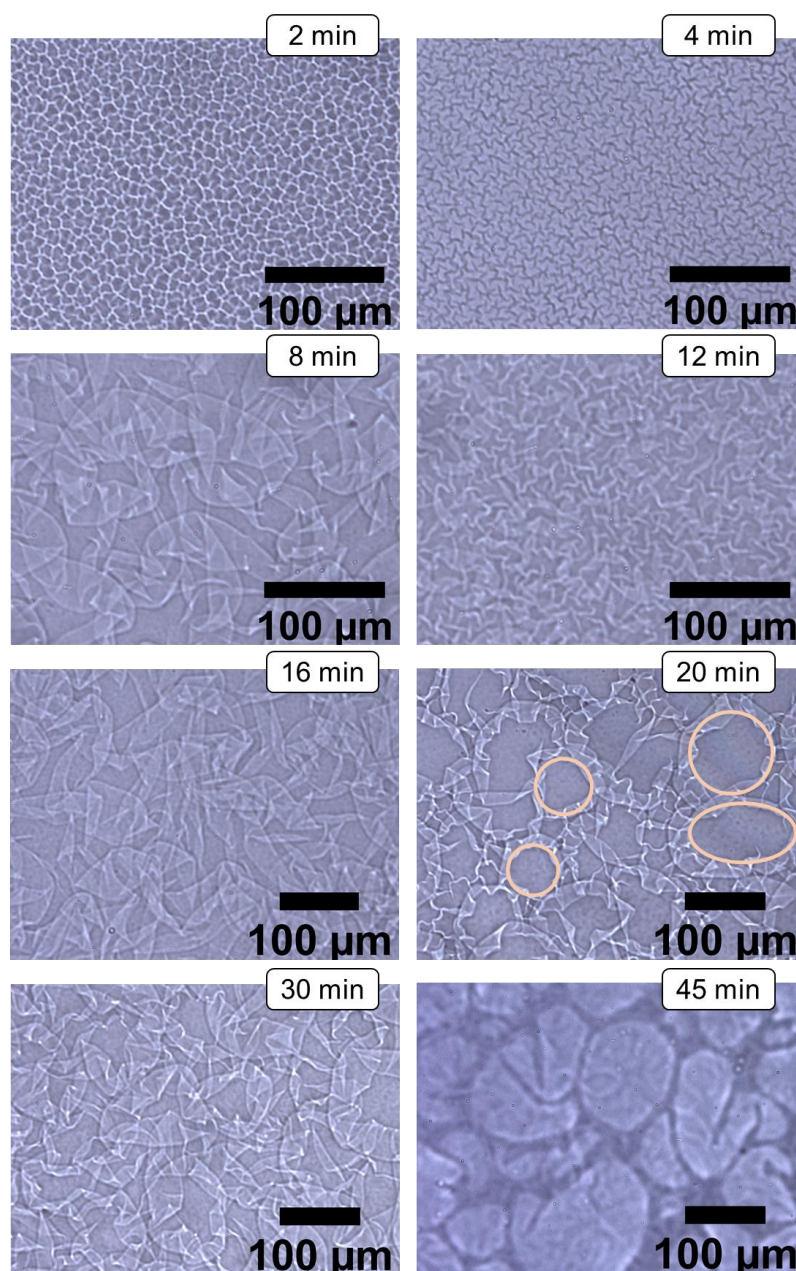


Figure 5.12. Morphology of polymer films prepared at 90 °C using bright field transmitted light post contact with 0.01 M HCl. At times 2, 4, 8, 12, 16, 20, 30, and 45 minutes. Area of polymer chains opening highlighted at 20 minutes.

The mechanism of dissolution follows the same process, however, at 90 °C there is an increase in time before dissolution is complete. Furthermore, the structural changes in the polymer film appear on a larger scale.

From the observed morphological response of the polymer structure to an acidic medium along with the knowledge from the literature. The suggested mechanism of 'degradation' for the KCSS is firstly swelling of the polymer, which occurs as a prelude to polymer dissolution and lastly degradation by erosion (specifically for a continuous isolated film).^{17,25,26} The swelling of the polymer is due to the electrostatic (Coulombic) repulsion of the positively charged neighbouring groups, which leads to changes to its conformational structure and hydrodynamic volume. This swelling ultimately allows for the release of the drug into the external environment.¹³⁻¹⁹ Therefore, the polymers structural changes observed in this study show that in this case the drug is released in gastric fluid and insoluble in salivary fluid.

5.3.2. Dissolution Comparison of Polymer Isolated Films to Polymer Coated Multiparticulates

Whilst examining the polymer as an isolated entity is valuable and provided an important insight to the polymer's pH responsiveness. It is not however in the form of a coating of an API, as it would be as a MP formulation. As the MP are of a large spherical shape (*ca.* 950 μm) and its soft nature, it was not practically sustainable to study many MP beads under the atomic force microscope. Thus, a brief inquiry was undertaken to study a small sample of polymer coated multiparticulates.

Figure 5.13 shows the AFM topography of a spray coated polymer coating at 70 $^{\circ}\text{C}$ upon a placebo bead before and after 20 minutes of contact with 0.01 M HCl solution. It should be noted that the polymer particle shape and size differ in its appearance compared to polymer coated glass slide images *vide supra* which is predominately attributed to the fluidised bed application of polymer but also the MCC substrate. This is known from preliminary testing of AFM imaging of both polymer-coated multiparticulates and glass slide substrates. Before the addition of acid, particles are visible within the polymer structure. After 20 minutes of contact with acid the particles have increased in size, suggesting swelling has occurred. To quantify this observation, cross-sectional profiles were drawn as shown on the AFM images. These correspond to the graphical profile shown in Figure 5.14, where there is a clear indication of 'pores' indicated by the depth and width of the line profile. This suggests that the dissolution mechanism described previously occurs for KCSS polymer coating in the form of a MP formulation.

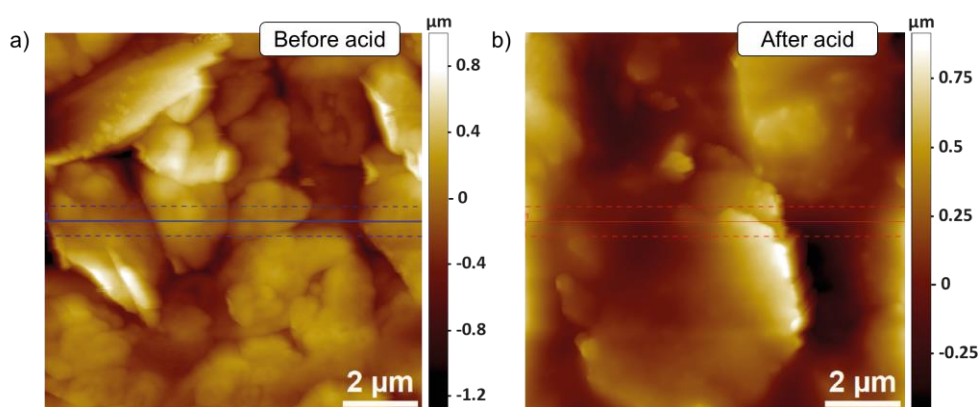


Figure 5.13. AFM topographical maps of a KCSS polymer coating formed at 70 $^{\circ}\text{C}$ onto a MCC bead, using the Wurster process in fluidised bed coater, a) before addition of acid and b) after 20 minutes of contact with acid (0.01 M HCl).

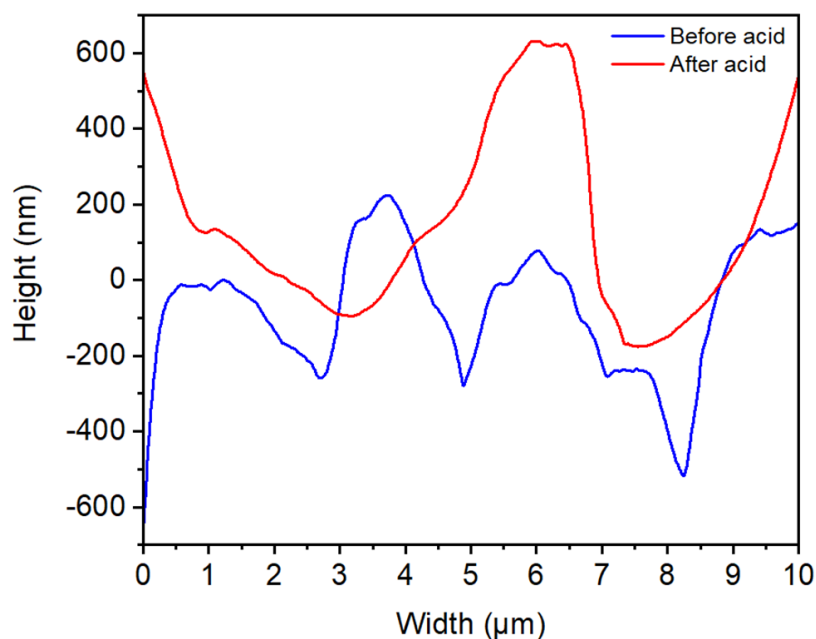


Figure 5.14. Corresponding line profile for cross-sectional analysis of AFM topographical map of MP bead (Figure 5.13), before (blue) and after (red) 20 minutes of contact with 0.01 M HCl.

In Figure 5.14 similar line profiles to the polymer films formed at both 70 and 90 °C, are observed in response to an acidic environment. As a result, the pore formation mechanisms discussed previously (Figure 5.8) are applicable. This suggests that the dissolution of the polymer is intrinsic to the polymer layer itself, rather than the substrate it is produced on or temperature of film formation (as long as it is above the T_g and MFFT).

5.3.3. ^1H NMR of Acid Treated Kollicoat[®] Smartseal 30 D Emulsion

The penetration of solvent is the first step to many polymer dissolution processes.^{7, 27} Due to the defined number of tertiary amine groups, upon contact with acidic media, these amine groups are protonated and the polymer swells and dissolves as a result. This protonation reaction makes the polymer more water soluble. It is known that the pH for hydrolysis of PDEAEMA to occur is insignificant below 7,^{28,29} with the hydrolysis half-life to occur in 4.54 days at pH 7 and 3.31 hours at pH 9 at 25 °C.^{30,31} The pK_a of DEAEMA monomer is 8.8 and the pK_a of its corresponding homopolymer is 7.5.^{25,26} As previously discussed, an increase in pH (above its pK_a) the polymer would be in its collapsed state and therefore, no significant swelling would occur.^{7,9,29,30,33} DEAEMA is characteristically immiscible in water and therefore insoluble at neutral pH. It therefore exists in the hydrophilic phase in acidic conditions and hydrophobic phase at pH 6 and above.³⁴ The resultant conformational change is attributed to the neutralisation of the charged amine groups by the presence of OH groups upon the addition of a base.³⁵ In the study led Darabi *et al.*, 2015 it has been shown that in an environment of pH 6, the pH is low enough for DEAEMA to be solubilised in water and at elevated temperatures inhibit hydrolysis.²⁸ Therefore, for these reasons, solution NMR was employed to demonstrate that hydrolysis does not occur as a mechanism of degradation under the conditions of this study.

Highfield ^1H NMR was employed to deduce the chemical changes to the structure of the copolymer. KCSS in its pure form and its acid treated form, under 0.01 M HCl (*ca.* pH 2) conditions were analysed and compared. These structures are illustrated in Figure 5.15.

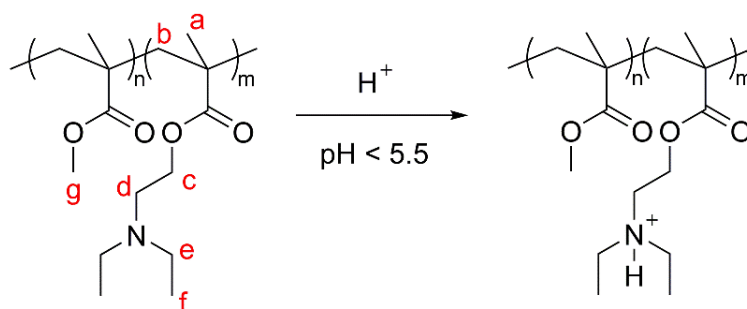


Figure 5.15. KCSS polymer structure before and after treatment with 0.01 M HCl.

Due to the tertiary amino group within the structure, the polymer is protonated in contact with acidic media of pH 5.5 and below.^{12,36} The NMR spectra (Figure 5.16) shows the observed peaks c, d, e, a and f that undergo spectral changes due to protonation. This protonation makes the polymer more hydrophilic and therefore more soluble, thus a physical rapid dissolution of the polymer film³ can be seen via the mechanism observed in the polymer morphology image analysis. It is worth noting that the NMR spectra shows a molar ratio of 10:4 for MMA:DEAEMA which slightly differs to the manufacturers ratio of 7:3.^{11,12}

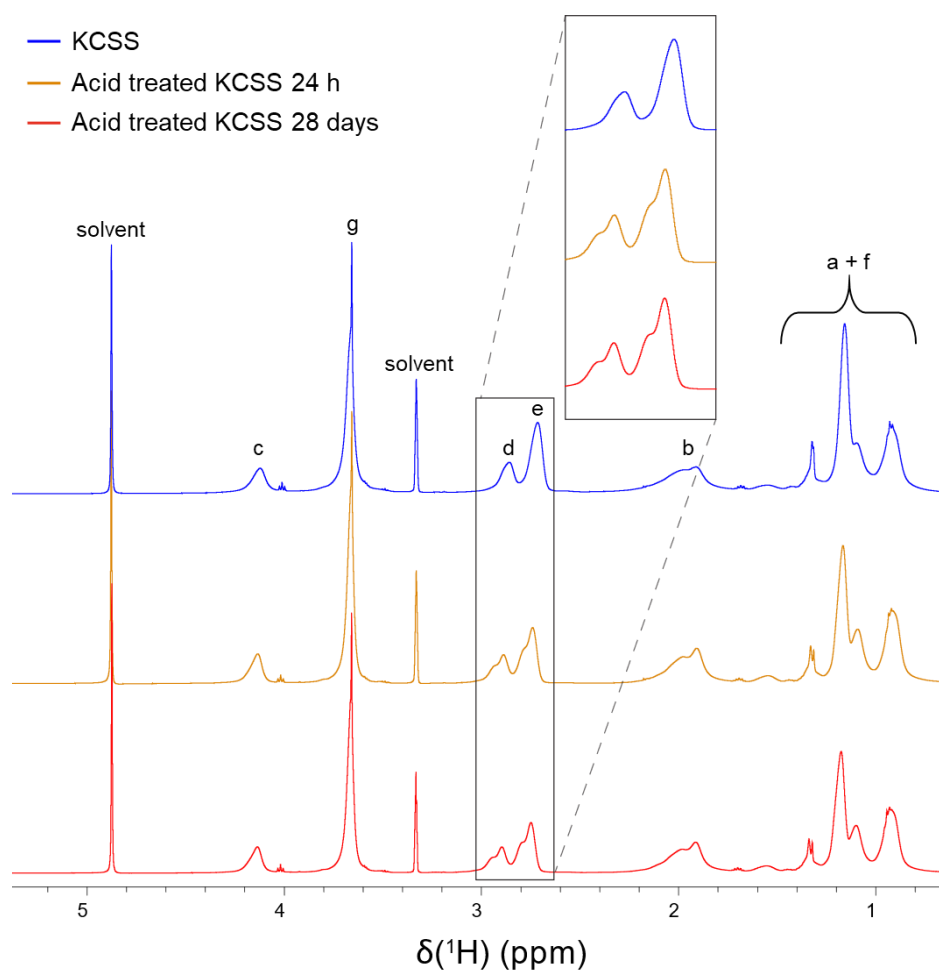


Figure 5.16. NMR spectra of pure KCSS polymer (blue), and 0.01 M HCl acid treated polymer after 24 h (yellow) and after 28 days (red).

It is observed that the DEAEEMA has not hydrolysed as no new peaks emerged from the hydrolysis product. The changes within the spectra (Figure 5.16) between 24 h and 28 days of acid treatment lies at peaks c and d, the slight splitting of the peaks occur at 24 hours and become more prominent by day 28. However, there is no significant change within the chemical structure to suggest a physical degradation, as mentioned previously hydrolysis would not occur under this pH condition. Thus, it can be concluded that dissolution of polymer is due to swelling and opening of the polymer chains, coinciding with that AFM topographical data discussed in this study.

5.4. Conclusions

In this study, the physical and chemical breakdown reaction of the Kollicoat[®] Smartseal 30 D upon contact with acid have been detailed, owing these conditions to its dissolution. In agreement with the literature, the dissolution of the polymer film occurs at acidic pH via the process of swelling, as expected. From the AFM images it can be concluded that the ‘mechanism’ of the polymer dissolution occurs by varying stages of pore formation and erosion of the polymer film. Furthermore, the chemical response observed in the NMR spectra is a result of a simple protonation reaction, rather than a change in its chemical structure. It is imperative to understand how the polymer degrades as its own entity, this was achieved by casting the polymer as a film. AFM analysis provided a deeper insight into the swelling mechanism, where the extent of swelling and the mechanistic phases in which the phenomenon occurs were able to be quantified. Furthermore, this study showed that the polymers dissolution is intrinsic to the polymer itself. This study complements the dissolution findings through the detection of API release from the KCSS polymer coating, both as a single bead and as a dosage form in the analysis of Chapters 3 and 4, respectively.

5.5. References

1. Joshi, S. & Petereit, H. U. Film coatings for taste masking and moisture protection. *Int. J. Pharm.* **457**, 395–406 (2013).
2. Felton, L. A. Use of polymers for taste-masking pediatric drug products. *Drug Dev. Ind. Pharm.* **44**, 1049–1055 (2018).
3. Subramaniam, A. & Sethuraman, S. Biomedical Applications of Nondegradable Polymers. in *Natural and Synthetic Biomedical Polymers* 301–308 (Elsevier, 2014). doi:10.1016/B978-0-12-396983-5.00019-3
4. Dinarvand, R., Dorkoosh, F., Hamidi, M. & Moghadam, S. H. Polymeric Delivery Systems for Biopharmaceuticals. *Biotechnol. Genet. Eng. Rev.* **21**, 147–182 (2004).
5. Uhrich, K. E., Cannizzaro, S. M., Langer, R. S. & Shakesheff, K. M. Polymeric Systems for Controlled Drug Release. *Chem. Rev.* **99**, 3181–3198 (1999).
6. Fu, Y. & Kao, W. J. Drug release kinetics and transport mechanisms of non-degradable and degradable polymeric delivery systems. *Expert Opin. Drug Deliv.* **7**, 429–444 (2010).
7. Göpferich, A. Mechanisms of polymer degradation and erosion. *Biomaterials* **17**, 103–114 (1996).
8. World Health Organization. *Concise International Chemical Assessment Document 4 METHYL METHACRYLATE*. (1998).
9. Mutalabisin, M. F., Chatterjee, B. & Jaffri, J. M. pH Responsive Polymers in Drug Delivery. *Res. J. Pharm. Technol.* **11**, 5115–5122 (2018).
10. Siepmann, J. & Siepmann, F. Stability of aqueous polymeric controlled release film coatings. *Int. J. Pharm.* **457**, 437–445 (2013).
11. BASF SE Care Chemicals Division Pharma Ingredients & Services. Kollicoat Smartseal 30 D Technical Information. *BASF Tech. Inf.* 1–12 (2011).
12. BASF. Kollicoat Smartseal 30 D Technical Information. *BASF* 1–13 (2019).
13. Thermal Transitions of Homopolymers: Glass Transition & Melting Point. *Sigma Aldrich* Available at: <https://www.sigmaaldrich.com/technical-documents/articles/materials-science/polymer-science/thermal-transitions-of-homopolymers.html>.
14. Yang, C.-F., Wang, H.-C. & Su, C.-C. Enhancing the Compatibility of Poly (1,4-butylene adipate) and Phenoxy Resin in Blends. *Materials (Basel)*. **10**, 692 (2017).

15. Cannon, L. A. & Pethrick, R. A. Effect of the glass-transition temperature on film formation in 2-ethylhexyl acrylate/methyl methacrylate emulsion copolymers. *Macromolecules* **32**, 7617–7629 (1999).
16. Maver, U. *et al.* Polymer Characterization with the Atomic Force Microscope. in *Polymer Science* (ed. Yilmaz, F.) 113–132 (InTech, 2013). doi:10.5772/51060
17. Miller-Chou, B. A. & Koenig, J. L. A review of polymer dissolution. *Prog. Polym. Sci.* **28**, 1223–1270 (2003).
18. Kucera, S. A., Felton, L. A. & McGinity, J. W. Physical aging in pharmaceutical polymers and the effect on solid oral dosage form stability. *Int. J. Pharm.* **457**, 428–436 (2013).
19. Yang, Q. W. *et al.* European Journal of Pharmaceutics and Biopharmaceutics Curing of aqueous polymeric film coatings : Importance of the coating level and type of plasticizer. *Eur. J. Pharm. Biopharm.* **74**, 362–370 (2010).
20. Bodmeier, R. & Paeratakul, O. Plasticizer uptake by aqueous colloidal polymer dispersions used for the coating of solid dosage forms. *Int. J. Pharm.* **152**, 17–26 (1997).
21. Wang, Y., Juhué, D., Winnik, M. A., Leung, O. M. & Goh, M. C. Atomic Force Microscopy Study of Latex Film Formation. *Langmuir* **8**, 760–762 (1992).
22. Amit, C., Viral, P., Prakash, S. O. & Atul, G. Application and Functional Characterization of Kollicoat Smartseal 30D as a Solid Dispersion Carrier for Improving Solubility. **14**, 1–9 (2020).
23. Schmaljohann, D. Thermo- and pH-responsive polymers in drug delivery. *Adv. Drug Deliv. Rev.* **58**, 1655–1670 (2006).
24. Schattling, P., Jochum, F. D. & Theato, P. Multi-stimuli responsive polymers—the all-in-one talents. *Polym. Chem.* **5**, 25–36 (2014).
25. Narasimhan, B. & Peppas, N. A. The Physics of Polymer Dissolution: Modeling Approaches and Experimental Behavior. *Adv. Polym. Sci.* **128**, 157–207 (1997).
26. L.Bruschi, M. Main mechanisms to control the drug release. in *Strategies to Modify the Drug Release from Pharmaceutical Systems* (ed. Bruschi, M. L.) 37–62 (Elsevier, 2015). doi:10.1016/B978-0-08-100092-2.00004-7
27. Mathiowitz, E., Jacob, J. & Pekarek, K. Morphological Characterization of Bioerodible Polymers . Characterization of the Erosion and Intact Zones in Polyanhydrides Using Scanning Electron Microscopy. *Macromolecules* 6756–6765 (1993).
28. Darabi, A., Shirin-Abadi, A. R., Jessop, P. G. & Cunningham, M. F. Nitroxide-Mediated Polymerization of 2-(Diethylamino)ethyl Methacrylate (DEAEMA) in Water. *Macromolecules* **48**, 72–80 (2015).

-
29. Ho, J. *et al.* Water-borne coatings that share the mechanism of action of oil-based coatings. *Green Chem.* **20**, 1899–1905 (2018).
 30. PubChem Database. Diethylaminoethyl methacrylate. *Natl. Cent. Biotechnol. Inf.* (2005).
 31. Darabi, A., Shirin-Abadi, A. R., Jessop, P. G. & Cunningham, M. F. Nitroxide-mediated polymerization of 2-(diethylamino)ethyl methacrylate (DEAEMA) in water. *Macromolecules* **48**, 72–80 (2015).
 32. Van De Wetering, P., Moret, E. E., Schuurmans-Nieuwenbroek, N. M. E., Van Steenberghe, M. J. & Hennink, W. E. Structure-activity relationships of water-soluble cationic methacrylate/methacrylamide polymers for nonviral gene delivery. *Bioconjug. Chem.* **10**, 589–597 (1999).
 33. Bartil, T., Bounekhel, M., Cedric, C. & Jeerome, R. Swelling behavior and release properties of pH-sensitive hydrogels based on methacrylic derivatives. *Acta Pharm.* **57**, 301–314 (2007).
 34. Othman, N. A. F. *et al.* Radiation grafting of DMAEMA and DEAEMA-based adsorbents for thorium adsorption. *J. Radioanal. Nucl. Chem.* **324**, 429–440 (2020).
 35. Shahalom, S., Tong, T., Emmett, S. & Saunders, B. R. Poly(DEAEMA-*c o*-PEGMa): A New pH-Responsive Comb Copolymer Stabilizer for Emulsions and Dispersions. *Langmuir* **22**, 8311–8317 (2006).
 36. Dashevskiy, A. *et al.* Micropellets coated with Kollicoat® Smartseal 30D for taste masking in liquid oral dosage forms. *Drug Dev. Ind. Pharm.* **43**, 1548–1556 (2017).

Chapter 6

Surface Charge Mapping of Polymer-Coated Multiparticulates: The Application of Scanning Ion Conductance Microscopy

In this study, Kollicoat[®] Smartseal 30 D (KCSS) pH dependence is utilised to map the surface charge of this polymer coating in the multiparticulates (MP) form, for solutions of pH 5 – 9 using scanning ion conductance microscopy (SICM). By understanding the nature of charges at the surface in solution, this provides valuable information regarding the dissolution process of the polymer, which coats the drug-containing MP. Here, topographical maps using atomic force microscopy (AFM) and SICM are compared. Furthermore, functional mapping of the polymers surface charge density is constructed.

6.1. Introduction

Scanning ion conductance microscopy (SICM) is a scanning probe microscopy technique used for topographical mapping of a substrate submerged in electrolyte, established by Hansma *et al.*, 1989.^{1,2} With careful application of the applied bias and detailed analysis of the corresponding current it is possible to probe the local ion concentration of the substrate.^{3,4} The non-contact nature of the technique makes it highly suitable for analysing membranes and thin films, and in our case a multiparticulate formulation coated with a soft polymeric layer. This study utilises the surface charge mapping technique which provides information regarding charged domains on the surface,^{2,5} whilst atomic force microscopy (AFM) provides high resolution topography of the polymer film layer. SICM, is suitable for soft interfaces which provides more chemical information than AFM, however, this additional information may result in a trade off in resolution, with a probe dependant resolution in SICM of 100 nm per pixel for a 150 nm nanopipette, compared with a typical sub-nanometre resolution in AFM.

In SICM a potential bias is applied between a quasi-reference counter electrode (QRCE) within a nanopipette and another in the bulk electrolyte solution, this therefore induces a direction ion current (DC) through the end of the nanopipette, from the movement of charged species through the electrolyte solution, as shown in Figure 6.1. When the nanopipette approaches the substrates surface, the tip-surface distance decreases, the flow of ions is obstructed and thus increases the solution resistance, which results in the reduction of the ion current. This decrease in ion current is then used as a feedback mechanism, which is utilised as a mapping signal to sense the surface via the tip-surface distance and consequently produces topographical images by recording the z height at each approach and plotting them on an x - y grid.^{2-4,6-9}

This chapter builds upon the microstructural changes observed in Chapter 5, by analysing the Kollicoat[®] Smartseal 30 D (KCSS) polymer, in the form of an isolated film, as well as in a multiparticulate (MP) oral dosage bead. From the previous chapters, it has been established that rapid dissolution times of the polymer occur at low pHs. Therefore, given the experimental set up that SICM requires, a pH range of electrolyte solutions between 5 and 9 were selected in this study to ensure that structural polymer changes were captured.

This study is based on the culmination from the previous chapters, where an electrochemical scanning probe method is used. In particular, the SICM technique uses nanopipettes to position the electrode above a MP bead with precision, which was a particular experimental factor observed in the single bead analysis study in Chapter 3. It also complements the findings of the polymers structural implications in response to an acidic environment observed in Chapter 5, by using a tangible formulation system *in situ*.

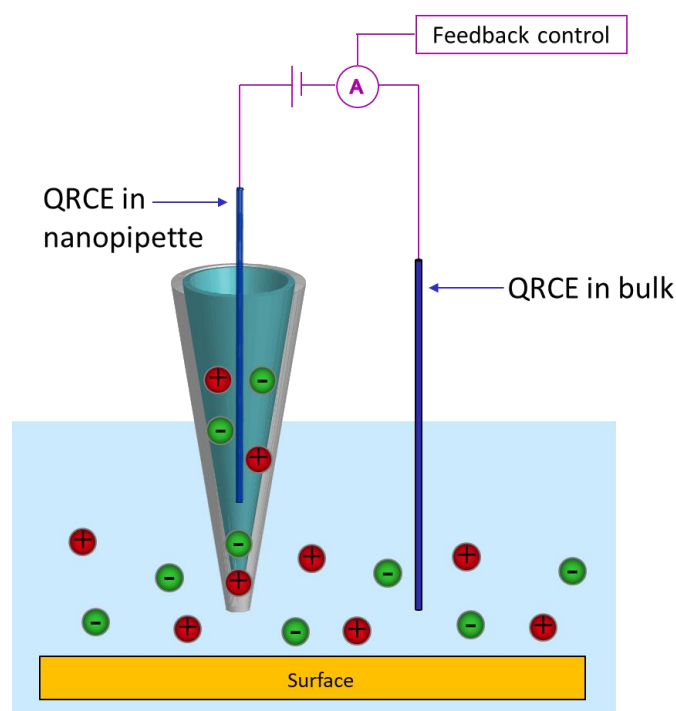


Figure 6.1. Schematic of SICM set up with electrolyte solution filled in the nanopipettes and in the substrate contained bath. One QRCE is placed in the nanopipette, and the other in the bulk electrolyte solution.

The work presented herein demonstrates the versatility of scanning probe techniques by providing a novel insight into the dissolution of the KCSS coating as an isolated film and a MP bead by exploiting the advantages of both SICM and AFM. Furthermore, utilising SICMs ability to map the surface charge of a substrate, the KCSS polymer coated placebo multiparticulate can be examined under electrolyte solution of varying pH, without the interference of drug release. Finite element method simulations were employed in conjunction with SICM to assess the localised charge of the polymer layer and use this to monitor subtle structural changes initiated by the pH of the local environment.

6.1.1. Surface Charge and the Electric Double Layer

When a solid is placed into an aqueous solution, ions may interact and adsorb on the surface or become dissociated. This results in a net positive or net negative charge on the surface,^{3,4,8,10} resulting in the formation of the electric double layer (EDL) at the surface-solution interface. The EDL forms due to the attraction of oppositely charged ions of the surface, or repulsion of ions if they are of the same charge as the surface.

The EDL structure and length from the surface into the solution are dependent on the ionic composition, concentration of bulk solution and the magnitude of the surface charge.^{4,8} There are three main models of the electric double layer, as shown in Figure 6.2. These EDL and the models are discussed in more detail in Chapter 1, Section 1.5.2.2.

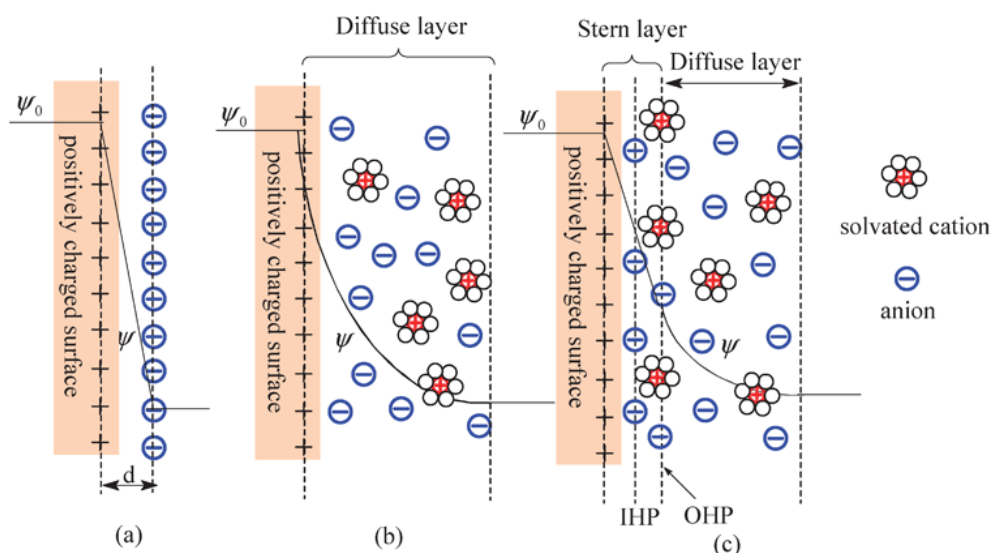


Figure 6.2. Models of the electric double layer at a positively charged surface. a) The Helmholtz model, b) the Gouy-Chapman model, and c) the Stern model. The IHP and OHP are the inner and out Helmholtz plane respectively, d is the double layer distance and Ψ_0 and Ψ are the potentials at the electrode surface and the electrode/electrolyte solution interface, respectively. (Reproduced from Zhang and Zhao, 2009).¹¹

For electrolyte solutions that are dilute and where moderate potentials are used, the Gouy-Chapman model is suitable, whereby the electric potential exponentially decays with increasing distance from charged surface within a solution.^{8,12,13} This decaying distance that the diffuse double layer (DDL) expands into solution is referred to as the Debye length,¹⁴ therefore the EDL can be characterised as a DDL.⁸

In the Gouy-Chapman model, the relationship between the surface charge and the surface potential for a symmetrical electrolyte solution, can be given by,^{8,15}

$$\sigma = (8RT\varepsilon\varepsilon_0C \times 10^3)^{1/2} \sinh\left(\frac{Z\phi_0 F}{2RT}\right) \quad (6.1)$$

where R is the gas constant, T is the absolute temperature, ε the relative dielectric constant of water, ε_0 the permittivity of free space, C the molar concentration, Z the ionic charge of the electrolyte, and F the Faradays constant.

However, for low potentials the double layer thickness (or Debye length) is given by the Debye parameter,^{8,14-16}

$$\kappa = \left(\frac{2F^2 I \times 10^3}{RT\varepsilon\varepsilon_0}\right)^{1/2} \quad (6.2)$$

where I is the ionic strength of the electrolyte by which the reciprocal is the DDL thickness. Thus, the Debye length is given by $1/\kappa$.¹⁴

Therefore, as the value of I increases, the characteristic DDL thickness decreases and *vice versa*.^{8,12} As such, the Debye length characterises the diffuse layer independent of surface charge density which controls the magnitude.¹⁴ This applies when working in low electrolyte concentrations of < 100 mM.¹⁷ For this reason, the SICM experiments conducted herein use 50 mM electrolyte. At high electrolyte concentrations, the DDL becomes compressed (to the point at which the size of individual ions becomes unimportant), the surface charge becomes too great, thus the surface potential is too high, and the Gouy-Chapman model can no longer be accurately relied upon.⁸ This is because there is no parameter that factors the finite size of ions, thus unrealistic surface potentials are calculated at higher concentrations.¹⁸ For the FEM modelling carried out at the end of this chapter the Gouy-Chapman model is used to estimate surface charges as the model holds true for the lower electrolyte concentrations employed.

6.1.2. Ion Current Response

Given that the nanopipette is the probe in the detection of the localised surface charge, its behaviour in the bulk solution must first be considered. A nanopipette is typically made from glass or quartz and as such these materials have a surface chemistry of their own (primarily due to presence of silanol groups), and therefore the surface charge produced at the interface in an electrolyte solution is dependent on the solution properties, such as pH.^{3,8,19} The pK_a for the silanol group dissociation is *ca.* 7.5, depending on the type of glass used. Therefore, for a probe made from a glass of neutral pH typically has a negative surface charge.^{4,8,19} Upon the application of a bias between two Ag/AgCl QRCEs in a bulk solution, without the presence of a nanopipette, the current response is ohmic and linear, and the current is directly proportional to the electrolyte concentration and potential applied.

Therefore, when one QRCE is confined in a nanopipette, this alters the once linear current response, and a rectified current response is observed due to the charge on the walls of the nanopipette shown in Figure 6.3. The geometry of the nanopipette coupled with the asymmetric mass transport rates inside and outside this nanopipette results in the response known as ion current rectification (ICR).^{3,8,20}

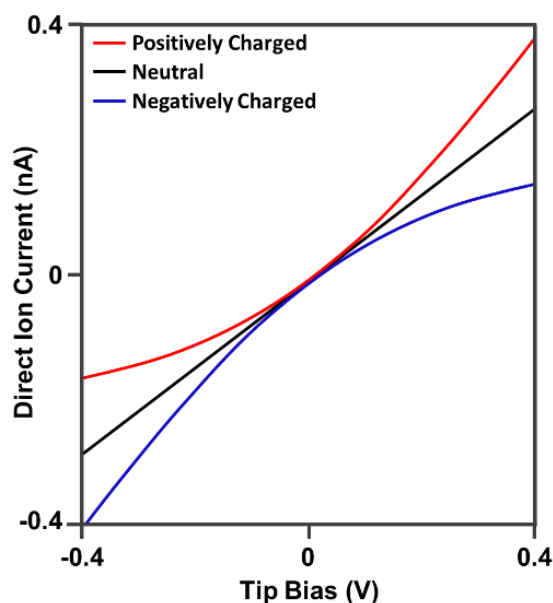


Figure 6.3. Schematic of current-voltage curve for the dependence of surface charge on a nanopipette in bulk solution. Neutral charge of a nanopipette displays an ohmic-current-voltage response, whilst charged nanopipettes have an enhanced current at one bias polarity and a reduction at the other.⁸

If a nanopipette has a negative surface charge, this enhances the current at the negative voltages and a reduction at the positive voltages, relative to the ohmic response. If a nanopipette has a positive surface charge, the inverse is true, resulting in an reverse shape of the current-voltage response (Figure 6.3).⁸

When the nanopipette lumen size is comparable to the size of the DDL, the negative charge at the nanopipette walls produces a region in which positively charged cations can pass, however, the anion flow is inhibited. Therefore, upon the application of a negative bias to the nanopipette QRCE with respect to the bulk, an aggregation of cations occurs as now the diffusion/migration of cations towards the nanopipette is greater than the movement upwards in the nanopipette due to the geometry. Consequently, this enhances the conductance in the nanopipette and produces a greater ionic current. When the bias polarity is reversed, a zone of depletion is formed now that the movement of cations away from the nanopipette is larger than the replacement of cations further inside the nanopipette.²¹⁻²³ Coupled with the surface charge of the nanopipette, this ICR response, is also dependent on the ionic strength of electrolyte within the nanopipette and bulk solution, as well as the size and shape of the nanopipette.^{20,21,24}

As mentioned previously, the SICM substrate can exhibit surface charge, depending on its surface chemistry as well as the electrolyte solution, resulting in the formation of the DDL.^{3,4,23} Typically, SICM experiments are carried out in aqueous solution with a relatively high ionic strength (>10 mM). Thus, the resultant DDL that forms is small, at a sub-nanometre level.^{4,25}

Low biases are used on approach the SICM nanopipette to the surface, as the surface topography can accurately be reproduced independent of the surface charge. This is because the electric field strength from the tip is weak and therefore does not perturb the double layer at the surface.^{5,8,26} When a (high) potential is applied to the tip (pulse potential), the SICM response becomes sensitive to the surface charge of the substrate, resulting in a drop in potential predominately at the tip orifice/tip-substrate channel due to the gap resistance, which causes a flux of ions, as a result the relative surface-solution potential changes. This can occur at large probe-substrate distances as the DDL is perturbed by the electric field at the end of the nanopipette, which results in the extension beyond the usual Debye length.^{26,27}

SICM is sensitive to localised charge at a substrates surface and for tip-substrate distances of similar distances where a standard SICM response is observed. This equates to approximately one tip diameter away from the surface.^{3-5,8} Therefore SICM can provide details regarding the polarity and charge magnitude of a substrate. Upon approach to a charged surface, the ion current response differs to that of on the approach of an uncharged surface. This response depends on the magnitude and the sign applied to the bias, the characteristics of the nanopipette (as previously discussed) and the ionic strength and pH of the bulk solution. This results in surface-induced rectification (SIR).^{3,4,8,26,28}

To be able to understand the mapping of surface charge and the SIR, FEM simulations are employed in order to quantify the surface charge relative to the substrate. This study on the KCSS polymer-coated glass slide and multiparticulate oral dosage form utilises simultaneous topographical and surface charge mapping SICM.

6.2. Experimental

6.2.1. Solutions

The polymer suspension was prepared as described in Chapter 2, Section 2.2, which was then applied to the glass slide for AFM sample preparation. Potassium chloride electrolyte solution (50 mM KCl at pH 5, 7 and 9) for SICM charge mapping were made and the pH adjusted using 0.1 M HCl and 0.1 M NaOH. All solutions were prepared using Purite 18.2 M Ω cm (25 °C) water.

6.2.2. Substrate Preparation

6.2.2.1. Polymer Film Glass Slides

The polymer suspension was spray coated on to the microscopic slide via a spray gun. This differs to the polymer films cast in Chapter 5 which used a control blade coater to coat a glass slide substrate. Once coated, the polymer-coated glass slide was annealed at 70 °C for overnight, in accordance with the literature.^{29–32} The polymer glass slide was then adhered to a glass-bottomed petri dish with detachable coverslips (5000, WillcoWells).

6.2.2.2. Multiparticulate Formulations

Microcrystalline cellulose (MCC) cores were used as starting material was coated with 15 % w/w KCSS 30 D, Stage 2P of formulation, a placebo KCSS coated multiparticulate bead. The KCSS polymer was spray coated using a fluid bed coater via the Wurster process method. The formulation of the MP beads has been discussed in detail in Chapters 2 – 4. A single multiparticulate bead (*ca.* 900 μ m) was adhered to a glass-bottomed petri dish with detachable coverslips (3512, WillcoWells).

6.2.3. Nanopipettes and Electrodes

Nanopipettes were pulled from borosilicate glass capillaries (o.d. 1.2 mm, i.d. 0.69 mm, Harvard Apparatus) using a laser puller (P-2000, Sutter Instruments; pulling parameters 150 nm pipettes: Line 1: Heat 330, Fil 3, Vel 30, Del 220, Pul -; Line 2: Heat 330, Fil 3, Vel 40, Del 180, Pul 120). This pulling of pipettes process results in two identical or ‘sister’ nanopipettes. The inner radius of the probe was measured using a Zeiss Gemini 500 SEM (operating in scanning transmission electron microscopy mode) was found to be $75 \text{ nm} \pm 10 \%$. Two Ag/AgCl electrodes were used, one placed in the nanopipette filled with electrolyte and a second in bulk solution.

6.2.4. Scanning Ion Conductance Microscopy Instrumentation

The setup of basic instrumentation and the SICM charge mapping images were collected using direct current feedback mode, self-referencing hopping scanning mode of SICM has been previously described in detail in Chapter 1, Section 1.6.2.1.^{5,3} The SICM instrumentation was set up within a Faraday cage fitted a camera (Pixelink PL-B776U, 4.0x magnification.) Lateral movement of the probe was controlled using a two-axis *xy* piezoelectric positioning system with a range of $300 \mu\text{m}$ (NanoBioS300, Mad City Laboratories, Inc.), with movement in the *z* direction to the substrate was controlled using a piezoelectric positioning stage of range $38 \mu\text{m}$ (P-753-3CD, Physik Intrumente). The probe position, voltage output, and data collection were user controlled via custom-made programs in LabVIEW (2017, National Instruments) through an FPGA card (7852R, National Instruments). The electrometer and current-voltage converter used were both made in-house but are capable of sub-picoamp current and voltage tracking.

6.2.5. Scanning Ion Conductance Microscopy Maps

Two-dimensional surface maps were generated in hopping mode with a resolution of 40×40 pixels over a $6 \times 6 \mu\text{m}$ area. The SICM probe approached the surface at $3 \mu\text{m/s}$ at an approach bias of -60 mV , until the surface was detected, using a feedback threshold of 2 % of the bulk current value. Upon the tip reaching close contact with the surface (from the defined current decrease), the tip potential was stepped to pulse at 400 mV for 0.5 s , and then back to -60 mV as the tip was retracted from the surface by $3 \mu\text{m}$. The ion current and the z position were recorded continuously and the values at each hop set point, spaced 150 nm apart (x,y) used to create the topography and normalised current maps. This was done by dividing the current measured at the surface by the current measured in the bulk solution at each hop. The topography is simply the recorded z height plotted on a xy grid. All data were processed using MATLAB (2019a, MathWorks).

6.2.6. Atomic Force Microscopy

Before the topographical mapping of the substrates by SICM, topographical maps were recorded in air using an Innova AFM (Bruker, UK) in tapping mode as a comparison. Si-tips on a nitride cantilever were used with a spring constant of 0.35 N/m (RESP-10, Bruker). The scan rate was kept at 3 Hz with a resolution of 512 lines and 512 samples per line. AFM images were processed using the Scanning Probe Image Processor program (SPIP™ 6.0.14, Image Metrology). Details of the image processing is discussed in Chapter 5, Sections 5.2.3 and 5.2.4.

6.2.7. Finite Element Method Simulations

A model of the nanopipette in bulk solution and near a substrate was simulated in COMSOL Multiphysics® (v. 5.4) using the modules Transport of Diluted Species and Electrostatics. Briefly, the dimensions of the nanopipettes were calculated from SEM images of the sister pipettes pulled for each experiment in transmission electron microscopy TEM mode. The design, model and COMSOL calculations were carried out by James Teahan following protocols previously established by the Unwin group.^{3,4,8,26} Further details regarding the modelling are described in Section 6.3.2.2.1, *vide infra*.

6.3. Results and Discussion

From the literature and the results obtained in the previous chapters, it is known that the DEAEMA group in the KCSS polymer becomes protonated at pHs less than its pK_a . The pK_a of DEAEMA monomer is 8.8 pK_a of its corresponding homopolymer are *ca.* 7.3–7.5.^{33–35} This property can therefore be utilised to map the charge of the surface in electrolytes solutions below this pK_a . Firstly, the polymer was topographically mapped as a polymer film and experimental parameters and conditions were established. The swelling nature of the polymer was imaging the film was challenging. However, this preliminary experimentation was the foundation in which the multiparticulate beads could be imaged.

6.3.1. Topographical Mapping of Polymer Film on a Glass Slide

Spray-coated KCSS polymer slides were analysed in air by AFM and were also analysed by SICM (*in situ*) as shown in Figure 6.4.

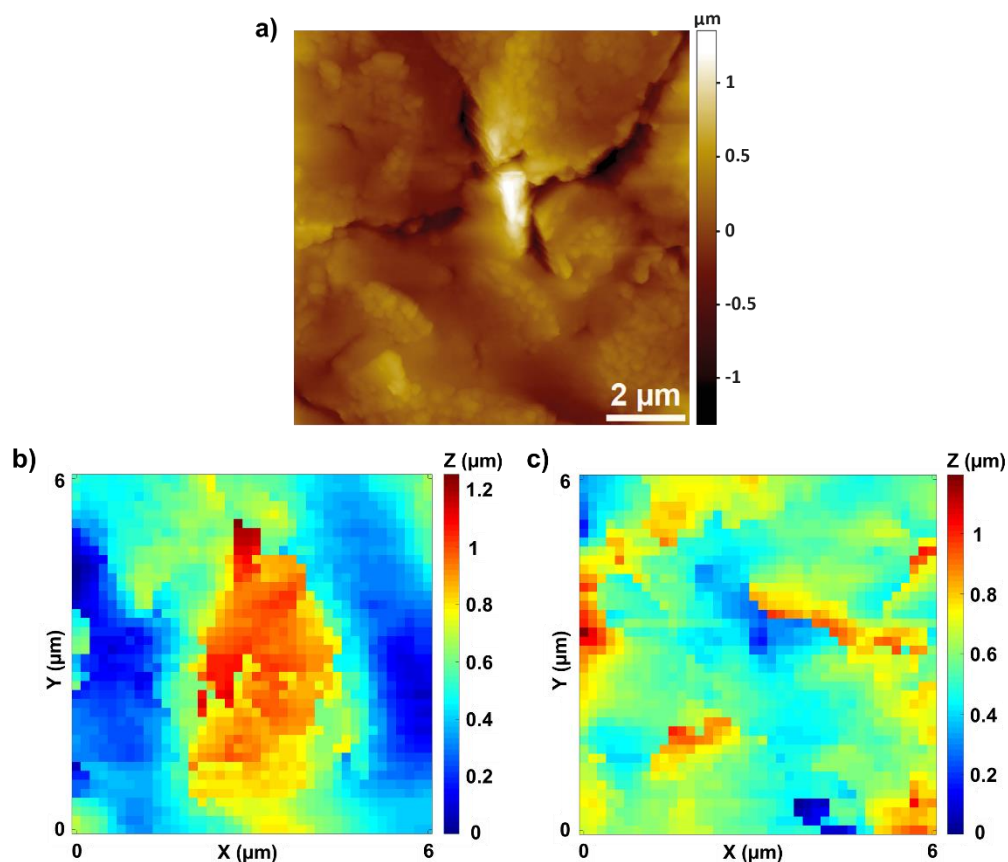


Figure 6.4. AFM and SICM topographical image of KCSS polymer film cast onto a glass slide. a) 10×10 μm area of polymer imaged by in air, b) and c) 6×6 μm area mapped by SICM in 50 mM KCl at pH 7.

From Figure 6.4, the topographical features are observed under AFM analysis show particles of the polymer, along with ‘cracks’ within the polymer film. These ‘cracks’ in the film formation can be observed as boundary layers in the SICM topographical map. Polymer particles are also observable by SICM. The topography between these two techniques is comparable, however, the in-solution effects of the SICM will account of slightly larger height maps and enlarged features due to water uptake.

6.3.2. Simultaneous Topographical and Surface Charge Mapping of a Single Multiparticulate in various pHs

6.3.2.1. Experimental SICM Establishment for Analysis of a Multiparticulate Bead

This section builds upon the electrochemical detection of acetaminophen (APAP) release from a single bead discussed in Chapter 3. However, a high electrode placement precision was achieved due to the use of a nanopipette and a piezo positioner. Additionally, the sample analysed was a placebo KCSS polymer coated multiparticulate, as only the polymers surface and corresponding charge were of interest. Furthermore, any release of APAP may have hindered the overall surface charge, the electrolytes pH and stability, as well as incurring blockages to the nanopipettes tip.

Many variables had to be taken into consideration before performing SICM analysis on the multiparticulate beads. This included, i) the curvature of the bead, ii) the stability of the MP bead in electrolyte solution across a large pH range (pH 5 – 9). It should be noted, that due to the length of time required to set up an SICM experiment (which includes the approach to the substrate), the experiments were not carried out a pHs below 5, as from the data observed in the previous chapters demonstrated the KCSS polymers solubility is much too fast for SICM analysis.

As SICM is an *in situ* technique (Figure 6.5), the resultant images demonstrate the native topography in solution conditions. Therefore, an uptake of water is to be expected, particularly for pH 5 and 7 (due to the pK_a of DEAEMA).^{33–35} Thus, height differences for images produced in air (AFM) and in solution (SICM) are apparent.

Furthermore, the formulation process of the isolated polymer film and the film coating on a multiparticulate will present different results due to the manufacturing process and the substrate itself.

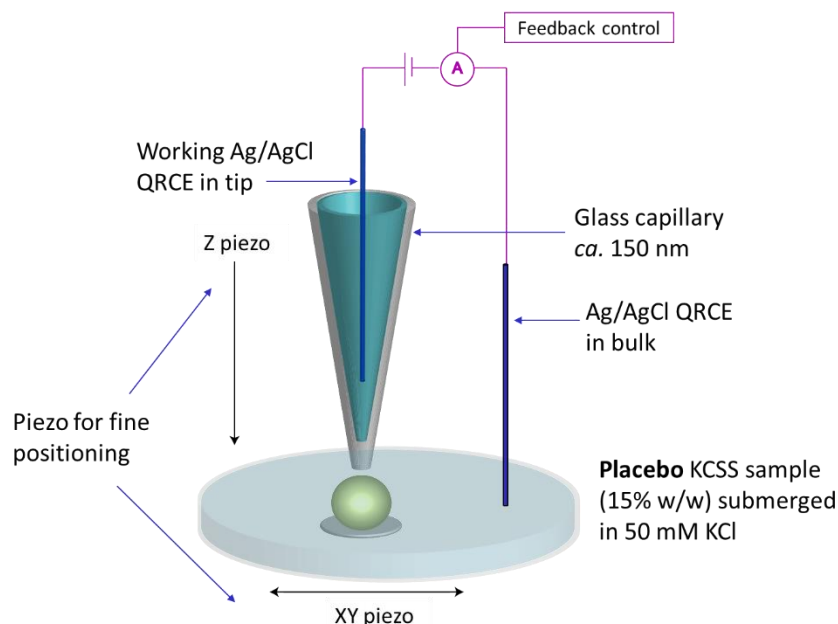


Figure 6.5. Schematic of SICM set up for analysis of a placebo KCSS MP bead in an electrolyte bath, with two QRCE – one placed inside the glass nanopipette and the other placed directly in the bulk. Piezo positioner used for precision of tip positioning. Tip voltage (-60 mV) and pulse (400 mV) used. 0.15 μm hops. (Not to scale).

The topography of a KCSS coated placebo MP bead via AFM imaging is shown in Figure 6.6. Polymer particles are observed that present height differences in the topographical map. Additional images of the KCSS coated placebo MP bead can be found in Chapter 5, Section 5.3.2.

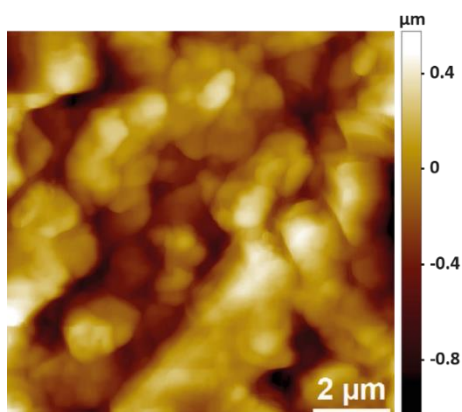


Figure 6.6. AFM image of a $10 \times 10 \mu\text{m}$ area KCSS polymer coated of a MP placebo bead in air.

6.3.2.2. *Topographical and Surface Charge Mapping*

The surface charge information is the measurement of a current-time (i-t) graph both at the surface of the substrate and in bulk solution, whereby the rectification of the current-voltage relationship is a direct result of the DDL between the surface and tip.^{5,36}

A hopping protocol was used in which the probe was translated from the bulk solution to within close proximity of the surface. The approach speed of the probe was 3 $\mu\text{m/s}$ with an applied bias of -60 mV versus the QRCE in bulk. This generated a current of -500 pA, which was utilised in a feedback loop, as the ionic current decreases as the probe approaches the surface. When the current dropped by 2% of its bulk value the probe motion was halted, giving rise to the sensitive positional feedback.

A potential pulse to the nanopipette when at the surface, of +400 mV, was applied for *ca.* 0.5 s. Upon the application of this pulse potential the double layer at the surface is disturbed, causing its ionic constituents to contribute to the measured current. No such enhancement of the current is seen in bulk. This current is then normalised to calculate the contribution of the charged ions at the surface resulting in a functional charge map to complement the topographic image.

From the data in Figure 6.7, it can be observed that at pH 5, topographical boundary layers are observed, these boundary layers appear to correlate to the surface charge. The surface charge data in Figures 6.7 – 6.9 is given in terms of the normalised current, whereby this normalised current value is relative to the direct ion current, where the tip current at the surface is divided by the bulk response during a potential pulse.⁸

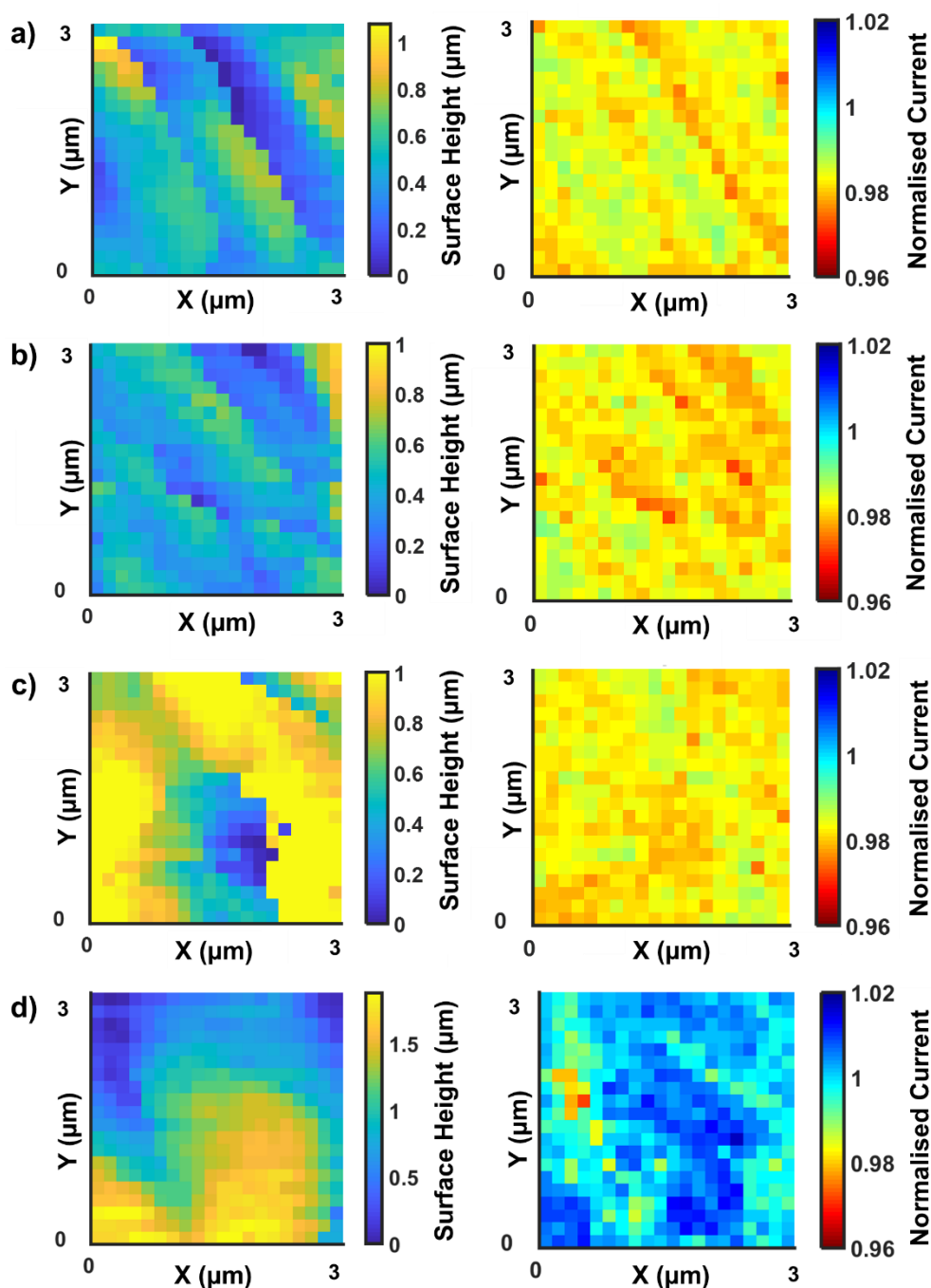


Figure 6.7. Topography and surface charge (as reflected in the normalised current measurement) of a $6 \times 6 \mu\text{m}$ area of a placebo KCSS coated MP bead at pH 5. a) – d) indicates different scans of different placebo beads, topographical maps (left) and corresponding surface charge maps (right). In the normalised current scale red denotes positively charged and blue denotes negatively charge.

At pH 5 and 7, Figures 6.7 and 6.8, when the surface is at its lowest height this relates to the most positively charged (red) area of the sample. At the highest point of the surface the inverse is true. Similar features are shown in both the topographical and charge maps thus demonstrates the relationship between the two.

From this, it can be construed that there is some protonation of the tertiary amine groups giving rise to the positive charge of the surface. The separation of charge occurs in boundary lines and circular openings from the expansion of polymer chains. These features from topographical and the corresponding charge maps correlate with the structural changes of the polymer dissolution under acidic conditions in Chapter 5.

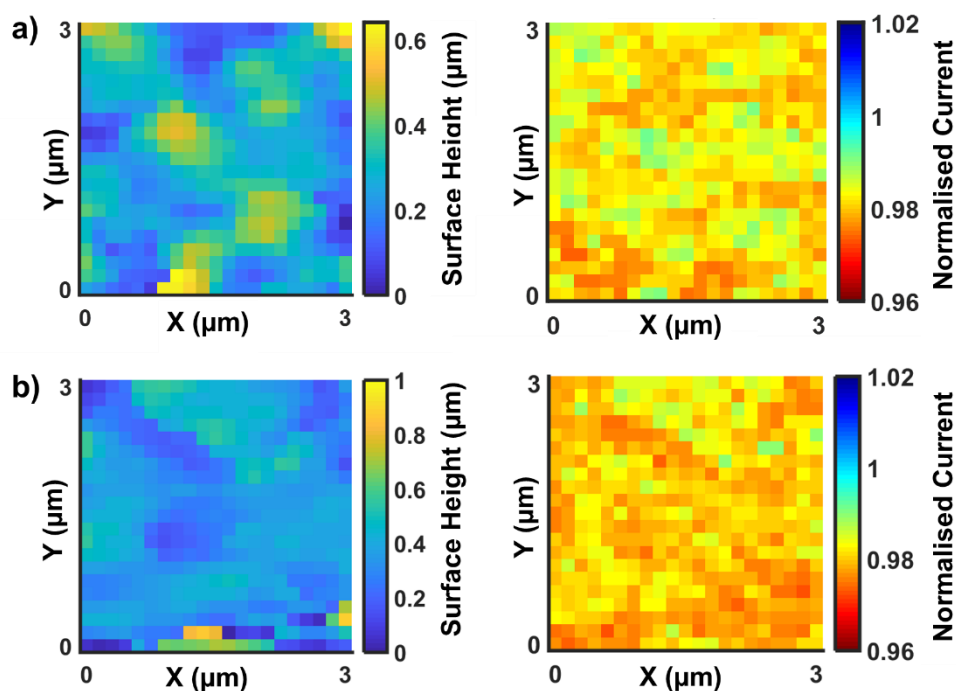


Figure 6.8. Topography and surface charge (as reflected in the normalised current measurement) of a $6 \times 6 \mu\text{m}$ area of a placebo KCSS coated MP bead at pH 7. a) and b) indicates different scans of different placebo beads, topographical maps (left) and corresponding surface charge maps (right). In the normalised current scale red denotes positively charged and blue denotes negatively charge.

This normalised ion current, is subsequently converted into surface charge density via FEM modelling simulations *vide infra*, Section 6.2.7.

For pH 9 (Figure 6.9), from the topography and charge maps produced, a slight separation of charge is observed. However, the normalised current values are not directly comparable to the values observed for pH 5 and 7. This is due to an increase in the surface charge of the nanopipette which causes an increase in the ICR in the bulk and at the surface. The FEM modelling for the conversion of the normalised current to the surface charge (*vide infra*) was unable to match the experimental rectification, which was way beyond the model limitations and would have estimated surface charge very poorly.

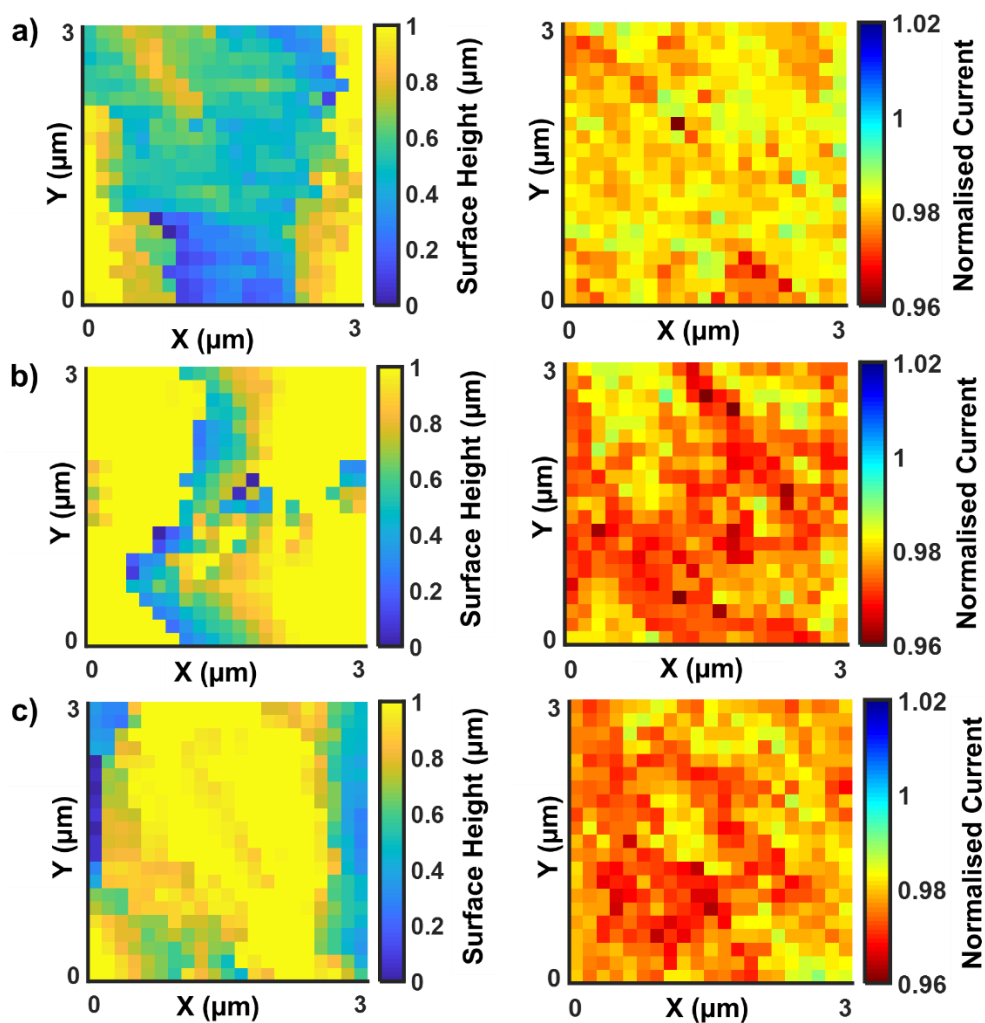


Figure 6.9. Topography and surface charge (as reflected in the normalised current measurement) of a $6 \times 6 \mu\text{m}$ area of a placebo KCSS coated MP bead at pH 9. a) – c) indicates different scans of different placebo beads, topographical maps (left) and corresponding surface charge maps (right). In the normalised current scale red denotes positively charged and blue denotes negatively charge.

From the literature it is known that at higher pHs, above the pK_a the tertiary amine groups of DEAEMA are deprotonated, and the polymer is largely uncharged in a collapsed state.³⁷ This results in the domination of hydrophobic interactions over electrostatic repulsion forces.^{37,38} However, the hydrolysis half-life of DEAEMA is 3.31 hours at pH 9 at 25 °C.^{34,39} Therefore, under these conditions the methacrylic acid (MAA) could be present at the surface as a result of hydrolysis of DEAEMA. MMA is a small molecule with a free carboxyl group that is negatively charged at physiological pH.⁴⁰ However, without the FEM modelling, the surface charge of the polymer layer at this pH cannot be confidently determined.

6.3.2.2.1. *Conversion of Normalised Current to Surface Charge Density by FEM Simulations*

As briefly mentioned in Experimental Section 6.2.7, the geometry of the nanopipette is measured using scanning transmission electron microscopy (STEM) images from different angles. Typically, the ‘sister’ pipette of the nanopipette used during the SICM scan is imaged to ensure the model is as accurate as possible. Additionally, the components of the electrolyte and the biases applied to the electrode upon approach to the surface during the scan are also incorporated into the model. Figure 6.10 shows the STEM images taken of the ‘sister’ nanopipette for the SICM scan of the MP bead at pH 5.

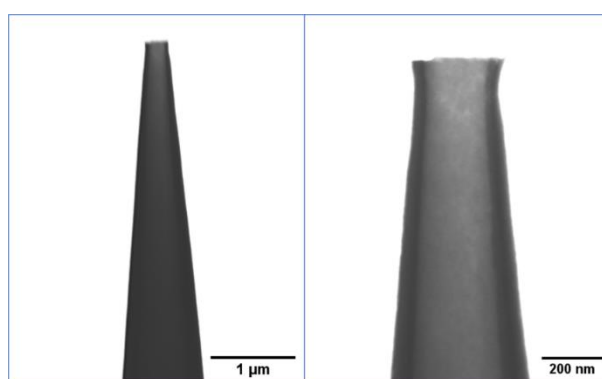


Figure 6.10. STEM images of sister nanopipettes used in SICM mapping of KCSS polymer coated placebo beads. Example of STEM images of borosilicate glass nanopipettes pulled with an inner radius of $75 \text{ nm} \pm 10 \%$. (sister nanopipettes of probes used in one of the pH 5 SICM scans.)

The dimensions and geometry (inner and outer radius) from the STEM images of the nanopipettes is then used to produce the nanopipettes simulation domain of the model in COMSOL. This is shown in Figure 6.11, where the resultant model has been taken from COMSOL. The model is in a 2D axisymmetric cylindrical geometry, making use of the cylindrical symmetry axis. The surface charge of the glass nanopipettes is then modelled and the boundaries defined by the areas where there is no flux. The initial values of the voltages are the applied to the boundary at the top of the nanopipette as well as the right-hand side of the bulk solution, which represents a distance of $100\ \mu\text{m}$ from the nanopipette. This region extends beyond the where static interactions occur and sufficiently far away to be considered as bulk concentrations.

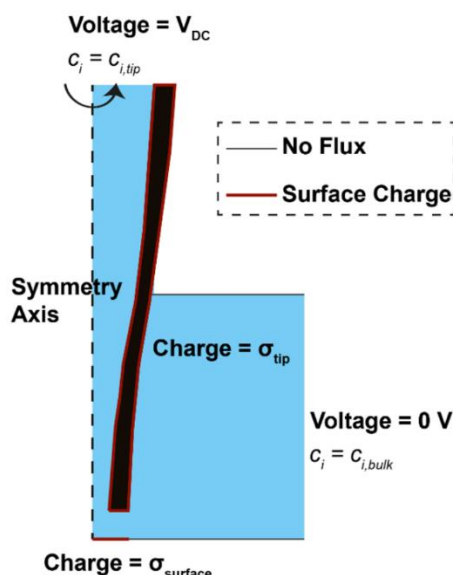


Figure 6.11. Schematic of typical nanopipette geometry used in FEM simulation modelling of the boundary conditions, where no flux is applied to the nanopipette walls and bulk boundaries. The red line at the bottom left indicates the surface charge of the sample. The tip potential V_{DC} was applied to the nanopipettes top boundary with respect to the bulk boundary. Obtained and reproduced from COMSOL.

Once the geometry has been constructed, the electrolyte concentrations, initial biases and permanent fluxes are applied to the corresponding boundaries. The current-voltage is modelled in bulk solution (at a distance of $1\ \mu\text{m}$ from the surface) and this is compared to the experimentally obtained current-voltage graph, as shown in (Figure 6.12).

If the simulated and experimental current-voltage graph is comparable, then the nanopipette current at variable distance, d , from the charge surface can be simulated. If they are not the same, adjustments to the surface charge on the nanopipette and minor geometric changes are made to the nanopipette to get a better match.

Consequently, a 2 % drop in current is simulated to obtain a model for the approach to the substrates surface at the approach distance, d at each hop. Then the nanopipette is modelled at different separation distances from a nominally charged surface, *i.e.* starting at 1 μm , followed by sequentially smaller increments of 0.1 μm until *ca.* 0.7 μm , increments then follow on from 200 nm decreasing in increments of 10 nm until reaching 30 nm which provides the current at each distance. When the current value produced by the model is 98 % of the bulk value calculated in the simulation, this demonstrates how close the nanopipette is on each approach, this is usually around 40 nm.

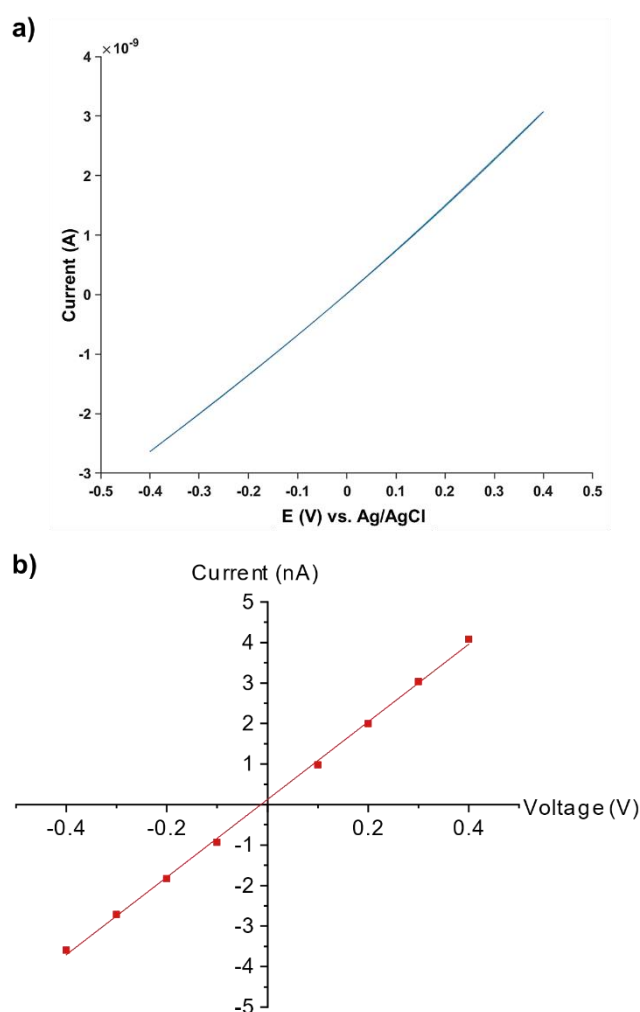


Figure 6.12. Current-voltage graphs obtained from the electrolyte bulk. a) experimentally for pH 5 and b) FEM simulation in bulk for both pH 5 and 7.

Once the distance, d value is obtained, different surface charge values in the area underneath the nanopipette is then simulated. A range of values from -150 mC m^{-2} to $+150 \text{ mC m}^{-2}$ are calculated in a step wise manner, usually in increments of 10 mC m^{-2} . This produces a calibration curve that allows the conversion of the normalised current and approximated surface charge.

Thus, the COMSOL model simulates the nanopipette geometry with the surface and corresponding environmental factors and calculates the perceived surface charge of a substrate, which results in the conversion of the normalised current to a value of surface charge. The i - t pulses in the bulk solution and the distance from the surface with a varying surface charge, σ is simulated. Thus, the calibration for the surface charge relative to the normalised current at distance d is obtained as shown in Figure 6.13.

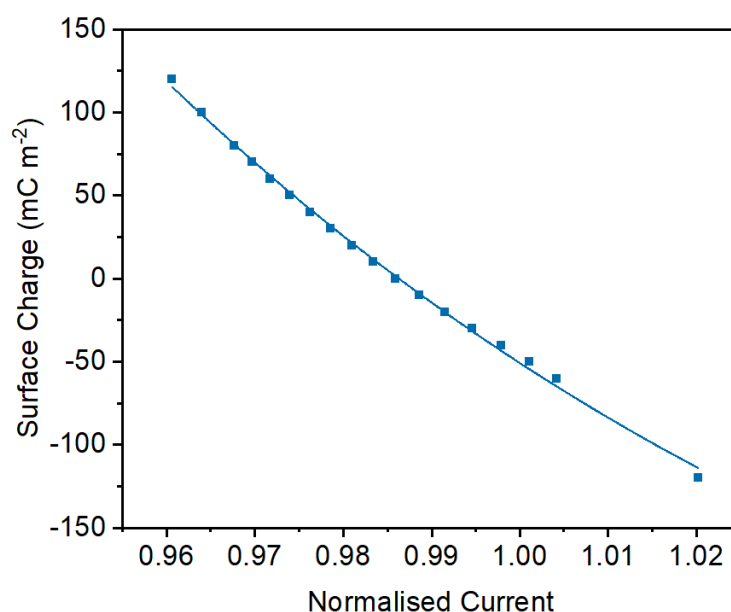


Figure 6.13. Simulated dependence of the normalised current on the surface charge density values in mC m^{-2} of the KCSS coated placebo MP bead, used to generate the quantified charge maps shown for pH 5 and 7 in Figure 6.8.

Therefore, from the application of this model, under the conditions for pH 5 and 7 a normalised ion current of 1.02 and 0.96 equates to -120 and 120 mC m^{-2} , respectively. The resultant charge maps for pH 5 and 7 are shown in Figure 6.14.

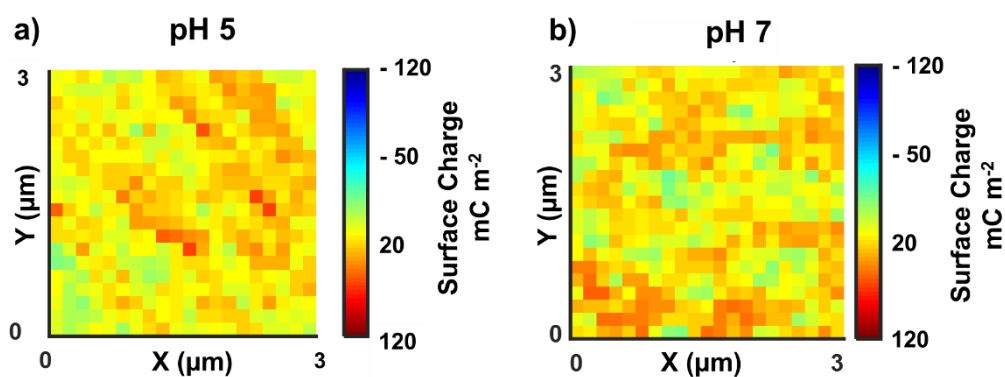


Figure 6.14. FEM calculated surface charge for the KCSS polymer layer of a placebo MP bead at pH 5 and 7.

At pH 9, this COMSOL model was not valid, which could be attributed to the surface charge of the borosilicate glass nanopipette itself, where at this pH the charge on the nanopipette walls is too great. This was confirmed by the model and in the literature,¹⁹ as the values produced were unreasonable and did not align with the experimental values.

6.4. Conclusions

This chapter demonstrated the simultaneous application of topographical and surface charge mapping using FEM modelling as a valuable tool for elucidating the charge distribution of a polymer coated multiparticulate oral dosage form surface in various pH electrolyte solutions. One drawback in the SICM method for this particular analysis, was that the pH conditions had to be higher than desired, as the set up and approach to the surface is a lengthy process and the protonation of the KCSS polymer occurs on a rapid scale as observed in earlier chapters of this thesis. However, the charge distribution was able to be shown under the chosen pH range, which have a clear correlation to the topography observed. Furthermore, the *in situ* SICM topographical and surface charge maps demonstrate a visual correspondence with the topographical maps obtained in air by AFM.

The application of SICM to this substrate has exhibited a wider platform of substrates that can be analysed. This, therefore, sets the foundation for further analysis of pharmaceutical substrates under *in situ* conditions. For further application of this technique, future work would include the improved capability of the modelling at higher pHs, to understand the polymer surface outside of a physiological pH range. Moreover, the use of a smaller nanopipette size would increase the resolution of the images and consequently provide a deeper insight.

6.5. References

1. Hansma, P., Drake, B., Marti, O., Gould, S. & Prater, C. The Scanning Ion-Conductance Microscope. *Science* (80-.). **243**, 641–643 (1989).
2. Chen, C.-C., Zhou, Y. & Baker, L. A. Scanning Ion Conductance Microscopy. *Annu. Rev. Anal. Chem.* **5**, 207–228 (2012).
3. Perry, D., Al Botros, R., Momotenko, D., Kinnear, S. L. & Unwin, P. R. Simultaneous Nanoscale Surface Charge and Topographical Mapping. *ACS Nano* **9**, 7266–7276 (2015).
4. McKelvey, K., Kinnear, S. L., Perry, D., Momotenko, D. & Unwin, P. R. Surface Charge Mapping with a Nanopipette. *J. Am. Chem. Soc.* **136**, 13735–13744 (2014).
5. Page, A. *et al.* Fast nanoscale surface charge mapping with pulsed-potential scanning ion conductance microscopy. *Anal. Chem.* **88**, 10854–10859 (2016).
6. Korchev, Y. E., Bashford, C. L., Milovanovic, M., Vodyanoy, I. & Lab, M. J. Scanning ion conductance microscopy of living cells. *Biophys. J.* **73**, 653–658 (1997).
7. Zhu, C., Zhou, L., Choi, M. & Baker, L. A. Mapping Surface Charge of Individual Microdomains with Scanning Ion Conductance Microscopy. *ChemElectroChem* **5**, 2986–2990 (2018).
8. Page, A., Perry, D. & Unwin, P. R. Multifunctional scanning ion conductance microscopy. *Proc. R. Soc. A Math. Phys. Eng. Sci.* **473**, (2017).
9. Schäffer, T. E., Anczykowski, B. & Fuchs, H. Scanning Ion Conductance Microscopy. in *Applied Scanning Probe Methods II. NanoScience and Technology* (eds. Bhushan, B. & Fuchs, H.) 91–119 (Springer, 2006). doi:10.1007/3-540-27453-7_3
10. Kang, M., Momotenko, D., Page, A., Perry, D. & Unwin, P. R. Frontiers in Nanoscale Electrochemical Imaging: Faster, Multifunctional, and Ultrasensitive. *Langmuir* **32**, 7993–8008 (2016).
11. Zhang, L. & Zhao, X. S. Carbon-based materials as supercapacitor electrodes. *Chem. Soc. Rev.* **38**, 2520–2531 (2009).
12. Waegle, M. M., Gunathunge, C. M., Li, J. & Li, X. How cations affect the electric double layer and the rates and selectivity of electrocatalytic processes. *J. Chem. Phys.* **151**, 160902 (2019).
13. Unwin, P. R. & Bard, A. J. Scanning electrochemical microscopy. 14. Scanning electrochemical microscope induced desorption: a new technique for the measurement of adsorption/desorption kinetics and surface diffusion rates at the solid/liquid interface. *J. Phys. Chem.* **96**, 5035–5045 (1992).

14. Facci, P. Useful Notions in Electrochemistry. in *Biomolecular Electronics* 19–47 (Elsevier, 2014). doi:10.1016/B978-1-4557-3142-8.00002-9
15. Bard, A. J. & Faulkner, L. R. *Electrochemical Methods: Fundamentals and Applications*. (2001).
16. Selvamani, V. Stability Studies on Nanomaterials Used in Drugs. in *Characterization and Biology of Nanomaterials for Drug Delivery* 425–444 (Elsevier, 2019). doi:10.1016/B978-0-12-814031-4.00015-5
17. Elimelech, M., Gregory, J., Jia, X. & Williams, R. A. Electrical properties of interfaces. in *Particle Deposition & Aggregation* 9–32 (Elsevier, 1995). doi:10.1016/B978-075067024-1/50002-9
18. Westall, J. & Hohl, H. A comparison of electrostatic models for the oxide/solution interface. *Adv. Colloid Interface Sci.* **12**, 265–294 (1980).
19. Behrens, S. H. & Grier, D. G. The charge of glass and silica surfaces. *J. Chem. Phys.* **115**, 6716–6721 (2001).
20. White, H. S. & Bund, A. Ion Current Rectification at Nanopores in Glass Membranes. *Langmuir* **24**, 2212–2218 (2008).
21. Momotenko, D. *et al.* Ion current rectification and rectification inversion in conical nanopores: a perm-selective view. *Phys. Chem. Chem. Phys.* **13**, 5430 (2011).
22. Perry, D., Momotenko, D., Lazenby, R. A., Kang, M. & Unwin, P. R. Characterization of Nanopipettes. *Anal. Chem.* **88**, 5523–5530 (2016).
23. Perry, D. *et al.* Surface Charge Visualization at Viable Living Cells. *J. Am. Chem. Soc.* **138**, 3152–3160 (2016).
24. Wei, C., Bard, A. J. & Feldberg, S. W. Current Rectification at Quartz Nanopipet Electrodes. *Anal. Chem.* **69**, 4627–4633 (1997).
25. Klenerman, D., Korchev, Y. E. & Davis, S. J. Imaging and characterisation of the surface of live cells. *Current Opinion in Chemical Biology* **15**, 696–703 (2011).
26. Maddar, F. M., Perry, D., Brooks, R., Page, A. & Unwin, P. R. Nanoscale Surface Charge Visualization of Human Hair. *Anal. Chem.* **91**, 4632–4639 (2019).
27. Perry, D., Page, A., Chen, B., Frenguelli, B. G. & Unwin, P. R. Differential-Concentration Scanning Ion Conductance Microscopy. *Anal. Chem.* **89**, 12458–12465 (2017).
28. Soltys, M. M., Yaremko, Z. M., Tkachenko, N. H. & Havryliv, V. D. Poly(methacrylic acid) Adsorption and Electrical Surface Properties of Titanium Dioxide Suspensions. *Adsorpt. Sci. Technol.* **20**, 633–645 (2002).

-
29. Kucera, S. A., Felton, L. A. & McGinity, J. W. Physical aging in pharmaceutical polymers and the effect on solid oral dosage form stability. *Int. J. Pharm.* **457**, 428–436 (2013).
 30. Yang, Q. W. *et al.* European Journal of Pharmaceutics and Biopharmaceutics Curing of aqueous polymeric film coatings : Importance of the coating level and type of plasticizer. *Eur. J. Pharm. Biopharm.* **74**, 362–370 (2010).
 31. Bodmeier, R. & Paeratakul, O. Plasticizer uptake by aqueous colloidal polymer dispersions used for the coating of solid dosage forms. *Int. J. Pharm.* **152**, 17–26 (1997).
 32. Wang, Y., Juhué, D., Winnik, M. A., Leung, O. M. & Goh, M. C. Atomic Force Microscopy Study of Latex Film Formation. *Langmuir* **8**, 760–762 (1992).
 33. Van De Wetering, P., Moret, E. E., Schuurmans-Nieuwenbroek, N. M. E., Van Steenberghe, M. J. & Hennink, W. E. Structure-activity relationships of water-soluble cationic methacrylate/methacrylamide polymers for nonviral gene delivery. *Bioconjug. Chem.* **10**, 589–597 (1999).
 34. Darabi, A., Shirin-Abadi, A. R., Jessop, P. G. & Cunningham, M. F. Nitroxide-Mediated Polymerization of 2-(Diethylamino)ethyl Methacrylate (DEAEMA) in Water. *Macromolecules* **48**, 72–80 (2015).
 35. Constantinou, A. P., Lan, T., Carroll, D. R. & Georgiou, T. K. Tricomponent thermoresponsive polymers based on an amine-containing monomer with tuneable hydrophobicity: Effect of composition. *Eur. Polym. J.* **130**, 1–11 (2020).
 36. Sa, N. & Baker, L. A. Rectification of nanopores at surfaces. *J. Am. Chem. Soc.* **133**, 10398–10401 (2011).
 37. Willott, J. D. *et al.* Anion-Specific Effects on the Behavior of pH-Sensitive Polybasic Brushes. *Langmuir* **31**, 3707–3717 (2015).
 38. Aguilar, M. R. & San Román, J. Smart Polymers and their Applications. *Smart Polym. their Appl.* **3**, 1–568 (2014).
 39. Information, N. C. for B. Compound Summary for CID 61012; 2-(Diethylamino)ethyl methacrylate. *PubChem Compound Database* (2004).
 40. Park, S. E., Chao, M. & Raj, P. A. Mechanical Properties of Surface-Charged Poly(Methyl Methacrylate) as Denture Resins. *Int. J. Dent.* **2009**, 1–6 (2009).

Chapter 7

Conclusions

The fundamental understanding of the dissolution kinetics and mechanisms for polymer-coated oral dosage forms are of great importance in pharmaceutical science. Thus, the use of electrochemical and scanning probe methods for pharmaceutical analysis is of increasing interest.

This thesis focuses on the development of electrochemical and scanning probe methods to study the release of an active pharmaceutical ingredient (API) from a model multiparticulate (MP) solid oral dosage form, coated in a pH responsive taste masking polymer. The MP formulation was prepared in the laboratory of an industrial partner (Pfizer, Sandwich, UK) from redox active acetaminophen (APAP) and coated in the methyl methacrylate (MMA), 2-(diethylamino)ethyl methacrylate (DEAEMA) copolymer, the Kollicoat[®] Smartseal 30 D (KCSS, BASF). As a pH responsive polymer, KCSS is known to be soluble in acidic media for $\text{pH} \leq 5.5$, due to protonation of the tertiary amine groups present in DEAEMA.

Chapter 3 examined the constituent beads of the MP formulation as single entities. Firstly, the particle size distribution and the variation of the APAP and KCSS layer thickness that resulted from the formulation process was investigated using optical microscopy and scanning electron microscopy at each layering stage. It was found that the APAP and the KCSS layer thicknesses varied in between MP beads. Furthermore, the variation of the APAP layer only (absent of the KCSS polymer layer) was also studied by placing a single MP bead in 0.1 M HCl dissolution media (DM) that mimicked the pH of gastric acid for a 24-hour period. The resultant solution was electrochemically analysed with and without agitation of the solution the using cyclic voltammetry with an ultramicroelectrode (UME). It was shown that agitation increased the current density, resulting in an increase in the APAP concentration released. The variation observed in the particle size distribution matched the variation detected in the electrochemical cyclic voltammograms performed on the resultant solution after APAPs release into the bulk DM.

The release of APAP from the MP formulation with and without the KCSS layer in DM 0.1 M and 0.01 M HCl was investigated *in situ* in real time, using a microwire electrode closely positioned to the surface of the MP bead. This method allowed for the detection of API release at the early stages, which is typically missed under the traditional dissolution methods.

It was found that without the polymer layer, the release of APAP was almost instant, and when coated with KCSS, this delayed APAPs release into the bulk solution. Furthermore, it was observed that increasing the pH further delayed APAPs release.

Whilst this method provided valuable insight to the modulation of the API release from this KCSS coating, experimental challenges such as accurate determination of the electrode tip-bead distance had a significant effect on the results, highlighting the need for further developments in this area. However, as an exploratory study into the variation between beads in MP formulations and using the ability to detect API release electrochemically on a small scale, it was successful.

Chapter 4 built upon the foundations in Chapter 3, but this time considered the case of dissolution from multiple MP beads to mimic a real dose. It utilised the rotating disc electrode (RDE) in a way that differs from typical RDE use in the literature. Whereas the drug containing tablet or powder is conventionally compressed onto the electrode's surface, the RDE method explored here suspended the MP beads in the DM. This is a modification of the USP apparatus II, where now hydrodynamic parameters are known and the API concentration can be assessed *in situ*, in contrast to conventional dissolution testing that requires additional analytical methods such as HPLC to quantify the drug release and kinetics.

This study investigated the release of APAP from the KCSS polymer-coated MP beads in buffered and unbuffered dissolution media of varying pH (pH 2 – 6.8) at different temperatures and concentrations. It was found that for gastric conditions mimicked using HCl DM, complete dissolution of APAP occurred for pH 2 – 3, as observed by similar final concentrations found in the resultant bulk solution, with the majority of dissolution occurring within 15 minutes. However, for pH 3.5 and 4, minimal dissolution occurred after a longer time period of 90 minutes. It was observed that increasing the temperature of the HCl DM in the range of 20 – 40 °C increased the rate of release, however, the final concentration was unaffected. In contrast, for buffered media (acetate and citrate at 25 and 100 mM for pHs up to 5), complete dissolution was shown to occur for all pHs (up to 5), yielding a similar final concentration across the pHs. The resultant APAP concentrations for pH above 3.5 were comparable to the unbuffered HCl DM below pH 3.

This phenomenon was described as the ‘buffer effect’, where a reserve of H^+ provided by the buffered DM contributed to the protonation of the tertiary amine groups of DEAEMA. Conversely, simulated saliva (pH 6.8), whilst a buffered media, led to negligible amounts of APAP being released over a 90 minute period. KCSS is typically protonated by pHs ≤ 5.5 , thus, at the neutral pH of simulated saliva there was minimal release of APAP across an extended period of time. This therefore demonstrates the suitability of the KCSS polymer as an effective taste masking layer

Through a simplified calculation of the diffusion in the system, it was estimated that the KCSS polymer does not require complete protonation for APAP to be released, partially explaining the speed at which APAP is detected following the onset of dissolution. While this study has demonstrated significant advantages of the RDE for dissolution testing, one particular challenge remains, relating to the fouling of the electrode at long times or elevated temperatures. It is demonstrated that this can be mitigated by working at short timescales and in future this could potentially be remedied by the use of an electrode of more fouling-resistant material. Overall, this method has been shown to be an effective method for tracking the dissolution profile under rapid dissolution conditions at short timescales, capturing information that may otherwise be lost with traditional methods.

The *in situ* dissolution measurements in the previous chapters highlighted the rapid onset of API release following the onset of dissolution at both the single bead and dosage level. Furthermore, from the literature, the protonation of DEAEMA results in the swelling of the polymer due to electrostatic repulsion. Therefore, to investigate the mechanisms underlying API release, further microstructural analysis was carried out in Chapter 5. This study was carried out on an isolated polymer film, where the KCSS polymer was cast onto a glass slide and a film was formed at two temperatures (70 °C and 90 °C), both above the minimum film forming temperature and glass transition temperature required to make a continuous film from the KCSS polymer. and the films were placed into contact with an acidic environment (0.01 M HCl) and subsequently removed and imaged using atomic force microscopy (AFM) at different time intervals during the dissolution process.

Here, the swelling process and opening of the polymer chains were topographically investigated and pore-particle analysis was conducted on the resultant AFM images using the Scanning Probe Image Processor program (SPIP™ 6.0.14, Image Metrology).

It was observed that polymer particles were present within the film formed at 70 °C, but these particles were not present in the film formed at 90 °C. The dissolution process demonstrated the same mechanism at both temperatures, however. At the higher temperature, the dissolution took approximately three times longer to be complete – *i.e.*, the time taken for the film to disappear, and the glass underneath to be exposed. This demonstrated the effect the film forming process had on the resultant dissolution and indicates its importance in designing formulations for API release.

Furthermore, the chemical composition of the polymer was investigated using nuclear magnetic resonance (NMR) spectroscopy and compared to the chemical composition that had been treated with 0.01 M HCl for 24 hours, 7, 14 21 and 28 days. It was confirmed that protonation of the tertiary amine group on DEAEMA had occurred and that no other reactions were involved.

To investigate the morphology of the polymer *in situ* during dissolution, *in situ* AFM studies were attempted, however, the acidic conditions made the film ‘tacky’ and unsuitable for further analysis. Thus, scanning ion conductance microscopy (SICM) was implemented in Chapter 6. SICM measures the variation in the flux of ions through a nanopipette as it is translated towards a surface. This method allows the topography to be measured and under certain conditions is also sensitive to localised charge at the surface.

The topography and the charge distribution of the KCSS polymer surface of a MP bead was studied *in situ* at pH 5, 7 and 9. By comparison with finite element method (FEM) simulations, it was shown that at pH 5 and 7 the lower height regions appeared to possess a more positively charged surface, compared to higher neighbouring regions. This complements the observed microstructural changes seen under AFM analysis in Chapter 5.

Measurements at pH 9, would be expected to show a more neutral surface in a basic environment was not as easily analysed due to limitations of the FEM simulation model at the high nanopipette wall charges expected at this pH. This technique was demonstrated to be a useful tool for *in situ* topographical and charge mapping analysis of a pH responsive substrate.

As SICM experiments are a lengthy process and therefore it has been demonstrated that some protonation occurs at a neutral pH on a microstructural level on an extended time period, this seems likely given that the pK_a of DEAEMA is *ca.* 7.3. However, as observed in Chapter 4 at this pH, any protonation that may occur is not critical enough to allow for significant dissolution to occur on a more practical time scale. Thus, demonstrating the KCSS polymers effectiveness as a taste masker.

Overall, this thesis utilised micro- and macro-scale electrochemical methods and scanning probe methods in a unique way to study API dissolution kinetics, as well as the investigation of a pH responsive taste masking polymer. The work presented has achieved the initial research goals in gaining insight into API dissolution kinetics and the mechanism by which the polymer releases the API. Whilst rapid acidic dissolution conditions represent challenges for conventional characterisation techniques (USP dissolution methods of analysis), novel methods based on electrochemical and scanning probe methods can be applied to provide informative, complementary data.

Appendix

MATLAB Script

Full MATLAB script for the topographical and charge mapping analysis of the polymer film presented in Chapter 6.

A) SICM Topography Only Script

```
%A=load('Filename.tsv');%load data in as A, comment out after
already loaded to save time on future runs
%%
%CV at surface only
set(0,'DefaultFigureColormap',feval('jet'))
close all
movie=0;
Extract_data=0;%1 if running for first time, 0 if data already
loaded
time_to_plot=180000;%what part of IT curve to plot in us (can
change time to plot single frame still)
hopping_distance=0.15;%in um
channel_to_plot=3;% 3 is topography
channel_line_number=11;
channel_voltage=8;
channel_dc=4;
channel_xdata=1;
channel_ydata=2;
channel_zdata=3;
channel_phase=13;
channel_amp=12;
frame_to_plot=0;%0 whole movie, or individual frame if not 0.
remove_topog_drift=1;%1 (drift removed) or 0 (topo drift)
startpoint=1;
endpoint=6500;
correctstart=1;
correctend=6561;
datapointtime=4*256;
pulsetime=20000;
normalise=2;%0 no normalise, 1 normalise to bulk subtraction,2
normalise to bulk division, 3 plot bulk
fixcbar=2;
%1. Fix between maximum and minimum over whole scan
%2. Colourbar for each frame
labelsize=20;
last_line = max(A(channel_line_number,:));
lines_in_hop=7;%number of lines between each approach
```

```

first_approach=2;%9 normally, 2 if small hopping distance
<=150nm
first_surface_IT=first_approach+1;%line number for first part
of first cv
first_bulk_IT=first_surface_IT+3;
%If you want to crop
if Extract_data==0
XMIN=1;%line number you want to crop from and to
XMAX=61;
YMIN=1;
YMAX=61;
end
if Extract_data==1
%%
%Make X, Y Grid for plots
%Extract topography
count1=1;
count2=1;
h1 = waitbar(0, 'Initializing Topography waitbar...');
for i=[first_approach:lines_in_hop:last_line]
    %if(mod(count2,x+1)~=1)
        b=A(:,A(channel_line_number,:)==i);%picks out
approaches by line number
        XMapreal(count1)=mean(b(channel_xdata,:));
        YMapreal(count1)=mean(b(channel_ydata,:));
        appcurrent(count1)=mean(b(channel_dc));
        Applinecheck(count1)=b(channel_line_number,1);
        zdata=b(channel_zdata,:);
        if numel(zdata)==0
            ZMap(count1)=ZMap(count1-1);%if empty
approach, topography same as last
        else
            ZMap(count1)=zdata(end);
        end
        count1=count1+1;
    %end
    count2=count2+1;
    waitbar(i/last_line,h1, 'Topography Progress')
end
close(h1)
zr2=ZMap;
appcurrentraw=appcurrent;
XMapraw=XMapreal;
YMapraw=YMapreal;

%ZMap(end)=[];
%Next section of code reshapes to grid and checks right
number of hops

%Map_b = zeros(floor((last_line-
first_approach)/lines_in_hop)+1,no_frames);

%Now extract CV data
count1=1;
count2=1;

```

```

        h2 = waitbar(0, 'Initializing Functional waitbar...');
        for i=first_surface_IT:lines_in_hop:last_line%forward
part of cv V0 to V1
            %if(mod(count2,x+1)~=1)
                ibulk=i+(first_bulk_IT-first_surface_IT);
                b=A(:,A(channel_line_number,')==i);%extracts
data of these line numbers
                bbulk=A(:,A(channel_line_number,')==ibulk);
                if(numel(b)>0&&numel(bbulk)>0)

currenttimesurf(count1,1:length(b))=b(channel_dc,:);

currenttimebulk(count1,1:length(bbulk))=bbulk(channel_dc,:);
                else

currenttimesurf(count1,:)=currenttimesurf(count1-1,:);

currenttimebulk(count1,:)=currenttimebulk(count1-1,:);
                end
                count1=count1+1;
            %end
            count2=count2+1;
            waitbar(i/last_line,h2, 'Functional Progress')

        end
        close(h2)
    end
    if Extract_data==0
    %%
    %%
    ZMap=zr2;
    XMapreal=XMapraw;
    YMapreal=YMapraw;
    currenttimebulkreal=currenttimebulk;
    currenttimesurfreal=currenttimesurf;
    tol=hopping_distance/5;
    countsame=1;
    for i=2:length(XMapreal)
        if(abs(XMapreal(i)-XMapreal(i-1))<tol && abs(YMapreal(i)-
YMapreal(i-1))<tol)
            list_same(countsame)=i-1;
            countsame=countsame+1;
        end
    end
    for j=length(list_same):-1:1
        XMapreal(list_same(j))=[];
        YMapreal(list_same(j))=[];
        ZMap(list_same(j))=[];
        currenttimebulkreal(list_same(j),:)=[];
        currenttimesurfreal(list_same(j),:)=[];
    end
    countx=1;
    county=1;
    listx=XMapreal(1);
    listy=YMapreal(1);
    for k=2:length(XMapreal)

```

```

    if(XMapreal(k)>max(listx)+tol)
        listx(length(listx)+1)=XMapreal(k);
        countx=countx+1;
    end
    if(YMapreal(k)>max(listy)+tol)
        listy(length(listy)+1)=YMapreal(k);
        county=county+1;
    end
end
listtoremovex=[];
countxremove=1;
for o=1:length(listx)
    countox=0;
    for i=1:length(XMapreal)
        if(abs(XMapreal(i)-listx(o))<tol)
            countox=countox+1;
        end
    end
    if(countox==1)
        listtoremovex(countxremove)=listx(o);
        countxremove=countxremove+1;
        countx=countx-1;
    end
end
listtoremovey=[];
countyremove=1;
for o=1:length(listy)
    countoy=0;
    for i=1:length(YMapreal)
        if(abs(YMapreal(i)-listy(o))<tol)
            countoy=countoy+1;
        end
    end
    if(countoy==1)
        listtoremovey(countyremove)=listy(o);
        countyremove=countyremove+1;
        county=county-1;
    end
end
listtoremovefinal=[];
countfinal=0;
for p=1:length(XMapreal)
    for q=1:length(listtoremovex)
        if(abs(XMapreal(p)-listtoremovex(q))<tol)
            countfinal=countfinal+1;
            listtoremovefinal(countfinal)=p;
        end
    end
    for q=1:length(listtoremovey)
        if(abs(YMapreal(p)-listtoremovey(q))<tol)
            countfinal=countfinal+1;
            listtoremovefinal(countfinal)=p;
        end
    end
end
if(isempty(listtoremovefinal)~=1)

```

```

    for j=length(listtoremovefinal):-1:1
        XMapreal(listtoremovefinal(j))=[];
        YMapreal(listtoremovefinal(j))=[];
        ZMap(listtoremovefinal(j))=[];
        currenttimebulkreal(listtoremovefinal(j),:)=[];
        currenttimesurfreal(listtoremovefinal(j),:)=[];
    end
end
x=countx;
y=county;
if (XMAX>x)
    XMAX=x;
end
if (YMAX>y)
    YMAX=y;
end

ZMap=max(ZMap)-ZMap;
ZMap=ZMap';
XMapreal=XMapreal';
YMapreal=YMapreal';
ZMap=reshape(ZMap,x,y);
XMapreal=reshape(XMapreal,x,y);
YMapreal=reshape(YMapreal,x,y);
ZMap=ZMap';
XMapreal=XMapreal';
YMapreal=YMapreal';
flipstart=2;
for i=flipstart:2:y
    ZMap(i,:)=fliplr(ZMap(i,:));
    XMapreal(i,:)=fliplr(XMapreal(i,:));
    YMapreal(i,:)=fliplr(YMapreal(i,:));
end
ZMap=ZMap-min(min(ZMap));
if remove_topog_drift==1
    %ZMap=test2;
    ZMap3=ZMap; %comment this line out for pixel
picker
    for i=1:y
        datap=1:x;
        [xData, yData] = prepareCurveData( datap,
ZMap(i,:) );
        ft = fittype( 'poly1' );
        opts = fitoptions( ft );
        opts.Lower = [-Inf -Inf];
        opts.Upper = [Inf Inf];
        driftfit2 = fit( xData, yData, ft, opts );
        MyCoeffs3=coeffvalues(driftfit2);
        ZMap3(i,:)=ZMap(i,)-MyCoeffs3(1)*datap-
MyCoeffs3(2);
        ZMap(i,:)=ZMap3(i,:);
    end
end
set(0,'defaultfigurecolor',[1 1 1])
minlength_IT=min([size(currenttimebulkreal,2),size(currenttime
surfreal,2)]);

```

```

timelist=0:datapointtime:datapointtime*(minlength_IT-1);
if(normalise==2)

Map=currenttimesurfreal(:,1:minlength_IT)./currenttimebulkreal
(:,1:minlength_IT);
elseif(normalise==0)
    Map=currenttimesurfreal(:,1:minlength_IT);
elseif(normalise==3)
    Map=currenttimebulkreal(:,1:minlength_IT);
elseif(normalise==1)
    Map=currenttimesurfreal(:,1:minlength_IT)-
currenttimebulkreal(1:minlength_IT);
end
%next section plots topography
if channel_to_plot==3
    zcorrected=ZMap;
    zcorrected=zcorrected-min(min(zcorrected));
    figure( 'Name', 'Topography' );
    imagesc(zcorrected(YMIN:YMAX,XMIN:XMAX))
    view( [0, 90] );
    caxis([nanmin(nanmin(zcorrected))
nanmax(nanmax(zcorrected))])
    figset_9channel
    colormap(parula)
    set(gca, 'XTick', [XMIN,XMAX])
    set(gca, 'XTickLabel', [0,hopping_distance*(XMAX-XMIN)])
    set(gca, 'YTick', [YMIN,YMAX])
    set(gca, 'YTickLabel', [hopping_distance*(YMAX-YMIN),0])
end
end

```

B) SICM Surface Charge Mapping Script

```
%A=load('Filename.tsv');%load data in as A, comment out after
already loaded to save time on future runs
%%
%CV at surface only
set(0,'DefaultFigureColormap',feval('jet'))
close all
movie=0;
Extract_data=0;%1 if running for first time, 0 if data already
loaded
time_to_plot=180000;%what part of IT curve to plot in us (can
change time to plot single frame still)
hopping_distance=0.15;%in um
average=0;%frames to average
plot_movie=0;%plot IT as a movie with settings chosen later
(0=still not movie at time point from time to plot)
channel_to_plot=4;% 3 is topography and 4 normalised current
(charge map)
channel_line_number=11;
channel_voltage=8;
channel_dc=4;
channel_xdata=1;
channel_ydata=2;
channel_zdata=3;
channel_phase=13;
channel_amp=12;
frame_to_plot=0;%0 whole movie, or individual frame if not 0.
remove_topog_drift=1;%1 or 0
startpoint=1;
endpoint=6500;
correctstart=1;
correctend=6561;
datapointtime=4*256;
pulsetime=20000;
normalise=2;%0 no normalise, 1 normalise to bulk subtraction,2
normalise to bulk division, 3 plot bulk
fixcbar=2;
%1. Fix between maximum and minimum over whole scan
%2. Colourbar for each frame
labelsize=20;
%Shouldnt need to change anything below here
last_line = max(A(channel_line_number,:));
lines_in_hop=7;%number of lines between each approach
first_approach=2;%9 normally, 2 if small hopping distance
<=150nm
first_surface_IT=first_approach+1;%line number for first part
of first cv
first_bulk_IT=first_surface_IT+3;
%If you want to crop
if Extract_data==0
XMIN=1;%line number you want to crop from and to
XMAX=61;
YMIN=1;
YMAX=61;
```

```

end
if Extract_data==1
    %%
    %Make X, Y Grid for plots
    %Extract topography
    count1=1;
    count2=1;
    h1 = waitbar(0, 'Initializing Topography waitbar...');
    for i=[first_approach:lines_in_hop:last_line]
        %if(mod(count2,x+1)~=1)
            b=A(:,A(channel_line_number,:)==i);%picks out
approaches by line number
            XMapreal(count1)=mean(b(channel_xdata,:));
            YMapreal(count1)=mean(b(channel_ydata,:));
            appcurrent(count1)=mean(b(channel_dc));
            Applinecheck(count1)=b(channel_line_number,1);
            zdata=b(channel_zdata,:);
            if numel(zdata)==0
                ZMap(count1)=ZMap(count1-1);%if empty
approach, topography same as last
            else
                ZMap(count1)=zdata(end);
            end
            count1=count1+1;
        %end
        count2=count2+1;
        waitbar(i/last_line,h1, 'Topography Progress')
    end
    close(h1)
    zr2=ZMap;
    appcurrentraw=appcurrent;
    XMapraw=XMapreal;
    YMapraw=YMapreal;

    %ZMap(end)=[];
    %Next section of code reshapes to grid and checks right
number of hops

    %Map_b = zeros(floor((last_line-
first_approach)/lines_in_hop)+1,no_frames);

    %Now extract CV data
    count1=1;
    count2=1;
    h2 = waitbar(0, 'Initializing Functional waitbar...');
    for i=first_surface_IT:lines_in_hop:last_line%forward
part of cv V0 to V1
        %if(mod(count2,x+1)~=1)
            ibulk=i+(first_bulk_IT-first_surface_IT);
            b=A(:,A(channel_line_number,:)==i);%extracts
data of these line numbers
            bbulk=A(:,A(channel_line_number,:)==ibulk);
            if (numel(b)>0&&numel(bbulk)>0)

currenttimesurf(count1,1:length(b))=b(channel_dc,:);

```

```

currenttimebulk(count1,1:length(bbulk))=bbulk(channel_dc,:);
    else

currenttimesurf(count1,:)=currenttimesurf(count1-1,:);

currenttimebulk(count1,:)=currenttimebulk(count1-1,:);
    end
    count1=count1+1;
%%end
count2=count2+1;
waitbar(i/last_line,h2,'Functional Progress')

    end
    close(h2)
end
if Extract_data==0
%%
%%
ZMap=zr2;
XMapreal=XMapraw;
YMapreal=YMapraw;
currenttimebulkreal=currenttimebulk;
currenttimesurfreal=currenttimesurf;
tol=hopping_distance/5;
countsame=1;
for i=2:length(XMapreal)
    if(abs(XMapreal(i)-XMapreal(i-1))<tol && abs(YMapreal(i)-
YMapreal(i-1))<tol)
        list_same(countsame)=i-1;
        countsame=countsame+1;
    end
end
for j=length(list_same):-1:1
    XMapreal(list_same(j))=[];
    YMapreal(list_same(j))=[];
    ZMap(list_same(j))=[];
    currenttimebulkreal(list_same(j),:)=[];
    currenttimesurfreal(list_same(j),:)=[];
end
countx=1;
county=1;
listx=XMapreal(1);
listy=YMapreal(1);
for k=2:length(XMapreal)
    if(XMapreal(k)>max(listx)+tol)
        listx(length(listx)+1)=XMapreal(k);
        countx=countx+1;
    end
    if(YMapreal(k)>max(listy)+tol)
        listy(length(listy)+1)=YMapreal(k);
        county=county+1;
    end
end
listtoremovex=[];
countxremove=1;

```

```

for o=1:length(listx)
    countox=0;
    for i=1:length(XMapreal)
        if(abs(XMapreal(i)-listx(o))<tol)
            countox=countox+1;
        end
    end
    if(countox==1)
        listtoremovex(countxremove)=listx(o);
        countxremove=countxremove+1;
        countx=countx-1;
    end
end
listtoremovey=[];
countyremove=1;
for o=1:length(listy)
    countoy=0;
    for i=1:length(YMapreal)
        if(abs(YMapreal(i)-listy(o))<tol)
            countoy=countoy+1;
        end
    end
    if(countoy==1)
        listtoremovey(countyremove)=listy(o);
        countyremove=countyremove+1;
        county=county-1;
    end
end
listtoremovefinal=[];
countfinal=0;
for p=1:length(XMapreal)
    for q=1:length(listtoremovex)
        if(abs(XMapreal(p)-listtoremovex(q))<tol)
            countfinal=countfinal+1;
            listtoremovefinal(countfinal)=p;
        end
    end
    for q=1:length(listtoremovey)
        if(abs(YMapreal(p)-listtoremovey(q))<tol)
            countfinal=countfinal+1;
            listtoremovefinal(countfinal)=p;
        end
    end
end
if(isempty(listtoremovefinal)~=1)
    for j=length(listtoremovefinal):-1:1
        XMapreal(listtoremovefinal(j))=[];
        YMapreal(listtoremovefinal(j))=[];
        ZMap(listtoremovefinal(j))=[];
        currenttimebulkreal(listtoremovefinal(j),:)=[];
        currenttimesurfreal(listtoremovefinal(j),:)=[];
    end
end
x=countx;
y=county;
if(XMAX>x)

```

```

        XMAX=x;
end
if (YMAX>y)
    YMAX=y;
end

ZMap=max (ZMap) -ZMap;
ZMap=ZMap';
XMapreal=XMapreal';
YMapreal=YMapreal';
ZMap=reshape (ZMap, x, y);
XMapreal=reshape (XMapreal, x, y);
YMapreal=reshape (YMapreal, x, y);
ZMap=ZMap';
XMapreal=XMapreal';
YMapreal=YMapreal';
flipstart=2;
for i=flipstart:2:y
    ZMap (i, :)=fliplr (ZMap (i, :));
    XMapreal (i, :)=fliplr (XMapreal (i, :));
    YMapreal (i, :)=fliplr (YMapreal (i, :));
end
ZMap=ZMap-min (min (ZMap));
if remove_topog_drift==1
    %ZMap=test2;
    ZMap3=ZMap;
    for i=1:y
        datap=1:x;
        [xData, yData] = prepareCurveData ( datap,
ZMap (i, :)) ;
        ft = fittype ( 'poly1' );
        opts = fitoptions ( ft );
        opts.Lower = [-Inf -Inf];
        opts.Upper = [Inf Inf];
        driftfit2 = fit ( xData, yData, ft, opts );
        MyCoeffs3=coeffvalues (driftfit2);
        ZMap3 (i, :)=ZMap (i, :)-MyCoeffs3 (1)*datap-
MyCoeffs3 (2);
        ZMap (i, :)=ZMap3 (i, :);
    end
end
set (0, 'defaultfigurecolor', [1 1 1])
minlength_IT=min ([size (currenttimebulkreal, 2), size (currenttime
surfreal, 2)]);
timelist=0:datapointtime:datapointtime*(minlength_IT-1);
if (normalise==2)

Map=currenttimesurfreal (:, 1:minlength_IT) ./currenttimebulkreal
(:, 1:minlength_IT);
elseif (normalise==0)
    Map=currenttimesurfreal (:, 1:minlength_IT);
elseif (normalise==3)
    Map=currenttimebulkreal (:, 1:minlength_IT);
elseif (normalise==1)
    Map=currenttimesurfreal (:, 1:minlength_IT) -
currenttimebulkreal (1:minlength_IT);

```

```

end
%next section plots topography
if channel_to_plot==3
    zcorrected=ZMap;
    zcorrected=zcorrected-min(min(zcorrected));
    figure( 'Name', 'Topography' );
    imagesc(zcorrected(YMIN:YMAX,XMIN:XMAX))
    view( [0, 90] );
    caxis([nanmin(nanmin(zcorrected))
nanmax(nanmax(zcorrected))])
    figset_9channel
    colormap(parula)
    set(gca, 'XTick', [XMIN,XMAX])
    set(gca, 'XTickLabel', [0,hopping_distance*(XMAX-XMIN)])
    set(gca, 'YTick', [YMIN,YMAX])
    set(gca, 'YTickLabel', [hopping_distance*(YMAX-YMIN),0])
else%plot the chosen variable
    if(plot_movie==1)
        frames_that_will_be_plotted=1:1:minlength_IT;%all data
        movie=1;
    else
        difference=abs(time_to_plot-timelist);
        [idx2 idx2] = min(difference);
        frames_that_will_be_plotted=idx2;
        movie=0;
    end
    count=0;
    frame_count=1;
    for i=frames_that_will_be_plotted
        str = num2str(round(timelist(i)));
        comb=strcat(str, ' \mus');
        if(average==0)
            topplot_s=Map(:,i);
        else
            topplot_2=Map(:,i-average:i);
            topplot_s=Map(:,i);
            for j=1:length(topplot_s)
                topplot_s(j)=mean(topplot_2(j,:));
            end
        end
        topplot_s=topplot_s';
        topplot_s=reshape(topplot_s,x,y);
        topplot_s=topplot_s';
        for i=flipstart:2:y
            topplot_s(i,:)=fliplr(topplot_s(i,:));
        end
        h4 = imagesc(topplot_s(YMIN:YMAX,XMIN:XMAX));
        cbar=colorbar;
        colormap(flipud(jet))
        caxis([nanmin(nanmin(topplot_s))
nanmax(nanmax(topplot_s))]);
        caxis([0.96,1.02]);% scale for charge map for dc
        if fixcbar==1
            if channel_to_plot==channel_dc

```

```

caxis([nanmin(nanmin(Map(:, find(v_list==min(v_list))))))
nanmax(nanmax(Map(:, find(v_list==max(v_list)))))]);
    else
        caxis([nanmin(nanmin(Map))
nanmax(nanmax(Map))]);
    end
    end
    if fixcbar==3
        caxis([cbarmin, cbarmax])
    end
    title(comb, 'fontsize', labelsize, 'fontweight', 'bold' )
    figset_9channel
    %axis off
    set(gca, 'XTick', [XMIN, XMAX])
    set(gca, 'XTickLabel', [0, hopping_distance*(XMAX-XMIN)])
    set(gca, 'YTick', [YMIN, YMAX])
    set(gca, 'YTickLabel', [hopping_distance*(YMAX-YMIN), 0])
    pause(0.001)
   (gcf);
    F(frame_count) = getframe(gcf);
    frame_count=frame_count+1;
    pause(0.001)
end
end
end

```

*“Education never ends, Watson,
It is a series of lessons,
with the greatest for the last”*

*– Sherlock Holmes, His Last Bow
by Sir Arthur Conan Doyle*

